



Review Paper

Advancements in the preparation of high-performance liquid chromatographic organic polymer monoliths for the separation of small-molecule drugs

Xiali Ding^a, Jing Yang^a, Yuming Dong^{a,b,*}

^a Institute of Pharmaceutical Analysis, School of Pharmacy, Lanzhou University, Lanzhou, Gansu 730000, PR China

^b Lanzhou University-Techcomp (China) Ltd. Joint Laboratory of Pharmaceutical Analysis, Lanzhou, Gansu 730000, PR China



ARTICLE INFO

Article history:

Received 27 January 2017

Received in revised form

26 January 2018

Accepted 1 February 2018

Available online 13 March 2018

Keywords:

High-performance liquid chromatography

Polymer monolith

Preparation methods

Small molecules

ABSTRACT

The various advantages of organic polymer monoliths, including relatively simple preparation processes, abundant monomer availability, and a wide application range of pH, have attracted the attention of chromatographers. Organic polymer monoliths prepared by traditional methods only have macropores and mesopores, and micropores of less than 50 nm are not commonly available. These typical monoliths are suitable for the separation of biological macromolecules such as proteins and nucleic acids, but their ability to separate small molecular compounds is poor. In recent years, researchers have successfully modified polymer monoliths to achieve uniform compact pore structures. In particular, microporous materials with pores of 50 nm or less that can provide a large enough surface area are the key to the separation of small molecules. In this review, preparation methods of polymer monoliths for high-performance liquid chromatography, including ultra-high cross-linking technology, post-surface modification, and the addition of nanomaterials, are discussed. Modified monolithic columns have been used successfully to separate small molecules with obvious improvements in column efficiency.

© 2018 Xi'an Jiaotong University. Production and hosting by Elsevier B.V. This is an open access article under the CC BY-NC-ND license (<http://creativecommons.org/licenses/by-nc-nd/4.0/>).

Contents

1. Introduction	76
2. Factors affecting the polymerization reaction of monolithic column	76
2.1. Selection of monomer and crosslinker	76
2.2. Proportion of monomer, crosslinker, and porogen	77
2.3. Porogen choice	78
2.4. Polymerization time and temperature	79
3. Modified polymer monoliths	81
3.1. Functionalization of polymer monoliths	81
3.1.1. Click chemistry and grafting	81
3.1.2. Zwitterionic monomers	81
3.2. Hypercrosslinking polymerization technique	81
3.3. Metal-organic frameworks	82
3.4. Nanomaterials	82
3.4.1. Metal nanoparticles	82
3.4.2. Carbon nanotubes	83
3.4.3. Graphene	83
4. Conclusions and outlook	83
References	84

Peer review under responsibility of Xi'an Jiaotong University.

* Corresponding author at: Institute of Pharmaceutical Analysis, School of Pharmacy, Lanzhou University, Lanzhou, Gansu 730000, PR China.

E-mail address: dongym@lzu.edu.cn (Y. Dong).

<http://dx.doi.org/10.1016/j.jpha.2018.02.001>

2095-1779/© 2018 Xi'an Jiaotong University. Production and hosting by Elsevier B.V. This is an open access article under the CC BY-NC-ND license (<http://creativecommons.org/licenses/by-nc-nd/4.0/>).

1. Introduction

As a new fourth generation of chromatographic separation media, monolithic columns with good permeability and high mass transfer speed play an increasingly important role in analytical investigations in the fields of environmental science, pharmaceutical analysis, food and chemistry [1,2]. Depending on the type of substrate, monoliths can be divided into three categories: organic polymer monoliths, inorganic monoliths (mainly silica monoliths) and hybrid monoliths [3–5]. Inorganic silica monoliths use the alkoxysilane as the main material, with columns prepared by direct sintering or the use of a sol-gel. The preparation of organic polymer monolithic columns usually involves light- or heat-induced polymerization using crosslinking agents, porogens and initiators [6,7] as raw materials. Compared with inorganic silica monoliths, the preparation process for polymeric monoliths is relatively simple, with an abundant choice of monomer species, a wide pH range (2–12) and easy surface modification [8]. Therefore, polymeric monoliths have wide range of applications, and are extensively used for the separation and enrichment of complex samples. The overall structure of micropores is an important factor that determines the separation performance of organic polymer monoliths. Therefore, a suitable pore structure is essential to obtain good resolution. Although organic polymer monoliths prepared by traditional methods have many advantages, there have few mesopores and almost no micropores, and thus their ability to separate small molecules is poor [9,10]. According to the International Union of Pure and Applied Chemistry (IUPAC), micropores have pore sizes of ≤ 2 nm, mesopores have pore sizes of 2–50 nm, and macropores have pore sizes of > 50 nm. Thus, in recent years, studies on high-performance liquid chromatographic monoliths have concentrated on polymeric materials, which are suitable for separating small molecules. To improve the performance of organic polymer monoliths for separating small molecules, researchers have mainly examined optimization of the preparation conditions and surface modifications with metal-organic frameworks or nanomaterials [11,12].

2. Factors affecting the polymerization reaction of monolithic column

The structure of a polymer monolithic column must provide a large surface area, similar to those achieved using silica monoliths. Although macropores are necessary to achieve monolithic columns with good permeability, they have little effect on the overall surface area of a polymer monolithic column [13]. Therefore, the current literature has focused mostly on finding preparation processes that both retain the advantages of high velocity and increase the overall surface area of the column. From the viewpoint of chemical polymerization, several factors can influence the surface area and permeability of the column, including the selection of monomer and crosslinker; the proportion of monomer, crosslinker, and porogen; and the polymerization temperature and reaction time [14].

2.1. Selection of monomer and crosslinker

The selection of monomer and crosslinker not only affects the formation of the pore structure in the polymer monolith, but also determines the chemical composition of the polymer monolith, which is the main factor affecting the performance of the monolith. Note that the density and rigidity of the prepared column depend, to a large extent, on the nature and the initial concentration of the monomer [15]. Therefore, to obtain high column efficiency and strong mechanical stability, the selection of the monomer is a very important step.

Table 1
Properties of different monomer types.

Monomer type	Monomer properties	Advantages	Disadvantages
Acrylamides	Strong hydrophilicity	For gel electrophoresis	Poor stability
Styrenes	High hydrophobicity	High hardness, stable properties	Difficult modification
Acrylates	With epoxy active functional groups	Easy to modify	Unstable properties

At present, because various monomers have been used to prepare different monoliths for the separation of different small molecules, investigations into the influence of monomer type on the structure of the monolith are ongoing.

Based on the type of monomer, organic polymer-based monolithic columns can be divided into three categories: styrenes [16], acrylates [17], and acrylamides [18]. Different monomers have different advantages and disadvantages, as summarized in Table 1.

In 2014, Bai [19] prepared a monolithic column with a uniform framework, good permeability, and high column efficiency. The monolith was applied as a high-performance liquid chromatography (HPLC) stationary phase to separate alkaline, acidic and neutral small molecules. The results showed that alkaline, acidic small molecular compounds were separated quickly and efficiently on the monolithic column (Fig. 1). The good performance of the column was related to the uniform pore structure, originating from the use of trimethylolpropane triacrylate (TMPTA), which contains three terminal double bonds (Fig. 2).

Liu et al. [20] used a 1-dodecene polymeric monolith to separate benzotriazole, benzene, biphenyl, anthracene, and other small molecules successfully. The combination of 1-dodecene, which is highly hydrophobic, with an acrylate results in a monolith with the desired pore structure. They also optimized the preparation conditions and found that the amount of crosslinking agent directly affected the column pressure. Excessive amounts of crosslinking agent caused a high column pressure, which decreased the permeability of the column. On the contrary, when the amount of crosslinking agent is too low, the monolith structure will be loose. They also found that too much porogen led to low mechanical strength, as well as a loose monolith structure.

It has been reported that higher crosslinker concentrations can provide higher mechanical stability and a higher surface area [21]. Liu et al. [22] has suggested that significant advantages are realized when a single-monomer/crosslinker is used, including straightforward optimization of the polymerization solution, improved column-to-column reproducibility, better mechanical stability, and higher surface area owing to a highly crosslinked network. The effect of monomer content on the overall column efficiency, porosity, and surface area was investigated. It was found

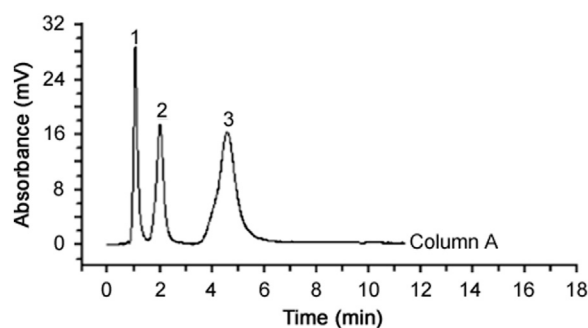


Fig. 1. Chromatogram showing the separation of small molecules on the poly(TMPTA-co-EDMA) column. Conditions: mobile phase: methanol:water (75:25, v/v); flow rate: 1.0 mL/min. Analytes: (1) 1H-benzotriazole, (2) p-xylene, (3) biphenyl [19].

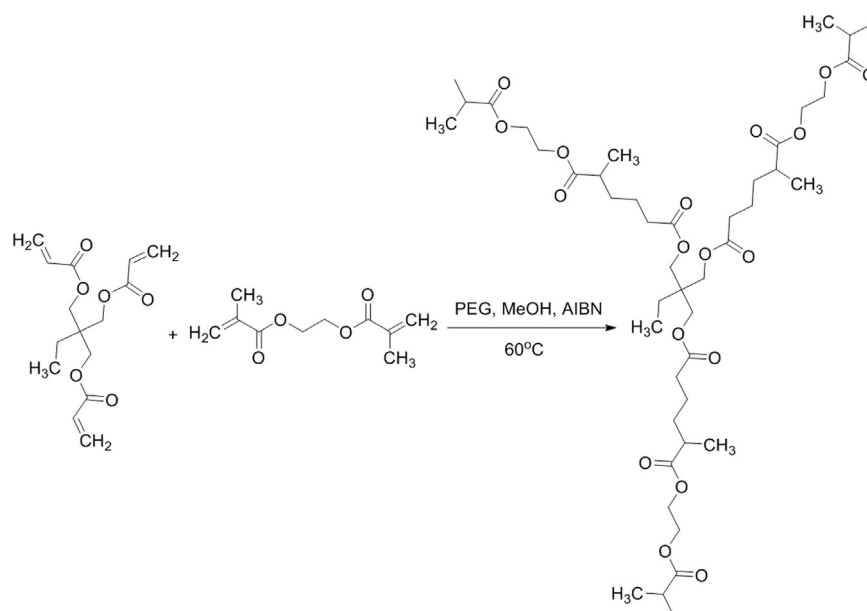


Fig. 2. Synthetic route for the poly(TMPTA-co-EDMA) monolith [19].

Table 2

Common monomers in the preparation of monoliths.

Polymerization method	Monomer	Crosslinking monomer	Porogen	Initiator	Analyte	Ref.
In-situ free-radical polymerization	TMPTA	EDMA	Polyethylene glycol methanol	AIBN	Alkaline, acidic, neutral small molecules.	[17]
In-situ free-radical polymerization	1-dodecene	TMPTA EDMA		AIBN	Benzotriazole, benzene, biphenyl, anthracene	[19]
In-situ free-radical polymerization	TVBS		Dodecanol toluene	AIBN	Aniline compounds	[23]
In-situ free-radical polymerization	Styrene divinylbenzene		Dodecanol toluene	AIBN	Alkylbenzenes	[25]
In-situ free-radical polymerization	1,3-BDDMA, 1,4-BDDMA, NPGDMA, 1,5-PDDMA, 1,6-HDDMA, 1,10-DDDMA, 1,12-DoDDMA		Dodecanol methanol	AIBN	Alkylbenzenes alkylparabens	[22]

Note: trimethylolpropane triacrylate(TMPTA), ethylene glycol dimethacrylate (EDMA), 2,2-azobisisobutyronitrile(AIBN), tetrakis(4-vinylbenzyl)silane (TVBS), 1,3-butanediol dimethacrylate (1,3-BDDMA), 1,4-butanediol dimethacrylate (1,4-BDDMA), neopentyl glycol dimethacrylate (NPGDMA), 1,5-pentanediol dimethacrylate(1,5-PDDMA), 1,6-hexanediol dimethacrylate (1,6-HDDMA), 1,10-decanediol dimethacrylate(1,10-DDDMA), 1,12-dodecanediol dimethacrylate (1,12-DoDDMA).

that the surface area, porosity, and column efficiency increased when the monomer content was reduced from 20% to 17.5% [23]. Highly crosslinked networks resulting from crosslinking a single monomer were found to enhance the concentrations of mesopores in and the surface areas of polymeric monoliths. Li et al. [24] synthesized monolithic columns with four different monomers and optimized the preparation processes. The optimized monoliths synthesized from each of the crosslinked monomers showed high permeability, with little swelling or shrinkage observed in solvents with different polarities. Some common monomers used in the preparation of monoliths [17,19,22,23,25] are shown in Table 2.

2.2. Proportion of monomer, crosslinker, and porogen

The proportion of monomer, crosslinker, and porogen is very important for the preparation of polymer monoliths. In particular, the proportion of monomer and crosslinking agent has a very significant impact on the pore structure and chemical properties of a monolith. If the ratio of monomer to crosslinking agent is too large, the pore size will be too small and reduce the permeability; in contrast, if the pore size is too large, efficient separation cannot be achieved.

Poly (vinyl ester resin-co-ethylene glycol dimethacrylate) (poly (VER-co-EDMA)) was prepared to investigate the influence on the proportion of crosslinking agent and monomer [26]. The results showed that the retention time of toluene increased as the monomer concentration increased, with the best efficiency obtained when the monomer concentration was 30%. When the monomer concentration was increased further, the column exhibited poor permeability (Fig. 3).

In 2014, Wei [27] employed pentaerythritol triacrylate (PETA) and triallyl isocyanurate (TAIC) as monomers, azodiisobutyronitrile (AIBN) as an initiator, cetyl alcohol as a porogen, and methanol as a solvent to prepare a monolith through a free radical polymerization process. As the content of TAIC or PETA increased, the pore structure of the monolith became too dense, causing an increase of the column pressure. In contrast, when the content of TAIC or PETA decreased, the pore structure was loose. Therefore, the proportion of monomers and crosslinker was important for the performance of this monolithic column.

Hao [28] used 1-dodecene as a monomer, VER as a crosslinking agent, dodecanol as a porogen, and a redox initiator to prepare a poly (C12-co-VER) monolithic column. Benzoic acid, *p*-xylene, *p*-amino azobenzene, benzene, terephthalic acid, naphthol,

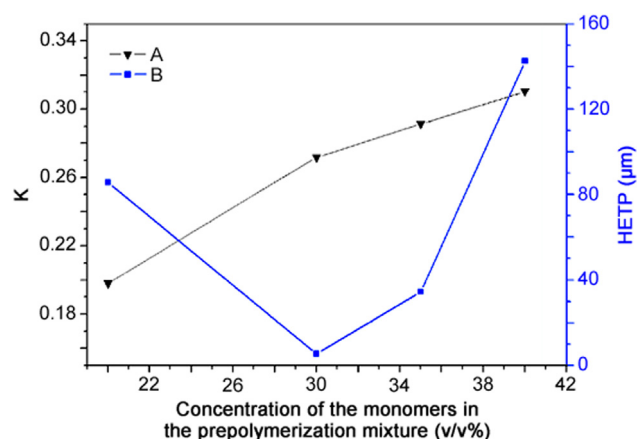


Fig. 3. (A) Effects of monomer content on the retention abilities of poly (VER-co-EDMA) monolithic columns. (B) Effects of monomer content on the efficiency of poly (VER-co-EDMA) monolithic columns. Conditions: effective length: 100 mm \times 150 μ m i.d.; test compound: toluene; mobile phase: methanol:water (80:20, v/v); flow rate: 3 μ L/min; UV detection at 214 nm [26].

anthrone, and other small molecules were separated successfully using this column (Fig. 4).

Several monoliths with different proportions of 1-dodecene, VER, and dodecanol were used to examine how the extent of polymerization impacts performance. The results indicated that increasing the amount of monomer or crosslinking agent increased the column pressure. Meanwhile, the initiation method also influences the speed of the polymerization reaction and the pore size obtained, thereby affecting the performance of monolith (Fig. 5). As shown in Fig. 5, the redox method is better than the thermal method for preparing poly (C12-co-VER) monolith columns.

Dou et al. [29] used [2-(methacryloyloxyethyl) ethyl] dimethyl (3-sulfopropyl) ammonium hydroxide (SPE) as a monomer, *N*-ethyl-*N*, *N*-dimethyl-1-dodecanaminium hydroxide (EDMA) as a crosslinking agent, AIBN as an initiator and *n*-propanol, 1, 4-butanediol, and water as porogens to prepare a SPE-co-EDMA monolithic column. The authors investigated the effect of the amount of initiator on the speed of the polymer reaction and the size of the pores. When the amount of initiator was too low, polymerization speed was very slow, and the reaction did not proceed to a significant extent. In contrast, when the amount of initiator was too large, the rate of monomer polymerization was fast, the polymer pore size was smaller, and the permeability decreased.

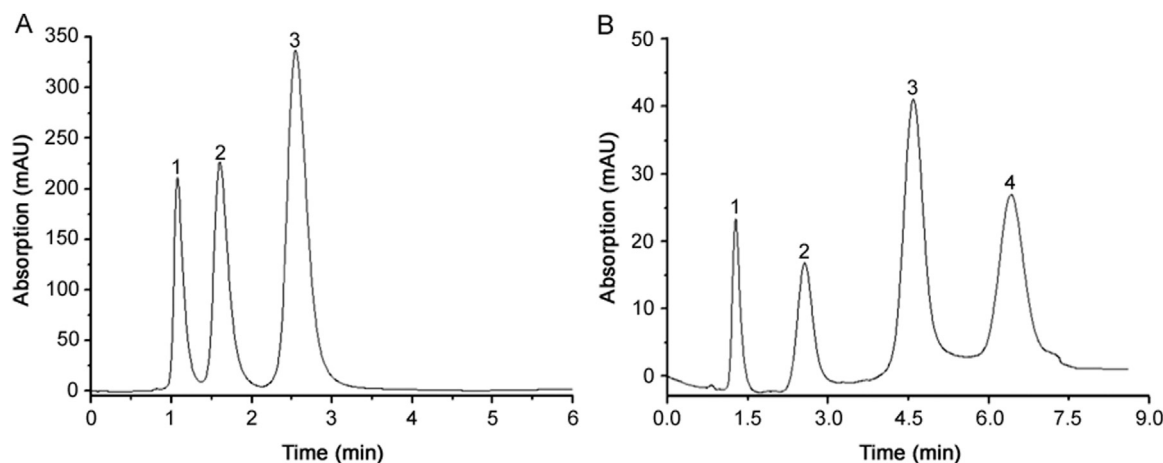


Fig. 4. Elution profiles of small molecules on a poly(C12-co-VER) column. Conditions: effective length: 50 mm \times 4.6 mm i.d.; mobile phase: methanol:water (75:25, v/v); flow rate: 1.0 mL/min, UV detection at 254 nm. Samples A: (1) benzoic acid, (2) xylene, (3) *p*-aminoazobenzene; Samples B: (1) benzene, (2) terephthalic acid, (3) 1-naphthol, (4) anthrone [28].

In summary, increasing the amount of crosslinking agent produces monoliths with smaller pore sizes and dense structures, whereas reducing the amount of crosslinking agent produces monoliths with larger pore sizes, leading to loose structures. The monomer polymerization speed is slow when less initiator is used, whereas using excessive initiator decreases pore size.

2.3. Porogen choice

An appropriate porogen is very important when preparing polymer monoliths, because the porogen can control the pore properties. The choice of porogen can affect the performance of the monolith significantly. Monoliths prepared with a single porogen have loose pore structures, poor stability, and low separation performance. Thus, two kinds of porogens have been commonly used. The first type of porogen, in which the monomer is soluble, results in polymer monoliths with relatively large pore sizes. The other type porogen, in which the monomer is insoluble, results in a smaller pore structure. In recent years, binary and ternary porogens have often been used in the preparation of monolithic organic polymer columns [30–41] (Table 3).

Liu et al. [22] investigated how the choice of porogen impacted column performance, and the results showed that dodecanol and methanol were good and poor solvents, respectively, when 1, 12-dodecanediol dimethacrylate (1,12-DoDDMA) was used to prepare the monolith. They also examined the impacts of others porogens, including methanol, isobutanol, toluene, tetrahydrofuran (THF), and acetonitrile (ACN), on the performance of the monolithic column. Toluene, THF, and ACN were found to be "good" solvents, whereas methanol and isobutanol were "poor" solvents for 1,12-DoDDMA. Methanol, isobutanol, and decanol or dodecanol formed a compact porous structure. However, a gel structure was formed when toluene, THF, or ACN was combined with decanol or dodecanol. Although decanol could also be used to prepare monolithic column, the performance of the prepared monolithic column was poor. When isobutanol and dodecanol were combined to prepare a monolithic column, the column pressure was high (more than 3000 psi at a flow rate of 100 nL/min). Therefore, methanol and dodecanol were the preferred porogen combination.

Gao et al. [37] used [3-(methacryloylamino) propyl]dimethyl(3-sulfopropyl)ammonium hydroxide inner salt (SPP) as a zwitterionic monomer, PETA as a crosslinking agent, and ethanol-ethylene glycol as a porogen to synthesize a hydrophilic SPP-co-PETA monolith, on which phenolic compounds were successfully

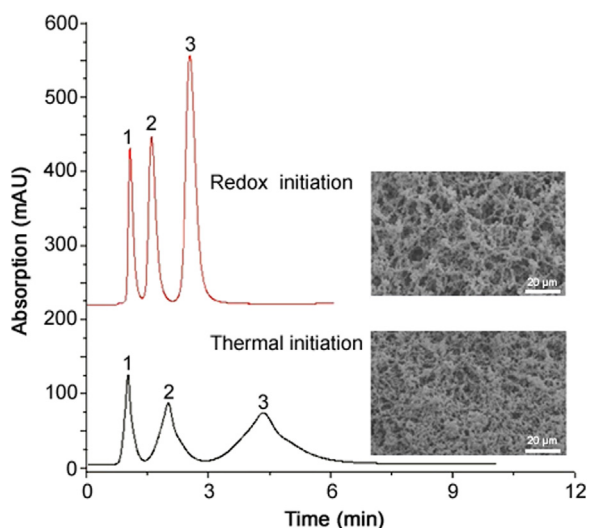


Fig. 5. Comparison of monolithic columns obtained using different initiation methods. Analytes: (1) benzoic acid, (2) xylene, (3) *p*-aminoazobenzene; mobile phase: methanol:water (75:25, v/v) [28].

separated. Then they compared the hydrophilic properties of monolithic columns prepared using various porogens when nuclear glycosides and phenolic compounds were used as model compounds. The results indicated that the monoliths obtained when ethanol-ethylene glycol was used as a porogen had high column efficiency and better separation performance, whereas the monolith obtained when methanol-1,4-butanediol glycol was used as a porogen had good permeability.

In 2014, Li et al. [38] used hexanediol dimethacrylate (HDDA) and butylmethacrylate (BMA) as monomers, EDMA as a cross-linking agent, and dodecyl alcohol as a porogen to prepare a polymer monolith with good permeability, high mechanical stability and a large surface area. Benzene, amines, and phenols were successfully separated on the prepared monolithic column. Subsequently, the effects of different porogens, including dodecanol, isopropyl alcohol, polyethylene glycol, cyclohexanol, and 1,4-butanediol, on the monolithic structure were examined. The results showed that using isopropyl alcohol, polyethylene glycol, cyclohexanol, or 1, 4-butanediol as a porogen to prepare the monolith resulted in poor permeability. Dodecanol was the best choice of porogen because the obtained structure had uniform pores and

the column had appropriate hardness, good permeability, and low back pressure. Zhong et al. [39] investigated the impact of different porogens on monolithic column preparation. The monolith was too soft to be used as a stationary phase when polyethylene glycol (PEG) 200 was used. Further, connections between pores were lacking when a single porogen (1, 2-propanediol or 1-hexadecanol) was used. The monoliths obtained using PEG-200 and 1, 2-propanediol as co-porogens had a robust granulous structure and low back pressure. The binary porogen realized both full solubility of the monomers and a robust stationary phase for HPLC (Fig. 6).

2.4. Polymerization time and temperature

The polymerization temperature controls the pore distribution in a monolith and is thus a very important factor, affecting the formation of the pore structure and the surface area. High temperatures reduce permeability and lead to high back pressures. In contrast, when the polymerization temperature is too low, the reaction speed is slow and the reaction may not proceed. The polymerization time significantly affects the internal structure of a polymer monolith. Longer polymerization times result in further reactions of the monomer, which reduces the polymer pore size and lowers the porosity.

Tong [42] compared the pore size distributions of polymer monoliths prepared using the same polymerization mixture at different temperatures. The results indicated that when the temperature was 70 °C, the pore size was about 100 nm, whereas when the temperature was 130 °C, the pore size was about 1000 nm. If temperature is too low, the polymerization reaction cannot proceed. As the temperature increases, the molecular weight of the polymer will increase and the number of macropores will also increase, which reduces the surface area of the column. However, when the temperature is too high, the reaction speed is too fast.

Niu [26] prepared a poly (VER-co-EDMA) monolith with a three-dimensional network structure when the polymerization temperature was 70 °C or 80 °C. However, the reaction rate was too fast, resulting in a microsphere-packed structure that caused poor permeability. When the reaction temperature was 40 °C or 50 °C, polymerization did not occur. AIBN was used as a radical initiator in this reaction, and as its decomposition temperature was 60–85 °C, it could not initiate the polymerization reaction when the reaction temperature was below 60 °C. However, when the

Table 3
Common porogens used in the preparation of monoliths.

Type of monoliths	Monolithic column	Porogen	Ref.
Poly(styrene-co-divinylbenzene)		Water, methanol, ethanol	[30]
		1-propanol, formamide	[31]
		Toluene, isooctane	[32]
Polymethacrylate-based monoliths	Poly(BMA-EDMA)	Toluene, isooctane methacrylic acid(micro-porogen)	[32]
	Poly(SMA-co-2-Me-1,8-ODDMA)	1-propanol, 1,4-butanediol, water	[33]
	Poly(BMA-co-EDMA)	Tert.-butanol, 1,4-butanediol	[34]
	Poly(BMA-co-META-co-EDMA)	1-propanol, 1,4-butanediol, water	[35]
	Poly(1,12-DoDDMA)	Water, 1,4-butanediol, 1-propanol	[36]
	Poly(VER-co-EDMA)	Methanol, dodecanol	[22]
	Poly(SPP- PETA)	<i>n</i> -butanol, 1,4-butanediol, water	[26]
	Poly(HDDA-co-BMA-co-EDMA)	Ethanol, ethylene glycol	[37]
	Poly(TAIC -TMPTA)	Dodecyl alcohol	[38]
		Polyethylene glycol 200, 1,2-propanediol	[39]
Polymers	Glycerol dimethacrylate	Polystyrene, chlorobenzene	[40]
	Poly(ethylene glycol methyl ether acrylate-co-polyethylene glycol diacrylate)	Ethyl ether, poly(ethyleneoxide)-poly(propylene oxide)-poly(ethylene oxide)	[41]

Note: butylmethacrylate (BMA), ethylenedimethacrylate (EDMA), stearyl methacrylate (SMA), 2-methyl-1,8-octanediol dimethacrylate (2-Me-1,8-ODDMA), [2-(methacryloyloxy)ethyl]-trimethyl ammonium chloride (META), 1,12-dodecanediol dimethacrylate (1,12-DoDDMA), vinyl ester resin(VER), triallyl isocyanurate (TAIC) -trimethylolpropane triacrylate (TMPTA), [[3-(methacryloylamino) propyl] dimethyl(3-sulfopropyl)ammonium hydroxide inner salt](SPP).

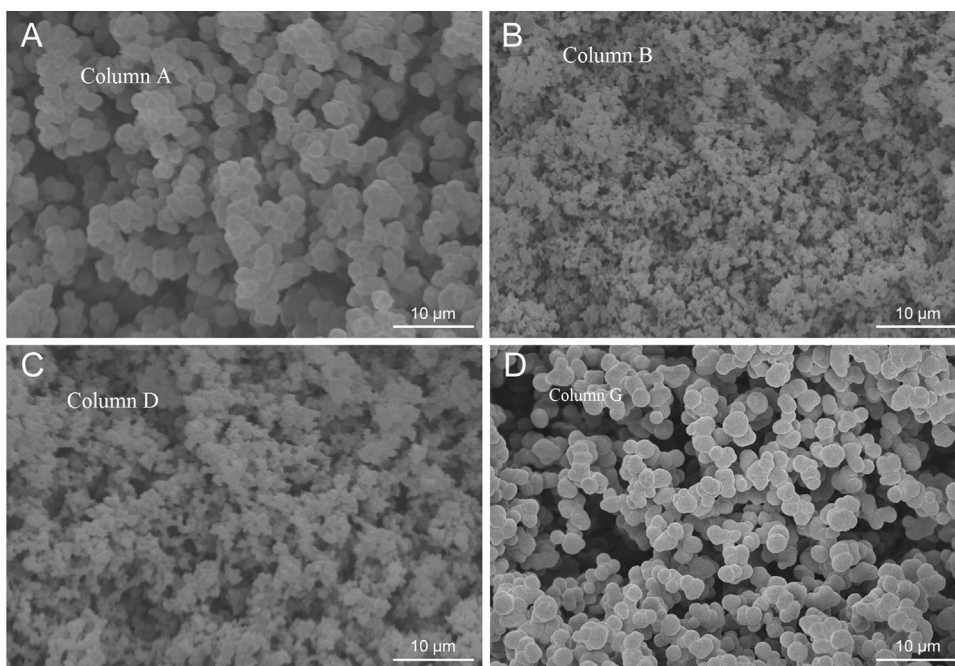


Fig. 6. SEM photographs of the porous structures obtained with different porogen compositions. (A) PEG-200, (B) 1, 2-propanediol, (C) 1-hexadecanol, and (D) PEG-200/1,2-propanediol (4:9,v/v) [39].

temperature was too high, the reaction was not controlled, leading to an uneven column structure.

In 2014, Liu et al. [43] used *N*-isopropylacrylamide (NIPAAm) and TMPTA as monomers and EDMA as a crosslinking agent to prepare polymer monoliths. The column temperature was adjusted to improve the column efficiency for separating small molecules. Increasing the column temperature from 25 °C to 70 °C was found to reduce the retention time of small compounds. Increasing the temperature improves diffusion of the solutes, which can help to achieve rapid separation. However, elution is only affected by the hydrophobicity of the compounds and the character of the stationary phase. As the hydrophobicity of nisoldipine is greater than that of nifedipine, nisoldipine has a faster elution rate. Considering the effect of temperature on poly(HDDA-co-BMA-co-EDMA) monolith, polymerization temperatures of 50 °C, 60 °C, 70 °C, and 80 °C were investigated. When the temperature was 50 °C, the pore structure was relatively loose and the stability was poor. When the temperature was 70 °C or 80 °C, the pore structure was too compact and the monolith had a high back pressure. Thus, the ideal temperature for a good pore structure and permeability was 60 °C [38].

Nischang and Brüggemann [44] examined the effect of polymerization time on the performance of monolithic poly (BMA-co-EDMA) columns. The authors demonstrated that a monolithic column prepared under incomplete conversion conditions exhibited good performance for the separation of alkylbenzenes, whereas a similar column polymerized for 48 h failed completely. They also observed a significant decrease in permeability with increasing polymerization time, as supported by SEM micrographs (Fig. 7).

3. Modified polymer monoliths

Although organic polymer monoliths have many advantages, their weak mechanical stabilities and low surface areas are not suitable for the separation of small molecules, which limits their application to pharmaceutical analysis. Hence, many studies have

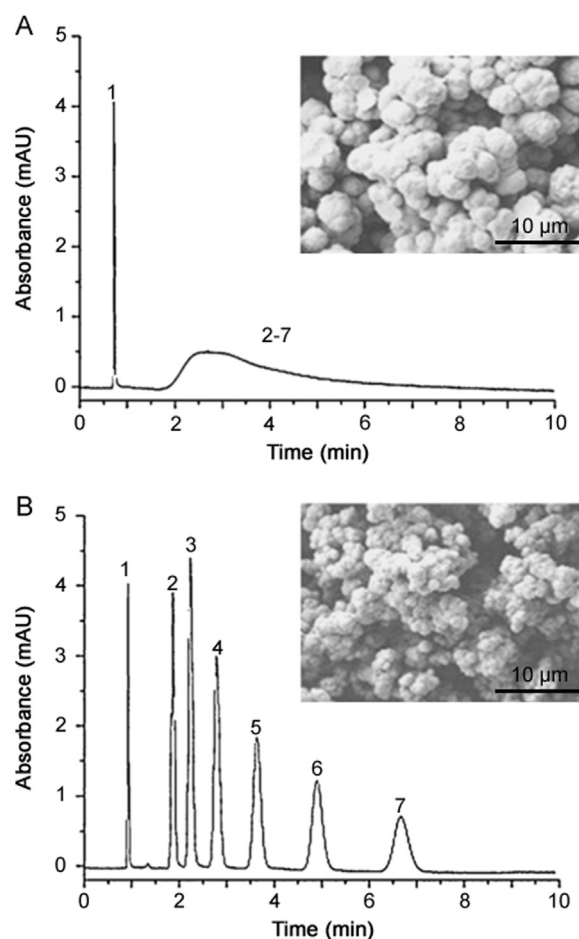


Fig. 7. Isocratic separation of alkylbenzenes using monolithic poly(BMA-co-EDMA) capillary columns polymerized for (A) 48 h and (B) 0.5 h in a 100 μm i.d. capillary. Conditions: column: 200 mm × 100 μm i.d.; mobile phase: 50% aqueous acetonitrile; flow rate: 1.6 μL/min; linear flow velocity: 4.6 mm/s (A) and 3.6 mm/s (B); back pressure: 3.92 MPa (A) and 1.14 MPa (B). Analytes: (1) uracil, (2) benzene, (3) toluene, (4) ethylbenzene, (5) propylbenzene, (6) butylbenzene, (7) pentylbenzene. The inset SEM micrographs show the morphologies of the monoliths [44].

focused on overcoming these disadvantages in recent years. Modification of polymer realizes significant improvements in performance. For example, click chemistry reactions can be used in increasing the surface areas. Monoliths modified using ultra-high crosslinking technologies have large surface areas, good stabilities, and high column efficiencies. Monoliths modified with metal-organic frameworks have a network structure skeletons, adjustable pore sizes, and good thermal and chemical stabilities. Adding nanomaterials into monoliths provides relatively good mechanical stability. There are two main ways to functionalize polymer monoliths. The first method uses functional monomers to prepare polymer monoliths. The second one is the modification after polymerization. Current methods for modifying polymer monoliths include whole column functionalization, hypercrosslinking, incorporation of metal-organic frameworks, and addition of nanomaterials.

3.1. Functionalization of polymer monoliths

3.1.1. Click chemistry and grafting

Click chemistry was proposed by Kolb et al. in 2001 [45]. Subsequently, thiol-ene and thiol-alkyne click chemistry have also been suggested. The thiol-ene click reaction is a rapid and simple process that has a very important role in the preparation of functional polymers and surface modification [46–48]. In particular, over the past two years, the thiol-ene click reaction has been applied in the field of monolith preparation, allowing expansion of the scope of available monomers. Therefore, monolith surface functional groups have become more diverse [49,50]. Functional groups can be grafted onto the surface of a monolith by click chemistry, and reports on the use of this method to prepare monolithic columns with high efficiency and good permeability have increased recently. When functional monomers are used to prepare a monolith, the monolith has active surface. Two-step grafting methods have been explored to functionalize monoliths. In the first step, an initiating group is formed under UV irradiation. A hydrogen atom on the surface of the polymer is removed by benzophenone as a grafted initiator, releasing a free radical. In the second step, a reaction occurs with a single monomer. A monolithic column prepared by the two-step grafting method has the function of blocking protein adsorption [51–54].

Tijunelyte et al. [55] prepared a polymeric material using *N*-acryloxysuccinimide and ethylene dimethacrylate, and then grafted ethylene glycol and mercaptoethanol on the surface using a two-step thiol-ene click reaction. The reaction was carried out at a high temperature. The prepared monolithic column could be used for hydrophilic interaction liquid chromatography (HILIC) and reversed-phase chromatography. Replacement of the allyl amine with propargylamine allowed preparation of a hydrophilic monolith containing amine moieties that could be used for the separation of phenols by HILIC.

Lv et al. [56] used thiol-ene click chemistry to modify the surface of a poly (glycidyl methacrylate/ethylene dimethacrylate) (GMA-EDMA) monolith. The monolith was an excellent substrate for functionalization via the thiol-ene click reaction and suitable for reversed-phase and HILIC separations.

Sun et al. [57] developed a simple one-step in situ “click” modification strategy for the preparation of hydrophobic organic monolithic columns. Compared with the blank column, the stationary phases with higher hydrophobicities obtained by “click” modification had longer retention times with better resolution for five proteins.

3.1.2. Zwitterionic monomers

To obtain high efficiencies for high throughput separation, it is important to consider monomers of different natures. Many types

of monomers have been reported, including hydrophilic, ionic, chiral, and zwitterionic monomers. Recently, an increasing number of zwitterionic monomers have been reported that can be used to adjust the surface chemistry of a polymer monolith. Owing to their good chemical and thermal stabilities and pH tolerance, zwitterionic monomers have attracted increasing interest.

In 2012, Gao et al. [37] used SPP as a zwitterionic monomer, PETA as a crosslinking agent, AMPS as an electroosmotic flow donator, AIBN as an initiator, and ethanol-ethylene glycol as a porogen to synthesize a hydrophilic (SPP-co-PETA) monolith, on which phenolic compounds were successfully separated. The use of ethanol-ethylene glycol as the porogen provided the prepared monolithic column with high column efficiency and better separation performance.

In 2014, sulfobetaine-based zwitterionic hydrophilic monoliths were synthesized by using PEG/methanol as a novel binary porogen. The obtained monolithic column exhibited good performance for the separation of nucleosides, phenols, amines, and other polar compounds [58].

In recent years, ionic liquids (ILs) have been used as comonomers to synthesize monolithic columns. IL-based monolithic columns have structural homogeneity of the structure and good column efficiency as a result of the properties of ILs, including high thermal stability, low volatility, good adjustability, high electrolytic conductivity, and miscibility [59]. Compared with a column prepared without an IL, the IL-based column has a uniform and porous skeleton structure, with good permeability and performance (Fig. 8) [60].

3.2. Hypercrosslinking polymerization technique

The hypercrosslinking polymerization technique was first reported by Davankov et al. [61–63] in the late 1960s. The technique can increase surface areas and has mostly been used to prepare poly (styrene-divinylbenzene). Increasing the surface area of a column will help to improve the performance for separating small molecules [64].

Škeříková and Urban [65] functionalized the surface of monoliths with 4, 4'-azobis (4-cyanovaleric acid) (ACVA), followed by surface grafting polymerization of [2-(methacryloyloxy) ethyl]dimethyl(3-sulfopropyl)ammonium hydroxide (MEDSA) as a functional monomer, to prepare hypercrosslinked stationary phases applicable for HILIC. Interestingly, the prepared monolithic columns provided a dual retention mechanism, combining reversed-phase and hydrophilic interaction chromatography, controlled by the composition of the mobile phase. The column has been used in 1D and 2D chromatography of polar phenolic compounds.

Maya and Svec [66] hypercrosslinked poly (styrene-divinylbenzene) monoliths using a Fe^{3+} catalyzed Friedel-Crafts reaction involving 4,4'-bis (chloromethyl)-1,1'-biphenyl as an external crosslinker, and the column exhibited good chromatographic performance. The hypercrosslinked column was tested for the isocratic reversed-phase liquid chromatography separation of a mixture comprising acetone and six alkylbenzenes, and the column efficiencies for the retained analytes exceeded 70,000 plates/m.

In 2015, Simona [67] used 1,8-diaminooctane to hypercrosslink a poly (styrene-co-vinylbenzyl chloride-co-divinylbenzene) monolithic column via a nucleophilic substitution reaction. The concentration of 1,8-diaminooctane, together with the hypercrosslinking time and temperature, was optimized. To improve the permeability of the prepared columns, the hypercrosslinking modification process was combined with early termination of the polymerization reaction and a decreased polymerization temperature. Further, modification of the residual chloromethyl groups with 2-aminoethanesulfonic acid (taurine) provided

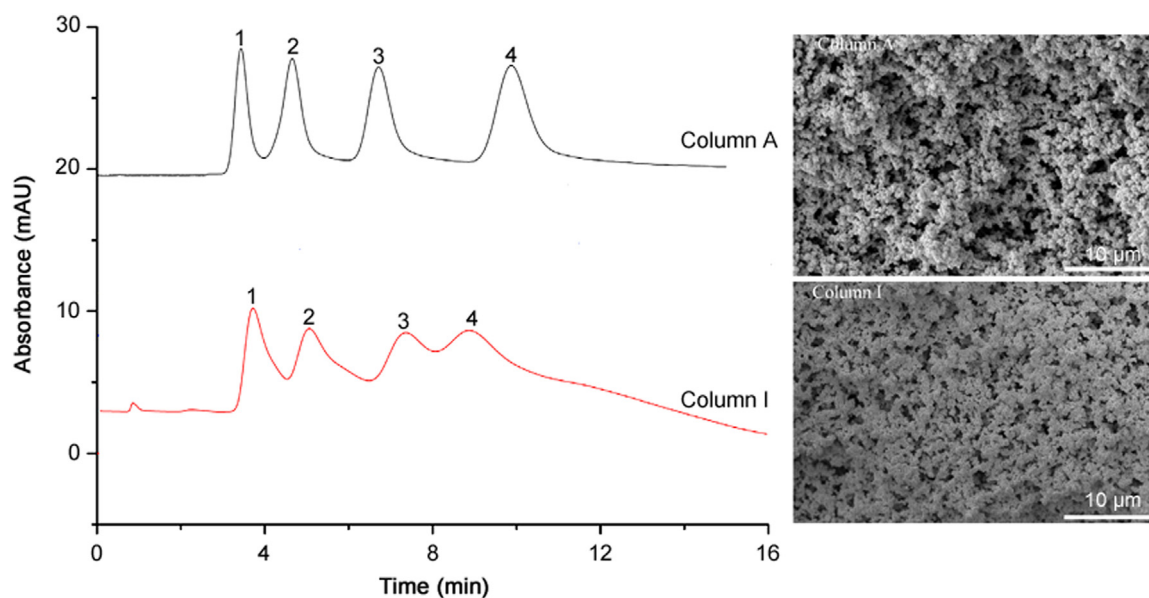


Fig. 8. Separation of toluene and its homologues on different monoliths. Conditions: monolith size: 50 mm × 4.6 mm i.d.; mobile phase: ACN:water (42:58, v/v); flow rate: 1.0 mL/min; concentration: 0.01 mol/L; injection volume: 2.0 μ L; detection wavelength: 254 nm. Analytes: (1) toluene, (2) ethylbenzene, (3) propylbenzene and, (4) butylbenzene. Column A: IL-based monolithic column; column I: without IL. The inset SEM micrographs show the morphologies of the monoliths [60].

monolithic columns suitable for separating small polar molecules by HILIC. The prepared column provided a dual-retention mechanism, including hydrophilic interactions and reversed-phase liquid chromatography, that can be controlled by the composition of the mobile phase. The prepared column was successfully used for the isocratic separation of low-molecular-weight phenolic acids.

Until now, hypercrosslinking has only been demonstrated with styrene-based monoliths and it has been proven useful for separating small molecules in the reversed-phase and HILIC modes. Although several other polymers, such as polyaniline, polypyrrole, polyarylate, polyxylylene, polyamide, and polypyridine, have already been hypercrosslinked [68], they have not yet been prepared as monolithic columns. In addition, the development of hypercrosslinking polymerization methods is required for the preparation of polyacrylate- and polymethacrylate-based monolithic columns.

3.3. Metal-organic frameworks

Metal-organic frameworks (MOFs), also called porous coordination polymers, are a new class of hybrid inorganic-organic microporous crystalline materials self-assembled from metal ions and organic linkers via coordination bonds [69]. Owing to their fascinating structures and unusual properties, such as large surface areas, structural diversity, good thermal and chemical stabilities, uniform and regular pore sizes, and the availability of framework functionality, MOFs have great potential for separation applications [70].

In 2013, Fu et al. [71] investigated the incorporation of MOF UiO-66 into a porous poly (MAA-co-EDMA) monolith to enhance the HPLC separation of small molecules with high column efficiency and good reproducibility. The introduction of UiO-66 increased the strength of hydrophobic interactions between the analyte and the monolithic column, resulting in longer retention times. Huang et al. [72] prepared the MOF MIL-101 (Cr), which has a large surface area and good stability. Then they prepared a MOF monolith by proportionate mixing of MIL-101 (Cr), BMA, EDMA, AMPS, and AIBN. Compared with the column without MOF modification, the MOF monolith column had a larger surface area, improved permeability, and a nanoporous structure, which allowed the efficient separation of xylene isomers.

MOF HKUST-1 nanoparticles have been incorporated into poly (glycidylmethacrylate-co-ethylene dimethacrylate) (HKUST-1-poly (GMA-co-EDMA)) monoliths to afford stationary phases with enhanced chromatographic performance for small molecule separation in the reversed-phase capillary liquid chromatography. While the bare poly(GMA-co-EDMA) monolith exhibited poor resolution ($R_s < 1.0$) and low efficiency (800–16,300 plates/m), the addition of a small amount of HKUST-1 nanoparticles to the polymerization mixture provided increased resolution ($R_s \geq 1.3$) and high efficiency, ranging from 16,300 to 44,300 plates/m [73].

3.4. Nanomaterials

Nanotechnology had a major impact and promoted advances in medicine, biology, environmental science, energy, electronics, and other fields [74,75]. In recent years, gold nanoparticles, carbon nanotubes, and other nanomaterials have been used in functionalized organic polymer monoliths. The introduction of nanomaterials, such as carbon nanotubes and graphene, has revealed the potential for such materials in the enrichment and separation of complex samples [76,77]. Since the discovery of zero-dimensional fullerenes, researchers have been particularly concerned with the use of carbon nanomaterials to overcome the poor mechanical stability of polymer monoliths [78–80].

3.4.1. Metal nanoparticles

Nanoparticles (NPs) are ultrafine particles with sizes of 1–100 nm. The particle size decreases rapidly as the ratio of surface atoms in a NP and the total number of atoms increases, resulting in a strong volume effect (small size effect), the quantum size effect, and surface and macroscopic quantum tunneling effects.

In recent years, metal NPs have received attention in many fields of science. Polymer monoliths modified by metal NPs retain the original physical and chemical characteristics of the metal NPs and the advantages of organic polymer monolith. Therefore, this modification method might lead to high column efficiency, good permeability, and selective separation performance. Gold nanoparticles (Au NPs) are the most common metal NPs used for the modification of polymer monoliths.

A novel approach has been developed for porous polymer monoliths hypercrosslinked to obtain large surface areas and modified with zwitterionic functionalities through the attachment of Au NPs in a layered architecture. The combination of hypercrosslinking hydrophobic poly(4-methylstyrene-co-vinylbenzene chloride-co-divinylbenzene) monoliths with a hydrophilic layered structure including Au NPs embedded in a polyethyleneimine layer and functionalized with cysteine enabled the preparation of a very efficient monolithic stationary phase for the separation of small molecules by HILIC. A column efficiency of 51,000 plates/m was achieved for cytosine [81].

A porous polymethacrylate ester-based monolith was prepared using BMA and EDMA in a binary porogenic solvent of 1, 4-butanediol and 1-propanol [82]. Injecting a Au NP colloid into the monolith resulted in a homogeneous coverage of Au NPs, which were physically adsorbed on the monolith surface. The Au NP-modified poly (BMA-EDMA) monolith was found to show obvious SERS enhancement, with the SERS activity dependent on the size of the Au NPs.

3.4.2. Carbon nanotubes

Carbon nanotubes can be used to prepare monoliths for the efficient separation of various compounds. The surfaces of such monoliths are strongly hydrophobic. Hence, monoliths containing carbon nanotubes are very useful as stationary phases for the reversed-phase separation of small molecules. Owing to the unique characteristics of nanoparticles, such as their large surface-to-volume ratios and their properties that differ from those of the corresponding bulk materials, the application of nanomaterials in separation science is growing [83–85].

Li et al. [86] prepared a poly (vinylbenzyl chloride-ethylene dimethacrylate) (VBC-EDMA) column that incorporated single-wall carbon nanotubes (SWNT). The retention behavior of neutral compounds on the poly (VBC-EDMA-SWNT) monolith was examined by separating a mixture of small organic molecules using micro-HPLC. The results indicated that the incorporation of SWNT enhanced the chromatographic retention of small neutral molecules in reversed-phase HPLC presumably because of their strongly hydrophobic characteristics.

Multiwalled carbon nanotubes have been entrapped in monolithic poly (glycidyl methacrylate-co-ethylene dimethacrylate) columns to afford a stationary phase with enhanced performance for the separation of small molecules by reversed-phase chromatography [87]. While the column with no nanotubes exhibited an efficiency of only 1800 plates/m, the addition of a small amount of nanotubes to the polymerization mixture increased the efficiency to over 35,000 plates/m. The addition of THF to the typical aqueous ACN eluent improved the peak shape and increased the column efficiency to 44,000 plates/m, as calculated for the benzene peak.

In 2015, Qi [88] prepared two polymer monolithic columns. One was modified by In_2O_3 NPs and the other was modified by 3-trimethoxysilyl propyl methacrylate (γ -MAPS) and sodium titanate nanotubes (NaTiNTs). The prepared monolithic columns were used to determine organic residues in food by HPLC or HPLC-MS/MS.

In 2012, Li et al. [89] used GMA as a monomer and EDMA as a crosslinking agent to prepare a polymer monolith containing carbon nanotubes. The column efficiency was considerably improved compared with that of the polymer monolith without adding carbon nanotubes. Benzenes, alkyl ketones, and other small molecules were successfully separated on the prepared monolithic column.

3.4.3. Graphene

Graphene (GN) is a two-dimensional sp^2 -hybridized nanocarbon material. Similar to metal NPs, carbon nanotubes, and

other nanocarbon materials, GN can be incorporated into polymer monoliths to modify the surface of the polymer monolith and improve the efficiency for the separation of small molecules. However, polymer monoliths modified with GN and used for the separation of small molecules have rarely been reported. Therefore, further investigations of GN-modified monoliths are required to determine the possible potential applications and advantages of such materials.

In 2013, Li et al. [90] used graphene oxide as a crosslinking agent to prepare a methyl acrylate polymer monolith from GMA and EDMA. The prepared monolith was used as a HPLC stationary phase for the isocratic separation of model compounds, such as hydrophobic steroids and polar aniline. Compared with the polymer monolith that prepared by a traditional method, the co-functionalized graphene oxide polymer monolith showed greatly improved ability for the separation of model small molecules. This study reported a new preparation method for polymer monoliths containing nanomaterials.

In 2015, Zheng [91] prepared a poly (BMA-co-EDMA-ALA- β -CD- Cu_2O) monolith by using graphene and beta-cyclodextrin(β -CD). Owing to the addition of inorganic nanomaterials and GN, the polymer monolith exhibited considerable improvement in separation effects. The polymer monolith had a homogeneous structure with good penetrability. Under certain conditions, the prepared monolith showed enrichment efficiency for the trace analysis of polychlorinated biphenyls (PCBs) in wine samples.

4. Conclusions and outlook

Over the past few years, the technology for preparing polymer monoliths has been developed. Many achievements have been made in methods for preparing polymer monoliths that are suitable for the separation of small molecules. Many polymer monoliths have been successfully prepared with high column efficiency, good permeability and high efficiency for the separation of small molecules. In this review, we have summarized the methods reported in recent studies, such as carefully selecting the monomer and crosslinker; adjusting the ratio of monomer, crosslinking agent, and porogen; controlling polymerization temperature and polymerization time; modifying the polymer monolithic column using click chemistry and boron affinity technology; using zwitterionic monomers and super-high crosslinking technology; and adding nanomaterials, which can be applied to achieve uniform columns with compact pore structures and sufficiently large surface areas.

Although some defects that made monoliths unsuitable for the separation of small molecules have been improved using these methods, there are still some problems. We can know from the reported literatures that it is easy for organic polymer monolithic column to form accumulation structure in the process of reaction, which lead to unexpected pores structure of monolithic columns. This is still a problem to be solved in the preparation of a polymer monolithic column. Therefore, research efforts are still being directed toward obtaining uniform, compact network structures when preparing polymer monoliths.

The preparation of polymer monoliths containing nanomaterials is a promising research area. Although some examples of such polymer monolithic columns have been reported in recent years, most of them are monolithics silica columns containing nanomaterials. Relatively few polymer monoliths containing nanomaterials have been reported. However, the addition of nanomaterials improves the separation performance of polymer monoliths, realizing columns with good reproducibility and selectivity. Although many optimized methods for preparing polymer monoliths have been reported, they are not always simple and efficient. Thus,

there is considerably scope for improving the preparation methods for polymer monoliths. With rapid developments in science and technology, we will gain a deeper understanding of important problems in monolith polymerization processes, such as the process of forming the pore structure and the factors that affect pore formation and swelling. In this way, we will not only be able to improve reported methods, but also discover new, more convenient, and efficient ways to prepare polymer monoliths that can be used to separate small molecules.

The requirements for separating complex matrices are becoming more stringent, for example, environmental issues receive considerable worldwide attention owing to their direct influence on human health. Therefore, it is very important to find methods for the effective and selective enrichment of pollutants. Modified polymer monoliths may be applicable to this important task. For example, polymer monoliths modified with large ring polyamine compounds have enhanced abilities for ion exchange and hydrophobic interactions, which can largely improve the selective enrichment performance and the enrichment efficiency. As polymer monoliths have increasingly played an important role in the fields of medicine and environmental science, the preparation of these materials has become an important research subject. Further theoretical and practical insight for the development of new application areas and the separation of actual samples will allow new methods to be established for the preparation of polymer HPLC monolithic column for the separation of small molecules drugs.

Conflicts of interest

The authors declare that there are no conflicts of interest.

References

- [1] F. Svec, Organic polymer monoliths as stationary phases for capillary HPLC, *J. Sep. Sci.* 27 (2004) 1419–1430.
- [2] R.D. Arrua, M. Talebi, T.J. Causon, et al., Review of recent advances in the preparation of organic polymer monoliths for liquid chromatography of large molecules, *Anal. Chim. Acta* 738 (2012) 1–12.
- [3] K. Liu, P. Aggarwal, J.S. Lawson, et al., Organic monoliths for high-performance reversed-phase liquid chromatography, *J. Sep. Sci.* 36 (2013) 2767–2781.
- [4] Z. Liu, J. Ou, Z. Liu, J. Liu, et al., Separation of intact proteins by using polyhedral oligomeric silsesquioxane based hybrid monolithic capillary columns, *J. Chromatogr. A* 1317 (2013) 138–147.
- [5] K. Cabrera, D. Lubda, H.M. Eggenweiler, et al., R & D biochemistry and separation, Merck KgaA: A new monolithic-type HPLC column for fast separations, *J. High Resolut. Chromatogr.* 23 (2000) 93–99.
- [6] N. Ishizuka, H. Minakuchi, K. Nakanishi, et al., Chromatographic properties of miniaturized silica rod columns, *J. High Resolut. Chromatogr.* 21 (1998) 477–479.
- [7] Z. Lin, X. Tan, R. Yu, et al., One-pot preparation of glutathione–silica hybrid monolith for mixed-mode capillary liquid chromatography based on "thiol-ene" click chemistry, *J. Chromatogr. A* 1355 (2014) 228–237.
- [8] P. Jandera, Advances in the development of organic polymer monolithic columns and their applications in food analysis—a review, *J. Chromatogr. A* 1313 (2013) 37–53.
- [9] J.D. Hayes, A. Malik, Sol–gel monolithic columns with reversed electroosmotic flow for capillary electrochromatography, *Anal. Chem.* 72 (2000) 4090–4099.
- [10] Z. Liu, J. Ou, H. Lin, et al., Preparation of polyhedral oligomeric silsesquioxane-based hybrid monolith by ring-opening polymerization and post-functionalization via thiol-ene click reaction, *J. Chromatogr. A* 1342 (2014) 70–77.
- [11] H. Wang, J. Ou, H. Lin, et al., Chromatographic assessment of two hybrid monoliths prepared via epoxy-amine ring-opening polymerization and methacrylate-based free radical polymerization using methacrylate epoxy cyclosiloxane as functional monomer, *J. Chromatogr. A* 1367 (2014) 131–140.
- [12] Z. Zhang, F. Wang, B. Xu, et al., Preparation of capillary hybrid monolithic column with sulfonate strong cation exchanger for proteome analysis, *J. Chromatogr. A* 1256 (2012) 136–143.
- [13] F. Svec, Quest for organic polymer-based monolithic columns affording enhanced efficiency in high performance liquid chromatography separations of small molecules in isocratic mode, *J. Chromatogr. A* 1228 (2012) 250–262.
- [14] J. Seidl, J. Malinský, K. Dušek, et al., Makroporöse Styrol-Divinylbenzol-Copolymere und ihre Verwendung in der Chromatographie und zur Darstellung von Ionenaustauschern, *Adv. Polym. Sci.* 5 (1967) 113–213.
- [15] G. Guiochon, Monolithic columns in high-performance liquid chromatography, *J. Chromatogr. A* 1168 (2007) 101–168.
- [16] M.J. Gray, P.J. Slonecker, G. Dennis, A column capacity study of single, serial, and parallel linked rod monolithic high performance liquid chromatography columns, *J. Chromatogr. A* 1096 (2005) 92–100.
- [17] Z. Xu, L. Yang, Q. Wang, Different alkyl dimethacrylate mediated styryl methacrylate monoliths for improving separation efficiency of typical alkylbenzenes and proteins, *J. Chromatogr. A* 1216 (2009) 3098–3106.
- [18] A. Maruška, A. Rocco, O. Komyšova, et al., Synthesis and evaluation of polymeric continuous bed (monolithic) reversed-phase gradient stationary phases for capillary liquid chromatography and capillary electrochromatography, *J. Biochem. Biophys. Methods* 70 (2007) 47–55.
- [19] X.M. Bai, Study on the Preparation and Application of TMPTA Monolithic Columns, Hebei University, Baoding, China, 2014.
- [20] H.Y. Liu, Y.M. Ma, X. Qin, et al., Preparation of poly dodecane monolithic column for HPLC separations of small molecules, *J. Hebei Univ.: Nat. Sci. Ed.* 35 (2015) 147–152.
- [21] A. Greiderer, L. Trojer, C.W. Huck, et al., Influence of the polymerisation time on the porous and chromatographic properties of monolithic poly(1,2-bis(p-vinylphenyl)ethane) capillary columns, *J. Chromatogr. A* 1216 (2009) 7747–7754.
- [22] K. Liu, H.D. Tolley, M.L. Lee, Highly crosslinked polymeric monoliths for reversed-phase capillary liquid chromatography of small molecules, *J. Chromatogr. A* 1227 (2012) 96–104.
- [23] S.H. Lubad, M.R. Buchmeiser, Fast separation of low molecular weight analytes on structurally optimized polymeric capillary monoliths, *J. Chromatogr. A* 1217 (2010) 3223–3230.
- [24] Y. Li, H.D. Tolley, M.L. Lee, Preparation of monoliths from single crosslinking monomers for reversed-phase capillary chromatography of small molecules, *J. Chromatogr. A* 1218 (2011) 1399–1408.
- [25] I. Nischang, I. Teasdale, O. Brüggemann, Towards porous polymer monoliths for the efficient, retention-independent performance in the isocratic separation of small molecules by means of nano-liquid chromatography, *J. Chromatogr. A* 1217 (2010) 7514–7522.
- [26] W.J. Niu, Preparation and Evaluation of Capillary Columns of Poly(vinyl ester resin), Hebei University, Baoding, China, 2013.
- [27] D. Wei, The Preparation and Application of Poly(PETA-co-TAIC) and poly(modified epoxy acrylate resin) Monolithic Columns, Hebei University, Baoding, China, 2014.
- [28] M.B. Hao, Preparation of Poly C12 Monolith and its Application in the Separation of Benzene Series, Hebei University, Baoding, 2014.
- [29] A. Dou, C. Zou, Y. Shan, et al., Preparation and application of mixed-mode capillary polymer monolithic column, *Chin. J. Chromatogr.* 32 (2014) 447–451.
- [30] I. Gusev, X. Huang, C. Horváth, Capillary columns with in situ formed porous monolithic packing for micro high-performance liquid chromatography and capillary electrochromatography, *J. Chromatogr. A* 855 (1999) 273–290.
- [31] Z. Kucerová, M. Szumski, B. Buszewski, et al., Alkylated poly(styrene-divinylbenzene) monolithic columns for mu-HPLC and CEC separation of phenolic acids, *J. Sep. Sci.* 30 (2007) 3018–3026.
- [32] A. Svobodová, T. Krížek, J. Sirc, et al., Monolithic columns based on a poly(styrene-divinylbenzene-methacrylic acid) copolymer for capillary liquid chromatography of small organic molecules, *J. Chromatogr. A* 1218 (2011) 1544–1547.
- [33] P. Coufal, M. Cihák, J. Suchánková, et al., Methacrylate monolithic columns of 320 µm I.D. for capillary liquid chromatography, *J. Chromatogr. A* 946 (2002) 99–106.
- [34] Z. Xu, L. Yang, Q. Wang, Different alkyl dimethacrylate mediated styryl methacrylate monoliths for improving separation efficiency of typical alkylbenzenes and proteins, *J. Chromatogr. A* 1216 (2009) 3098–3106.
- [35] D. Moravcová, P. Jandera, J. Urban, et al., Characterization of polymer-monolithic stationary phases for capillary HPLC, *J. Sep. Sci.* 26 (2003) 1005–1016.
- [36] Y. Huo, P.J. Schoenmakers, W.T. Kok, Efficiency of methacrylate monolithic columns in reversed-phase liquid chromatographic separations, *J. Chromatogr. A* 1175 (2007) 81–88.
- [37] Y. Gao, Y. Wang, C. Wang, et al., Preparation of new hydrophilic monolithic columns and their applications in capillary liquid chromatography and pressurized capillary electrochromatography, *Chin. J. Chromatogr.* 30 (2012) 487–494.
- [38] R. Li, J. Zhong, M. Hao, et al., Preparation of a porous functional polymer and its application in the separation of small molecules in conjunction with HPLC, *Anal. Methods* 6 (2014) 589–595.
- [39] J. Zhong, M. Hao, R. Li, et al., Preparation and characterization of poly(triallyl isocyanurate-co-trimethylolpropane triacrylate) monolith and its applications in the separation of small molecules by liquid chromatography, *J. Chromatogr. A* 1333 (2014) 79–86.
- [40] H. Aoki, T. Kubo, T. Ikegami, et al., Preparation of glycerol dimethacrylate-based polymer monolith with unusual porous properties achieved via viscoelastic phase separation induced by monodisperse ultra high molecular weight poly(styrene) as a porogen, *J. Chromatogr. A* 1119 (2006) 66–79.
- [41] Y. Li, H.D. Tolley, M.L. Lee, Preparation of polymer monoliths that exhibit size exclusion properties for proteins and peptides, *Anal. Chem.* 81 (2009) 4406–4413.

- [42] S.S. Tong, Development of Novel Separation and Enrichment Approaches Based on Carbon Nanomaterials, Jilin University, Changchun, China, 2013.
- [43] H. Liu, X. Bai, D. Wei, et al., High-performance liquid chromatography separation of small molecules on a porous poly (trimethylol propane triacrylate-co-N-isopropylacrylamide-co-ethylene dimethacrylate) monolithic column, *J. Chromatogr. A* 1324 (2014) 128–134.
- [44] I. Nischang, O. Brüggemann, On the separation of small molecules by means of nano-liquid chromatography with methacrylate-based macroporous polymer monoliths, *J. Chromatogr. A* 1217 (2010) 5389–5397.
- [45] H.C. Kolb, M.G. Finn, K.B. Sharpless, Click chemistry: diverse chemical function from a few good reactions, *Angew. Chem. Int. Ed. Engl.* 40 (2001) 2004–2021.
- [46] G. Jian, Y. Liu, X. He, et al., Click chemistry: a new facile and efficient strategy for the preparation of Fe₃O₄ nanoparticles covalently functionalized with IDA-Cu and their application in the depletion of abundant protein in blood samples, *Nanoscale* 4 (2012) 6336–6342.
- [47] J.E. Moses, A.D. Moorhouse, The growing applications of click chemistry, *Chem. Soc. Rev.* 36 (2007) 1249–1262.
- [48] M. Slater, M. Snauko, F. Svec, et al., “Click Chemistry” in the preparation of porous polymer-based particulate stationary phases for μ -HPLC separation of peptides and proteins, *Anal. Chem.* 78 (2006) 4969–4975.
- [49] H. Huang, Y. Jin, M. Xue, et al., A novel click chitoooligosaccharide for hydrophilic interaction liquid chromatography, *Chem. Commun.* 45 (2009) 6973–6975.
- [50] L. Moni, A. Cioqli, I. D’Acquarica, et al., Synthesis of sugar-based silica gels by copper-catalysed azide-alkyne cycloaddition via a single-step azido-activated silica intermediate and the use of the gels in hydrophilic interaction chromatography, *Chemistry* 16 (2010) 5712–5722.
- [51] T. Suksrichavalit, K. Yoshimatsu, V. Prachayasittikul, et al., “Clickable” affinity ligands for effective separation of glycoproteins, *J. Chromatogr. A* 1217 (2010) 3635–3641.
- [52] Z. Liu, J. Ou, H. Lin, et al., Preparation of monolithic polymer columns with homogeneous structure via photoinitiated thiol-yne click polymerization and their application in separation of small molecules, *Anal. Chem.* 86 (2014) 12334–12340.
- [53] H. Lin, J. Ou, Z. Liu, et al., Thiol-epoxy click polymerization for preparation of polymeric monoliths with well-defined 3D framework for capillary liquid chromatography, *Anal. Chem.* 87 (2015) 3476–3483.
- [54] L. Chen, J. Ou, Z. Liu, et al., Fast preparation of a highly efficient organic monolith via photo-initiated thiol-ene click polymerization for capillary liquid chromatography, *J. Chromatogr. A* 1394 (2015) 103–110.
- [55] I. Tijunelyte, J. Babinot, M. Guerrouache, et al., Hydrophilic monolith with ethylene glycol-based grafts prepared via surface confined thiol-ene click photoaddition, *Polymer* 1 (2012) 29–36.
- [56] Y. Lv, Z. Lin, F. Svec, “Thiol-ene”click chemistry: a facile and versatile route for the functionalization of porous polymer monoliths, *Analyst* 137 (2012) 4114–4118.
- [57] X. Sun, D. Lin, X. He, et al., A facile and efficient strategy for one-step in situ preparation of hydrophobic organic monolithic stationary phases by click chemistry and its application on protein separation, *Talanta* 82 (2010) 404–408.
- [58] Y. Kuang, Synthesis and chromatographic evaluation of sulfobetaine-based capillary zwitterionic hydrophilic monolithic column using a binary porogenic agent of polyethylene glycol/methanol, *Se Pu* 32 (2014) 388–394.
- [59] M. Armand, F. Endres, D.R. MacFarlane, et al., Ionic-liquid materials for the electrochemical challenges of the future, *Nat. Mater.* 8 (2009) 621–629.
- [60] H. Zhang, L. Bai, Z. Wei, et al., Fabrication of an ionic liquid-based macroporous polymer monolithic column via atom transfer radical polymerization for the separation of small molecules, *Talanta* 149 (2016) 62–68.
- [61] V.A. Davankov, S.V. Rogozhin, M.P. Tsyurupa, Influence of polymeric matrix structure on performance of ion-exchange resins, *Solvent Extr. Ion. Exc.*, 1977: 29–81.
- [62] V.A. Davankov, M.P. Tsyurupa, Structure and properties of hypercrosslinked polystyrene—the first representative of a new class of polymer networks, *React. Polym.* 13 (1990) 27–42.
- [63] V.A. Davankov, M. Tsyurupa, M. Ilyin, et al., Hypercross-linked polystyrene and its potentials for liquid chromatography: a mini-review, *J. Chromatogr. A* 965 (2002) 65–73.
- [64] A.V. Pastukhov, M.P. Tsyurupa, V.A. Davankov, Hypercrosslinked polystyrene: a polymer in a non-classical physical state, *J. Polym. Sci. Polym. Phys.* 37 (1999) 2324–2333.
- [65] V. Škeříková, J. Urban, Highly stable surface modification of hypercrosslinked monolithic spillary columns and their application in hydrophilic interaction chromatography, *J. Sep. Sci.* 36 (2013) 2806–2812.
- [66] F. Maya, F. Svec, A new approach to the preparation of large surface area poly (styrene-co-divinylbenzene) monoliths via knitting of loose chains using external crosslinkers and application of these monolithic columns for separation of small molecules, *Polymer* 55 (2014) 340–346.
- [67] S. Janků, V. Škeříková, J. Urban, Nucleophilic substitution in preparation and surface modification of hypercrosslinked stationary phases, *J. Chromatogr. A* 1388 (2015) 151–157.
- [68] V. Davankov, M. Tsyurupa, *Hypercrosslinked Polymeric Networks and Adsorbing Materials*, Elsevier 2011: 315–358.
- [69] Y.Y. Fu, *Metal-organic Frameworks and its Composites for Liquid Chromatographic Separation*, Nankai University, Tianjin, China, 2013.
- [70] S. Yang, F. Ye, C. Zhang, et al., In situ synthesis of metal-organic frameworks in a porous polymer monolith as the stationary phase for capillary liquid chromatography, *Analyst* 140 (2015) 2755–2761.
- [71] Y.Y. Fu, C.X. Yang, X.P. Yan, Incorporation of metal-organic framework UiO-66 into porous polymer monoliths to enhance the liquid chromatographic separation of small molecules, *Chem. Commun.* 49 (2013) 7162–7164.
- [72] H.Y. Huang, C.L. Lin, C.Y. Wu, et al., Metal organic framework-organic polymer monolith stationary phases for capillary electrochromatography and nano-liquid chromatography, *Anal. Chim. Acta* 779 (2013) 96–103.
- [73] S. Yang, F. Ye, Q. Lv, et al., Incorporation of metal-organic framework HKUST-1 into porous polymer monolithic capillary columns to enhance the chromatographic separation of small molecules, *J. Chromatogr. A* 1360 (2014) 143–149.
- [74] A.Z. Zhang, G.F. Ye, J.Y. Lu, et al., Preparation and characterization of polymer solid phase microextraction monolith modified with gold nanoparticle, *Chin. J. Anal. Chem.* 39 (2011) 1247–1250.
- [75] Z. Zhang, Z. Wang, Y. Liao, et al., Applications of nanomaterials in liquid chromatography: opportunities for separation with high efficiency and selectivity, *J. Sep. Sci.* 29 (2006) 1872–1878.
- [76] C. Nilsson, S. Birnbaum, S. Nilsson, Use of nanoparticles in capillary and microchip electrochromatography, *J. Chromatogr. A* 1168 (2007) 212–224.
- [77] C. Wu, Y. Liang, Q. Zhao, et al., Boronate affinity monolith with a gold nanoparticle modified hydrophilic polymer as a matrix for the highly specific capture of glycoproteins, *Chemistry* 20 (2014) 8737–8743.
- [78] S. Wang, C. Liu, H. Wang, et al., A surface-enhanced Raman scattering optrode prepared by in situ photoinduced reactions and its application for highly sensitive on-chip detection, *ACS Appl. Mater. Interfaces* 6 (2014) 11706–11713.
- [79] Y.C. Pan, X. Wang, H. Zhang, et al., Gold-nanoparticle functionalized-porous polymer monolith enclosed in capillary for on-column SERS detection, *Anal. Methods* 7 (2015) 1349–1357.
- [80] O. Sedlacek, J. Kucka, F. Svec, et al., Silver-coated monolithic columns for separation in radiopharmaceutical applications, *J. Sep. Sci.* 37 (2014) 798–802.
- [81] Y. Lv, Z. Lin, F. Svec, Hypercrosslinked large surface area porous polymer monoliths for hydrophilic interaction liquid chromatography of small molecules featuring zwitterionic functionalities attached to gold nanoparticles held in layered structure, *Anal. Chem.* 84 (2012) 8457–8460.
- [82] H. Ren, L. Liu, H. Liu, et al., Preparation of porous polymer monolith modified with gold nanoparticles and on-column surface-enhanced Raman spectroscopy detection, *J. Hubei Univ.* 36 (2014) 238–247.
- [83] Z. Zhang, B. Yan, Y. Liao, et al., Nanoparticle: is it promising in capillary electrophoresis? *Anal. Bioanal. Chem.* 391 (2008) 925–927.
- [84] C. Nilsson, S. Nilsson, Nanoparticle-based pseudostationary phases in capillary electrochromatography, *Electrophoresis* 27 (2006) 76–83.
- [85] C.D. Tran, S. Challa, Fullerene-impregnated ionic liquid stationary phases for gas chromatography, *Analyst* 133 (2008) 455–464.
- [86] Y. Li, Y. Chen, R. Xiang, et al., Incorporation of single-wall carbon nanotubes into an organic polymer monolithic stationary phase for μ -HPLC and capillary electrochromatography, *Anal. Chem.* 77 (2005) 1398–1406.
- [87] S.D. Chambers, F. Svec, J.M. Fréchet, Incorporation of carbon nanotubes in porous polymer monolithic capillary columns to enhance the chromatographic separation of small molecules, *J. Chromatogr. A* 1218 (2011) 2546–2552.
- [88] R.F. Qi, Preparation of Monolithic Polymeric Column Modified by Nanomaterials and its Application in Analysis of Organic Residues in Food, Jilin University, Changchun, China, 2015.
- [89] Q. Li, Y. Du, H. Tang, et al., Ultra sensitive surface-enhanced Raman scattering detection based on monolithic column as a new type substrate, *J. Raman Spectrosc.* 43 (2012) 1392–1396.
- [90] Y. Li, L. Qi, H. Ma, et al., Preparation of porous polymer monolithic column using functionalized graphene oxide as a functional crosslinker for high performance liquid chromatography separation of small molecules, *Analyst* 138 (2013) 5470–5478.
- [91] H.J. Zheng, Preparation of Macrocyclic Compound Modified Polymer Monolithic Column and its Application in Separation and Analysis, Jilin University, Changchun, China, 2015.



Contents lists available at ScienceDirect

Journal of Pharmaceutical Analysis

journal homepage: www.elsevier.com/locate/jpa
www.sciencedirect.com

Original Research Article

Novel degradation products of argatroban: Isolation, synthesis and extensive characterization using NMR and LC-PDA-MS/Q-TOF

Vinodh Guvvala^{a,b}, Venkatesan Chidambaram Subramanian^{b,*}, Jaya Shree Anireddy^a, Mahesh Konda^{b,*}^a Centre for Chemical Science & Technology, Institute of Science & Technology, JNTUH, Kukatpally, Hyderabad 500085, India^b Gland Pharma Ltd., Research and Development, D.P.Pally, Hyderabad 500043, India

ARTICLE INFO

Article history:

Received 4 January 2017

Received in revised form

29 May 2017

Accepted 3 July 2017

Available online 5 July 2017

Keywords:

Argatroban

Forced degradation

NMR

LC-PDA

LC-MS/Q-TOF-MSⁿ

ABSTRACT

Forced degradation study of argatroban under conditions of hydrolysis (neutral, acidic and alkaline), oxidation, photolysis and thermal stress, as suggested in the ICH Q1A (R2), was accomplished. The drug showed significant degradation under hydrolysis (acidic, alkaline) and oxidation (peroxide stress) conditions. The drug remained stable under thermal and photolytic stress conditions. In total, seven novel degradation products (DP-1 to DP-7) were found under diverse conditions, which were not reported earlier. The chemical structures of these degradation products were characterized by ¹H NMR, ¹³C NMR, 2D NMR, Q-TOF-MSⁿ and IR spectral analysis and the proposed degradation products structures were further confirmed by the individual synthesis.

© 2018 Xi'an Jiaotong University. Production and hosting by Elsevier B.V. This is an open access article under the CC BY-NC-ND license (<http://creativecommons.org/licenses/by-nc-nd/4.0/>).

1. Introduction

Argatroban, a derivative of L-arginine (Fig. 1), is a competitive inhibitor [1] of thrombin and only interacts with active site of thrombin. It directly prevents the activity of thrombin (factor IIa) and has no direct effect on the generation of thrombin. The function of argatroban is independent of the antithrombin in the body. Argatroban inactivates not only thrombin in free state in blood, but also inactivates the thrombin combined with fibrin thrombus. Argatroban has a small molecular weight and thus it enters into thrombus and directly inactivates the thrombin already combined with fibrin thrombus, and even exhibits an antithrombotic effect against an early formed thrombosis. Argatroban is given intravenously and the drug plasma concentration reaches steady state in 1–3 h [2].

ICH Q3A(R2) and Q3B(R2) recommend the characterization of impurities/degradation products that are present at a level greater than the identification threshold in a drug substance or drug product [3–9]. The study of formation of impurities/degradants in the drug substance, their isolation and characterization is very important since it can help to understand the degradation pattern of the drug substance. This gives precious information about the drug stability under various conditions, so such information is significant for determining storage and other conditions of the bulk and formulated drug

substance. In addition, improvements in the manufacturing process of bulk drug substance are difficult to achieve without understanding the possible degradation pathways.

The present investigation deals with all degradation studies including acid, base, thermal and photo stability on the drug substance as per the above prescribed guidelines. The formed degradation products were identified through LC-MS-Ion trap and Q-TOF NMR spectral analysis and the proposed structures were confirmed by comparing with individually synthesized compounds. Even though there is no report on the degradants identified in the present study, recently Secretan et al. [10] reported photo degradation study of argatroban in aqueous solution based on the LC-MS. Nevertheless, the present study deals with the behaviour of argatroban drug substance in acid, base, peroxide and thermal stress. The formed degradation products were characterized completely by using advanced analytical techniques such as LC-MS/MS, IR and NMR.

2. Experimental

2.1. Chemicals and reagents

Argatroban drug substance was prepared by Gland Pharma Ltd. (Hyderabad, India). Analytical reagent grade sodium hydroxide (NaOH) was purchased from S.D. Fine-Chem Ltd. (Mumbai, India), hydrochloric acid (HCl), HPLC grade methanol (MeOH) and acetonitrile (ACN) from Merck Specialities Pvt. Ltd. (Mumbai, India) and hydrogen peroxide (H₂O₂) from Qualigens Fine Chemicals Pvt. Ltd. (Mumbai, India). Ammonium formate (HCOONH₄) and formic acid were purchased from

Peer review under responsibility of Xi'an Jiaotong University.

* Corresponding authors.

E-mail addresses: venkatesan@glandpharma.com (V. Chidambaram Subramanian), maheshk@glandpharma.com (M. Konda).<https://doi.org/10.1016/j.jpha.2017.07.001>2095-1779/© 2018 Xi'an Jiaotong University. Production and hosting by Elsevier B.V. This is an open access article under the CC BY-NC-ND license (<http://creativecommons.org/licenses/by-nc-nd/4.0/>).

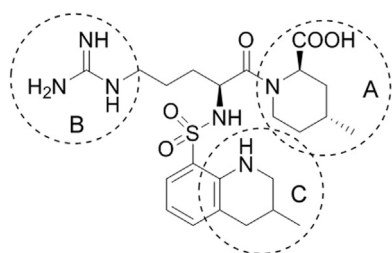


Fig. 1. Argatroban and its structural elements (A–C) susceptible to chemical changes.

Merck. Ultra pure water obtained from Millipore water purification system (Bangalore, India) was used throughout the studies.

2.2. Instrumentation

The forced degradation samples were analyzed on an Agilent HPLC (series 1200) equipped with a vacuum degasser, binary pump, auto injector, diode array detector (DAD), and coupled to an Agilent Ion-trap (6310)/Q-TOF 6530 (Agilent technologies, USA, location Gland Pharma R&D, Hyderabad, India) operating in +ESI-MS and –ESI-MS modes. Chromatographic separation was achieved on Inertsil ODS 3 V (250 mm × 4.6 mm, 3 μm) column. Mobile phase was degassed using transonic sonicator bath (570/HELMA, Germany). The LC–MS system operation was controlled using Chemstation and Mass hunter software.

The IR spectra of the compounds were taken from Shimadzu FTIR Spectrophotometer (Model No: IR PRESTIGE-21, location Gland Pharma R&D, Hyderabad, India) by using KBr disc technique. The ¹H, ¹³C NMR, and 2D NMR spectral analysis were carried out on Bruker (400 MHz, Location ALR fine chemical Pvt. limited, Hyderabad, India). The samples were dissolved in DMSO-*d*₆ and CD₃OD by using tetramethylsilane (TMS) as an internal standard. Melting points in °C were recorded on DSC-60 Shimadzu instrument.

Hydrolytic and thermal forced degradations were carried out using autoclave and hot air oven equipped with digital temperature control capable of controlling temperature within the range of ± 1 and ± 2 °C, respectively (Cintex precision hot air oven, Mumbai, location Gland Pharma R&D, Hyderabad, India). Photo degradation was carried out in photo stability chamber (Thermo lab Scientific equipments, Vasai, location Gland Pharma R&D, Hyderabad, India) equipped with fluorescent lamp for 1.2 million lux hours and UV light for 200 W h/m² and capable of controlling temperature and humidity in the range of ± 2 °C and ± 3% RH, respectively. The chamber was set at a temperature of 25 °C and at relative humidity (RH) of 60%. The light

system complies with option 2 of the ICH guideline Q1B. The autoclave studies were carried out in Fedegari instrument (USA).

2.3. Forced degradation study

Argatroban drug substance sample was subjected to stress under different conditions individually as well as in combination as per ICH guidelines. All stress samples were diluted with water prior to the injection to obtain a final concentration of 1 mg/mL. Acidic and alkaline hydrolysis of argatroban was conducted in 0.1 M HCl and 0.1 M NaOH, respectively. The drug substance was diluted with acidic and alkaline solutions to obtain a concentration of 1 mg/mL and hydrolytic studies were carried out at 80 °C for 2 h. For oxidative stress study, the sample was diluted with 0.3% peroxide solution to obtain a concentration of 1 mg/mL subsequently and the drug was exposed to autoclave at 120 °C for 30 min. Photo degradation studies were carried out by exposing the drug substance to a light energy of 1.2 million lux hours and an integrated UV energy of 200 W h/m². A parallel set of the drug solutions were stored in dark at the same temperature to serve as a control. Thermal studies were conducted on the solid drug substance by heating at 80 °C for 7 days in a hot air oven. All the reaction solutions were diluted with the mobile phase before HPLC analysis.

2.4. HPLC method and sample preparation

The forced degradation samples were analyzed on Agilent HPLC (series 1200) equipped with a vacuum degasser, binary pump, auto injector, DAD. The drug and its degradation products were optimally resolved on Inertsil ODS 3 V, C₁₈ (250 mm × 4.6 mm, 3 μm) column and eluted with mobile phases A (20 mM of ammonium formate at pH 3.5 adjusted with formic acid) and B (acetonitrile). The gradient profile is as follows: linear gradient 10%–35% of B in 25 min, 65% B in 40 min, 70% B in 55 min and re-equilibration of the column from 58 to 65 min with 10% of B. The flow rate was 0.8 mL/min; UV detection at λ_{max} 259 nm was used for monitoring. All the stress study samples (acid and base hydrolytic, oxidative, thermal and photolytic stress) were neutralized and diluted with the mobile phase and filtered through a 0.22 μm membrane filter before injection.

2.5. LC-MS-Ion trap and Q-TOF-MSⁿ parameters

The chromatographic conditions for LC–MS-Ion trap and Q-TOF-MSⁿ studies were the same as those for the HPLC method. The LC–MS-Ion trap and Q-TOF-MSⁿ studies were carried out using positive

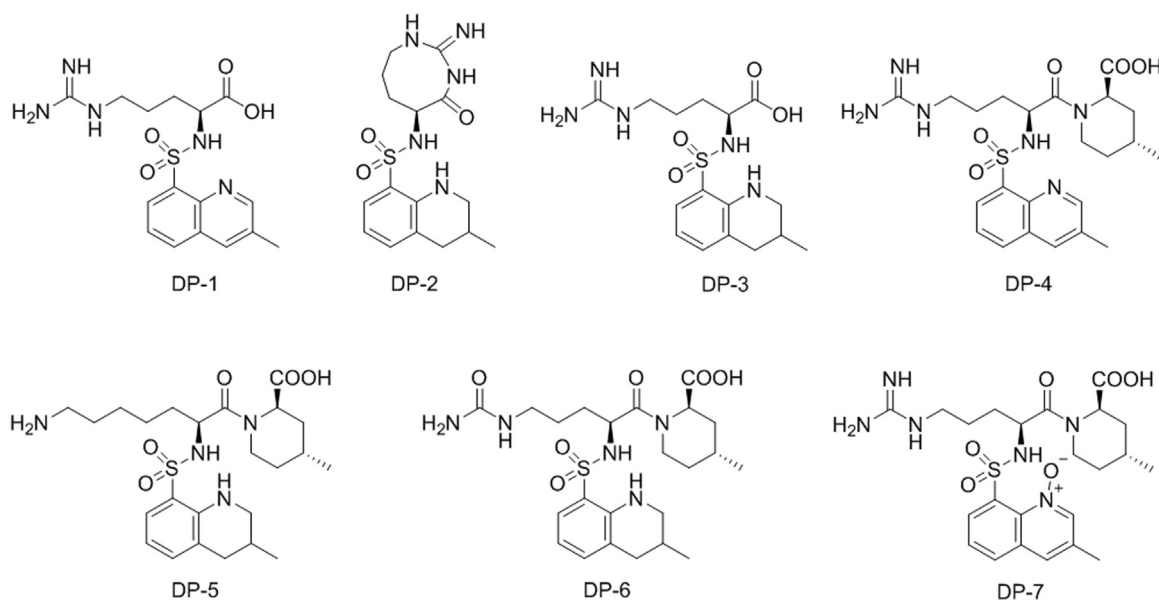


Fig. 2. Argatroban degradation products (DP-1 to DP-7).

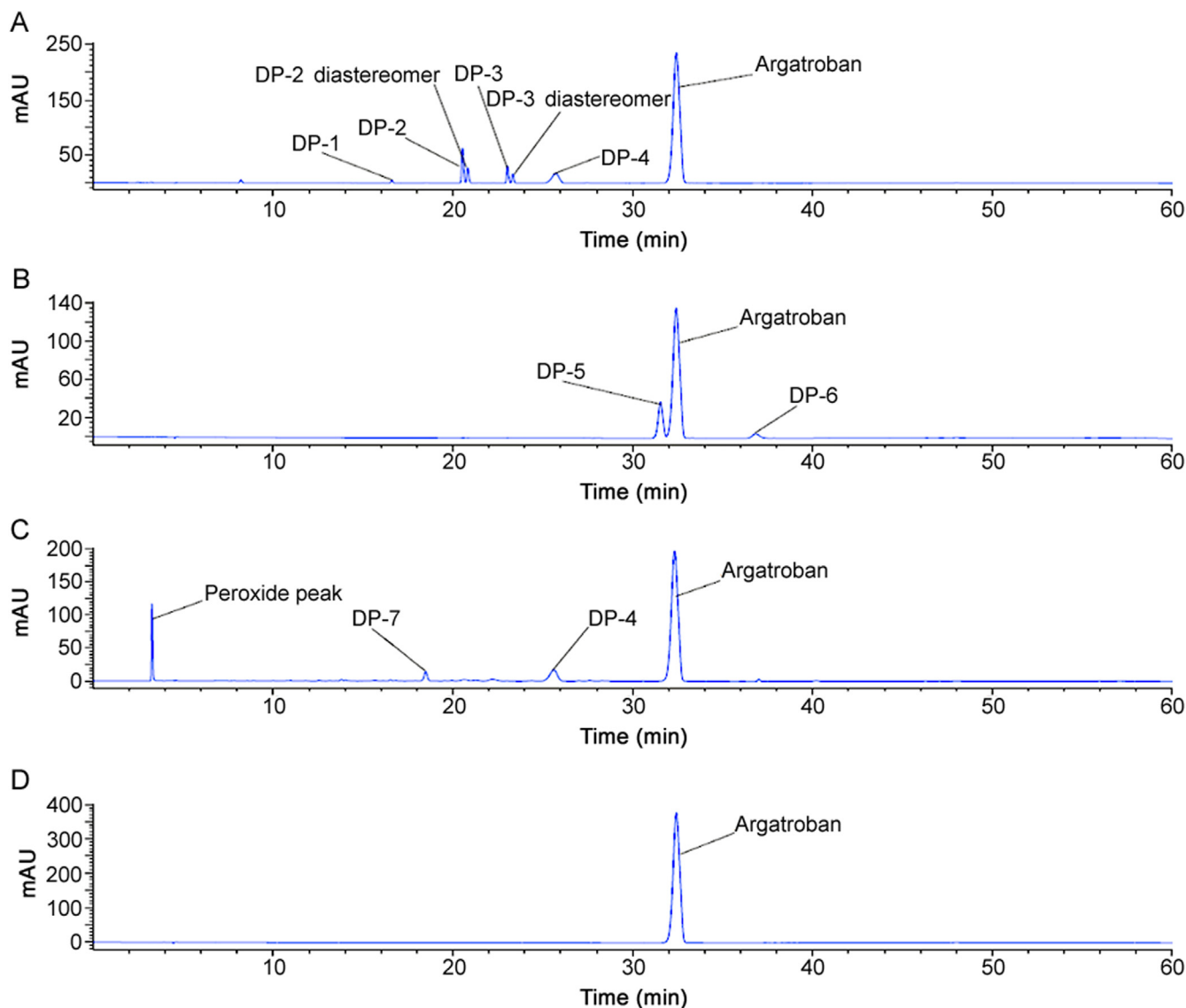


Fig. 3. HPLC chromatogram of force degradation products (DP-1 to DP-7) and standard solution of argatroban. (A) acid hydrolysis, (B) alkaline hydrolysis, (C) peroxide hydrolysis, and (D) argatroban API.

as well as negative electro spray ionization. The operating conditions for LC–MS–Ion trap 6310 scan of argatroban and degradation products in +ESI mode were optimized as follows: Octopole RF amplitude, 187.1 Vpp; capillary exit, 128.5 V; capillary, 3500 V; skimmer, 40.0 V; Octopole, 1 DC 12.0 V; Octopole, 1 DC 1.7 V; nebulizer, 65.0 psi; dry gas, 9.0 L/min, and dry temperature, 350 °C; vaporizer temperature, 250 °C; and the mass scan range, 120–1000 *m/z*.

The operating conditions for QTOF 6530 model Agilent scan of argatroban and degradation products in +ESI mode were optimized and the source parameters are as follows: gas temp, 290 °C; gas flow, 8 L/min; nebulizer, 40 psig; sheath gas temp, 290 °C; sheath gas flow, 11 L/min; and scan segment, positive polarity. The scan source parameters were as follows: VCap, 3500; nozzle voltage, 1000 V; fragmentor, 150; skimmer1, 65 and Octopole RF peak, 750. The operating conditions for MSⁿ scan of all the degradation products of the drug were in +ESI mode and the mass spectra were recorded across the range of 100 – 1000 *m/z*.

2.6. Isolation of degradation products (DP-2&DP-7) by preparative HPLC

A Shimadzu preparative HPLC equipped with UV–visible detector was employed for the isolation of DP-2 using Sunfire C₁₈

(250 mm × 19 mm, 10 μm) column. The flow rate was 15 mL/min and the detection was carried out at 259 nm. The mobile phase consisted part A (0.1% formic acid) and part B (acetonitrile). A gradient elution of T (min)/% of B: 0.01/10, 15/30, 21/60, 22/10, and 26/10 was followed for linear gradient.

3. Results and discussion

3.1. Stress decomposition behavior

The UV absorption spectrum of argatroban showed an absorption maximum λ_{\max} at 259 nm and hence, it was chosen as detection wavelength in HPLC. Numerous variations in mobile phase compositions and columns led to the optimized chromatographic conditions that resolved argatroban and all degradation products formed under different conditions in a single run. These chromatographic conditions were used to study degradation behavior of argatroban as well as for LC–MS–Ion trap/Q–TOF–MSⁿ studies. There was no degradation observed in LC–PDA chromatogram of the standard solution of argatroban.

In total, argatroban drug substance was degraded into seven major degradants which were denoted as DP-1 to DP-7 (Fig. 2) in

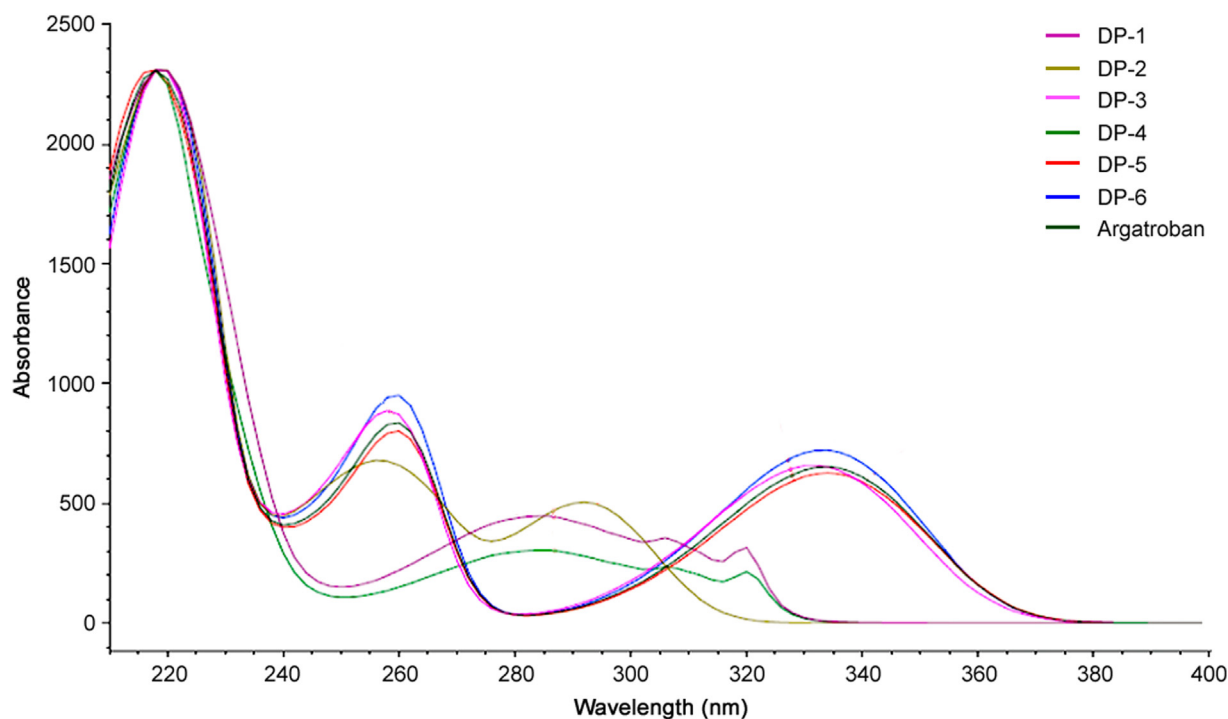


Fig. 4. UV spectra of argatroban and its degradation products (DP-1 to DP-6).

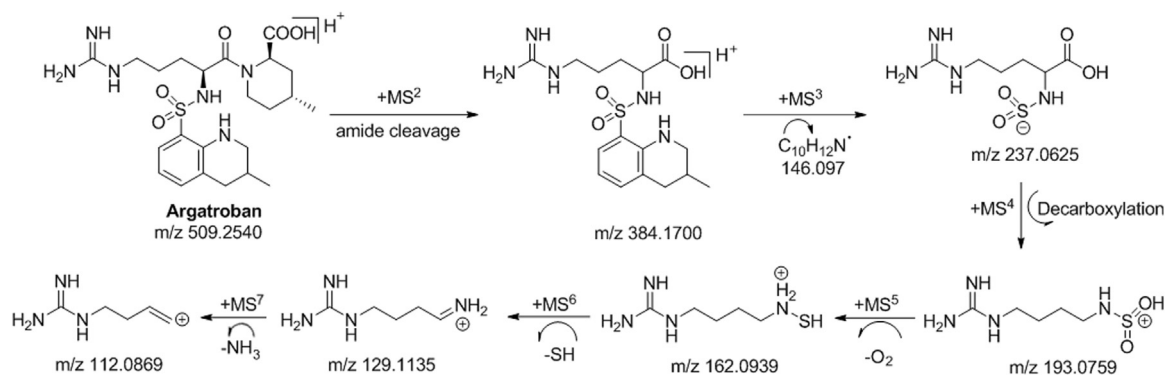


Fig. 5. Proposed mass fragmentation pattern of argatroban in +ESI mode.

accordance with the sequence in which the peak appeared from left to right in the chromatogram under various stress conditions. However, DP-4 (6.5%) was observed in both acid and peroxide stress. Besides, DP-4 further converted into corresponding N-oxide product (DP-7) in peroxide stress. Subsequently, DP-4 further degraded into DP-1 (0.5%) by hydrolysis of the amide functionality under acid stress. Similarly, DP-2 (8.8%) was also one of the major degradants in acid stress and formed through internal cyclization of DP-3 (4.4%), which in turn degraded from argatroban under acid stress. The chemical structure of DP-2 was confirmed by high resolution mass spectrometry (HRMS), NMR and heteronuclear multiple bond correlation (HMBC) studies. Apart from these, two major degradants were also observed in base stress, DP-5 (15.0%) and DP-6 (3.0%). There was no degradation observed under thermal and photolytic conditions and hence argatroban drug substance was found to be stable in thermal and photolytic conditions.

3.2. LC-PDA study

LC-PDA chromatogram showing separation of all the degradation products of argatroban using a PDA detector is shown in Fig. 3. The UV absorption behavior of degradation products (DP-1, DP-2,

DP-3, DP-4, DP-5 and DP-6) was similar to that of argatroban (λ_{\max} 259 nm) and the UV absorption spectra is shown in Fig. 4. However, DP-1, DP-4 and DP-7 showed maximum absorbance at 280 nm, which indicates that these degradant products have different chromophoric nature with respect to argatroban, which indirectly gave evidence that these three degradants have an extended conjugation in their structural motif.

3.3. Fragmentation pathway of argatroban

Seven stages mass spectra (MS^7) of argatroban were performed to outline its mass fragmentation pattern for supplementary characterization of the degradation products (Fig. 5). The drug was detected as parent ion (M^1) at m/z 509.2478 corresponding to its molecular mass of 508.2467 Da. Fragmentation of M^1 in MS^2 spectrum produced product ion of m/z 384.1700 possibly due to the loss of 4-methylpiperidine-2-carboxylic acid (143.0946 Da). The MS^2 fragmented ions, further fragmented in MS^3 at m/z 237.0652 and m/z 146.0970, were proposed to be formed by the loss of *N*-sulfo-5-guanidinopentanoic acid (237.0652 Da) and loss of 3-methyl-1, 2, 3,4-tetrahydroquinoline (146.0970 Da), from MS^2 moiety, respectively. The MS^3 which was employed as precursor

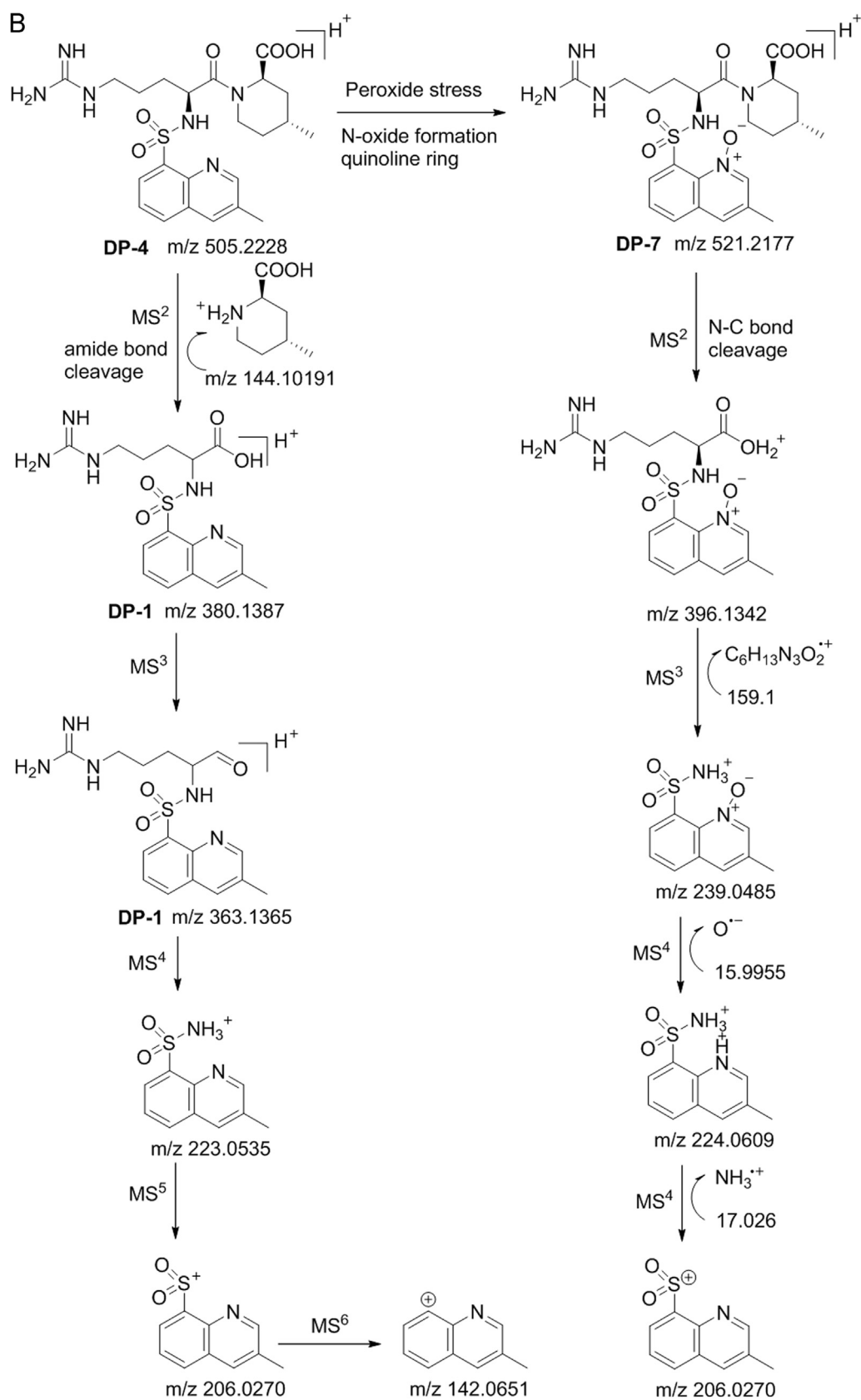


Fig. 6. (continued)

spectrum produced a product ion of m/z 321.0903 (MS²) due to the elimination of guanidyl moiety (58.0405 Da). The further MS³ fragmentation of MS² ion produced an ion at m/z 223.0535. The

MS⁴ fragmentation of MS³ formed a daughter ion at m/z 206.0270 due to the elimination of ammonium ion. In addition, MS⁵ fragmentation of MS⁴ generated a daughter ion at m/z 142.0651 due to

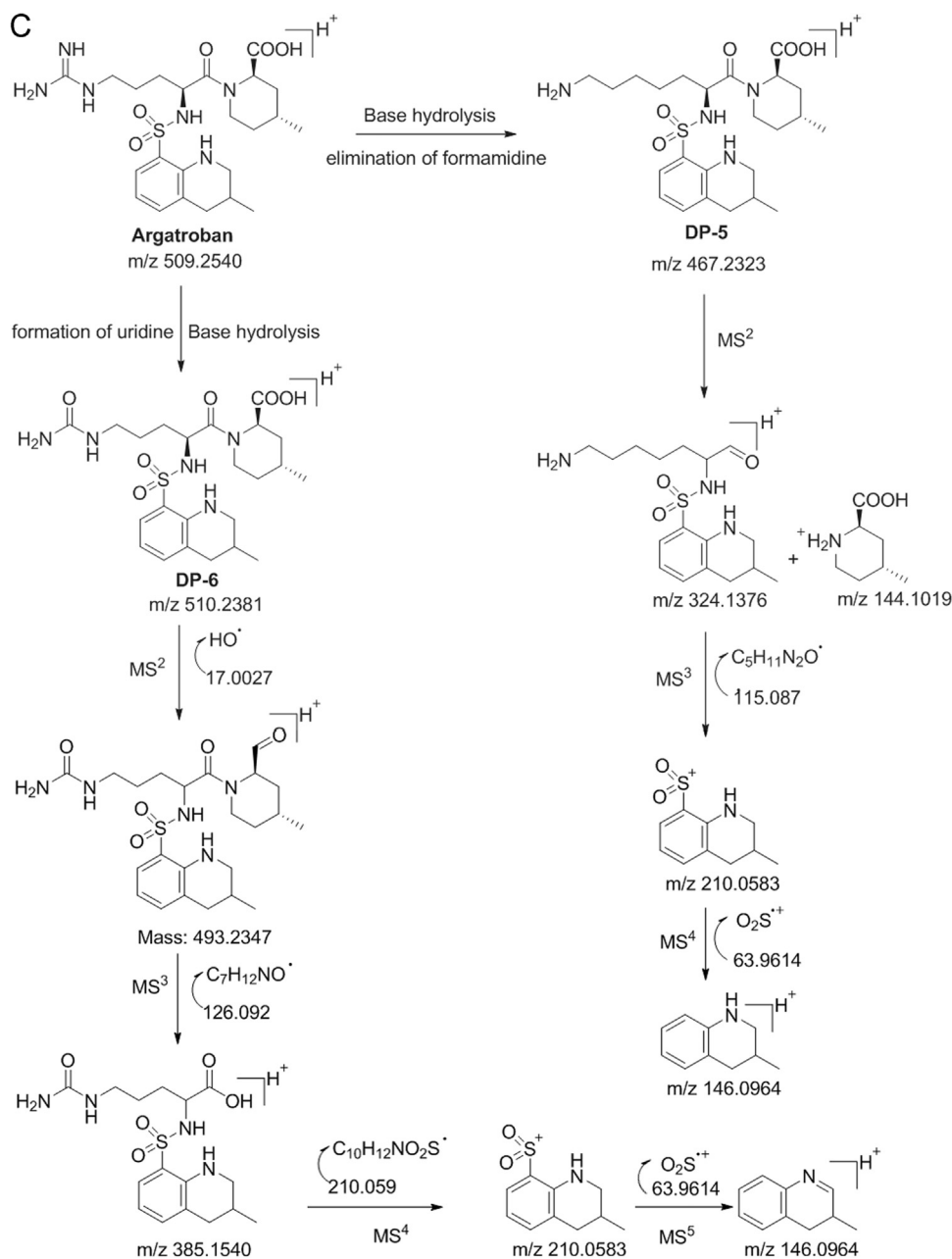


Fig. 6. (continued)

elimination of sulfonyl group. Based on the fragmentation, it is suggested that the compound has a quinoline ring in the structural motif. Based on LC–MS results and MS/MS fragmentation pattern it is concluded that DP-1 is formed by the acid hydrolysis of DP-4. The compound was further confirmed by ¹H (Fig. S1), ¹³C NMR and IR spectral analysis.

3.4.2. Characterization of DP-2

Four stage MS/MS fragmentation studies were performed to characterize DP-2. The LC–MS result shows that the mass was found at *m/z* 366.1594 for the parent ion (M¹) in positive mode. The probability of the formation of the degradant by internal cyclization of DP-3 is due to loss of water molecule. The further MS² fragmentation of M¹ produced a daughter ion at *m/z* 307.1110 by the elimination of guanidyl group, which confirmed that the degradant has an eight membered cyclic ring. Besides, MS³ fragmentation of MS² ion generated a daughter ion at *m/z* 210.0583 by

the cleavage of sulfonamide bond, confirming that the compound has a tetrahydro quinoline ring attached through sulfonamide group. Further, MS⁴ fragmentation of MS³ generated a daughter ion at *m/z* 146.0964 by the elimination of sulfonyl group, which confirms that the compound has a sulfonyl moiety. Based on the above MS/MS fragmentation pattern, DP-2 was confirmed as containing an eight membered cyclic ring attached with quinoline sulfonyl group. The structure of the compound was further confirmed by ¹H (Fig. S2), ¹³C NMR and HMBC studies.

3.4.3. Characterization of DP-3

Similarly, LC–MS/Q–TOF results of DP-3 show that the mass at *m/z* 384.1700 for the parent ion (M¹) confirms that the compound is generated by the direct hydrolysis of argatroban. For further confirmation of the structure, MS/MS fragmentation study was chosen. The MS² fragmentation of M¹ at *m/z* 384.1700 shows a daughter ion at *m/z* 175.189 which matches with the arginine

Table 1
LC–MS/Q-TOF data of (DP-1 to DP-7) along with their possible molecular formulae and major fragments.

Degradation impurities	Experimental mass	Best possible molecular formula	Theoretical mass	Error in mmu	Major fragments (error in mmu, chemical formula)
Argatroban	509.2478 384.1647 237.0622 162.0894 146.0946 129.1117 112.0853	C ₂₃ H ₃₇ N ₆ O ₅ S ⁺	509.2540	– 6.2	384.1700 (– 5.3, C ₁₆ H ₂₆ N ₅ O ₄ S ⁺) 237.0652 (– 3.0, C ₆ H ₁₃ N ₄ O ₄ S ⁺) 162.0839 (– 5.5, C ₅ H ₁₅ N ₄ S ⁺) 146.0964 (– 1.8, C ₁₀ H ₁₂ N ⁺) 129.1135 (– 1.8, C ₅ H ₁₃ N ₄ ⁺) 112.0869 (– 1.6, C ₅ H ₁₀ N ₃ ⁺)
DP-1	380.1347 363.1284 223.0509 206.0247 42.0633	C ₁₆ H ₂₂ N ₅ O ₄ S ⁺	380.1387	– 4.0	363.1365 (– 8.1, C ₁₆ H ₂₁ N ₅ O ₃ S) 223.0535 (– 2.6, C ₁₀ H ₁₁ N ₂ O ₂ S ⁺) 206.0270 (– 2.3, C ₁₀ H ₈ NO ₂ S ⁺) 142.0651 (– 1.8, C ₁₀ H ₈ N ⁺)
DP-2	366.1564 307.1081 210.0579 146.0948	C ₁₆ H ₂₃ N ₅ O ₃ S ⁺	366.1594	– 3.0	307.1010 (– 2.9, C ₁₅ H ₁₉ N ₂ O ₃ S ⁺) 210.0583 (0.4, C ₁₀ H ₁₂ NO ₂ S ⁺) 146.0964 (– 1.6, C ₁₀ H ₁₂ N ⁺)
DP-3	384.1656 175.1165 210.0577 112.0857	C ₁₆ H ₂₅ N ₅ O ₄ S ⁺	384.1700	– 4.4	175.1189 (– 2.4, C ₆ H ₁₅ N ₄ O ₂ ⁺) 210.0583 (0.6, C ₁₀ H ₁₂ NO ₂ S ⁺) 112.0869 (– 1.2, C ₅ H ₁₀ N ₃ ⁺)
DP-4	505.2168 380.1337 223.0508 206.0268 142.0637	C ₂₃ H ₃₃ N ₆ O ₅ S ⁺	505.2227	– 5.9	380.1387 (– 5.0, C ₁₆ H ₂₂ N ₅ O ₄ S ⁺) 223.0536 (– 2.8, C ₁₀ H ₁₁ N ₂ O ₂ S ⁺) 206.0270 (– 2.0, C ₁₀ H ₈ NO ₂ S ⁺) 142.0651 (– 1.4, C ₁₀ H ₁₀ N ⁺)
DP-5	467.2266 324.1341 210.0558 144.1004 146.0948	C ₂₂ H ₃₅ N ₄ O ₅ S ⁺	467.2322	– 5.6	324.1376 (– 6.2, C ₁₅ H ₂₂ N ₃ O ₃ S ⁺) 210.0583 (– 2.5, C ₁₀ H ₁₂ NO ₂ S ⁺) 144.1019 (– 1.5, C ₇ H ₁₄ NO ₂ ⁺) 146.0964 (– 1.6, C ₁₀ H ₁₂ N ⁺)
DP-6	510.2312 493.2356 385.1476 210.0553 146.0946	C ₂₃ H ₃₆ N ₅ O ₆ S ⁺	510.2380	– 6.8	493.2347 (0.9, C ₂₃ H ₃₅ N ₅ O ₅ S) 385.1440 (– 3.6, C ₁₆ H ₂₅ N ₄ O ₅ S ⁺) 210.0583 (– 3.0, C ₁₀ H ₁₂ NO ₂ S ⁺) 146.0964 (– 1.8, C ₁₀ H ₁₂ N ⁺)
DP-7	521.2176 396.1354 239.0503 224.0612 206.0288	C ₂₃ H ₃₃ N ₆ O ₆ S ⁺	521.2177	– 0.1	396.1342 (1.2, C ₁₆ H ₂₂ N ₅ O ₅ S ⁺) 239.0499 (0.4, C ₁₀ H ₁₁ N ₂ O ₃ S ⁺) 224.0609 (– 0.3, C ₁₀ H ₁₂ N ₂ O ₂ S ₂ ⁺) 206.0270 (1.8, C ₁₀ H ₈ NO ₂ S ⁺)

moiety due to the cleavage of sulfonamide, confirming that the compound has L-arginine connected with quinoline ring through sulfonamide linkage. Further, MS³ fragmentation of MS² ion delivered a daughter ion at m/z 131.1291 by the elimination CO₂ moiety from CO₂H group. Furthermore, the MS⁴ fragmentation of MS³ ion generated a daughter ion at m/z 112.0869 by the elimination of ammonia. Based on the MS/MS fragmentation results the structure of the compound was assigned and is shown in Fig. 6. The structure of the product was further confirmed by ¹H (Fig. S3), ¹³C NMR and IR spectral analysis.

3.4.4. Characterization of DP-4

The LC–MS/MS QTOF results revealed that the parent ion mass was found at m/z 505.2168 (M¹) for DP-4. Based on the difference in UV absorbance and four mass units less than that of the parent drug, oxidation might happen in the degradant. In order to identify the structure, further MS/MS fragmentation study was conducted. The MS² fragmentation of M¹ generated a daughter ion at m/z 380.1387, confirming the cleavage of amide bond, and is similar to the fragmentation observed in the parent drug but only differs in mass by 4 units, indirectly revealing that DP-4 has fully aromatized ring. Moreover, the MS³ fragmentation of MS² by the loss of 17 units due to the elimination of OH group from carboxylic acid indicates that the compound has a carboxylic acid group in the structure. Further, MS⁴ fragmentation of MS³ produced a daughter ion at m/z 223.0535 due to the heterolytic cleavage of C–N bond in the precursor ion and further MS⁵ and MS⁶ fragmentations finally delivered

a daughter ion at m/z 142.0651, confirming the 4-methyl quinoline ring. Based on the MS⁶ fragmentation, DP-4 has a 4-methyl quinoline ring in the structure. Based on the LC–MS/QTOF and MS/MS fragmentation the structure of the compound is deduced as fully aromatized compound and the structure is shown in Fig. 6. The degradation product structure was further evidenced by ¹H (Fig. S4), ¹³C NMR and IR spectral analysis.

3.4.5. Characterization of DP-5

The mass was found for DP-5 at m/z 467.2323 for the parent ion (M¹), which was formed by the cleavage of formamidinium group from the guanidyl moiety of argatroban under base hydrolysis. The MS² fragmentation of the parent ion at m/z 467.2323 produced two daughter ions at m/z 324.1378 and at m/z 144.1019, respectively by the cleavage of the amide bond. The fragmentation pattern suggested that DP-5 has a tetrahydro quinoline as well as a 4-methyl-piperidine-2-carboxylic acid moiety. Similarly, the MS³ (at m/z 210.0583) and MS⁴ (m/z 146.0964) fragmentations confirm that the compound has a tetrahydro quinoline ring. Based on the LC–MS/QTOF and MS/MS fragmentation, the structure of the compound is deduced and is shown in Fig. 6. The proposed structure was further confirmed by ¹H NMR (Fig. S5) and ¹³C NMR spectral data.

3.4.6. Characterization of DP-6

The LC–MS/MS QTOF results of DP-6 show a mass at m/z 510.2381 for the parent ion (M¹) in positive mode and it is found

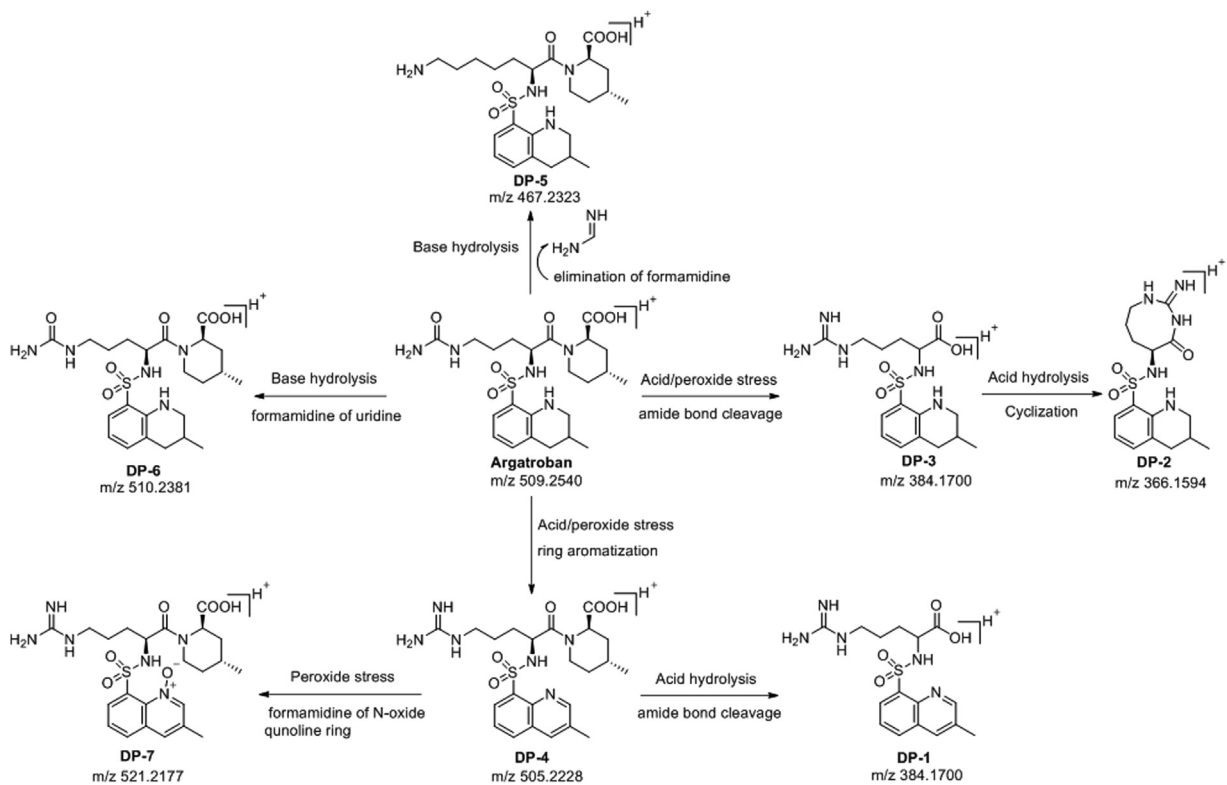


Fig. 7. Argatroban and degradation products (DP-1 to DP-7) degradation pathway.

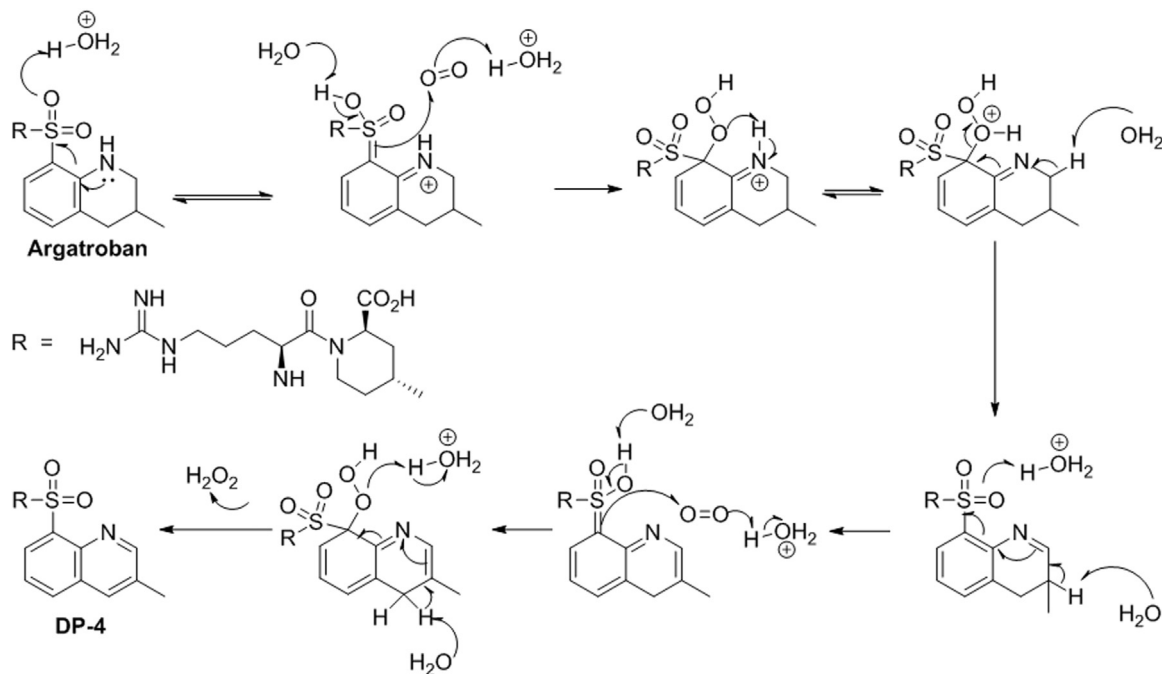


Fig. 8. Proposed mechanism for the formation of DP-4.

that it has only one mass unit more than that of the parent drug argatroban. This suggests that some hydrolysis happened under base stress and the guanidine was hydrolyzed to uridyl moiety, which confirms the mass difference. Further, MS^2 fragmentation of M^1 produced a daughter ion at m/z 493.2347 due to elimination of hydroxyl radical from carboxylic acid. The MS^3 fragmentation of MS^2 ion produced a fragmented ion at m/z 385.1540 by the elimination of 4-methyl piperidine-2-aldehyde fragment, which suggests that the degradant has a structure similar to that of

argatroban except the uridine moiety. Further, MS^4 and MS^5 fragmentations showed daughter ions at m/z 385.1540 and m/z 146.0964, confirming that the compound has a tetrahydro quinoline ring. The proposed structure of the compound was further confirmed by 1H NMR (Fig. S6) and ^{13}C NMR analysis.

3.4.7. Characterization of DP-7

Under peroxide stress conditions, two degradation products (DP-4 and DP-7) were observed. Among these two impurities, DP-

4 is major and DP-7 is minor. The DP-4 was confirmed by the individual synthesis and the synthetic sample retention time was perfectly in agreement with the retention time of the degradant formed in the stress study. Besides, DP-7 (*N*-oxide) formed from DP-4, which was confirmed by mass. In order to confirm the same, peroxide stress study was also performed with the synthetic DP-4 and the generated *N*-oxide HPLC retention time matched with that of the DP-7 formed from argatroban peroxide stress.

Hence, the structure of the *N*-oxide was further confirmed by ^1H (Fig. S7), ^{13}C NMR, HRMS and MS/MS fragmentation studies. The ^1H NMR spectrum of the isolated compound displayed a singlet at lower chemical shift value δ_{H} 8.24 ppm due to imine proton of quinoline ring, whereas the DP-4 shows chemical shift for imine proton around δ_{H} 8.91 ppm, providing strong evidence that the compound has *N*-oxide on the quinoline ring. Other proton chemical shift values observed for DP-7 were almost similar to that of DP-4. Besides, NH, NH₂ and OH protons were confirmed by disappearance with D₂O exchange. The MS² fragmentation of DP-7 produced a daughter ion at m/z 396.1342 due to heterolytic cleavage of amide, which confirms that DP-7 has an amide linkage in the back bone of the structure. Further, MS³ fragmentation of ion at m/z 396.1342 produced a daughter ion at m/z 239.0485 by the heterolytic cleavage of sulfonamide, which indicates that the *N*-oxide formation took place on the quinoline ring. Similarly, MS⁴ fragmentation of ion at m/z 239.0485 produced a fragmented ion at m/z 224.0609 by loss of 16 mass units due to loss of oxide, which confirms that the *N*-oxide formation happened on the quinoline ring. Besides, MS⁵ fragmentation of ion at m/z 224.0609 gave a daughter ion at m/z 206.0270 by the elimination of ammonia. Based on the MS/MS fragmentation pattern, the structure of DP-7 was established and is shown in Fig. 6. The chemical composition of DP-7 was further confirmed by HRMS analysis and the observed mass 521.21762 was correlated for the chemical composition of C₂₃H₃₃O₆N₆S [M+H]⁺ and the calculated mass is 521.21776 for C₂₃H₃₃O₆N₆S [M+H]⁺. The chemical compositions and the HRMS data of all degradation products (DP-1 to DP-7) obtained and the MS/MS fragmentation results are shown in Table 1.

3.5. Postulated degradation pathway mechanism

The most probable mechanistic explanation for the formation of degradation products DP-1 to DP-7 from argatroban is depicted in scheme (Fig. 6). The degradation product DP-4 was formed by acid hydrolysis, followed by ring aromatization in 3-methyl-1,2,3,4-tetrahydroquinoline of argatroban. Similarly, the degradation product DP-1 was expected to be formed by acid hydrolysis of amide bond in DP-4. However, DP-3 was generated by the acid hydrolysis of amide of 4-methylpiperidine-2-carboxylic acid in argatroban. Apart from these, DP-2 was formed in acid hydrolysis by the internal cyclization of DP-3 with the elimination of a water molecule. In addition, product DP-5 was formed by the elimination of formamidine from guanidyl moiety of argatroban under alkaline medium. Besides, DP-6 was formed due to base hydrolysis of imine group in the guanidyl resulting in the formation urea derivative of argatroban. Furthermore, peroxide stress conditions produced two degradation products (DP-4 and DP-7), among which DP-4 is major and DP-7 is minor. Subsequently, DP-7 (*N*-oxide) was formed due to the oxidation of DP-4 under peroxide stress. The *N*-oxide formation was evidenced by HRMS and MS/MS fragmentation pattern. The degradation product (DP-4) was confirmed by the individual synthesis. The degradation pathway is depicted in Fig. 7. A probable mechanism was proposed for the formation of DP-4 and is shown in Fig. 8. Initial protonation of sulfone followed by imine formation and subsequent protonation and aromatization gave the corresponding quinoline ring under acidic and peroxide stress conditions.

4. Conclusion

Degradation behavior of argatroban was explored by exposing it to ICH defined stress conditions. The drug showed significant degradation under hydrolysis (acidic, alkaline) and oxidation (peroxide stress) conditions. The drug remained stable under thermal and photolytic stress conditions. In total, seven degradation products (DP-1 to DP-7) were formed under varied conditions which were found to be previously unknown. DP-1 to DP-4 were formed as common hydrolytic degradation products under acid stress conditions and DP-5 and DP-6 were formed as common hydrolytic degradation impurities under alkaline stress conditions. The two major degradation products (DP-4 and DP-7) were generated under peroxide stress conditions. The degradation products were completely characterized with the help of advanced analytical techniques LC–MS–Ion trap/QTOF and NMR, and confirmed by individual chemical synthesis.

Conflicts of interest

The authors declare that there are no conflicts of interest.

Acknowledgments

The authors are grateful to Gland Pharma Limited, Hyderabad, for providing facilities to carry out the work and thankful to Mr. S. Sathiyarayanan, Synthesis R&D, Gland Pharma, for the fruitful discussions and also to Prof. D. B. Ramachary and Dr. Anbouselvy, School of Chemistry, University of Hyderabad, Hyderabad, for their valuable suggestions and helpful discussions in the preparation of the manuscript.

Appendix A. Supplementary material

Supplementary data associated with this article can be found in the online version at doi:10.1016/j.jpha.2017.07.001.

References

- [1] M. DiNisio, S. Middeldorp, H.R. Buller, Direct thrombin inhibitors, *N. Engl. J. Med.* 353 (2005) 1028–1040.
- [2] S. Dhillon, Argatroban: a review of its use in the management of heparin-induced thrombocytopenia, *Am. J. Cardiovasc. Drugs* 9 (4) (2009) 261–282.
- [3] Guidance for industry Q1A (R2), Stability testing of new drug substances and products, Proceedings of the International Conference on Harmonization (ICH) Guidelines, Geneva, 2003.
- [4] Guidance for industry Q1B, photostability testing of new drug substances and products, Proceedings of the International Conference on Harmonization (ICH) Guidelines, Geneva, 1998.
- [5] Guidance for industry Q3A (R2), Impurities in new drug substances, Proceedings of the International Conference on Harmonization (ICH) Guidelines, Geneva, 2006.
- [6] P. Elkins, D. Coleman, J. Burgess, et al., Characterization of the isomeric configuration and impurities of (Z)-endoxifen by 2D NMR, high resolution LC–MS, and quantitative HPLC analysis, *J. Pharm. Biomed. Anal.* 88 (2014) 174–179.
- [7] A. Awasthi, M. Razzak, R. Al-Kassas, et al., Isolation and characterization of degradation products of moxidectin using LC, LTQ FT–MS, H/D exchange and NMR, *Anal. Bioanal. Chem.* 8 (2012) 2203–2222.
- [8] R. Rapolu, Ch.K. Raju, K. Srinivas, et al., Isolation and characterization of a novel acid degradation impurity of amlodipine besylate using Q-TOF, NMR, IR and single crystal X-ray, *J. Pharm. Biomed. Anal.* 99 (2014) 59–66.
- [9] R. Rapolu, A.K. Pandey, Ch.K. Raju, et al., A novel UV degradation product of ebastine: isolation and characterization using Q-TOF, NMR, IR and computational chemistry, *J. Pharm. Biomed. Anal.* 107 (2015) 488–494.
- [10] P.H. Secretan, M. Karoui1, M. Bernard, et al., Photodegradation of aqueous argatroban investigated by LC/MSⁿ: photoproducts, transformation processes and potential implications, *J. Pharm. Biomed. Anal.* 131 (2016) 223–232.



Contents lists available at ScienceDirect

Journal of Pharmaceutical Analysis

journal homepage: www.elsevier.com/locate/jpa
www.sciencedirect.com

Original Research Article

Structural confirmation of sulconazole sulfoxide as the primary degradation product of sulconazole nitrate

Qun Xu^{*}, Ashraf Khan¹, Di Gao², Kristie M. Adams, Fatkhulla Tadjimukhamedov, Shane Tan, John T. Simpson

Compendial Development Laboratory, United States Pharmacopeia, Rockville, MD 20852, USA

ARTICLE INFO

Article history:

Received 27 October 2017

Received in revised form

15 December 2017

Accepted 18 December 2017

Available online 19 December 2017

Keywords:

Sulconazole nitrate

Sulconazole sulfoxide

Forced degradation

Structural characterization

LC–MS/MS

ABSTRACT

Sulconazole has been reported to degrade into sulconazole sulfoxide via sulfur oxidation; however, structural characterization data was lacking and the potential formation of an *N*-oxide or sulfone could not be excluded. To clarify the degradation pathways and incorporate the impurity profile of sulconazole into the *United States Pharmacopeia–National Formulary (USP–NF)* monographs, a multifaceted approach was utilized to confirm the identity of the degradant. The approach combines stress testing of sulconazole nitrate, chemical synthesis of the degradant via a hydrogen peroxide-mediated oxidation reaction, semi-preparative HPLC purification, and structural elucidation by LC–MS/MS and NMR spectroscopy. Structural determination was primarily based on the comparison of spectroscopic data of sulconazole and the oxidative degradant. The mass spectrometric data have revealed a McLafferty-type rearrangement as the characteristic fragmentation pathway for alkyl sulfoxides with a β -hydrogen atom, and was used to distinguish the sulfoxide from *N*-oxide or sulfone derivatives. Moreover, the generated sulconazole sulfoxide was utilized as reference material for compendial procedure development and validation, which provides support for USP monograph modernization.

© 2018 Xi'an Jiaotong University. Production and hosting by Elsevier B.V. This is an open access article under the CC BY-NC-ND license (<http://creativecommons.org/licenses/by-nc-nd/4.0/>).

1. Introduction

Sulconazole, 1-[2,4-dichloro- β -[(4-chlorobenzyl)thio]phenethyl]-imidazole, is an azole antifungal drug belonging to the family of the imidazole class, and is typically used as a topical antifungal cream or solution for the treatment of dermatomycoses, pityriasis versicolor, and cutaneous candidiasis [1]. Sulconazole nitrate was among the drug substances that were undergoing United States Pharmacopeia (USP) monograph modernization [2]. The USP sulconazole nitrate monograph describes an HPLC procedure for assay, but lacks any organic impurity procedures [3]. Sulconazole nitrate is currently not included in other major pharmacopeias.

A literature search indicated that limited information is available regarding the stability and chromatographic analysis of this drug substance. HPLC methods have been reported for the analysis of sulconazole in biological samples or drug products [4–7], but

sulconazole related compounds were not included for method development or evaluation. In terms of stability studies, comprehensive degradation studies under various stress conditions have not been reported. Chen et al. [8] investigated the kinetics of oxidation of sulconazole with peracetic acid and hydrogen peroxide; sulconazole sulfoxide and sulfone were assumed to be the oxidation products. Iwasawa et al. [9] reported the pharmacological studies of the metabolites of sulconazole and highlighted the liability of the molecule towards oxidative conditions. However, no structural information was disclosed in either of those papers.

Oxidation of organic sulfides (thioethers) to sulfoxides is an important degradation and metabolic pathway for a variety of sulfur-containing pharmaceutical agents, such as montelukast [10], ranitidine [11], penicillin [12], pergolide [13], and methionine- or cysteine-containing peptides [14]. The oxidation process could be complicated as *N*- or *S*-oxidation might occur [11], and over-oxidation of a sulfoxide to the corresponding sulfone is frequently a competing reaction [15]. To gain a better understanding of the stability of sulconazole nitrate and incorporate the impurity profile into USP monographs, it is critical to differentiate the oxidation pathways and confirm the structures of the degradation products [16].

Here we report the structural determination of a major degradation product of sulconazole nitrate, sulconazole sulfoxide, which was generated under oxidative conditions. In addition, this material was subsequently employed as an impurity reference for

Peer review under responsibility of Xi'an Jiaotong University.

* Correspondence to: United States Pharmacopeia (USP), 12601 Twinbrook Parkway, Rockville, MD 20852, USA.

E-mail address: qzx@usp.org (Q. Xu).¹ Present Address: Quality Control, AstraZeneca, 660 Research Court, Frederick, MD 21703, USA.² Consultant, United States Pharmacopeia, 12601Twinbrook parkway, Rockville, MD 20852, USA.<https://doi.org/10.1016/j.jpha.2017.12.007>2095-1779/© 2018 Xi'an Jiaotong University. Production and hosting by Elsevier B.V. This is an open access article under the CC BY-NC-ND license (<http://creativecommons.org/licenses/by-nc-nd/4.0/>).

compendial procedure development and validation. The monograph modernization efforts have eventually culminated in an official compendial procedure and a newly introduced impurity, sulconazole related compound A [17,18].

2. Material and methods

2.1. Chemicals and reagents

The drug substance sulconazole nitrate was obtained from the USP Reference Standard. Commercial samples of sulconazole nitrate were purchased from Sigma-Aldrich (St. Louis, MI, USA), Spectrum Chemical (New Brunswick, NJ, USA), Glentham Life Sciences (Corsham, UK), and Erregierre (Sovere, Italy). Hydrochloric acid (37%), glacial acetic acid ($\geq 99.7\%$), sodium hydroxide solution (10 N, J.T.Baker), trifluoroacetic acid (TFA, 99.5%, Acros Organics), ammonium acetate (LC/MS), methanol (LC/MS), and acetonitrile (HPLC and LC/MS) were purchased from Fisher Scientific (Waltham, MA, USA). Hydrogen peroxide ($\sim 30\%$) was obtained from Sigma-Aldrich. Water was purified with a Milli-Q plus system from Millipore (Bedford, MA, USA).

2.2. Instrument and analytical parameters

2.2.1. UHPLC/HPLC

UHPLC–UV analyses were performed on an Agilent Infinity 1290 UHPLC system (Santa Clara, CA, USA). Separation was carried out on an Acquity BEH C_{18} column (2.1 mm \times 100 mm, 1.7 μm) from Waters (Milford, MA, USA) using a mobile phase system consisting of mobile phase A: methanol and ammonium acetate buffer (pH 5.0; 0.1 mM) (20:80, v/v); and mobile phase B: methanol and acetonitrile (40:60, v/v). Analyses were performed at ambient temperature with a flow rate of 0.5 mL/min and a gradient elution varied according to the following program: 0 min, 40% B; 8 min, 90% B; 8.1 min, 40% B; and 10 min, 40% B. UV detection wavelength was set at 230 nm. The injection volume was 5 μL .

HPLC–UV analyses were performed on a Waters Alliance 2695 HPLC system using a Waters Atlantis C_{18} column (4.6 mm \times 150 mm, 5 μm) and a mobile phase system consisting of 0.05% TFA in water and acetonitrile. Separations were achieved at ambient temperature with a flow rate of 1.0 mL/min and an isocratic program of 0.05% TFA in water and acetonitrile (50:50, v/v). UV detection wavelength was set at 210 nm. The injection volume was 10 μL .

Preparative chromatography was performed on a Waters semi-preparative HPLC system consisting of a 2335 quaternary gradient module, a 2998 photodiode array detector, a 2707 autosampler, and a Waters fraction collector III. Separations were carried out on an Agilent Prep- C_{18} column (20.1 mm \times 150 mm, 5 μm) using a mobile phase system consisting of 0.05% TFA in water and acetonitrile (65:35, v/v). The flow rate was 10.0 mL/min and the run time was 13 min. UV detection was performed at 210 nm. The injection volume was 0.4 mL. Fractions were collected based on time mode.

Waters Empower 2 for chromatography software was used for instrument operation control and data acquisition and processing.

2.2.2. NMR analysis

NMR experiments were recorded using a Bruker Avance III NMR Spectrometer (Billerica, MA, USA) with operating frequencies of 600.13 MHz (^1H) and 150.90 MHz (^{13}C). Samples were dissolved in $\text{DMSO}-d_6$ and all NMR spectra were recorded at 25 $^\circ\text{C}$. Chemical shifts were reported in ppm downfield from tetramethylsilane (TMS, $\delta = 0$) as the internal reference.

2.2.3. LC–MS/MS analysis

The LC–MS/MS was performed on an Agilent 6540 UHD Accurate-Mass QTOF LC–MS using an Agilent 1290 UHPLC as an inlet with UV detection at 210 nm prior to the mass spectrometer. Data acquisition and analysis were performed using Agilent MassHunter software. ESI was used in positive ion mode. Except for the injection volume (2 μL), LC conditions were the same as those used for UHPLC–UV analysis in Section 2.2.1. The mass spectrometer was tuned in 2 GHz extended dynamic range mode (24,350 FWHM resolution at m/z 1521.9715) for accurate mass analyses. Mass accuracy was less than 0.2 ppm for reference masses across the mass range of m/z 100–1700. The mass range analyzed was m/z 100–1200.

2.3. Solution and sample preparation for UHPLC method

A solution of water and methanol (60:40, v/v) was used as the diluent. A resolution solution was prepared by dissolving sulconazole nitrate and sulconazole sulfoxide in the diluent to give a solution having a concentration of 0.15 mg/mL for sulconazole and 1.5 $\mu\text{g}/\text{mL}$ for sulconazole sulfoxide. The standard solution was prepared at a concentration of 1.5 $\mu\text{g}/\text{mL}$ for sulconazole and sulconazole sulfoxide. The sample solution at a concentration of 1.5 mg/mL was prepared by dissolving a sulconazole nitrate bulk material in the diluent.

3. Results and discussion

3.1. HPLC method development

In light of the structural similarities between sulconazole and econazole (another azole antifungal drug), the mobile phases used in the European Pharmacopoeia econazole monographs (econazole and econazole nitrate) were directly adopted as a starting point for UHPLC method development [19]. Column optimization led to the identification of ethylene bridged hybrid (BEH) C_{18} silica as the choice of stationary phase. The effective chromatographic separation between sulconazole and the major degradant was achieved using a Waters Acquity BEH column (2.1 mm \times 100 mm, 1.7 μm) and a mobile phase of methanol–ammonium acetate buffer and methanol–acetonitrile in a gradient elution. In addition to the separation of the major degradant and sulconazole, the method was also capable of separating the major degradant from a minor secondary degradant with a resolution of 1.4.

An HPLC method was also developed as a guiding method for subsequent preparative HPLC operation (Section 2.2.1). Complete separation was achieved for sulconazole and the major degradant using a Waters Atlantis column and a mobile phase of acetonitrile and 0.05% TFA. Although the method did not provide sufficient resolution for the major degradant and the secondary degradant, our initial scale-up experiments on preparative HPLC revealed that the lack of resolution did not pose a problem for the overall purification.

3.2. Forced degradation of sulconazole nitrate

Forced degradation studies of sulconazole nitrate were performed under thermal, thermal and humidity, photolytic, hydrolytic (acid and base), and oxidative conditions (Fig. 1). The degradation was monitored and analyzed using the UHPLC method with UV and MS detection and both detection techniques revealed that degradation of sulconazole only occurred under oxidative conditions (Table S1 and Fig. S1). In addition to the major degradant, a trace amount of secondary degradant was also detected when the stress time was prolonged or the concentration of the

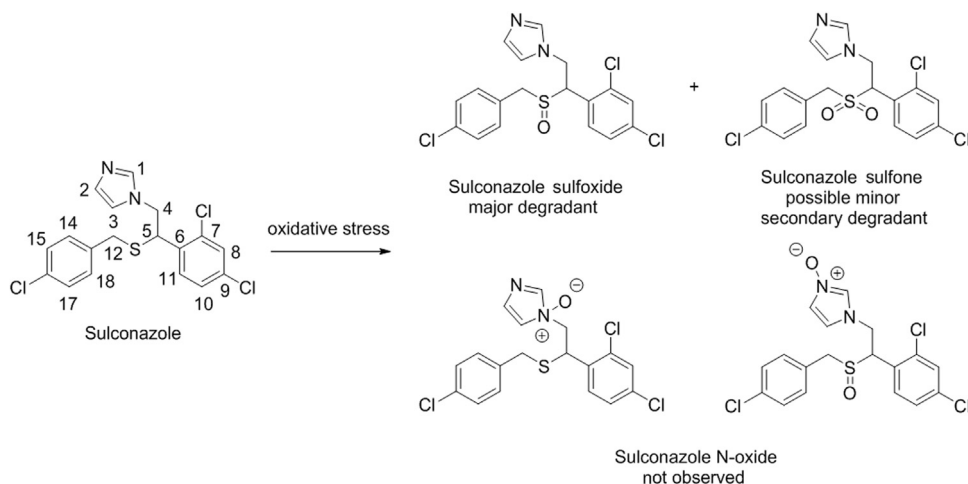


Fig. 1. Oxidative stress of sulconazole nitrate.

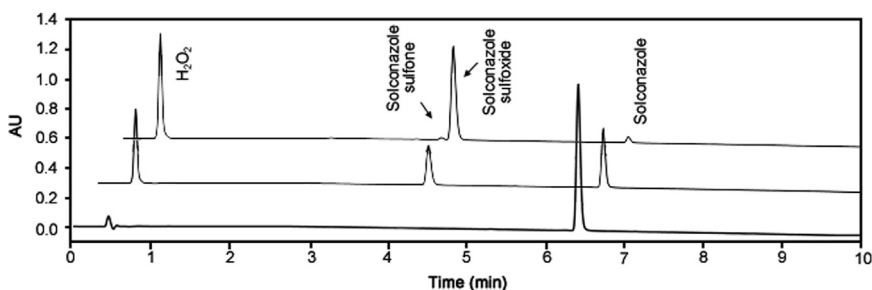


Fig. 2. Overlaid chromatograms of oxidative stress of sulconazole nitrate (from bottom to top: chromatogram of sulconazole, chromatograms of sulconazole under oxidative stress for 3 days and 12 days).

oxidant was increased (Fig. 2). PDA peak purity testing and LC–MS were performed for the sulconazole peak and no co-elution of impurities was detected.

The LC–MS analysis showed that the masses of sulconazole and a major oxidation product were m/z 397.0094 and 413.0045, respectively (Fig. S1). The major oxidative degradant showed a protonated molecule that had a delta of 16 amu difference from sulconazole, suggesting a single *N* or *S* oxidation. A minor ion at m/z 428.9997 with a mass change from sulconazole of 32 amu indicated that a secondary degradation, the possible oxidation of sulfoxide to sulfone, or *S*-oxidation followed by *N*-oxidation, might occur.

N-oxidation of the imidazole of miconazole nitrate, a similar imidazole antifungal drug, has been reported under hydrogen peroxide-mediated oxidation conditions [20]. It is well-documented that both *N*- and *S*-oxidation could be competing pathways for drug substances containing both *N* and *S* sites susceptible to oxidation, such as ranitidine [21]. More importantly, *S*-oxidation is not always inherently favored over *N*-oxidation [22]. For instance, zofenopril was recently demonstrated to undergo *N*-oxidation selectively using hydrogen peroxide as an oxidant [23]. On the basis of these precedents, the possibility of *N*-oxide products of sulconazole cannot be excluded at this stage.

3.3. Synthesis and preparative isolation of the degradation product

The scale-up oxidation experiment was performed in a concentrated sample solution using 30% hydrogen peroxide. Complete conversion of sulconazole nitrate to the major degradant was achieved within 20 h (Fig. S2). The experiment was halted when an over-oxidation started to occur. As the reaction proceeded to 100% conversion, the challenge of the purification step was the

removal of the minor degradant, which had a retention time close to that of the major peak.

The injection and loading amount were carefully evaluated on an analytical column (Waters Atlantis C_{18} , 4.6 mm \times 150 mm, 5 μ m) to ensure the sufficient separation of the two peaks on the similar preparative column (Prep- C_{18} , 20.1 mm \times 150 mm, 5 μ m) while maintaining separation efficiency. To this end, the heart-cutting technique was applied and multiple injections of the crude reaction mixture at an appropriate concentration were performed (Fig. S3). The isolated compound was re-analyzed on both analytical HPLC and UHPLC to confirm the identity and purity (Fig. S4). The degradant was isolated as a colorless oil in 93% yield and 98% purity based on HPLC.

3.4. Structural characterization of the major degradation product

3.4.1. NMR studies of sulconazole and sulconazole sulfoxide

Samples of sulconazole nitrate and the isolated major degradation product were subjected to NMR spectroscopic analyses including one- and two-dimensional NMR such as gradient-selected correlation spectroscopy (gCOSY), heteronuclear single-quantum coherence (HSQC) and heteronuclear multiple bond correlation (HMBC) experiments. The NMR spectroscopic data were consistent with the proposed structures of sulconazole and sulconazole sulfoxide (Supplementary material). The ^1H and ^{13}C assignments were made based on characteristic chemical shifts (^1D NMR) and were supported by ^2D NMR data. The ^1H and ^{13}C NMR data and proposed assignments for the two compounds are presented in Table 1 for comparison.

Direct assignments for protons of the two substituted aromatic rings were difficult due to the high degree of similarity in

Table 1
Comparative ^1H NMR and ^{13}C NMR data of sulconazole nitrate and sulconazole sulfoxide (DMSO- d_6 , 25 °C).

Position	Sulconazole nitrate chemical shifts (ppm)				Sulconazole sulfoxide chemical shifts (ppm)			
	^{13}C	^1H	No. of H	multiplicity	^{13}C	^1H	No. of H	multiplicity
1	136.5	9.03	1H	s	136.2	9.06	1H	s
2	120.1	7.61	1H	d, $J = 1.5$	120.3	7.61	1H	m
3	122.3	7.61	1H	d, $J = 1.5$	122.4	7.65	1H	m
4	50.9	4.82, 4.75	2H	dd, $J = 18.0$ $J = 6.0$	46.7	5.02–5.14	2H	m
5	44.6	4.65	1H	t, $J = 6.0$	58.8 ^a	5.06	1H	m
6	133.3				133.1			
7	134.3				134.5			
8	129.1	7.58			129.4	7.67	1H	
9	133.7				131.1			
10	128.0	7.47		d, $J = 6.0$ $J = 2.0$	128.3	7.67	1H	m
11	130.5	7.57		d, $J = 6.0$	129.7 ^a	7.64	1H	m
12	34.2	3.89, 3.72	2H	d, $J = 12.0$	55.3	4.20, 4.26	2H	d, $J = 12.0$
13	135.9				134.7			
16	131.1				129.8			
14, 18	130.6	7.27	2H	d, $J = 6.0$	132.1	7.35	2H	d, $J = 6.0$
15, 17	128.4	7.34	2H	d, $J = 6.0$	128.7	7.43	2H	d, $J = 6.0$

^a ^{13}C signals were not readily apparent in the ^{13}C NMR spectrum, and C5 and C11 were identified using HMBC experimental data.

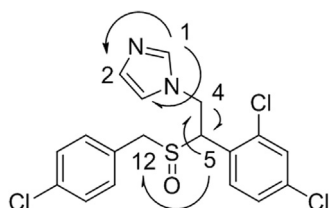


Fig. 3. Key ^1H – ^{13}C HMBC correlations of sulconazole sulfoxide. Correlations are shown with arrows. The numbering system is based on the NMR assignments presented in Table 1.

the ^1H and ^{13}C chemical shifts. In the ^1H NMR spectrum, a significant chemical shift was observed for methine **5** and methylene **12** protons (Table 1). The change of the splitting pattern indicated the corresponding conformational change after the oxidation of the sulfur [24]. More drastic downfield shifts of methine **5** and methylene **12** were detected in the ^{13}C NMR. In contrast, negligible changes of chemical shifts (^1H and ^{13}C) on the imidazole ring were observed, indicating that the *N*-oxidation of imidazole did not occur. Notably, a slight downfield shift was detected for methylene **4** in the ^1H NMR, and a slight upfield shift was observed for the same methylene in the ^{13}C NMR. These results were in good agreement with NMR data for alkyl groups in a β orientation to sulfur. The HMBC data showed connections between H1 and C2 and C3, H4 and C5, and H5 and C12 (Fig. 3). The ^1H and ^{13}C NMR data, in combination with the LC–MS results, provided reasonable evidence in support of the *S*-oxidation. However, the NMR data alone were not conclusive to differentiate sulfoxide from sulfone, the potential over-oxidation byproduct, as the influence of aliphatic sulfoxide and sulfone groups on the chemical shifts of the α , β , and γ substitutes is very similar [25,26].

3.4.2. LC–MS/MS studies

The LC–MS/MS analysis was performed using the same UHPLC method (Section 2.2.1). The presence of multiple chlorine atoms in the molecules allows for more precise determination of the fragment ions based not only on the exact mass but also the isotope abundance ratio. The LC–MS spectrum of the oxidative degradant of sulconazole showed a protonated molecule

$[\text{M}+\text{H}]^+$ at m/z 413.0048 (Fig S5), suggesting an elemental composition of $\text{C}_{18}\text{H}_{16}\text{Cl}_3\text{N}_2\text{OS}$, which is consistent with the structure resulting from *S*- or *N*-oxidation. The MS/MS spectrum and possible fragmentation pathways are shown in Fig. 4. The MS/MS fragmentation of the $[\text{M}+\text{H}]^+$ ion exhibited a diagnostic fragment ion at m/z 239.0136 (elemental composition of $\text{C}_{11}\text{H}_9\text{N}_2\text{Cl}_2$), which can be derived from the syn-elimination of alkyl sulfenic acid via a 5-membered cyclic transition state. This McLafferty-type fragmentation has been revealed as a dominant fragmentation pathway for peptides containing oxidized methionine or cysteine residues [27,28]. In addition, it was verified as the most facile fragmentation for the styryl- and alkyl-propenyl sulfoxides by deuterium labeling studies [29]. Mechanistically, for sulfur-containing molecules this fragmentation only occurs for sulfoxides with a β -hydrogen atom, and it was indeed observed in numerous reported cases [30–33]. The McLafferty-type fragmentation might be a characteristic fragmentation pathway for sulfoxides with a β -hydrogen atom and could also be used here to distinguish the sulfoxide from the sulfone. Initial examination of the isotopic pattern of this fragment ion indicated that there may be overlapping ion distributions, and a possible fragment **b** at m/z 240.0212 resulting from a proposed sulfinyl radical cleavage may be contributing to the overall isotopic pattern (Fig. 4). Another major fragment at m/z 171.9841 (**d**) may be derived from fragment **b** via loss of the imidazole ring. The fragment **c** at m/z 205.0527 was also generated via a McLafferty-type fragmentation after dechlorination of the $[\text{M}+\text{H}]^+$ ion [34–36]. In addition to major fragments, the ions at m/z 125.0147 ($\text{C}_7\text{H}_6\text{Cl}$, **e**) and 287.9879 ($\text{C}_{11}\text{H}_{10}\text{Cl}_2\text{N}_2\text{OS}$, **f**), generated from cleavage of *S*- CH_2 bond were also observed, but were much less abundant (0.05% and 0.02%, respectively), suggesting that this disassociation pathway is not favored.

The MS/MS results of sulconazole nitrate were significantly different from those of sulconazole sulfoxide (Fig. S6). As expected, McLafferty-type fragmentation corresponding to the cleavage of *S*- CH bond was not observed. The ion **g** at m/z 125.0158 is predominant under similar activation conditions, suggesting that the cleavage of *S*- CH_2 bond is the favored dissociation process resulting in the stable carbocation (Fig. S7). Another main fragment ion **j** at m/z 183.0030 was generated as a result of the consecutive loss of imidazole and chlorobenzene, which also led to the

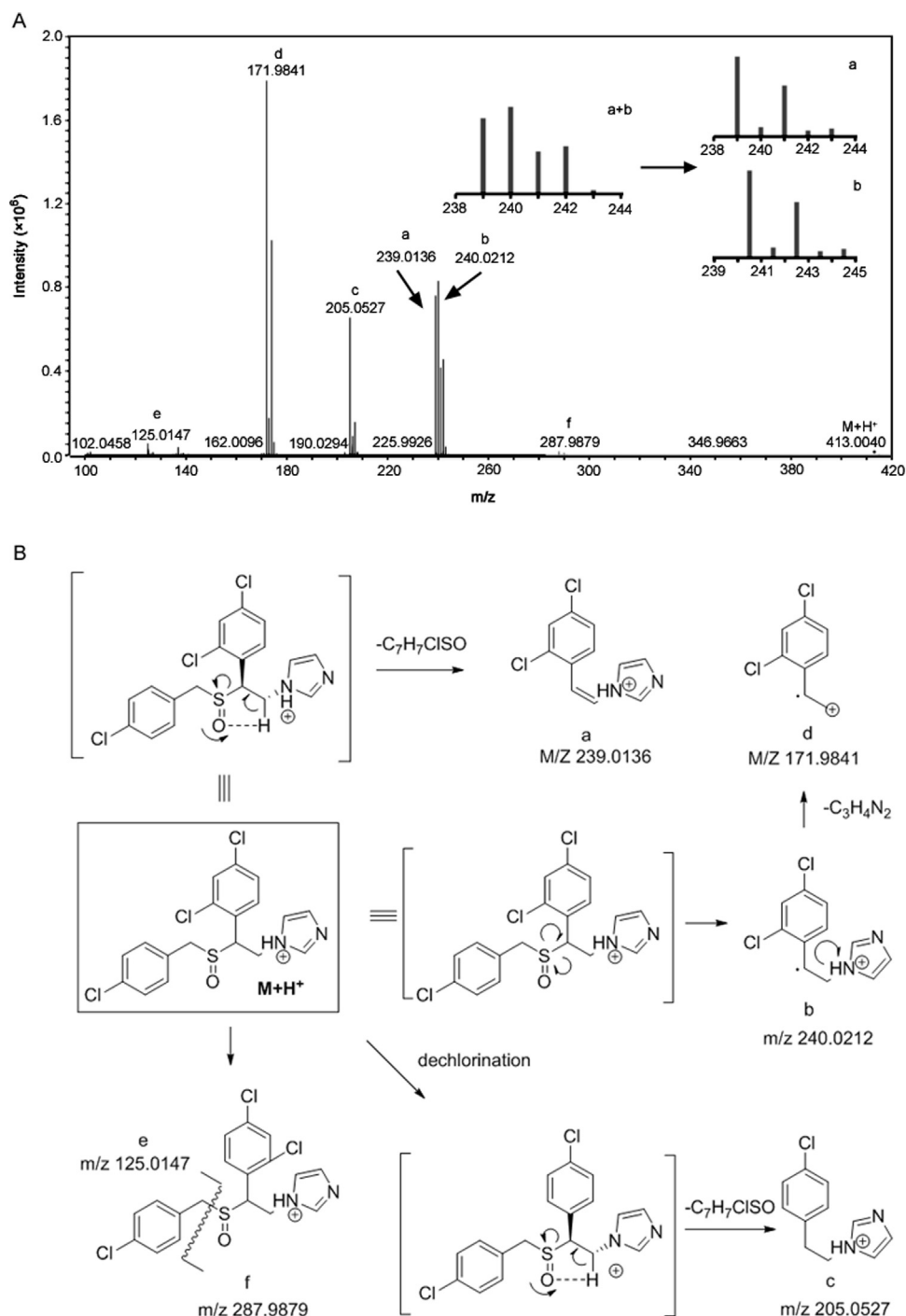


Fig. 4. (A) MS/MS spectrum of protonated molecular ion $[M+H]^+$ at m/z 413.0048 of sulconazole sulfoxide. (B) proposed fragmentation pathway. The isotope pattern of ion cluster at m/z 239.0136 matches the results of superimposition of two species of **a** and **b** as shown in the inserted frame.

formation of a stable benzyl thiirane methyl carbocation **j**. In addition, the intermediate ion **h** at m/z 328.9717 resulting from the loss of imidazole was also detected.

As shown in Table 2, all fragmentation assignments were supported by accurate mass data. The accuracy for the masses of these ions, determined relative to the values calculated from their assigned structures, was within 5 ppm error.

The comparative MS/MS studies provided compelling evidence that the oxidation occurred on the sulfur atom only, and that the sulfoxide was the primary degradant. Sulconazole sulfone is most

likely the product of over-oxidation. Moreover, previous investigations on *N*-oxides indicated that the mass spectrum of an *N*-oxide is in general similar to that of parent compound [20], which is also in agreement with our conclusion in support of *S*-oxidation.

3.5. UHPLC method validation

With the sulconazole sulfoxide in hand, the UHPLC method was validated for specificity, linearity, accuracy, precision and

Table 2

Accurate mass measurement of the molecular ions observed from the MS/MS data of sulconazole sulfoxide and sulconazole. The MS/MS spectrum of sulconazole nitrate and proposed fragmentation pathway are provided in Figs. S6 and S7.

Fragment	Observed mass m/z	Composition	Theoretical mass m/z	Error in ppm
[M + H] ⁺	413.0048	C ₁₈ H ₁₆ N ₂ Cl ₃ OS	413.0043	1.21
a	239.0136	C ₁₁ H ₉ N ₂ Cl ₂	239.0137	-0.42
b	240.0212	C ₁₁ H ₁₀ N ₂ Cl ₂	240.0216	-1.67
c	205.0527	C ₁₁ H ₁₀ N ₂ Cl	205.0527	0
d	171.9841	C ₈ H ₆ Cl ₂	171.9847	-3.49
e	125.0147	C ₇ H ₆ Cl	125.0153	-4.80
f	287.9879	C ₁₁ H ₁₀ Cl ₂ N ₂ OS	287.9885	-2.08
[M + H] ⁺	397.0089	C ₁₈ H ₁₆ N ₂ Cl ₃ S	397.0094	-1.26
g	125.0158	C ₇ H ₆ Cl	125.0153	4.00
h	328.9717	C ₁₅ H ₁₂ Cl ₃ S	328.9720	-0.91
i	361.0315	C ₁₈ H ₁₅ Cl ₃ N ₂ S	361.0328	-3.60
j	183.0030	C ₉ H ₈ ClS	183.0030	0

robustness. System suitability was verified by determining the % RSD of six injections of the standard solution. Retention time, tailing factor and resolution between the sulconazole and sulconazole sulfoxide were also determined (Table S2). The specificity of the method was established by determining peak purity of sulconazole nitrate subjected to a series of stressed conditions using photodiode array detection. Linearity of the detector responses was determined at five concentration levels of sulconazole nitrate and sulconazole sulfoxide covering 0.75, 1.125, 1.50, 1.875 and 2.25 µg/mL for each compound. To study method accuracy, recovery experiments were carried out by applying the standard addition method. Known quantities of sulconazole sulfoxide of 0.75, 1.50 and 2.25 µg/mL—corresponding to 50%, 100% and 150% impurity levels—were spiked into a 1.5 mg/mL sulconazole nitrate solution. Accuracy was expressed as the percentage of sulfoxide recovered by the HPLC analysis. Repeatability was studied by carrying out method precision, and determined from results of six independent injections of the 100% spiked solutions. Method robustness was evaluated by analyzing five replicate injections of the robustness solution, sulconazole nitrate (150 µg/mL) and sulconazole sulfoxide (1.5 µg/mL), under each of the varied conditions including temperatures, flow rates, buffer pH, mobile phase B initial compositions, mobile phase B final compositions, and different columns on different instruments.

The validation results are summarized in Table S3. The results demonstrated that the method is specific as sulconazole sulfoxide was separated from sulconazole and no interfering peak appeared at the retention time of the two peaks. Linear responses over the range of concentrations of 0.75–2.25 µg/mL were observed for both sulconazole and sulconazole sulfoxide (Fig. S8). Spike recoveries close to 100% at different levels indicated an acceptable accuracy of the method (Table S4). The low values of % RSD for method precision indicate that the method is reproducible. Finally, robustness studies showed that variations of the operating parameters did not significantly change the chromatographic profiles or the result, indicating that the method was robust under the experimental conditions (Table S5).

4. Conclusions

In summary, a systematic UHPLC study was conducted on sulconazole nitrate. The study included stress testing of sulconazole nitrate, preparative HPLC isolation of the major degradation product, structural confirmation of the degradant, and UHPLC method validation. Based on NMR and LC-MS/MS analysis, the S-oxidation of sulconazole to sulconazole sulfoxide was confirmed as the predominant

degradation pathway. In addition, the generated degradation product was utilized as a reference standard for organic impurity HPLC method development and validation. This work displays a typical approach used to support USP monograph modernization.

Conflicts of interest

The authors declare that there are no conflicts of interest.

Acknowledgments

We thank USP colleagues, Doug M. Podolsky, James R. Austgen, Praveen K. Pabba, Marcela Nefliu, and Sitaram Bhavaraju for help with preparing the manuscript.

Disclaimer

Certain commercial equipment, instruments, vendors, or materials may be identified in this manuscript to specify adequately the experimental procedure(s). Such identification does not imply approval, endorsement, or certification by USP of a particular brand or product, nor does it imply that the equipment, instrument, vendor, or material is necessarily the best available for the purpose or that any other brand or product was judged to be unsatisfactory or inadequate. All product names, logos, and brands are property of their respective owners.

Appendix A. Supplementary material

Supplementary data associated with this article can be found in the online version at doi:10.1016/j.jpha.2017.12.007.

References

- [1] R.A. Fromtling, Overview of medically important antifungal azole derivatives, *Clin. Microbiol. Rev.* 1 (1988) 187–217.
- [2] L.M. Santos, B. Davani, C.M. Anthony, et al., USP monograph modernization initiative, *Am. Pharm. Rev.* 18 (2) (2015).
- [3] USP35-NF30 monograph, Sulconazole Nitrate, 2012.
- [4] M. Fass, B. Zaro, M. Chaplin, et al., Reversed-phase high-pressure liquid chromatographic analysis of sulconazole in plasma, *J. Pharm. Sci.* 70 (1981) 1338–1340.
- [5] H.Y. Aboul-Enein, I. Ali, Comparison of the chiral resolution of econazole, miconazole, and sulconazole by HPLC using normal-phase amylose CSPs, *Fresenius J. Anal. Chem.* 370 (2001) 951–955.
- [6] H.Y. Aboul-Enein, I. Ali, Comparative study of the enantiomeric resolution of chiral antifungal drugs econazole, miconazole and sulconazole by HPLC on various cellulose chiral columns in normal phase mode, *J. Pharm. Biomed. Anal.* 27 (2002) 441–446.
- [7] E.J. Benjamin, D.L. Conley, On-line HPLC method for clean-up and analysis of hydrocortisone and sulconazole nitrate in a cream, *Int. J. Pharm.* 13 (1983) 205–217.
- [8] S.H. Chen, R.A. Kenley, J.S. Winterle, Sulconazole reactions with peracetic acid and hydrogen peroxide, *Int. J. Pharm.* 72 (1991) 89–96.
- [9] Y. Iwasawa, H. Tamaki, I. Yamaguchi, et al., Pharmacological studies on sulconazole nitrate (RS44872; SCZ) and its metabolites (2): effects on the cardiovascular, the respiratory, the digestive systems, and the renal and other functions, *Oyo Yakuri* 27 (1984) 717–727.
- [10] M.M. Al Omari, R.M. Zoubi, E.I. Hasan, et al., Effect of light and heat on the stability of montelukast in solution and in its solid state, *J. Pharm. Biomed. Anal.* 45 (2007) 465–471.
- [11] P. Viñas, N. Campillo, C. López-Erroz, et al., Use of postcolumn fluorescence derivatization to develop a liquid chromatographic assay for ranitidine and its metabolites in biological fluids, *J. Chromatogr. B: Biomed. Sci. Appl.* 693 (1997) 443–449.
- [12] P.G.J. Nieuwenhuis, Conversion of penicillins and cephalosporins to 1(S)-sulfoxides, US Patent 5442058, 1995 Aug. 15.
- [13] D.J. Sprankle, E.C. Jensen, Pergolide mesylate, in: H.G. Brittain (Ed.), *Analytical*

- Profiles of Drug Substances and Excipients, 21, Academic Press, New York, 1992: 375.
- [14] J.M. Froelich, G.E. Reid, Mechanisms for the proton mobility-dependent gas-phase fragmentation reactions of S-alkyl cysteine sulfoxide-containing peptide ions, *J. Am. Soc. Mass Spectrom.* 18 (2007) 1690–1705.
- [15] G. Caron, P. Gaillard, P. Carrupt, et al., Lipophilicity behavior of model and medicinal compounds containing a sulfide, sulfoxide, or sulfone moiety, *Helv. Chim. Acta* 80 (1997) 449–462.
- [16] ICH, Guidance for Industry Q1A(R2) Stability Testing of New Drug Substances and Products, 2003.
- [17] Pharmacopeial Forum, 41(5) In-Process Revision: Sulconazole Nitrate, 2016.
- [18] USP40–NF35, Monograph: Sulconazole Nitrate, 2017.
- [19] European Pharmacopeia, 8.4, Econazole Monograph, and Econazole Nitrate Monograph, 2015.
- [20] T.S. Belal, R.S. Haggag, Gradient HPLC-DAD stability indicating determination of miconazole nitrate and lidocaine hydrochloride in their combined oral gel dosage form, *J. Chromatogr. Sci.* 50 (2012) 401–409.
- [21] USP40–NF35, Ranitidine Hydrochloride, 2017.
- [22] G.H. Loew, Y.T. Chang, Theoretical studies of the oxidation of N- and S-containing compounds by cytochrome P450, *Int. J. Quantum Chem.* 48 (1993) 815–826.
- [23] T. Ramesh, P.N. Rao, R.N. Rao, LC–MS/MS characterization of forced degradation products of zofenopril, *J. Pharm. Biomed. Anal.* 88 (2014) 609–616.
- [24] H. Shin, H. Song, S. Cho, et al., The structure of 1-[2-[[[(4-chlorophenyl)-methyl]thio]-2-(2, 4-dichlorophenyl)ethyl]-1H imidazole (sulconazole) nitrate, C18H16Cl3N3O3S, *Bull. Korean Chem. Soc.* 18 (1997) 14–18.
- [25] P.S. Beauchamp, R. Marquez, A general approach for calculating proton chemical shifts for methyl, methylene and methine protons when there are one or more substituents within three carbons, *J. Chem. Educ.* 74 (1997) 1483–1484.
- [26] R.J. Abraham, J.J. Byrne, L. Griffiths, ¹H chemical shifts in NMR. Part 27: proton chemical shifts in sulfoxides and sulfones and the magnetic anisotropy, electric field and steric effects of the SO bond, *Magn. Reson. Chem.* 46 (2008) 667–675.
- [27] X. Jiang, J.B. Smith, E.C. Abraham, Identification of a MS-MS fragment diagnostic for methionine sulfoxide, *J. Mass Spectrom.* 31 (1996) 1309–1310.
- [28] H. Steen, M. Mann, Similarity between condensed phase and gas phase chemistry: fragmentation of peptides containing oxidized cysteine residues and its implications for proteomics, *J. Am. Soc. Mass Spectrom.* 12 (2001) 228–232.
- [29] L.K. Liu, C.Y. Su, W.S. Li, Hydrogen rearrangement in alkyl-, styryl- and alkyl propenyl sulfoxides, *Org. Mass Spectrom.* 24 (1989) 338–342.
- [30] R. Smakman, T.J. de Boer, The mass spectra of some aliphatic and alicyclic sulphoxide and sulphones, *Org. Mass Spectrom.* 3 (1970) 1561–1588.
- [31] P. Wright, A. Alex, D. Gibson, et al., Characterisation of sulphoxides by atmospheric pressure ionization mass spectrometry, *Rapid Commun. Mass Spectrom.* 19 (2005) 2005–2014.
- [32] S. Kern, R. Baumgartner, D.E. Helbling, et al., A tiered procedure for assessing the formation of biotransformation products of pharmaceuticals and biocides during activated sludge treatment, *J. Environ. Monit.* 12 (2010) 2100–2111.
- [33] G.S. Prasad, S. Girisham, S.M. Reddy, Studies on microbial transformation of albendazole by soil fungi, *Indian J. Biotechnol.* 8 (2009) 425–429.
- [34] K.P. Madhusudanan, V.S. Murthy, D. Fraisse, Dehalogenation reactions in chemical ionization mass spectrometry, *J. Chem. Soc., Perkin Trans. II* 9 (1989) 1255–1260.
- [35] H. Budzikiewicz, Reactions between substrate molecules and chemical ionization reagent gases prior to ionization, *Org. Mass Spectrom.* 23 (1988) 561–565.
- [36] D. Volmer, L. Karsten, Mass spectrometric analysis of nitrogen- and phosphorus-containing pesticides by liquid chromatography–mass spectrometry, *J. Am. Soc. Mass Spectrom.* 5 (1994) 655–675.



Original Research Article

Physicochemical characterization, the Hirshfeld surface, and biological evaluation of two meloxicam compounding pharmacy samples

Luciana F.A. Romani^a, Maria I. Yoshida^a, Elionai C.L. Gomes^a, Renes R. Machado^b, Felipe F. Rodrigues^b, Márcio M. Coelho^b, Marcelo A. Oliveira^c, Maria B. Freitas-Marques^a, Rosane A.S. San Gil^d, Wagner N. Mussel^{a,*}

^a Department of Chemistry, Institute of Exact Sciences, Federal University of Minas Gerais, Av. Antônio Carlos 6627, Belo Horizonte, MG, Brazil

^b Department of Pharmaceutical Products, Faculty of Pharmacy, Federal University of Minas Gerais, Av. Antônio Carlos 6627, Belo Horizonte, MG, Brazil

^c Health Science Department, Federal University of Espírito Santo, Campus São Mateus, ES, Brazil

^d Institute of Chemistry, Federal University of Rio de Janeiro, Campus Fundão, RJ, Brazil

ARTICLE INFO

Article history:

Received 11 June 2017

Received in revised form

15 December 2017

Accepted 18 December 2017

Available online 19 December 2017

Keywords:

Meloxicam

Polymorphism

Hirshfeld surface

Anti-inflammatory activity

ABSTRACT

Meloxicam (MLX) is an anti-inflammatory drug susceptible to variations and crystalline transitions. In compounding pharmacies, the complete crystallographic evaluation of the raw material is not a routine procedure. We performed a complete crystallographic characterization of aleatory raw MLX samples from compounding pharmacies. X-ray diffraction indicated the presence of two crystalline forms in one sample. DSC experiments suggested that crystallization, or a crystal transition, occurred differently between samples. The FTIR and ¹H NMR spectra showed characteristic assignments. ¹³C solid-state NMR spectroscopy indicated the presence of more than one phase in a sample from pharmacy B. The Hirshfeld surface analysis, with electrostatic potential projection, allowed complete assignment of the UV spectra in ethanol solution. The polymorph I of meloxicam was more active than polymorph III in an experimental model of acute inflammation in mice. Our results highlighted the need for complete crystallographic characterization and the separation of freely used raw materials in compounding pharmacies, as a routine procedure, to ensure the desired dose/effect.

© 2017 Xi'an Jiaotong University. Production and hosting by Elsevier B.V. This is an open access article under the CC BY-NC-ND license (<http://creativecommons.org/licenses/by-nc-nd/4.0/>).

1. Introduction

Meloxicam (MLX, Fig. 1), a non-steroidal anti-inflammatory drug (NSAID) and a partially selective cyclooxygenase (COX-2) inhibitor, belongs to the class of enolic acids and is derived from oxicam. Owing to its anti-inflammatory and analgesic effects as well as good safety profile, characterized by a low incidence of gastrointestinal side effects [1], it is widely prescribed. MLX, [4-hydroxy-2-methyl-N-(5-methyl-2-thiaolyl)-2H-1, 2-benzothiazine-3-carboxamide 1,1-dioxide] (C₁₄H₁₃N₃O₄S₂; 351.40 g mol⁻¹), is a yellow powder, practically insoluble in water, and slightly soluble in organic solvents, and well soluble in strong acids and bases [2,3].

In 2003, Coppi, Sanmarti, and Clavo [4] described five crystalline forms of MLX associated with the corresponding processes for preparation and interconversion. The forms have distinct network structures that may differ in biopharmaceutical aspects and

compromise their own functions. Luger and colleagues [5] described the crystalline form I as the most suitable for the preparation of pharmaceutical products. The interconversion between different polymorphs may occur during the storage, as a consequence of the synthetic route, or in improper storage conditions with variations in humidity and temperature. As raw pharmaceutical materials are susceptible to variations and transitions, their full crystallographic analysis is important and should be adopted as a routine practice for adequate quality control. Only proper control will ensure the efficacy and safety of public health [6–10].

In the present study, we characterized and evaluated the biological activity of meloxicam raw material that is freely used in compounding pharmacies.

2. Experimental

MLX samples were obtained from three compounding pharmacies, and anonymized as A, B, and C, which corresponded to different routine batches of Indian origin: TDM/ML/002/11/12–13, ALC/MLX/120102, and MLAH16081112#5, respectively.

Peer review under responsibility of Xi'an Jiaotong University.

* Corresponding author.

E-mail addresses: wdmussel@ufmg.br, wdmussel@yahoo.com.br (W.N. Mussel).

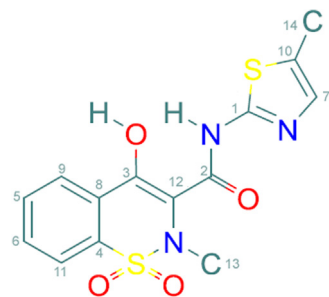


Fig. 1. The chemical structure of meloxicam.

2.1. Powder X-ray diffraction (PXRD)

PXRD data were collected by a XRD-7000 diffractometer (Shimadzu) at 22 °C at 40 kV and 30 mA, using $\text{CuK}\alpha$ ($\lambda = 1.54056 \text{ \AA}$) equipped with a polycapillary focusing optics under parallel geometry coupled with a graphite monochromator. The sample was subjected to spinning at 60 rpm, scanned over an angular range of $4 \text{ } 60^\circ$ (2θ) with a step size of 0.01° (2θ) and a time constant of 2 s/step. The software CrystalExplorer v 3.1 was used for the Hirshfeld surface analysis.

2.2. Differential scanning calorimetry (DSC)

DSC experiments were performed on a Shimadzu DSC60. The equipment cell was calibrated with indium (mp 156.6 °C; $\Delta H_{\text{fus}} = 28.54 \text{ J/g}$) and lead (mp 327.5 °C). Aluminum pans, containing approximately 1 mg of sample, were used under a dynamic N_2 atmosphere (50 mL/min) and a heating rate of 10 °C/min in the temperature range between 25 and 300 °C. As form III showed different thermal behavior, an isothermal experiment was conducted at 175 °C for periods of 15, 30, and 45 min.

2.3. Fourier transformed infrared spectroscopy (FTIR)

All experiments were conducted on a Perking Elmer IR spectrometer, with samples measured in KBr pressed pellets in the wavenumber range between 400 and 3400 cm^{-1} at room temperature, with a resolution of 4 cm^{-1} .

2.4. ^1H and ^{13}C -NMR analysis

Solution 1D and 2D NMR experiments (^1H , ^{13}C , DEPT-135, HSQC, and HMBC) spectra were performed by using a Bruker Avance DRX 400 spectrometer in DMSO-d_6 (deuterated dimethyl sulfoxide, up to 99.9%) solution at 300 K, which was used as an internal standard (^1H : $\delta = 2.50 \text{ ppm}$; ^{13}C : $\delta = 39.50 \text{ ppm}$).

Solid-state ^{13}C -NMR (ssNMR) spectra were collected by using a Bruker Avance DRX 400 (9.4T) running at rotation of 10 kHz with cross polarization and using glycine ($\text{C}=\text{O}$: $\delta = 176.03 \text{ ppm}$) as an internal standard.

2.5. UV spectrophotometry

Spectral scans were performed between the wavelengths of 200 and 400 nm on MLX samples dissolved at $10 \text{ }\mu\text{g/mL}$ in ethanol by using a Shimadzu 1800 spectrophotometer. Ethanol was used as the blank sample to correct for the instrumental background. Origin software (version 9.1) was used to analyze the data.

All described analyses were conducted within the validity period of all samples.

2.6. Evaluation of the biological activity

2.6.1. Animals

The anti-inflammatory activity was evaluated through the use of the carrageenan-induced paw edema test. Female Swiss mice (25–30 g) with free access to food and water were used. The animals were kept in a room with a 12 h light/dark cycle for a minimum of 3 days prior to the experiment, to allow acclimatization. The room temperature was maintained at 27 °C, which corresponds to the thermoneutral zone for mice [11]. This study was approved by the Ethics Committee on Animal Experimentation of the Federal University of Minas Gerais (Protocol 233/2016) and conducted in accordance with the S7A guide of the International Conference on Harmonization [12].

2.6.2. Paw edema induced by carrageenan

To measure paw volume, a plethysmometer (Model 7140, Ugo Basile, Italy) was used. The basal volume of the right hind paw was measured before the administration of any drug. Next, the animals were divided into the experimental groups in such a way that the mean volumes of each groups was similar. Carrageenan ($400 \text{ }\mu\text{g}/20 \text{ }\mu\text{L}$) was injected via the intraplantar (i.pl.) route. The vehicle (carboxymethylcellulose; CMC 1%), meloxicam A 15 mg/kg, meloxicam B 15 mg/kg, meloxicam A 30 mg/kg, meloxicam B 30 mg/kg, or dexamethasone (10 mg/kg; positive control) were administered per os (p.o.) 30 min prior to the carrageenan injection. The volume of p.o. administration was 10 mL/kg. The paw volume of each animal was again measured at 2, 4, and 6 h after injection of the inflammatory stimulus. The results are expressed as the change in paw volume (μL) relative to the basal values [13].

2.6.3. Statistical analysis

The results are presented as the mean \pm standard error mean (S.E.M.). Two-way ANOVA followed by Bonferroni's post hoc test was used to analyze paw volumes differences, with P values of < 0.05 considered significant. Statistical analyses were performed by using GraphPrism 5.0 (San Diego, USA) for Windows.

3. Results and discussion

As the samples from A and C showed identical X-ray diffraction patterns (form I; Fig. 2), we considered them to be the same material. Therefore, all other chemical and biological analyses were performed with samples from A (form I) and B (indicated by XRD as a mixture of some of form I and predominantly form III). The significant differences in peak positions and observed reflection planes, shown in Fig. 2, confirmed that there were two different polymorphs of the same material.

Thermal analysis was performed on separate aliquots. The DSC curves of samples from A and B are shown in Fig. 3. In the curve of the sample from pharmacy B, there is an incipient exothermic peak (4.47 J/g), at 206.6 °C. This peak was suggestive of crystallization or crystal transition, and was not present in the sample from pharmacy A (form I). After the melting point at approximately 260.0 °C, in both samples, similar behavior was observed.

Based on the observed thermal behavior, an isotherm at 175.0 °C, just below the beginning of the broad large transition peak, was analyzed to check the crystal transition observed at 206.6 °C. The XRD patterns shown in Fig. 4 were obtained after the isotherm, under tightly temperature control, after 15, 30, and 45 min. In all three distinct aliquots, we confirmed the occurrence of one phase transition. After 15 min, we observed the beginning of the conversion; after 45 min, the phenomenon was completed (Fig. 4).

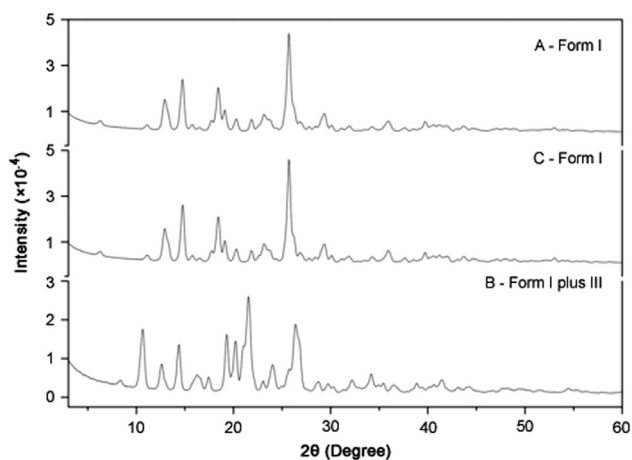


Fig. 2. X-ray diffraction patterns of samples from compounding pharmacies A, B, and C.

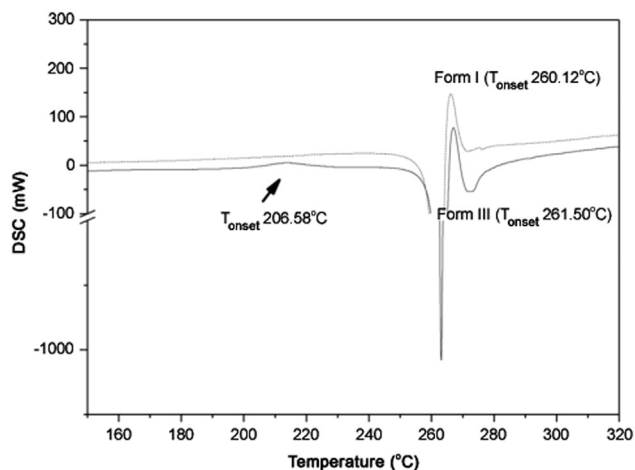


Fig. 3. DSC curves of samples from compounding pharmacies A and B superimposed, showing the presence of a small exothermic peak in the B sample. The y axis is broken for better visualization.

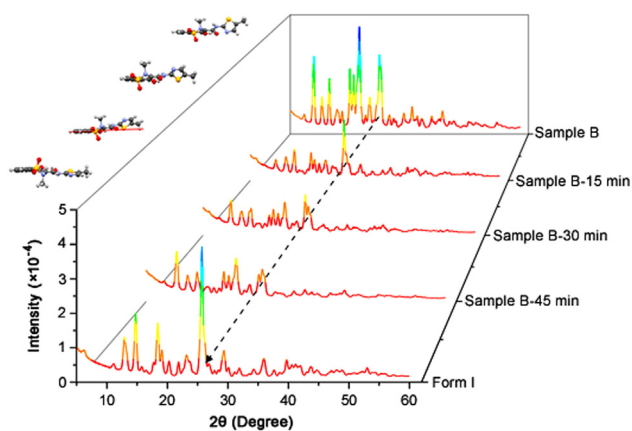


Fig. 4. Powder X-ray diffraction of compounding pharmacy B isotherm at 175 °C. The structures were fitted by using the Rietveld algorithm. The quotes indicate the sample from compounding pharmacy B, heated at 175 °C for 15, 30, and 45 min and the final product of the isotherm experiment (form I).

Through the comparison of the FTIR spectra from the samples from pharmacies A and B (Fig. 5), the absorptions were assigned to distinct peaks for each chemical functional group within the structure. The observed and assigned changes in the functional groups occurred at 1184–1176 cm^{-1} , 1526–1520 cm^{-1} , and 1550–

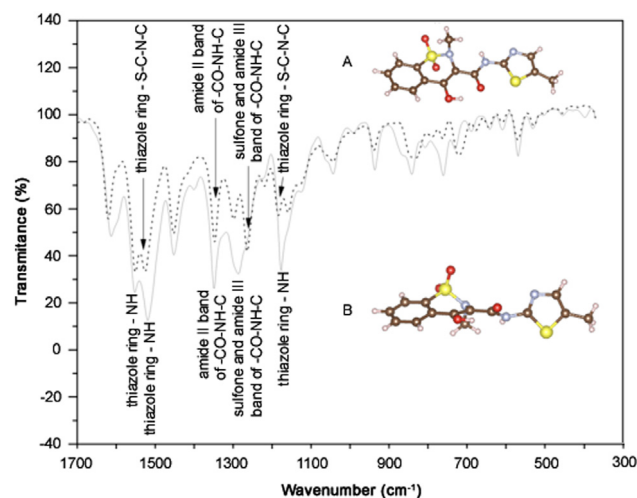


Fig. 5. Comparison of Fourier transform infrared spectra between form I and form III.

1552 cm^{-1} related to the stretching vibration of the thiazole ring, the asymmetric stretching vibration at 1264–1286 cm^{-1} of the sulfone, and amide III bands for the $-\text{CO}-\text{NH}-\text{C}-$ group.

As observed in ssNMR (Fig. 6), C14 showed a double signal centered at 13.9 and 9.7 ppm for sample B; however, only one signal at 12.8 ppm was observed for sample A (form I; Fig. 6, Table 1).

The ^1H and ^{13}C -NMR spectra of meloxicam were collected in $\text{DMSO}-d_6$ (Supplementary material). After the material was solubilized in $\text{DMSO}-d_6$, all polymorphic characteristics were lost through the dissolution process. In solution, the NMR spectra were identical for both samples. Thus, the discussion of these results is valid for both samples.

The 1D and 2D NMR spectra (^1H , ^{13}C , DEPT-135, HSQC, and HMBIC) were obtained under standard conditions (shown in Supplementary material). In the ^{13}C spectrum, the aromatic carbons C2, C3, C4, C5, C6, C7, and C16 resonated between 123.2 and 134.4 ppm, as expected. The methyl carbons C10 and C18 resonated at 37.9 and 11.7 ppm, respectively. The quaternary carbon C9 resonated at 114.2 ppm, whereas C8, which was connected to the OH group, resonated at 115.7 ppm. Finally, the carbonyl resonated at 168.4 ppm. These results were obtained through direct comparison with published data [4].

The solid-state ^{13}C -NMR spectra of the samples from compounding pharmacies A and B are shown in Fig. 6. All ^{13}C peaks were properly indexed and a higher number of carbon atoms for

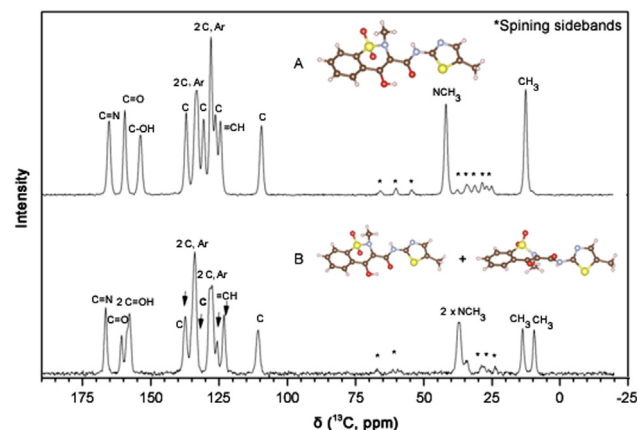


Fig. 6. ssNMR spectra for samples from compounding pharmacies A (form I) and B (form I plus form III).

Table 1
ssNMR assignment for ^{13}C signals.

Carbon	Chemical shift (δ , ppm)	
	Sample from A	Sample from B
C1	165.4	166.6
C2	159.6	160.8
C3	153.9	157.9
C4	137.1	137.4
C5	133.2	134.0
C6	133.2	134.0
C7	130.7	128.3
C8	130.7	128.3
C9	128.0	127.6
C10	126.4	125.8
C11	124.5	123.2
C12	109.5	110.7
C13	42.0	37.0
C14	12.8	13.9 / 9.7

sample from B was found compared with the expected spectrum. Through comparison with the spectrum of form I, this provided evidence of the existence of a mixture that contained some of form I and mainly form III (Table 1). This result was corroborated by the XRD measurements, which showed that form III was the major component of the mixture.

The UV analysis indicated common absorption maxima for forms I and III in ethanol solution at 205, 269 and 363 nm (Fig. 7). Special structural features may promote different solvation interactions that favor the appearance of tautomeric structures. This would be the case for forms I and III in water owing to the observed turn in the thiazole ring. However, the UV measurement conditions eliminate this possibility, as in standard literature procedures, the UV spectral measurement is obtained in ethanol, for solubility reasons. The contribution of each functional group to the absorption spectra of forms I and III is shown in Fig. 7.

In the UV spectra, a bathochromic shift from 215 nm to 219 nm and a hypsochromic displacement from 297 nm to 278 nm were observed. The Hirshfeld surface was calculated with the projection of the electrostatic potential highlighted by Spackman and Jayatilaka [14], Bojarska and Maniukiewicz [15], which allowed the complete assignment of UV spectra for both forms, I and III, respectively, in ethanol solution. There is a higher probability of interactions between the aromatic rings in form III, which favors the $\pi \rightarrow \pi^*$ transitions. The hydrogen on the OH group at C3 remains at a distance of approximately 1.69 Å in form I. In form III, the interaction is partial, mainly owing to the difficulties imposed by the increased distance to the same groups and atoms, now

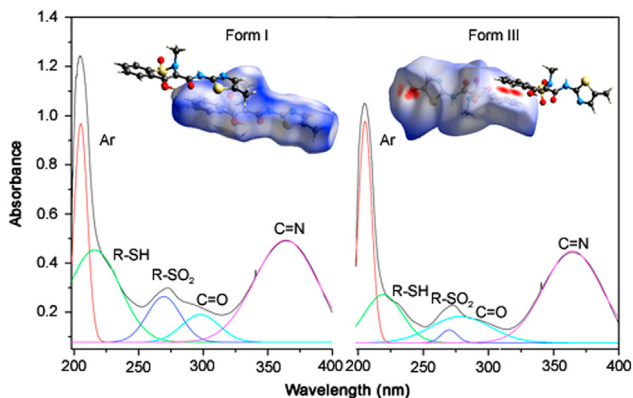


Fig. 7. Total UV-spectra assignments of forms I and III associated with surface potentials obtained from the Hirshfeld surface analysis.

approximately 1.88 Å. This longer distance interaction justifies the hypsochromic displacement, as it requires higher energy to occur.

The carrageenan injection induced a marked and long-lasting paw edema that was already evident at 2 h after injection. Dexamethasone 10 mg/kg resulted in the strongest anti-edematogenic effect ($P < 0.001$), as expected, because it is a steroidal anti-inflammatory agent that acts in the early stages of the inflammatory process; this drug is often used as a positive control in comparative studies [16–19]. Nevertheless, owing to the side effects observed in the medicinal uses of this class of materials, it is necessary to obtain effective drugs that result in fewer adverse events. At present, the oxicams play an important role as anti-inflammatory agents [19,20].

Another hypothesis from the results of the biological evaluation for a sample B refers to its identity. As the analyses by XRD and ssNMR indicated the presence of a certain amount of polymorph I in a mixture with polymorph III in the sample from the compounding pharmacy B, the anti-edematogenic effect may be associated with the amount. This result shows the importance of the study of the biological activity of different polymorphs in drugs usually present in raw materials of pharmaceutical interest, both mistral or industrial, as well as for proper characterization in quality control steps [9,10].

Both meloxicam samples (from pharmacies A and B) reduced paw edema when administered 30 min before carrageenan. Meloxicam from pharmacy A (15 mg/kg) reduced paw edema at 4 h ($P < 0.001$) and 6 h ($P < 0.001$). The highest dose of meloxicam from pharmacy A (30 mg/kg) reduced paw edema at 2 h ($P < 0.01$), 4 h ($P < 0.001$) and 6 h ($P < 0.001$). Meloxicam from pharmacy B was not as effective as meloxicam from pharmacy A. Both doses of meloxicam from pharmacy B (15 and 30 mg/kg) reduced paw edema, but only at 4 h ($P < 0.001$). The differences between the two samples were more pronounced at the highest dose at 4 h ($P < 0.001$) and 6 h ($P < 0.01$) after the injection of carrageenan (Fig. 8).

To study the effects of the two meloxicam samples on the carrageenan-induced paw edema, the positive control of dexamethasone 10 mg/kg, which is frequently used in preclinical assays [16–19], was used, and resulted in the highest anti-edematogenic activity, as expected. This steroidal anti-inflammatory drug markedly inhibits the early stages of the inflammatory process, but may also induce many side effects. Thus, there is an ongoing search for other anti-inflammatory drugs with a safer profile and oxicams appear to be good candidates [20,21].

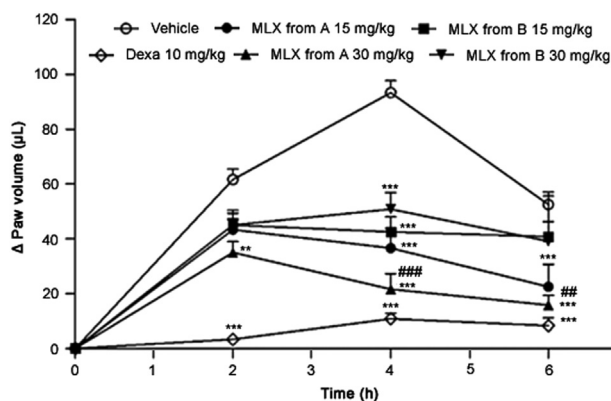


Fig. 8. Effect of meloxicam (MLX) from A and B compounding pharmacies (15 and 30 mg/kg, p.o.) or dexamethasone (Dexa; 10 mg/kg, p.o.) administered 30 min prior to the induction of the paw edema by i.p. injection of carrageenan (Cg, 400 µg/paw). Each point represents the mean \pm S.E.M. of six animals. ** and *** indicate significantly differences from the vehicle ($P < 0.01$ and $P < 0.001$, respectively). ## and ### indicate significantly difference from meloxicam B 30 mg/kg ($P < 0.01$ and $P < 0.001$, respectively).

The i.p. injection of carrageenan induced an acute and marked inflammatory response, characterized mainly by edema formation. This acute response most likely resulted from neutrophil migration and activation and also from the production of a variety of inflammatory mediators that induce vasodilation and increase vascular permeability [22,23]. In the present study, pre-treatment with both meloxicam samples reduced carrageenan-induced paw edema in mice. Others investigators have demonstrated the anti-inflammatory and analgesic activities of meloxicam in preclinical assays. These effects may result from reduced leukocyte migration and the reduced production of inflammatory mediators, as it has been shown that meloxicam attenuated the activation of nuclear factor- κ B, inhibited COX-2 expression, and increased IL-10 production [24–26].

Meloxicam form I was isolated from commercial samples from compounding pharmacies A and C. The sample from compounding pharmacy B, a mixture of forms I and III, was directly identified through the comparison of the X-ray diffraction patterns in patent US 20030109701 A1, [4]. Therefore, the sample from B was convoluted by the respective counterparts. Their Bragg reflections were independently indexed and extracted by the Pawley method. Once isolated and treated as one mixture, the crystallographic information for form III was extracted and used in order to obtain the Hirshfeld surface analysis for this polymorph alone (Fig. 9).

The Hirshfeld surface analysis assigns intermolecular interactions inside the unit cell packing. The analysis helps to understand the differences that were observed in the biological evaluation between samples from A (form I) and from the mixture in B (form I plus form III). The atomic distribution of form I, as shown in Fig. 9, contributes 89% of the overall interaction's distances (de \times di) to

the potential surface, starting from as low as 1.2 Å up to 2.4 Å (Fig. 9; form I). All expected interactions are $\pi \dots \pi$, between 5- (thiazole) and 6-membered rings and N-H...S=O internally. In contrast, the overall interactions calculated for form III, were present in (de \times di), as low as 1.0 Å and rose to over 2.8 Å (Fig. 9; form III) [14–26]. The observed turn around the thiazole ring in polymorph III increased the amount of interactions that contributed to different dissolution behavior. These observations not only explained the double signal of C14, but corroborated the increased intermolecular interactions seen for form III. From this data, we inferred that the intramolecular forces occurring at lower and also at higher distance in form III promoted stronger intermolecular interactions within and between the molecules inside the unit cell arrangement. This effect will result in a lower solubility (higher interactions inside the unit cell), as experimentally observed. In agreement with the observed behavior, meloxicam was classified as class II in the Biopharmaceutical Classification System [27,28].

Through those observations, we related the results of the biological evaluation found for sample B (form I plus form III, lower activity), with adverse pharmacokinetic parameters, such as bio-absorption and distribution. As form III presents intramolecular interactions at a lower distance (1.0 Å) in addition to higher distances (over 2.8 Å), when compared with the same parameters for pure form I, the internal cell packing forces will be increased, which results in a more difficult solubilization process. The Hirshfeld surface analysis showed C14 close to S in the thiazole ring on one side and to the hydroxyl group in the six-membered ring in the middle of the structure. For form I, only the hydroxyl group interaction was observed, which explained the ssNMR single signal for C14. In this case, a reduction of the amount of

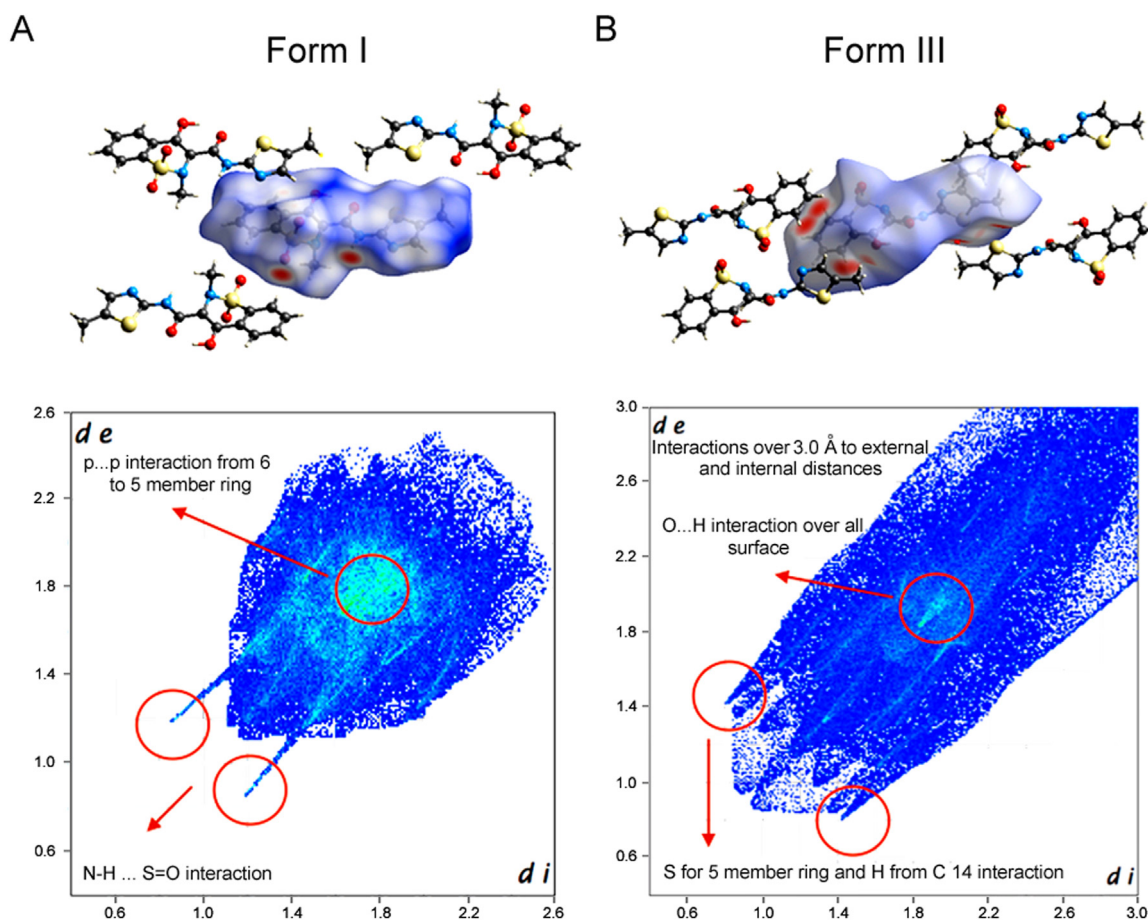


Fig. 9. Fingerprint plots: intermolecular interactions within the samples from compounding pharmacies A and B that show the total Hirshfeld surface area.

solubilized form III in comparison with form I, over the same solubilization time, will affect the available drug amount after administration differently for both forms.

4. Conclusion

X-ray diffraction, DSC, and ssNMR analysis indicated the presence of two polymorphs of meloxicam, forms I and III, in the sample from pharmacy B, freely sold in compounding pharmacies from which the samples were acquired.

The biological test indicated a lower degree of anti-edema activity for the polymorph III when present as major component in the sample from compounding pharmacy B, which also contained form I in the mixture. The Hirshfeld surface analysis of forms I and III provided an explanation of the solubility difference, which was experimentally observed for both compounds; form III is less soluble than form I.

Although less active, form III is a major component freely sold in compounding pharmacy B, which justified the difference in biological activity between the sample from compounding pharmacy A (form I) and the sample from pharmacy B (form I plus III) observed during the paw edema test conducted in female Swiss mice.

Our results highlighted the need for full crystallographic characterization and separation of freely used raw material in compounding pharmacies as an indispensable quality control protocol to ensure the desired drug dose/effect. The main concern over the lack of an adequate quality control was demonstrated to be unexpected differences in biological activity that could compromise human health.

Conflicts of interest

The authors declare that there are no conflicts of interest.

Acknowledgments

The authors are grateful to Fundação de Amparo à Pesquisa do Estado de Minas Gerais project APQ-01083-11, Conselho Nacional de Desenvolvimento Científico e Tecnológico grant 245914/2012-9, Coordenação de Aperfeiçoamento de Pessoal de Nível Superior grant PNPB 1648694 and Pró-Reitoria de Pesquisa/UFMG IE 27/2010 for financial support.

Appendix A. Supplementary material

Supplementary data associated with this article can be found in the online version at <http://dx.doi.org/10.1016/j.jpha.2017.12.006>.

References

- [1] I.I. Roberts, J.D. Morrow in: J.G. Hardman, L.E. Limbird, Goodman & Gilman's the pharmacological basis of therapeutics, McGraw-Hill, New York, 2001:713–714.
- [2] British Pharmacopoeia Commission, British Pharmacopoeia, Medicines & Healthcare products Regulatory Agency, TSO, London, 2013.

- [3] The United States Pharmacopoeia, third fourth ed., United States Pharmacopoeial Convention, Rockville:3403–3405, 2011.
- [4] L. Coppi, M.B. Sanmanti, M.C. Clavo, Crystalline forms of meloxicam and processes for their preparation and interconversion. Patent US 20030109701 A1, 2003.
- [5] P. Luger, K. Daneck, W. Engel, et al., Structure and physicochemical properties of meloxicam, a new NSAID, Eur. J. Pharm. Sci. 4 (1996) 175–187.
- [6] A. Burger, R. Ramberger, On the polymorphism of pharmaceuticals and other molecular crystals. I, Microchim. Acta 72 (1979) 259–271.
- [7] A. Burger, R. Ramberger, On the polymorphism of pharmaceuticals and other molecular crystals. II, Microchim. Acta 72 (1979) 273–316.
- [8] J. Haleblan, W. McCrone, Pharmaceutical applications of polymorphism, Pharm. Sci. 58 (1969) 911–929.
- [9] E.H. Lee, A practical guide to pharmaceutical polymorph screening & selection, Asian J. Pharm. Sci. 9 (14) (2014) 163–175.
- [10] M. Descamps, J.F. Willart, Perspectives on the amorphisation/milling relationship in pharmaceutical materials, Adv. Drug Deliv. Rev. 100 (2016) 51–66.
- [11] C.J. Gordon, Thermal biology of the laboratory rat, Physiol. Behav. 47 (1990) 963–991.
- [12] International Conference on Harmonization, Safety pharmacology studies for human pharmaceuticals (S7A), 2000: 13.
- [13] S.H. Ferreira, A new method for measuring variations of rat paw volume, J. Pharm. Pharmacol. 31 (1979) 648.
- [14] M.A. Spackman, D. Jayatilaka, Hirshfeld surface analysis, CrystEngComm 11 (2009) 19–32.
- [15] J. Bojarska, W.J. Maniukiewicz, Investigation of intermolecular interactions in finasteride drug crystals in view of X-ray and Hirshfeld surface analysis, Mol. Struct. 1099 (2015) 419–426.
- [16] H.J. Koo, K.H. Lim, H.J. Jung, et al., Anti-inflammatory evaluation of gardenia extract, geniposide and genipin, J. Ethnopharmacol. 103 (2006) 496–500.
- [17] M. Fezai, L. Senovilla, M. Jemaà, et al., Analgesic, anti-inflammatory and anticancer activities of extra virgin olive oil, J. Lipids 2013 (2013) 1–7.
- [18] D.G. Soares, A.M. Godin, R.R. Menezes, et al., Anti-inflammatory and antinociceptive activities of azadirachtin in mice, Planta Med. 80 (2014) 630–636.
- [19] T. Göncü, E. Oğuz, H. Sezen, et al., Anti-inflammatory effect of lycopene on endotoxin-induced uveitis in rats, Arq. Bras. Oftalmol. 79 (2016) 357–362.
- [20] H. Schäcke, W.-D. Döcke, K. Asadullah, Mechanisms involved in the side effects of glucocorticoids, Pharmacol. Ther. 96 (2002) 23–43.
- [21] S. Xu, C.A. Rouzer, L.J. Marnett, Oxycams, a class of nonsteroidal anti-inflammatory drugs and beyond, IUBMB Life 66 (2014) 803–811.
- [22] D.A.R. Valério, T.M. Cunha, N.S. Arakawa, et al., Anti-inflammatory and analgesic effects of the sesquiterpene lactone budlein A in mice: inhibition of cytokine production-dependent mechanism, Eur. J. Pharmacol. 562 (2007) 155–163.
- [23] A.C. Rocha, E.S. Fernandes, N.L. Quintão, et al., Relevance of tumour necrosis factor- α for the inflammatory and nociceptive responses evoked by carrageenan in the mouse paw, J. Pharmacol. 148 (2006) 688–695.
- [24] G. Engelhardt, D. Homma, K. Schlegel, et al., Anti-inflammatory, analgesic, antipyretic and related properties of meloxicam, a new non-steroidal anti-inflammatory agent with favourable gastrointestinal tolerance, Inflamm. Res. 44 (1995) 423–433.
- [25] G. Engelhardt, Pharmacology of meloxicam, a new non-steroidal anti-inflammatory drug with an improved safety profile through preferential inhibition of COX-2, Br. J. Rheumatol. 35 (1996) 4–12.
- [26] N.A. El-Shitany, E.A. El-Bastawissy, K. El-desoky, Ellagic acid protects against carrageenan-induced acute inflammation through inhibition of nuclear factor kappa B, inducible cyclooxygenase and proinflammatory cytokines and enhancement of interleukin-10 via an antioxidant mechanism, Int. Immunopharmacol. 19 (2014) 290–299.
- [27] F.P.A. Fabbiani, L.T. Byrne, J.J. McKinnon, et al., Solvent inclusion in the structural voids of form II carbamazepine: single-crystal X-ray diffraction, NMR spectroscopy and Hirshfeld surface analysis, CrystEngComm 9 (2007) 728–731.
- [28] D.R. Weyna, M.L. Cheney, N. Shan, et al., Improving solubility and pharmacokinetics of meloxicam via multiple-component crystal formation, Mol. Pharm. 9 (2012) 2094–2102.



Contents lists available at ScienceDirect

Journal of Pharmaceutical Analysis

journal homepage: www.elsevier.com/locate/jpa
www.sciencedirect.com

Original Research Article

Anti-diabetic activity of quercetin extracted from *Phyllanthus emblica* L. fruit: *In silico* and *in vivo* approachesPrabhu Srinivasan^a, S. Vijayakumar^{a,*}, Swaminathan Kothandaraman^b, Manogar Palani^a^a Computational Phytochemistry Lab, PG and Research Department of Botany and Microbiology, A. V. V. M Sri Pushpam College (Autonomous), Poondi 613 503, Tamil Nadu, India^b Department of Physics, RKM Vivekananda College (Autonomous), Mylapore, Chennai 600 004, India

ARTICLE INFO

Article history:

Received 6 April 2017

Received in revised form

27 October 2017

Accepted 30 October 2017

Available online 31 October 2017

Keywords:

Bioactive molecules

Glycogen phosphorylase

Molecular docking

Phyllanthus emblica

Quercetin

Albino Wister male rats

ABSTRACT

In this study, molecular interactions of the ligands, quercetin, gallic acid, and metformin with various diabetes mellitus-related protein targets, such as glycogen phosphorylase and peroxisome proliferator-activated receptor gamma, were assessed. It was revealed that quercetin possesses good binding affinity to both targets. Quercetin is a major constituent of methanolic extracts of *Phyllanthus emblica* fruit. The antihyperglycemic effect of quercetin in streptozotocin (STZ)-induced diabetic rats was examined. The isolated quercetin administered at a dose of 75 mg/kg body weight produced a maximum decrease of 14.78% in blood glucose levels in the diabetic rats after 7 days of treatment. Furthermore, quercetin doses of 50 and 75 mg/kg were shown to significantly improve the profiles of triglycerides, high-density lipoprotein, very-low-density lipoprotein, low-density lipoprotein, and total cholesterol at the end of the study in STZ-induced diabetic rats. The administration of quercetin (25, 50, and 75 mg/kg body weight) daily for 28 days in STZ-induced diabetic rats resulted in a significant decrease in blood glucose and urine sugar levels, with a considerable rise in plasma insulin and hemoglobin levels. Therefore, quercetin is a potential drug with antidiabetic and antihyperglycemic action mediated by changes in the levels of glucose, cholesterol, and triglycerides as indicated by *in silico* and *in vivo* studies.

© 2017 Xi'an Jiaotong University. Production and hosting by Elsevier B.V. This is an open access article under the CC BY-NC-ND license (<http://creativecommons.org/licenses/by-nc-nd/4.0/>).

1. Introduction

Diabetes mellitus (DM) is a metabolic disorder characterized by hyperglycemia resulting from defects in insulin action, insulin secretion from pancreatic beta cells, or both [1]. In addition, DM is a group of diseases characterized by chronic hyperglycemia due to deficiency of insulin action, a common basis of diabetes that leads to characteristic abnormalities in the metabolism of carbohydrate, lipid, and protein [2]. The total number of diabetic patients worldwide was estimated to increase from 171 million in the year 2000 to 366 million in 2030 [3], although the latter level was already attained in 2011 according to the International Diabetes Federation. A major part of this increase occurred in Asia, mainly China and India [4]. A popular theory on meal-induced insulin secretion (the “incretin effect”) states that glucose or any other drug is more effective on the pancreatic cells when administered orally than when given through intravenous or subcutaneous injections [5]. The World Health Organization (WHO) recommends plant-based drugs as an alternative

medicine [6]. Renewed attention to alternative medicines and natural therapies has raised researchers' interest in traditional herbal medicine. Because of their perceived effectiveness, with minimal side effects and relatively low costs, herbal drugs are prescribed widely, even when the contents of their biologically active constituents are unknown [7]. Hence, people are seeking traditional medicines for the management of DM.

Flavonoids are naturally occurring compounds widely distributed as secondary metabolites in the plant kingdom. They are recognized for having beneficial clinical properties, such as anti-inflammatory [8], cardioprotective [9], antiviral, antibacterial, and anticancer activities [10]. Quercetin is one of the flavonoids found in the fruits of medicinal plants, such as *Phyllanthus emblica* and *Vaccinium oxycoccos*. We have observed that the tribal people of Pachamalai hills use Amla fruits (*P. emblica*) as a traditional medicine for diabetes. *P. emblica* is referenced in “Rasayana,” a branch of the 5000-year-old Indian medical system “Ayurveda,” which focuses on enhancing good health, preventing diseases by boosting the immune system, as well as rejuvenating and revitalizing the body and mind [11]. It is still used extensively not only in India, but also in Iran, Iraq, Thailand, China, Italy, Germany, and other countries as a laxative, diuretic, astringent, and

Peer review under responsibility of Xi'an Jiaotong University.

* Corresponding author.

E-mail address: svijaya_kumar2579@rediffmail.com (S. Vijayakumar).

antiemetic. It is also used to treat other ailments, including anemia, jaundice, and tumors [12].

Computational biology and bioinformatics play an important role in drug design and screening. Molecular docking of a drug molecule with its target molecule can provide vital information about the drug-receptor binding and affinity. Bioinformatics and molecular docking studies helped us determine the efficacy of quercetin, found in *P. emblica*, in the treatment of DM. These computational results motivated us to further the study by purifying quercetin from the extract of *P. emblica* fruit. We then conducted in vivo studies in an animal model of diabetes with the purified quercetin.

2. Materials and methods

2.1. Computational tools and database source (ligand and protein)

This study was carried out using the Schrödinger software suite. Maestro (version 10.2) of the Schrödinger suite contains programs such as ligprep, sitemap, grid generation, and glide XP dock [13]. Suitable ligands were retrieved from the ChemSpider database [14]. These ligand molecules were converted to 3D structures in the Schrödinger suite. Protein molecules of glycogen phosphorylase (PDB: 1NOI) and peroxisome proliferator-activated receptor gamma (PPAR- γ , PDB: 3G9E) were retrieved from the protein data bank [15].

2.2. Protein preparation

The protein for docking was prepared using the protein preparation wizard of the Schrödinger suite. The missing side chains, back chains, and residues were updated. Occasional water molecules present in the crystal structure, owing to the prevailing conditions at the time of crystallization, may prove to be problematic; any such water molecules were removed in the protein preparation process. The removal of water molecules increases the entropy, but it is offset by an accompanying loss in enthalpy.

2.2.1. Validation of binding site

Binding site validation plays a vital role in molecular docking. Site validation analysis displays ligand-binding locations, amino acid residues, and site scores. The site map of the entire protein molecule is generated by validating the binding sites using the site map generation tool in Maestro version 10.2 of the Schrödinger suite. Once the site map was generated, we chose only one binding site based on the site score. The binding site of the largest volume was taken for grid generation.

2.2.2. Grid generation

Grid generation is very important for fixing the target site of protein molecules. The phytochemicals or commercial drugs were docked with the target in order to determine the docking parameters with the help of Grid-based ligand docking. A grid box was generated for docking the ligand at the centroid of the target site [16].

2.3. Ligand preparation

The ligand preparation was performed using the LigPrep (2.2) module [17]. The drawn ligand was geometry optimized via the Optimized Potentials for Liquid Simulations 2005 (OPLS2005) force field. LigPrep is a utility in the Schrödinger suite for the

purpose of combining tools to generate 3D structures from 1D (Smiles) and 2D (SDF) representations, which probes tautomers and stereoisomers for geometric minimization of ligands.

2.4. Molecular docking

Molecular docking was performed in the form of flexible docking for the prediction of binding affinity, ligand efficiency, and inhibitory constant. All the ligands were docked with the target active site using Glide Xtra precision (XP). Active compounds will only have positioning that avoids penalties and receives favorable scores for accurate hydrophobic contacts between the protein and ligand.

2.5. Plant material

The fruits of *P. emblica* were collected from the Pachamalai hills during January 2016. The plant was authenticated by taxonomists in the Rapinat herbarium, St. Josephs College, Trichy, India. A voucher specimen (PHC1125) of the plant material was deposited at the Pushpam Herbarium Cabinet, Department of Botany, A. V. V. M Sri Pushpam College (Autonomous), Poondi, Thanjavur, India.

2.6. Extract preparation

Fresh fruits were washed under running water, cleaned, and air-dried at 35 °C. After drying, the fruit was ground to powder and kept dry in an air tight container until extraction. This powder, dissolved in methanol, served as the extract tested in this study.

2.7. Phytochemical isolation

Methanolic fruit extract of *P. emblica* was chromatographed on a silica gel column. Solvent mixtures of increasing polarity composed of methanol and chloroform (methanol up to 90%) were used for elution, and the fractions were collected. The purity of all the fractions collected was determined by thin layer chromatography on silica gel with methanol and petroleum ether (90:10, v/v) as the mobile phase. Spots were visualized by spraying the plates with 20% antimony chloride in chloroform. The column fractions that showed a single spot of the same R_f value were pooled.

2.8. Experimental animals

Albino Wister male rats (7–8 weeks old, weighing 150–200 g) were purchased from the GSA Animal Farm, Mayiladuthurai, Tamil Nadu, India. The animals were fed with standard pellet diet (Chakan Oil Mills, Sangli) and water *ad libitum*. Ethical clearance was obtained from the Institutional Animal Ethics Committee and the experiments were conducted according to the Indian National Science Academy guidelines for the use and care of experimental animals (CPCSEA/265).

2.9. Induction of diabetes and treatments

Streptozotocin (STZ) was dissolved freshly in 100 mM citrate buffer (pH 4.5) and the calculated amount (60 mg/kg) of the solution was injected intraperitoneally to overnight fasted rats. Blood glucose was checked 48 h later and animals showing blood glucose values greater than 250 mg/dL were deemed diabetic and included in the experiments. Experimental rats were divided into six groups (one normal control group and five diabetic groups)

with six animals per group. Treatments were given orally, once a day, in the following manner:

- Group I: Normal control (without any drug treatment);
- Group II: Diabetes (STZ-injected rats);
- Group III: Diabetes (STZ-injected rats) treated with 25 mg/kg body weight quercetin;
- Group IV: Diabetes (STZ-injected rats) treated with 50 mg/kg body weight quercetin;
- Group V: Diabetes (STZ-injected rats) treated with 75 mg/kg body weight quercetin;
- Group VI: Diabetes (STZ-injected rats) treated with 10 mg/kg body weight metformin;

Quercetin and metformin were orally administered daily for 28 days. Body weights and blood glucose levels of overnight-fasted rats were measured weekly. At the end of the experimental period, the animals were fasted overnight and blood samples were collected for various biochemical estimations.

2.10. Biochemical determinations

The serum was separated by centrifugation of the blood samples at 3000g for 10 min in a microcentrifuge. Then, biochemical parameters, such as blood glucose, triglycerides (TG), high-density lipoprotein (HDL), low-density lipoprotein (LDL), total cholesterol (TC), and very-low-density lipoprotein (VLDL), were determined. The hepatic glycogen levels were measured as per the method described by Kemp and Kits Van Hejningen [18].

2.11. Histopathological study

After termination of the experiment and euthanasia of the rats, the livers were subjected to histopathological studies. They were cut into small species (1 mm × 1 mm × 1 mm), preserved in 10% formaldehyde in saline for 48 h, dehydrated by treating successively with increasing concentrations of ethyl alcohol (50%, 80%, 95%, and 100%), cleared in xylene, and embedded in paraffin. Samples were cut into ultrathin sections with an ultramicrotome, stained with hematoxylin and eosin dye, and mounted in neutral deparaffinated xylene (DPX) medium for microscopic observation of cells. The sections were examined for necrosis, fatty changes, hyaline degeneration, and ballooning degeneration.

2.12. Statistical analysis

All the data were statistically evaluated and the significance of various treatments was calculated. Results are expressed as means ± standard error (S.E) and comparisons among the groups were made by analysis of variance (ANOVA), followed by Student's *t*-tests. A value of *P* < 0.01 was considered significant.

3. Results and discussion

3.1. Validation of binding sites

Ligand binding site validation was performed for all binding sites in the target molecule and the binding cavity was chosen based on the site score (Table 1). The 3D structure of the target molecule is shown in Fig. 1A and the active site is shown in Fig. 1B.

Table 1

Target site score and ligand contact volume of binding cavity in glycogen phosphorylase (GP).

1NOI sites	Site score	Binding site volume
Sitemap-5	1.090184	1.417628
Sitemap-1	1.080538	1.094721
Sitemap-3	1.03978	0.882161
Sitemap-2	1.013763	0.972265
Sitemap-4	0.918663	0.834667

3.2. Molecular docking

3.2.1. Glycogen phosphorylase (GP) protein

Molecular docking studies clearly revealed that quercetin has a higher docking score with GP than does any other ligand. Inhibition of glycogenolysis has been proposed as a therapeutic strategy for the treatment of type 2 diabetes. GP catalyzes the first step in glycogen degradation as the rate limiting enzyme. It is expected that inhibition of GP will inhibit glycogenolysis, reduce hepatic glucose production, and lower blood glucose, thereby providing a potential new treatment for type 2 diabetes [19–21].

The fruit of *P. emblica*, contains quercetin and gallic acid also. The computational approach used involved docking of the ligands (quercetin and gallic acid) to form a complex with GP and PPAR- γ . Computational studies showed that quercetin interacts with GP residues GLY177, TRP173, THR85, and THR219 (Fig. 2A). The backbones of GLY177 and TRP173 formed hydrogen bonds with the ligand OH groups, while the side chains of THR85 and THR219 formed hydrogen bonds. These interactions are represented as two types of arrows from protein to ligand; the first is a solid blue line (H-bond backbone) and the other is a dotted blue line (H-bond side chain) (Fig. 2B). In addition, another ligand molecule, gallic acid, has the second docking score of -6.48347 (Table 2). The docked molecule interacts with GP residues ILE166, ARG40, ASN178, and TRP173 (Fig. 3A). The backbones of ILE166 and TRP173 residues form hydrogen bonds with the ligand OH groups, while the side chains of ARG40 and ASN173 form hydrogen bonds with the ligand OH groups (Fig. 3B). According to the report by Paramaguru et al. [22], quercetin interacts more favorably with GP than gallic acid affinity. They also suggest that quercetin has potent antihyperglycemic drug properties [22].

3.2.2. PPAR- γ protein

The other protein molecule, PPAR- γ , was docked with the two phytochemicals (quercetin and gallic acid) and one synthetic ligand, metformin. The 3D structure of the PPAR- γ binding cavity is represented in Fig. 4, and the site scores are displayed in Table 3. In this docking analysis, the interactions between protein and ligands were examined. The results show that quercetin is the best ligand and a potentially potent inhibitor for PPAR- γ . The docking scores are listed in Table 4. Quercetin interacts with PPAR- γ amino acid residue TYR473 (Fig. 5A). The side chain of TYR473 forms a hydrogen bond with the OH group of quercetin (Fig. 5B). The docking score of the other phytochemical, gallic acid, is lower than that of quercetin, but it also has good binding affinity (Fig. 6).

The electrostatic energy of the binding interface is important for protein-ligand complex formation. The major electrostatic interactions include hydrogen bonds (both from side chains and back bones), salt bridges, and π - π stacking. Hydrogen bonding is one of the most important interactions for biological

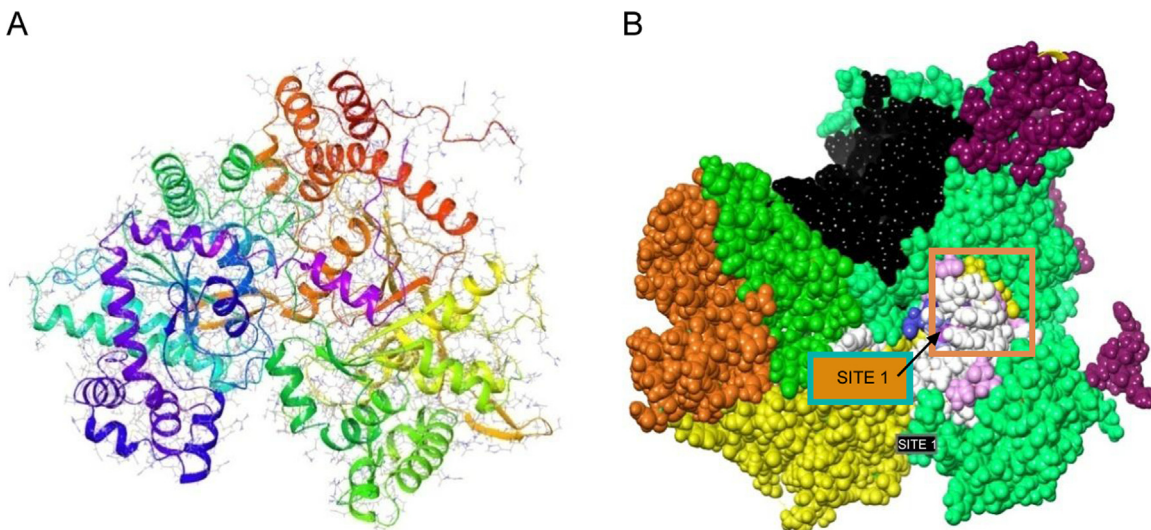


Fig. 1. Template of glycogen phosphorylase (1NOI) with ligand binding site. (A) 3D structure of the target molecule; (B) the active site.

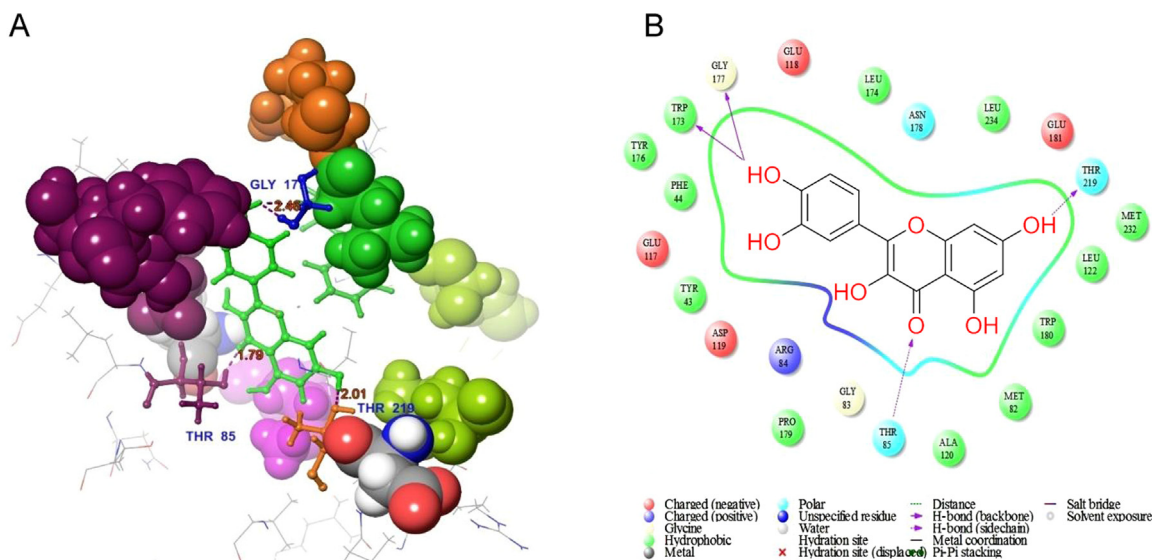


Fig. 2. Molecular structure represents the interaction of quercetin and GP. (A) 3D interaction shows residue interaction and their distance values; (B) The 2D interaction plot shows the contacts types.

Table 2

Docking score and H bond interaction of various phytochemicals with glycogen phosphorylase molecule (1NOI).

Phytochemicals	Docking score	H bond interactions	
		Back chain	Side chain
Quercetin	-8.36669	GLY177 (2.69)	THR85 & THR219
Gallic acid	-6.48347	ILE116, TRP173	ARG40 & ASN173

macromolecular interactions, crucial for conferring stability to protein molecules and selected protein-ligand interactions.

Metformin has the lowest docking score when compared with that of the phytochemicals. Metformin interacts with PPAR- γ amino acid residues SER42 and GLU291 (Fig. 7A). The backbone of SER342 formed a hydrogen bond with the ligand NH group. The side chain of GLU291 formed hydrogen bonds with the ligand NH/NH₂ groups (Fig. 7B).

According to reports, commercial antidiabetic drugs stimulate insulin production from the pancreas, with the other treatment being insulin injection. Various synthetic diabetes drugs are

available on the market, including the insulin secretagogues, sulfonylurea and meglitinides. Several insulin sensitizers, such as biguanides, thiazolidinediones, and metformin, as well as α -glycosidase inhibitors (e.g., acarbose) are also available. These medications have many side-effects such as hypoglycemia, idiosyncratic liver cell injury, lactic acidosis, digestive discomfort, permanent neurological deficit, headache, dizziness, and even death [23,24]. As mentioned previously, these drugs are often expensive [25]

3.3. Isolation of the phytochemical

The potential phytochemical was isolated from *P. emblica* fruit extracts. The identity of the purified sample was elucidated by ¹³C NMR, ¹H NMR, mass spectroscopy, and UV absorption spectroscopy. The functional groups of quercetin were analyzed by Fourier-transform infrared (FTIR) spectroscopy.

3.3.1. Structural determination and characterization

Different spectral analysis techniques were used to interpret the structure of the purified molecule. Precisely, the FTIR spectrum revealed peaks at 709 cm⁻¹ (C-H rocking), 1549 cm⁻¹ (C-C

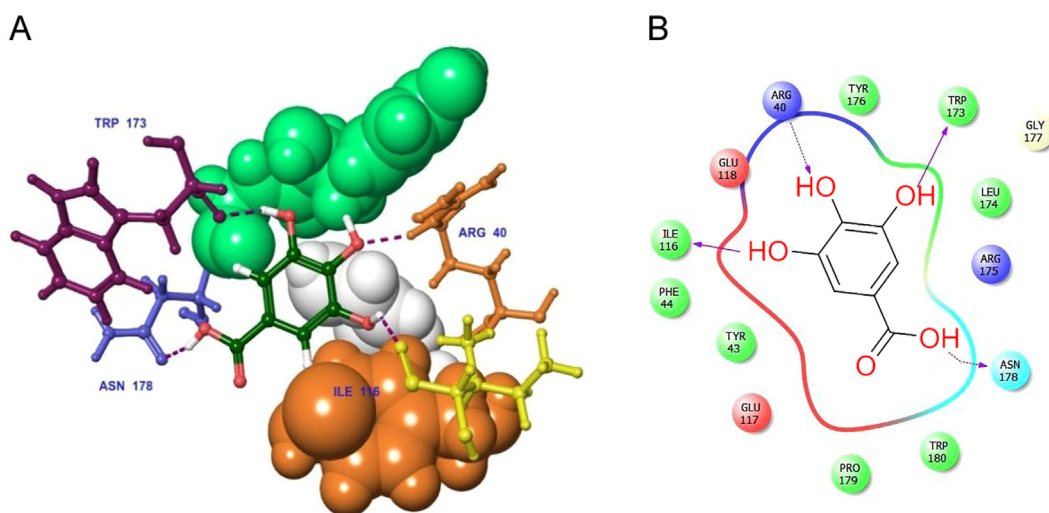


Fig. 3. Docked complex of gallic acid with GP. (A) 3D interaction shows the residue interaction and their distance values; (B) The 2D interaction plot shows contacts types.

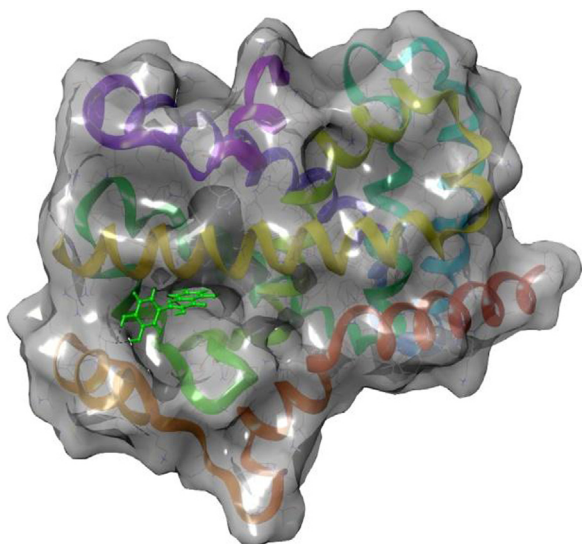


Fig. 4. Ligand binding cavity of PPAR- γ .

Table 3
Target site score and ligand contact volume in PPAR- γ (3G9E).

3G9E	Site scores	Binding site volume
Sitemap-1	1.05024	1.518028
Sitemap-2	1.030538	1.001731
Sitemap-3	1.03978	0.786131
Sitemap-4	1.003763	0.736214
Sitemap-5	0.918663	0.835692

Table 4
Docking score and H bond interaction of various phytochemicals with PPAR- γ (3G9E).

Phytochemicals	Docking score	H bond interactions	
		Side chain	Back chain
Quercetin	-6.958	TYR473	-
Gallic acid	-5.555	GLU291 & GLU295	GLU343
Metformin	-3.098	GLU291	SER342

stretching (Ar), 1709 cm^{-1} (C-O stretching), 3502 cm^{-1} (O-H stretching (bending)), 3066 cm^{-1} (C-H stretching (Ar)), and 3640 cm^{-1} (H-O stretching – free OH group present) (Fig. S1 and Table 5). ^1H NMR revealed the aromatic C-H proton at $\delta 7.00\text{--}7.24$ (S)-Ar (Fig. S1A), ^{13}C NMR revealed a carbonyl (C = O) at $\delta 170$, C-H carbon at $\delta 112$, tertiary cation at $\delta 124$, C-OH at $\delta 136$, and C-OH (L) at $\delta 147$ (Fig. S1B). Mass spectroscopy revealed the molecular ion peak of the compound at 302 (m+). The mass spectroscopy indicates the base is obtained at 115. The identified product is accomplished by determination of elemental physical constants (Fig. S1C). UV absorption spectroscopy was used to identify the presence of the conjugated π . As shown in Fig. S1D, Peak I is the conjugated π at 285 nm, and Peak II is the enone with external conjugated group at 356 nm (Fig. S1D). The product was yellow colored, with an attached chromophoric =O ring in the compound (Fig. 8).

3.3.2. Product characterization

After separating the extract by column chromatography, preliminary screening of the various fractions was accomplished by a thin layer chromatographic technique. However, different spectral analyses (i.e., FTIR, ^1H NMR, ^{13}C NMR, mass spectroscopy, and UV absorption) helped confirm that the compound was 2-(3,4-dihydroxyphenyl)-3, 5, 7-trihydroxy-4H-chromen-4-one (quercetin). Its molecular formula is $\text{C}_{15}\text{H}_{10}\text{O}_7$ and its molecular weight is 302.235. The compound is yellow crystalline, with a melting point of $316\text{ }^\circ\text{C}$. It is insoluble in water but soluble in methanol (Table 6). In computer modeling, the structure of the compound, 2-(3,4-dihydroxyphenyl)-3, 5, 7-trihydroxy-4H-chromen-4-one, strongly suggested its usefulness as an antidiabetic, so we tested it in an STZ-induced diabetic rat model.

3.4. Effect of quercetin on body weight and blood glucose

The experimental animals were treated with various concentrations of the potential lead compound, quercetin. In the present study, this phytochemical was selected via molecular docking analysis. Quercetin was orally administered at different doses (25, 50, and 75 mg/kg) in rats with experimentally induced hyperglycemia. The body weights of the rats are shown in Table 7. The baseline weight of the rats at the beginning of the study was similar among all groups. At the end of the treatment (after 4 weeks), the diabetic animals had lost weight due to the

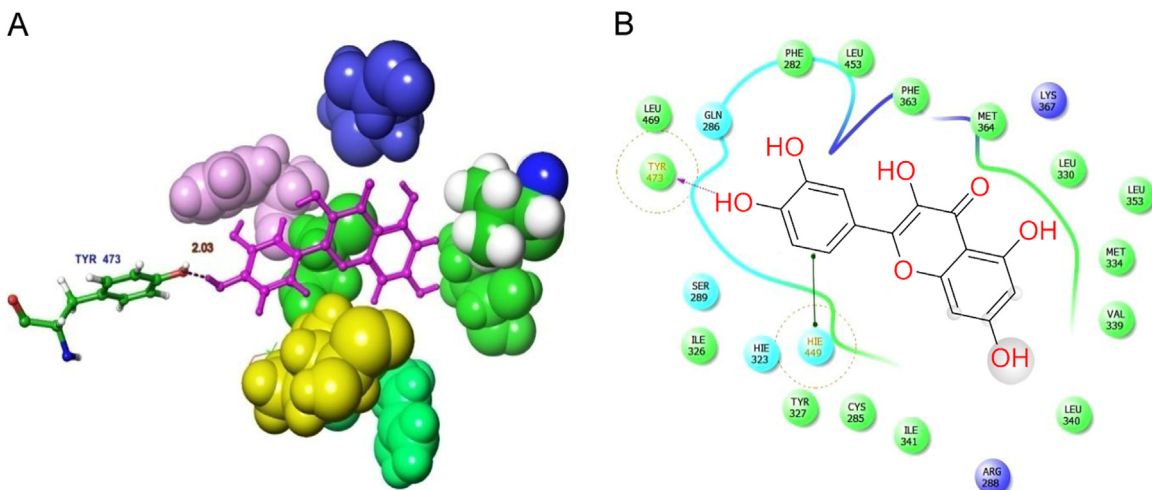


Fig. 5. Docked complex of quercetin with PPAR- γ . (A) 3D interaction shows the residue interaction and their distance values. (B) The 2D interaction plot shows contacts types.

catabolism of protein in muscle tissue caused by insulin deficiency [26]. However, the quercetin-treated diabetic rats had not lost body weight (Table 7). It is possible that the phytochemical was able to protect the pancreatic β -cells. Similar results were obtained by another group, and collectively, suggest that quercetin treatment protects against diabetic weight loss [27]. The use of medicinal plants is increasing due to the extraction and development of many successful drugs and chemotherapeutic agents from plants and their use as traditional rural herbal remedies [28]. STZ causes selective destruction of β -cells of the pancreatic islets, which leads to an increase in blood glucose levels. It is evident from the present investigation that STZ administration at a dose of 60 mg/kg causes significant diabetogenic response in the rats (Table 8). Blood glucose levels were measured randomly at baseline and on the 7th, 14th, 21st, and 28th days of the study. The increased glucose levels in the diabetic control group were found to be significant ($P < 0.05$) compared to that of the normal control group. The elevated blood glucose levels declined sharply after oral administration of quercetin (25, 50, and 75 mg/kg) or metformin (10 mg/kg). When comparisons were made between

baseline and the 28th day in the treated groups, there was a statistically significant ($P < 0.01$) decline in blood glucose levels. If the decline in blood glucose levels is the only index to be considered, then treatment with quercetin or metformin produced a highly effective antihyperglycemic response in STZ-induced diabetic rats. Considering the relative efficacy, although all tested concentrations of quercetin produced antihyperglycemic activity, quercetin of 75 mg was shown to produce the highest antihyperglycemic activity among all tested agents including metformin (Table 8). The reduction in blood glucose levels is the principal therapeutic goal of diabetes. According to Torres-Piedra et al. [29], quercetin significantly reduced the glucose levels in STZ-induced diabetic rats. The effective control of blood glucose levels by increasing the secretion of insulin and regeneration of β -cells in the pancreas is a vital step in preventing cardiovascular and diabetic complications and improving the quality of life in type 2 diabetic patients [30]. Based on the results of our experimental analysis, it is now well-established that quercetin is a plant-based natural drug that is sufficiently potent to reduce elevated glucose levels in diabetic rats.

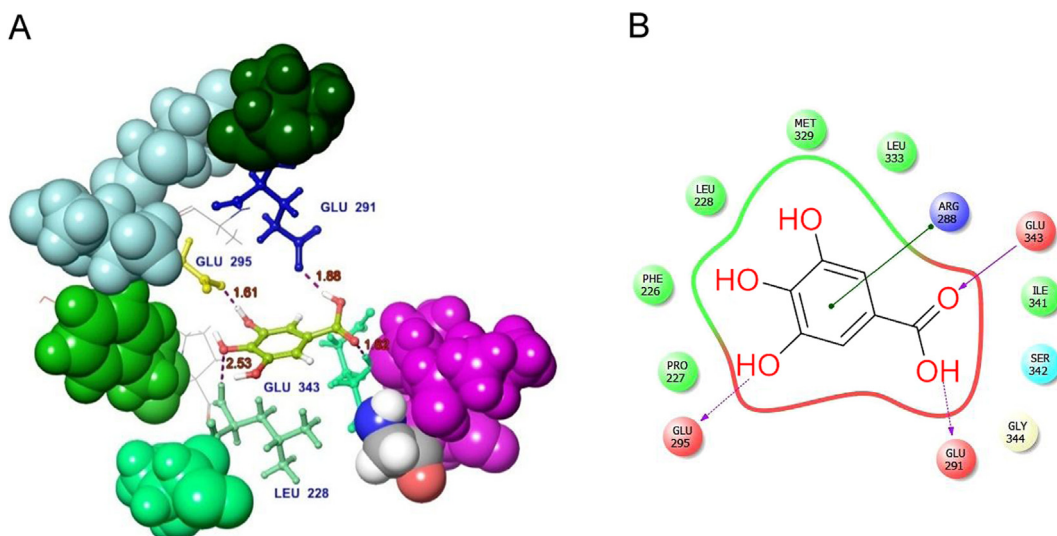


Fig. 6. Docked complex of gallic acid with PPAR- γ . (A) 3D interaction shows the residue interaction and their distance values. (B) The 2D interaction plot shows contacts types.

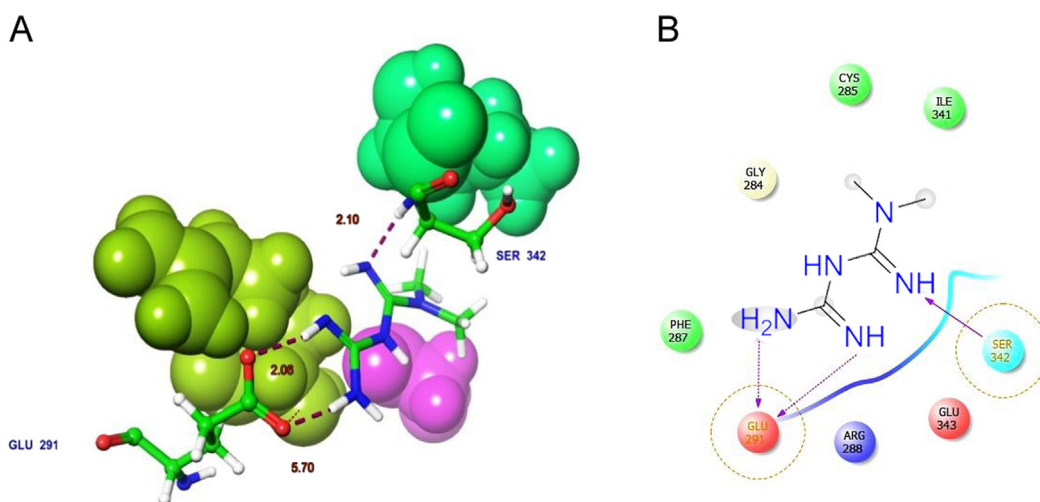


Fig. 7. Docked complex of synthetic drug molecule Metformin with PPAR- γ . (A) 3D interaction shows the residue interaction and their distance values. (B) The 2D interaction plot shows contacts types.

Table 5
Functional groups and their peak characters.

Functional groups	FTIR peaks (cm ⁻¹)	Peak characters
C-H	709	Rocking
C-C	1549	Stretching in aromatic ring
C=O	1709	Stretching (acid)
O-H	3502	Stretching (bending)
C-H	3066	Stretching in aromatic ring
H-O	3640	Stretching, free hydroxyl may be presence of phenol

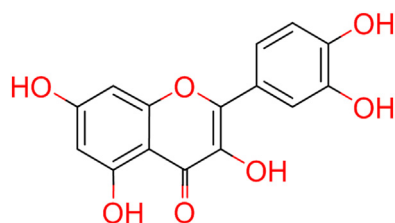


Fig. 8. Structure of 2-(3, 4-dihydroxyphenyl)-3, 5, 7-trihydroxy-4H-chromen-4-one (Quercetin).

Table 6
Elemental analysis.

Elements	Symbol of atom	Number of atom	Atomic mass	Mass percentage	Molar mass
Carbon	C	15	12.0107	59.6092	180.1605
Hydrogen	H	10	1.00794	3.3349	10.0794
Oxygen	O	7	15.9994	37.0557	111.9958
Total molecular weight					302.2357

3.5. Effect of quercetin on hemoglobin, plasma insulin, and urine sugar

The levels of hemoglobin, plasma insulin, and urine sugar in normal control and quercetin treated diabetic rats were measured.

Increased hemoglobin, plasma insulin, and lack of urine sugar were observed in the treated diabetic rats. These values were significantly improved close to normal after treatment with quercetin (25, 50, and 75 mg/kg) or metformin (10 mg/kg) (Table 9). The effect of quercetin on glycogen synthase and glycogen phosphorylase activities in the liver of diabetic rats is shown in Table 10. Diabetic rats showed increased activity of glycogen phosphorylase and decreased activity of glycogen synthase. These enzyme activities were significantly ($p < 0.05$) reverted to near normal levels after treatment with quercetin. In addition, it has been suggested that quercetin can improve insulin signaling and insulin sensitivity in rats with insulin resistance [31]. Quercetin could improve fasting hyperglycemia by enhancing insulin sensitivity via α -glucosidase inhibition and enhanced insulin signaling in diabetic rats [32].

3.6. Effect of quercetin on plasma lipid profiles

Diabetic rats showed significant increases in the blood levels of TC, TG, LDL, and VLDL. In contrast, HDL was significantly reduced compared to the values of normal control rats. Regular administration of quercetin for 4 weeks nearly normalized the lipid profiles in the diabetic rats. Oral administration of metformin significantly decreased the blood levels of TC, LDL, and VLDL. However, metformin did not significantly change the blood levels of TG compared to those of the diabetic control rats. In diabetic rats treated with quercetin (75 mg/kg), the blood levels of TC (24.02%↓), LDL (31.75%↓), and VLDL (48.23%↓) decreased significantly by the end of study (after 28 days); however, the blood level of HDL was significantly increased compared to the value in the diabetic rats (78.88%↑) (Table 11). In diabetes, LDL and VLDL carry cholesterol to the peripheral tissues where it is deposited, while HDL transports cholesterol from peripheral tissues to the liver to facilitate its excretion and metabolism. It has been reported that elevated serum LDL and VLDL are indicative of the atherogenic process [33]. As suggested by previous studies, an active phytochemical, such as quercetin, can decrease the levels of cholesterol and LDL in diabetic rats [34].

3.7. Histopathology observation

Representative histopathological changes in the pancreas are shown in Fig. 9. STZ administration elicited severe injury of the

Table 7
Effects of quercetin on the changes of body weight in normal control and experimental rats observed at weekly interval during the 28 days of study.

Groups	Body weight (g)				
	Day 0	Day 7	Day 14	Day 21	Day 28
Normal control	190.15 ± 17.11	192.18 ± 16.14	193.12 ± 15.11	197.14 ± 17.41	199.21 ± 19.13
Diabetes	187.40 ± 1.4	173.02 ± 1.90	164.26 ± 3.12	152.11 ± 14.23	146.11 ± 13.22 [*]
Diabetes + quercetin 25 mg/kg	184.05 ± 3.21	185.05 ± 4.12 (0.54%↑)	188.21 ± 3.21 [*] (2.26%↑)	191.20 ± 1.2 (3.78%↑)	192.18 ± 3.12 [*] (4.41%↑)
Diabetes + quercetin 50 mg/kg	185.13 ± 18.11 [*]	192.15 ± 11.07 [*] (3.79%↑)	193.11 ± 1.07 [*] (4.31%↑)	194.13 ± 12.10 [*] (4.85%↑)	195.15 ± 13.17 [*] (5.40%↑)
Diabetes + quercetin 75 mg/kg	185.11 ± 17.22 [*]	193.14 ± 14.21 [*] (4.33%↑)	198.09 ± 14.26 ^{**} (7.01%↑)	209.17 ± 14.23 (12.99%↑)	218.12 ± 12.33 ^{**} (17.83%↑)
Diabetes + metformin 10 mg/kg	184.15 ± 14.23 [*]	188.22 ± 12.33 [*] (2.21%↑)	192.12 ± 14.25 [*] (3.78%↑)	202.02 ± 15.37 ^{**} (9.70%↑)	209.15 ± 17.35 ^{**} (13.57%↑)

Values are expressed in Mean ± SD (n = 6 in each group).

^{*} p < 0.05,

^{**} p < 0.01 compared to diabetes group.

Table 8
Effects of quercetin on blood glucose levels in streptozotocin-induced diabetic rats.

Groups	Blood glucose (mg/dL)					
	Day 0	Day 1	Day 7	Day 14	Day 21	Day 28
Normal control	98.60 ± 0.48	98.40 ± 0.34	98.20 ± 0.38	99.85 ± 0.49	99.72 ± 0.43	100.12 ± 1.24
Diabetes	100.50 ± 0.30	360.20 ± 4.76	392.60 ± 2.41	412.60 ± 2.57	426.57 ± 2.14	465.30 ± 1.26
Diabetes + quercetin 25 mg/kg	98.00 ± 0.42	358.00 ± 2.09	348.00 ± 1.85 (2.79%↓)	325.73 ± 2.67 (9.01%↓)	284.25 ± 2.03 (20.60%↓)	224.50 ± 1.67 (37.29%↓)
Diabetes + quercetin 50 mg/kg	96.80 ± 0.20	357.40 ± 0.82	320.80 ± 2.34 [*] (10.39%↓)	270.56 ± 1.43 (24.46%↓)	246.53 ± 3.07 [*] (31.02%↓)	171.06 ± 2.68 ^{**} (52.13%↓)
Diabetes + quercetin 75 mg/kg	95.00 ± 0.20	358.50 ± 1.56	305.50 ± 2.17 ^{**} (14.78%↓)	225.82 ± 1.08 [*] (37.00%↓)	182.32 ± 5.24 ^{**} (49.14%↓)	119.00 ± 3.62 ^{**} (66.80%↓)
Diabetes + metformin 10 mg/kg	99.20 ± 0.48	359.80 ± 2.34	339.60 ± 2.34 (5.61%↓)	318.28 ± 3.21 (11.61%↓)	276.81 ± 1.40 [*] (23.06%↓)	219.30 ± 2.88 [*] (39.04%↓)

The data represent the mean ± SD (n = 6).

^{*} p < 0.05,

^{**} p < 0.01 when compared to diabetes group.

Table 9
Effects of quercetin on the levels of plasma insulin, total hemoglobin and urine sugar.

Groups	Plasma insulin (mg/dL)	Total hemoglobin (mg/dL)	Urine sugar
Normal control	17.21 ± 3.07	13.41 ± 9.11	NIL
Diabetes	8.13 ± 7.03	8.97 ± 0.49	++
Diabetes + quercetin 25 mg/kg	12.6 ± 9.36 [*]	12.08 ± 0.49 [*]	NIL
Diabetes + quercetin 50 mg/kg	14.05 ± 1.21 [*]	13.07 ± 1.58 [*]	NIL
Diabetes + quercetin 75 mg/kg	19.31 ± 2.01	13.98 ± 4.02 ^{**}	NIL
Diabetes + metformin 10 mg/kg	12.11 ± 7.14 ^{**}	12.99 ± 0.45 ^{**}	NIL

The data represent the mean ± SD (n = 6).

^{*} p < 0.05,

^{**} p < 0.01 compared to diabetes group.

pancreas, as indicated by decreasing numbers of islet cells and diminishing diameters of the pancreas islets (Fig. 9). The islets were smaller in diabetic rats than in normal control rats (Fig. 9B). Administration of quercetin (25, 50, and 75 mg/kg) or metformin (10 mg/kg) reduced pancreatic injury. The pancreas is a vital organ of metabolism and macronutrients digestion, which also secretes different digestive enzymes and pancreatic hormones [35]. Many studies have indicated that quercetin has the capacity to prevent pancreatic injury, promoting regeneration of the pancreatic islets and increasing its ability to maintain normal blood glucose levels in diabetes-induced rats [32,36].

Table 10
Effect of quercetin on activity of glycogen synthase and glycogen phosphorylase in the liver.

Groups	Glycogen synthase (mg/dL)	Glycogen phosphorylase (mg/dL)
Normal control	773.56 ± 27.06	572.21 ± 15.04
Diabetes	462.35 ± 12.11	752.41 ± 4.70
Diabetes + quercetin 25 mg/kg	572.21 ± 5.21 [*]	632.31 ± 4.02
Diabetes + quercetin 50 mg/kg	630.43 ± 21.34 ^{**}	610.13 ± 1.07 ^{**}
Diabetes + quercetin 75 mg/kg	652.31 ± 17.22 ^{**}	532.02 ± 11.17 ^{**}
Diabetes + metformin 10 mg/kg	643.27 ± 7.31 ^{**}	606.14 ± 33.01 ^{**}

The data represent the mean ± SD (n = 6).

^{*} p < 0.05,

^{**} p < 0.01 when compared to diabetes group.

4. Conclusion

The present molecular docking analysis showed a better binding affinity and lead docking score to glycogen phosphorylase with quercetin than with gallic acid. Quercetin was isolated from *P. emblica* fruit extract after the in silico finding. Different concentrations of quercetin showed remarkable antihyperglycemic effects and potent defense mechanisms in STZ-induced diabetic rats. Metformin is more commonly associated with gastrointestinal side effects than most other antidiabetic drugs. Finally, we conclude that quercetin is a remarkable antihyperglycemic

Table 11
Effect of quercetin on serum lipid profile.

Group	TG (mg/dL)	HDL (mg/dL)	VLDL (mg/dL)	LDL (mg/dL)	TC (mg/dL)
Normal control	88.31 ± 7.31	49.6 ± 2.71	17.03 ± 1.51	19.9 ± 4.25	99.7 ± 6.23
Diabetes	122.41 ± 7.03 (38.61%↓)	22.31 ± 1.64 (55.02%↓)	48.14 ± 2.86 (182.67%↑)	27.4 ± 8.12 (37.6%↓)	162.12 ± 3.21 (62.60%↓)
Diabetes + quercetin 25 mg/kg	113.19 ± 53.07 (7.53%↓)	27.56 ± 2.62 (23.53%↑)	43.24 ± 1.64 (10.17%↓)	26.19 ± 6.77 (4.41%↓)	57.14 ± 31.02 (3.07%↓)
Diabetes + quercetin 50 mg/kg	106.05 ± 9.32 [*] (12.99%↓)	32.25 ± 3.06 [*] (30.82%↑)	37.19 ± 2.8 [*] (22.74%↓)	21.41 ± 2.34 (21.86%↓)	141.11 ± 4.39 [*] (12.95%↓)
Diabetes + quercetin 75 mg/kg	93.00 ± 8.17 ^{**} (24.02%↓)	39.91 ± 5.14 ^{**} (78.88%↑)	24.92 ± 1.34 ^{**} (48.23%↓)	18.7 ± 2.66 ^{**} (31.75%↓)	119.27 ± 2.18 ^{**} (26.43%↓)
Diabetes + metformin 10 mg/kg	104.27 ± 7.38 ^{**} (14.81%↓)	29.27 ± 2.56 ^{**} (31.19%↑)	42.52 ± 3.4 ^{**} (11.67%↓)	25.27 ± 5.28 ^{**} (7.77%↓)	148.15 ± 72.19 ^{**} (8.61%↓)

The data represent the mean ± SD (n = 6).

TG: triglycerides; HDL: high density lipoprotein; LDL: low density lipoprotein; VLDL: very low density lipoprotein; TC: total cholesterol.

^{*} p < 0.05.

^{**} p < 0.01 compared to diabetes group.

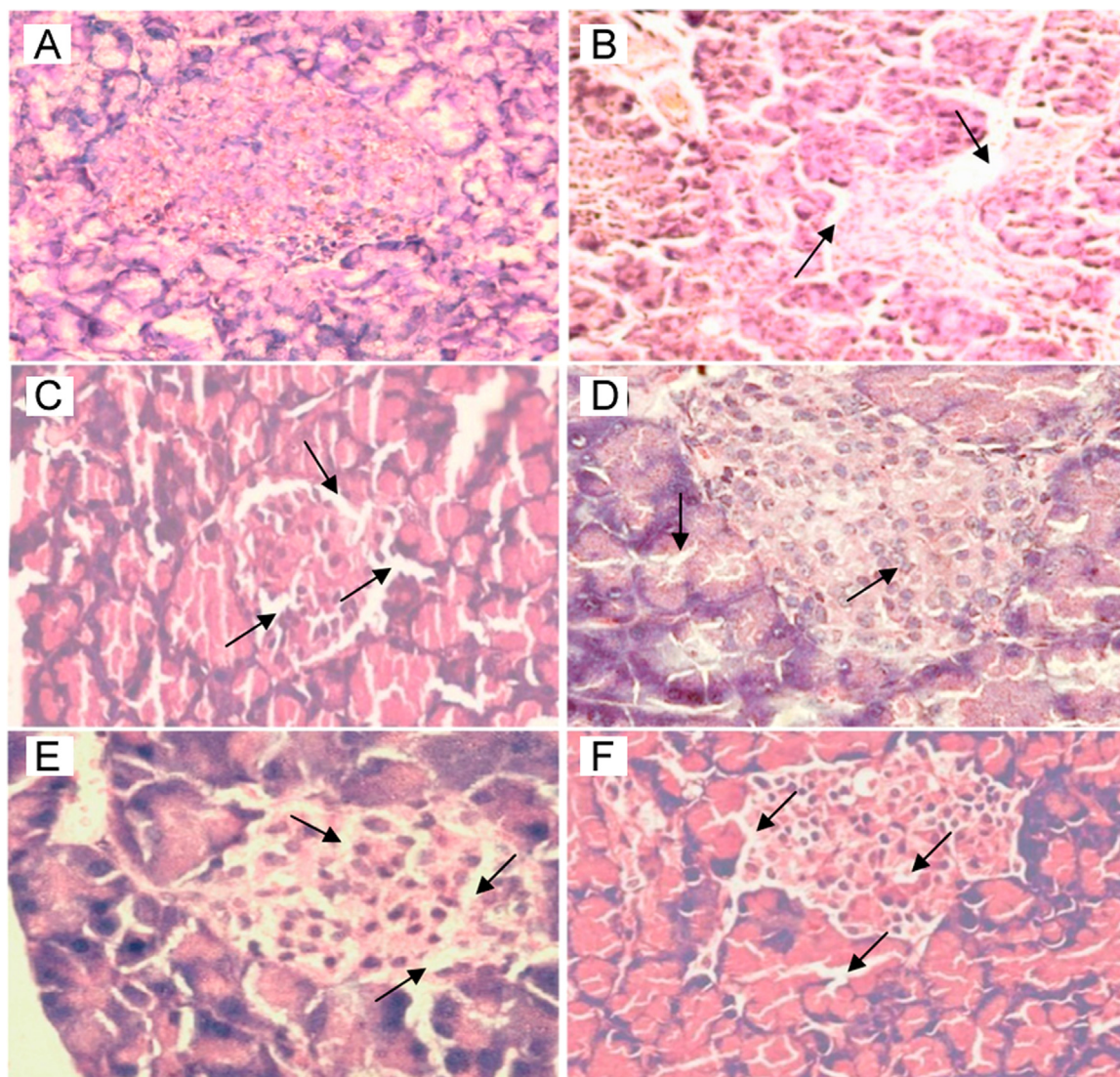


Fig. 9. Histopathology of pancreas at the end research with hematoxylin and eosin stain in different groups. (A) Normal control group: typical histological structure of pancreas and normal islets; (B) Streptozotocin induced diabetes model group showing severe necrotic changes, β -cells injury and breakdown of the islets after 72 h; (C) Diabetes + 25 mg/kg quercetin group showing slightly restored the necrotic changes and β cells with shrunken islets; (D and E) Diabetes + 50 mg/kg and Diabetes + 75 mg/kg groups presenting near normal histological structure; (F) Diabetes + 10 mg/kg metformin group showing significantly reduced pancreas injury and slightly restored the necrotic change.

agent, which can be considered as a potential drug candidate for diabetes mellitus with fewer side effects than metformin.

Conflicts of interest

The authors declare that there are no conflicts of interest.

Acknowledgements

The authors are grateful to the DST-SERB Major Research Project, New Delhi, India [Project File No. SB/YS/LS-109/2014] for funding this project. We especially express our thanks to the Management of A.V.V.M. Sri Pushpam College (Autonomous), Poondi, and Sharmila Institute of Medicinal Products Research Academy (SIMPRA), Thanjavur, India, for providing necessary facilities and support in carrying out this work.

Appendix A. Supplementary material

Supplementary data associated with this article can be found in the online version at [doi:10.1016/j.jpha.2017.10.005](https://doi.org/10.1016/j.jpha.2017.10.005).

References

- [1] M. Riaz, M. Zia-Ul-Haq, B. Saad, The role of anthocyanins in obesity and diabetes, *Anthocyanins and Human Health: Biomolecular and therapeutic aspects*, Springer Briefs in food, Health, and Nutrition, Springer, 2016: 109–123.
- [2] T. Kuzuya, S. Nakagawa, J. Satoh, et al., Report of the Committee on the classification and diagnostic criteria of diabetes mellitus, *Diabetes Res. Clin. Pract.* 1 (2002) 65–85.
- [3] S. Wild, G. Roglic, A. Green, et al., Global prevalence of diabetes: estimates for the year 2000 and projections for 2030, *Diabetes Care* 27 (2004) 1047–1053.
- [4] Y. Liu, J. Sun, S. Rao, Y. Su, et al., Antihyperglycemic, antihyperlipidemic and antioxidant activities of polysaccharides from *Catathelasma ventricosum* in streptozotocin-induced diabetic mice, *Food Chem. Toxicol.* 57 (2013) 39–45.
- [5] T. Vilsboll, J.J. Holst, Incretins, insulin secretion and Type 2 diabetes mellitus, *Diabetologia* 47 (2004) 357–366.
- [6] World Health Organization, *Chronicle*, 1985.
- [7] M.S. Valiathan, *Healing plants*, *Curr. Sci.* 75 (1998) 1122–1127.
- [8] J. Santosh kumar, M.S. Devarmani, M.M. Sajjanar, et al., Study of anti-inflammatory activity of fruit of *Emblca officinalis* (Amla) in Albino rats, *Med. Innov.* 2 (2013) 17–25.
- [9] W. Duan, Y. Yu, L. Zhang, Anti-atherogenic effects of *Phyllanthus emblica* associated with corilagin and its analogue, *Yakugaku Zasshi* 125 (2005) 587–591.
- [10] S. Madhuri, G. Pandey, K.S. Verma, Antioxidant, immunomodulatory and anticancer activities of *Emblca officinalis*: an overview, *Int. Res. J. Pharm.* 2 (2011) 38–42.
- [11] M. Krishnaveni, S. Mirunalini, Therapeutic potential of *Phyllanthus emblica* (amla): the ayurvedic wonder, *J. Basic. Clin. Physiol. Pharmacol.* 21 (2010) 93–105.
- [12] D.W. Unander, G.L. Webster, B.S. Blumberg, Records of usage or assays in *Phyllanthus* (Euphorbiaceae). I. Subgenera *Isocladus*, *Kirganelia*, *Cicca* and *Emblca*, *J. Ethnopharmacol.* 30 (1990) 233–264.
- [13] Schrödinger, LLC, New York, NY, 2015.
- [14] (<http://www.chemspider.com>).
- [15] (<http://www.rcsb.com>).
- [16] Glide v5.7, Schrödinger, LLC, New York, 2011.
- [17] LigPrep v2.5, Schrödinger, LLC, New York, 2011.
- [18] A. Kemp, A.J. Van Heijningen, A colorimetric micro-method for the determination of glycogen in tissues, *Biochem. J.* 56 (1954) 646–648.
- [19] J.C. McCormack, N. Westergaard, M. Kristiansen, et al., Pharmacological approaches to inhibit endogenous glucose production as a means of anti-diabetic therapy, *Curr. Pharm. Des.* 7 (2001) 1451–1474.
- [20] J.L. Treadway, P. Mendys, D.J. Hoover, et al., Glycogen phosphorylase inhibitors for treatment of type 2 diabetes mellitus, *Expert. Opin. Investig. Drugs* 10 (2001) 439–454.
- [21] R. Sarabu, J. Tilley, Recent advances in therapeutic approaches to type 2 diabetes, *Annu. Rep. Med. Chem.* 40 (2005) 167–181.
- [22] R. Paramaguru, P.M. Mazumder, D. Sasmal, et al., Antidiabetic activity of *Pterospermum acerifolium* flowers and glucose uptake potential of bioactive fraction in L6 muscle cell lines with its HPLC fingerprint, *BioMed. Res. Int.* (2014) 1–10.
- [23] H. Hui, G. Tang, V.L. Go, et al., Hypoglycemic herbs and their action mechanisms, *Chin. Med.* 4 (2009) 11–14.
- [24] J. Neustadt, S.R. Pieczenik, Medication-induced mitochondrial damage and disease, *Mol. Nutr. Food Res.* 52 (2008) 780–788.
- [25] S. Bibi, S. Kalsoom, H. Rashid, Ligand based approach for pharmacophore generation for identification of novel compounds having anti-diabetic activity, *Int. J. Pharm. Sci.* 4 (2013) 303–314.
- [26] R. Sundaram, R. Naresh, P. Shanthi, et al., Modulatory effect of green tea extract on hepatic key enzymes of glucose metabolism in streptozotocin and high fat diet induced diabetic rats, *Phytomedicine* 20 (2013) 577–584.
- [27] O. Coskun, M. Kanter, A. Korkmaz, et al., Quercetin, a flavonoid antioxidant, prevents and protects streptozotocin-induced oxidative stress and beta-cell damage in rat pancreas, *Pharmacol. Res.* 51 (2005) 117–123.
- [28] A.K. Tiwari, J.M. Rao, Diabetes mellitus and multiple therapeutic approaches of phytochemicals: present status and future prospects, *Curr. Sci.* 83 (2002) 30–38.
- [29] M. Torres-Piedra, R. Ortiz-Andrade, R. Villalobos-Molina, et al., A Comparative study of flavonoid analogues on streptozotocin-nicotinamide induced diabetic rats: quercetin as a potential antidiabetic agent acting via 11beta-hydroxysteroid dehydrogenase type 1 inhibition, *Eur. J. Med. Chem.* 45 (2010) 2606–2612.
- [30] R.A. DeFronzo, Pharmacologic therapy for type 2 diabetes mellitus, *Ann. Intern. Med.* 131 (1999) 281–303.
- [31] N. Arias, M.T. Macarulla, L. Aguirre L, et al., Quercetin can reduce insulin resistance without decreasing adipose tissue and skeletal muscle fat accumulation, *Genes. Nutr.* 9 (2014) 361.
- [32] J.H. Kim, M.J. Kang, H.N. Choi, et al., Quercetin attenuates fasting and postprandial hyperglycemia in animal models of diabetes mellitus, *Nutr. Res. Pract.* 5 (2011) 107–111.
- [33] J. Mohammadi, P.R. Naik, Evaluation of hypoglycemic effect of *Morus alba* in an animal model, *Indian J. Pharmacol.* 40 (2008) 15–18.
- [34] L. Nuraliev, G.A. Avezov, The efficacy of quercetin in alloxan diabetes, *Exp. Clin. Pharmacol.* 55 (1992) 42–44.
- [35] C. Guo, C. Zhang, L. Li, Hypoglycemic and hypolipidemic effects of oxymatrine in high-fat diet and streptozotocin-induced diabetic rats, *Phytomedicine* 21 (2014) 807–814.
- [36] M. Vessal, M. Hemmati, M. Vaside, Antidiabetic effects of quercetin in streptozotocin induced diabetic rats, *Comp. Biochem. Physiol. Toxicol. Pharmacol.* 135 (2003) 357–364.



Original Research Article

Quantitative determination of erlotinib in human serum using competitive enzyme-linked immunosorbent assay

Yuta Yamamoto, Tetsuya Saita*, Yutaro Yamamoto, Masashi Shin

Applied Life Science Department, Faculty of Biotechnology and Life Science, Sojo University, 4-22-1 Ikeda, Kumamoto 860-0082, Japan

ARTICLE INFO

Article history:

Received 10 July 2017

Received in revised form

20 October 2017

Accepted 24 October 2017

Available online 8 February 2018

Keywords:

Erlotinib

Enzyme-linked immunosorbent assay

O-desmethyl erlotinib

Tyrosine-kinase inhibitor

ABSTRACT

A selective and sensitive competitive enzyme-linked immunosorbent assay (ELISA) method was developed and validated for the quantification of erlotinib in 50 μ L of samples of human serum. Anti-erlotinib serum was obtained by immunizing mice with an antigen conjugated with bovine serum albumin and 3,4-bis(2-methoxyethoxy)benzoic acid using the *N*-succinimidyl ester method. Enzyme labeling of erlotinib with horseradish peroxidase was similarly performed using 3,4-bis(2-methoxyethoxy)benzoic acid. A simple competitive ELISA for erlotinib was developed using the principle of direct competition between erlotinib and the enzyme marker for anti-erlotinib antibody, which had been immobilized on the plastic surface of a microtiter plate. Serum erlotinib concentrations lower than 40 ng/mL were reproducibly measurable using the ELISA. This ELISA was specific to erlotinib and showed very slight cross-reactivity (6.7%) with a major metabolite, *O*-desmethyl erlotinib. Using this assay, drug levels were easily measured in the blood of mice after oral administration of erlotinib at a single dose of 30 mg/kg. ELISA should be used as a valuable tool for therapeutic drug monitoring and in pharmacokinetic studies of erlotinib.

© 2018 Xi'an Jiaotong University. Production and hosting by Elsevier B.V. This is an open access article under the CC BY-NC-ND license (<http://creativecommons.org/licenses/by-nc-nd/4.0/>).

1. Introduction

Erlotinib (Fig. 1), an epidermal growth factor receptor-tyrosine kinase inhibitor (EGFR-TKI), is widely used to treat non-small cell lung cancer and unresectable pancreatic cancer [1,2]. However, it is associated with a higher incidence of interstitial lung disease than other anticancer drugs, and many fatal cases have been reported [3]. It also frequently causes acneiform rashes by inhibiting the expression of EGFR in the stratum basale and skin appendages. These reactions are frequently reported as a reason for dose reduction or interruption of treatment in patients receiving erlotinib [4,5].

Erlotinib is metabolized by CYP3A4, CYP1A2, and CYP3A5 in the liver, and the induction of CYP3A4 via tobacco smoking has been shown to decrease the blood concentration of erlotinib by about 50% [6]. Food also influences the absorption of erlotinib. Taking erlotinib after consuming a high-fat, high-calorie meal has been shown to increase maximum blood concentrations by about 1.5-fold and the AUC about 2-fold [7]. The severity of skin damage caused by erlotinib has been shown to be correlated with the concentration of erlotinib in the blood [8], which indicates that therapeutic drug monitoring (TDM) is needed to minimize the toxicity of erlotinib and improve the response to treatment.

O-Desmethyl erlotinib is known as a major metabolite in humans (Fig. 1) [9]. During long-term therapy, the plasma concentration of *O*-desmethyl erlotinib is about 10% of that of erlotinib [10]. Therefore, an analytical method specific to erlotinib must be developed for TDM or pharmacokinetic studies. Previous TDM and pharmacokinetic studies of erlotinib have used high-performance liquid chromatography (HPLC) [11] and liquid chromatography with tandem mass spectrometry (LC-MS/MS) [12–17]. However, no immunoassay technique that compares favorably with these analytical methods has been developed. The reason for this is that it is very challenging to produce an anti-erlotinib antibody that is not cross-reactive with *O*-desmethyl erlotinib, the major metabolite of erlotinib. We previously created a specific antibody, which is not cross-reactive with the major metabolite, and changed part of the structure of the drug to a hapten antigenic structure, by considering the structure of the major metabolite, to develop an enzyme immunoassay technique that could be used for pharmacokinetic studies of the antibody [18–20]. Similarly, we created a specific anti-erlotinib antibody by changing part of the structure of erlotinib to a hapten antigenic structure to develop enzyme immunoassay techniques that could be used for pharmacokinetic studies on erlotinib.

In this study, we successfully developed the first specific and sensitive competitive enzyme-linked immunosorbent assay (ELISA) for erlotinib using a polyclonal antibody against part of the structure of erlotinib and herein report the technique. The initial application of the assay for the measurement of erlotinib

Peer review under responsibility of Xi'an Jiaotong University.

* Corresponding author.

E-mail address: sait1102@life.sojo-u.ac.jp (T. Saita).

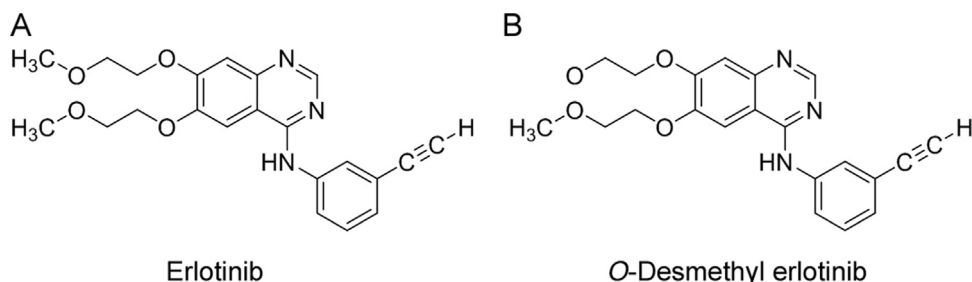


Fig. 1. Chemical structures of erlotinib and its major metabolite.

levels in mice demonstrates its usefulness for the assessment of basic pharmacokinetic parameters.

2. Materials and methods

2.1. Chemicals and reagents

Erlotinib hydrochloride and *O*-desmethyl erlotinib were obtained from AdooQ BioScience LLC (Irvine, CA, USA). Ethyl 3,4-bis(2-methoxyethoxy)benzoate (EBMB) was obtained from AK Scientific, Inc (Union City, CA, USA). 2,4,6-Trinitrobenzene sulfonic acid was obtained from Tokyo Chemical Industry Co., Ltd. (Tokyo, Japan). Horseradish peroxidase (HRP) and 3,3',5,5'-tetramethylbenzidine (TMB) were obtained from Boehringer Ingelheim Pharma GmbH (Ingelheim, Germany). Sodium hydroxide, hydrochloric acid, sulfuric acid, sodium dihydrogenphosphate dehydrate, disodium hydrogenphosphate 12-water, sodium azide, tris(hydroxymethyl)amino-methane (Tris), 1-ethyl-3-(3-dimethylaminopropyl) carbodiimide hydrochloride (EDC), *N*-hydroxysuccinimide, dioxane, ethyl acetate, *N,N*-dimethylformamide and bovine serum albumin (BSA) were purchased from Wako Pure Chemical Industries, Ltd. (Osaka, Japan). Hydrogen peroxide (30% in water) was obtained from Nacalai Tesque Inc. (Kyoto, Japan).

2.2. Preparation of the immunogen for erlotinib

The erlotinib immunogen was prepared with part of the structure of erlotinib (EBMB) as shown in Fig. 2. EBMB (10 mg, 33.5 μ mol) was dissolved in 500 μ L of 1 M NaOH and the resulting solution was left to stand at 60 $^{\circ}$ C for 1 h. The resulting EBMB carboxylate was acidified by the addition of 550 μ L of 1 M HCl and then extracted with ethyl acetate. The organic layer was separated and evaporated under reduced pressure. The residue was dissolved in 95% dioxane (1 mL). EDC (12.7 mg, 67 μ mol) and *N*-hydroxysuccinimide (7.7 mg, 67 μ mol) were added to the dioxane solution, and the solution was left to stand at room temperature for 2 h. The reaction mixture containing succinimidyl EBMB was immediately mixed with BSA (20 mg) in 1 mL of 0.1 M

phosphate buffer (pH 7.0) and incubated at room temperature for 2 h. The reaction solution was dialyzed in 1 mM phosphate buffer (pH 7.0) for 24 h. The purified conjugate was lyophilized and used as an immunogen for erlotinib. The trinitrobenzene sulfonic acid method was used to determine the primary amine [21], and about 18.1 EBMB molecules were found to be coupled with each molecule of BSA based on the reduction of the primary amine.

2.3. Preparation of erlotinib antibody

Five 5-week-old, female BALB/c mice (Kyudo Exp. Animals, Kumamoto, Japan) were injected intraperitoneally with 0.1 mg of EBMB-BSA conjugate emulsified in complete Freund's adjuvant. The mice received 3 injections of the con-jugate (0.05 mg) alone at 2-week intervals. Seven days after the final injection, the mice were euthanized and sera were collected, separated by centrifugation, heated at 55 $^{\circ}$ C for 30 min, and then stored at -30° C. The anti-erlotinib serum obtained was directly used as the anti-erlotinib antibody for ELISA. The experimental protocol was approved by the Ethics Review Committee for Animal Experimentation of Sojo University.

2.4. Preparation of the erlotinib-HRP conjugate

Erlotinib was labeled by binding to HRP, essentially by the same method as that used for the preparation of erlotinib immunogen. EBMB (10 mg, 33.5 μ mol) was dissolved in 500 μ L 1 M NaOH and the solution was left to stand at 60 $^{\circ}$ C for 1 h. The resulting EBMB carboxylate was acidified by the addition of 550 μ L of 1 M HCl and then extracted with ethyl acetate. The organic layer was separated and evaporated under reduced pressure. The residue was dissolved in 95% dioxane (1 mL). EDC (12.7 mg, 67 μ mol) and *N*-hydroxysuccinimide (7.7 mg, 67 μ mol) were added to the dioxane solution. The resulting solution was left to stand at room temperature for 2 h, and a 50 μ L aliquot of the reaction mixture, containing succinimidyl EBMB, was then added directly to HRP (0.5 mg, 12.5 nmol) in 0.5 mL of 0.1 M phosphate buffer (pH 7.0), followed by incubation at room temperature for a further 2 h. The mixture was chromatographed on a column of Sephadex G-75 (2.0 cm \times 30 cm) using PBS containing 0.1% BSA to remove any remaining small molecules. Fractions (4 mL)

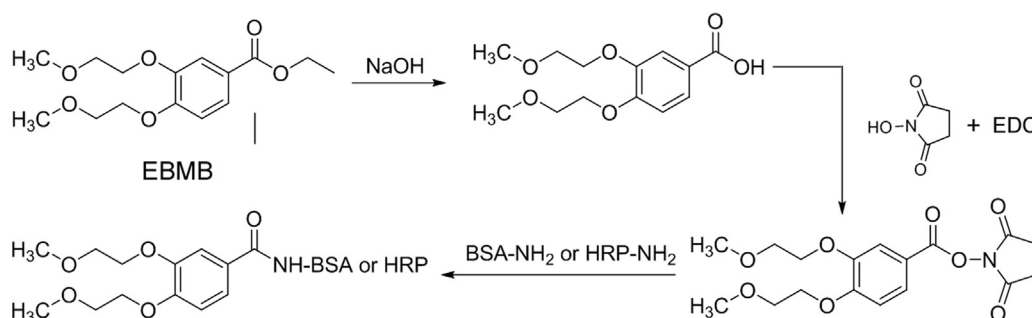


Fig. 2. Scheme showing the preparation of the immunogen and enzyme conjugate.

were collected and fractions 8 and 9, corresponding to the main peaks showing enzyme activity, were used as a label for ELISA.

2.5. ELISA procedure

ELISA is based on the principle of competition between enzyme-labeled and unlabeled drugs for an immobilized antibody, followed by measurement of the marker enzyme activity of the immunocomplex bound to the solid phase. Briefly, microtiter plate wells (Nunc F Immunoplates I; Nunc, Roskilde, Denmark) were coated with 100 μ L of anti-mouse-IgG antibody (2 μ g/mL) (Bethyl Laboratories, Montgomery, TX) in 10 mM Tris-HCl buffer (pH 8.5) containing 10 mM NaCl and 10 mM Na₂S₂O₃ and left to stand for 1 h at 37 °C. Plates were washed twice with PBS containing 0.1% BSA and incubated with 100 μ L of anti-erlotinib serum diluted 2000-fold with PBS containing 1% skim milk for 30 min at 37 °C. The anti-erlotinib antibody-coated wells were then filled with 50 μ L of either erlotinib-treated samples or PBS containing 0.1% BSA as a control, followed immediately by 50 μ L of the pooled erlotinib-HRP conjugate (diluted 1:20 in PBS containing 0.1% BSA for erlotinib). The wells were incubated overnight at 4 °C and once again washed thoroughly with PBS containing 0.1% BSA. The activity of the enzyme conjugate bound to each well was measured by the addition of 100 μ L of 0.42 mM TMB in 0.05 M acetate-citric acid buffer (pH 5.5) containing 3% *N,N*-dimethylformamide and 0.01% hydrogen peroxide, followed by incubation of the wells at 37 °C for a suitable period. The enzyme reaction was stopped by the addition of 100 μ L of 2.0 M H₂SO₄ to each well, and the resulting color intensity was measured spectrophotometrically at 450 nm using an ELISA analyzer (ImmunoMini NJ-2300, Nalge Nunc Int. Co., Ltd., Tokyo, Japan). Concentrations were calculated from the standard curve using semi-logarithmic graph paper.

2.6. Pharmacokinetic evaluation

Three 8-week-old female BALB/c mice (Kyudo Exp. Animals; Kumamoto, Japan) weighing 25–30 g were used in this study. Erlotinib was orally administered at a dose of 30 mg/kg using a sonde after an overnight fast. The drug was suspended in methyl cellulose (0.5%, m/v water) at 5 mg/mL concentration. Peripheral blood (5 μ L) was collected from the tail vein pre-administration and at 0.25, 0.5, 1, 2, 4, 8, 12, and 24 h after administration, diluted 25 times with PBS containing 0.1% BSA, and immediately vortexed for several seconds. Diluted blood samples were centrifuged at 3000g for 10 min at 4 °C, and each resulting supernatant was stored at –30 °C until the erlotinib concentration was assayed. The experimental protocol was approved by the Ethics Review Committee for Animal Experimentation of Sojo University.

3. Results and discussion

3.1. Preparation of the immunogen and enzyme conjugate for erlotinib

In long-term therapy, the plasma concentration of *O*-desmethyl erlotinib, the major metabolite of erlotinib in humans, is about 10% of that of erlotinib [10]. Therefore, an anti-erlotinib antibody that does not show cross-reaction with *O*-desmethyl erlotinib must be produced to develop an ELISA that can specifically measure the concentration of erlotinib in human plasma. Namely, antibodies against erlotinib must have high affinity for the bis(2-methoxyethoxy) group, which is the primary site of metabolism. In general, antibody specificity on the hapten appears to be towards the group farthest away from the region of conjugation to the carrier protein in the immunogen structure [22,23]. Therefore,

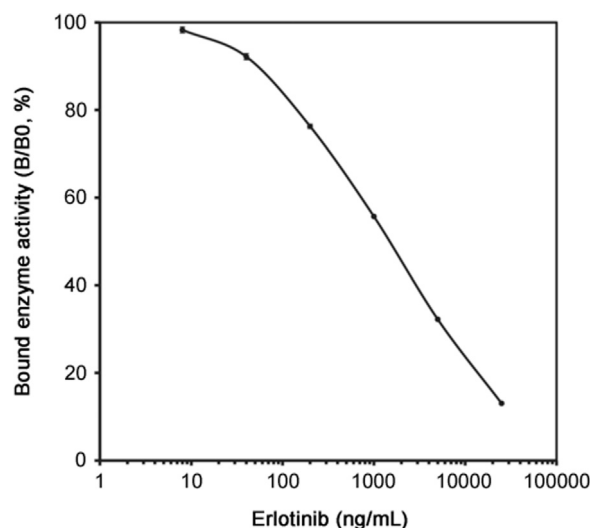


Fig. 3. Standard curve of the developed ELISA for erlotinib in human serum. The curve shows the bound enzyme activity (%) for various doses of erlotinib (B) as a ratio to that bound using erlotinib-HRP alone (B₀). Each point represents the mean \pm S.D. ($n=3$).

when creating erlotinib antigens, it must be ensured that the bis (2-methoxyethoxy) group within the hapten structure is as far away as possible from the carrier protein binding domain. Moreover, erlotinib has no suitable reactive structure for making immunogens such as the erlotinib-BSA conjugate. Based on these findings, erlotinib immunogen was prepared from part of the structure of erlotinib (EBMB) (Fig. 2). The EBMB carboxylate was coupled to BSA using the hydroxysuccinimide ester method [24], and the resulting EBMB-BSA conjugate (erlotinib immunogen), with about 18 mol of EBMB per mol of BSA, induced the formation of specific antibodies in each of the five mice immunized. EBMB-HRP conjugate (as a tracer) was also prepared by the same procedure. The conjugate was stable for more than 6 months in eluted buffer (pH 7.0) at 4 °C without any loss of the enzyme or immunoreactive enzyme activity.

3.2. Validation of method

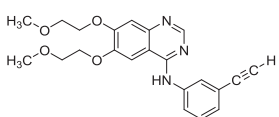
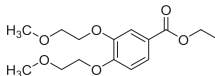
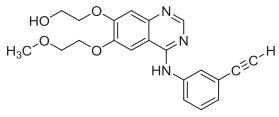
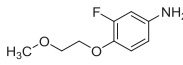
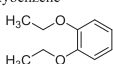
The optimal quantities and incubation times for each reaction were established. The standard dose-response curve of erlotinib obtained in the human serum system is shown in Fig. 3. The ELISA detection range was 8–25,000 ng/mL of erlotinib. The curve was essentially linear on a semilogarithmic plot between 40 and 25,000 ng/mL. For practical purposes, the working range was arbitrarily set to 40–5000 ng/mL based on the findings of precision and accuracy for the ELISA (Table 1), which showed this ELISA to be a reproducible technique. The recoveries of four different levels of erlotinib ranging from 40 to 5000 ng/mL were satisfactory at

Table 1
Recoveries of erlotinib from human serum and precision of ELISA for erlotinib.

Assay	Added (ng/mL)	Estimated (ng/mL)	Recovery (%)	CV (%)
Intra-assay	40.0	42.2 \pm 3.9	105.5	9.2
	200.0	197.6 \pm 10.2	98.8	5.2
	1000.0	979.0 \pm 25.7	97.9	2.6
	5000.0	4922.0 \pm 95.5	98.4	1.9
Inter-assay	40.0	43.1 \pm 1.8	107.5	4.2
	200.0	194.6 \pm 14.3	97.3	7.3
	1000.0	966.4 \pm 23.6	96.6	2.4
	5000.0	4964.4 \pm 114.5	99.2	2.3

Values represent the mean \pm S.D. ($n=5$).

Table 2
Percent cross-reactivity of metabolite and analogs measured by ELISA.

Compounds	Cross-reactivity (%)
Erlotinib 	100.0
Ethy 3,4-bio (3-methoxyethoxy) benzoate 	100.0
<i>O</i> -Desmethyl erlotinib 	6.7
3-Fluoro-4-(2-methoxyethoxy)aniline 	1.3
1,2-Diethoxybenzene 	0.8

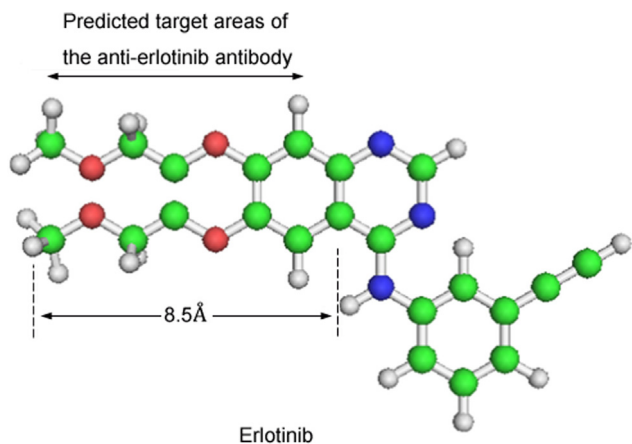


Fig. 4. The predicted target areas of the anti-erlotinib antibody. The length of epitope was approximately 8.5 Å.

96.6%–107.5% ($n=5$). The coefficients of variation (CV) for intra- and inter-assays of erlotinib at four different level concentrations in the range of 40–5000 ng/mL were 1.9%–9.2% and 2.3%–7.3% ($n=5$ for each), respectively. The detection limit of erlotinib in the ELISA was 40 ng/mL (student's t -test, $n=3$, $P < 0.01$ compared with the B0 value). The plasma concentration range for the usual clinical dose of erlotinib is about 0.6–2.5 µg/mL [25]. Therefore, this ELISA may be sensitive enough to quantify erlotinib in TDM and pharmacokinetic studies.

3.3. Specificity

Antibody cross-reactivity was determined by the displacement of bound erlotinib-HRP by similar compounds. Cross-reactivity values were defined as the ratio of each compound to erlotinib in the concentrations required for 50% inhibition of erlotinib-HRP binding to the antibody. The anti-erlotinib antibody showed 100% cross-reactivity with EBMB used as a hapten antigen, 6.7% with the major erlotinib metabolite, *O*-desmethyl erlotinib, 1.3% with

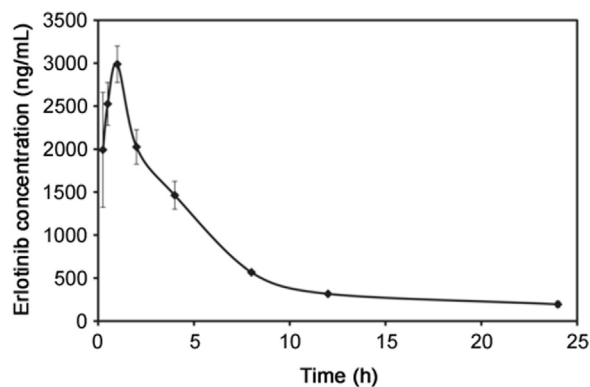


Fig. 5. Blood erlotinib levels in mice after a single oral administration of erlotinib. Three mice weighing 25–31 g were injected with 30 mg/kg erlotinib. At each interval, blood was collected and the levels of erlotinib were measured by ELISA. Each point represents the mean \pm S. D. ($n = 3$).

3-fluoro-4-(2-methoxyethoxy)aniline, and 0.8% with 1,2-diethoxybenzene (Table 2). Furthermore, the antibody showed high affinity for erlotinib and EBMB was used as a hapten antigen. However, it showed limited reactivity with the major metabolite *O*-desmethyl erlotinib and erlotinib analogs. These findings suggest that the antibody recognizes almost the whole EBMB structure, and thus is suitably specific to the structure of erlotinib. In addition, based on the predicted target area of the anti-erlotinib antibody, we estimated the length of the epitope to be approximately 8.5 Å (Fig. 4).

3.4. Pharmacokinetic study of erlotinib in mice

To demonstrate the potential of the ELISA, a preliminary pharmacokinetic study of erlotinib in mice was performed (Fig. 5). Erlotinib was rapidly absorbed, reached peak concentrations in the blood of 2987.5 ng/mL 60 min after oral administration, and then slowly decreased. The erlotinib levels in the blood samples were similar to those of the LC–MS results reported by Smith et al. [26]. Using the ELISA, erlotinib levels were easily measured in the blood of mice after a single oral dose of erlotinib. The ELISA determinations may have measured the total amount of erlotinib immunoreactivity and included erlotinib metabolites that cross-reacted with the anti-erlotinib antibody, such as the major metabolite in humans, *O*-desmethyl erlotinib [9]. However, during long-term therapy, the plasma concentration of *O*-desmethyl erlotinib is only about 10% of that of erlotinib [10]. Therefore, considering the specificity of the antibody and the plasma concentration of *O*-desmethyl erlotinib, there might not have any interference. The cross-reactivity of the other metabolites has not yet been confirmed, and their maximum concentrations detected in human plasma are relatively low [9]. Therefore, this ELISA may be specific enough to quantify erlotinib for TDM and pharmacokinetic studies in humans.

4. Conclusion

We have described the preparation of the first antibody against erlotinib by preparing immunogens from part of the structure of erlotinib. The generated antibody against erlotinib was used to develop the ELISA, which was shown to be sensitive, specific, and adaptable for high-throughput analyses. This ELISA will be a valuable tool in TDM and pharmacokinetic studies of erlotinib. Finally, our approach is expected to be invaluable in the development of new immunoassays for low-molecular-weight drugs that produce a variety of metabolites.

Conflicts of interest

The authors declare that there are no conflicts of interest.

References

- [1] F.A. Shepherd, J. Rodrigues Pereira, T. Ciuleanu, et al., Erlotinib in previously treated non-small-cell lung cancer, *N. Engl. J. Med.* 353 (2005) 123–132.
- [2] A.M. Czarnecka, P. Korzeń, A. Nowak-Dement, et al., Prolonged complete response following gemcitabine-erlotinib combined therapy in advanced pancreatic cancer, *Oncol. Lett.* 11 (2016) 1101–1104.
- [3] R. ter Heine, R.T. van den Bosch, C.M. Schaefer-Prokop, et al., Fatal interstitial lung disease associated with high erlotinib and metabolite levels. A case report and a review of the literature, *Lung Cancer* 75 (2012) 391–397.
- [4] S. Sato, K. Kurishima, K. Miyazaki, et al., Efficacy of tyrosine kinase inhibitors in non-small-cell lung cancer patients undergoing dose reduction and those with a low body surface area, *Mol. Clin. Oncol.* 2 (2014) 604–608.
- [5] K. Yamada, K. Azuma, M. Takeshita, et al., Phase II trial of erlotinib in elderly patients with previously treated non-small cell lung cancer: results of the Lung Oncology Group in Kyushu (LOGiK-0802), *Anticancer Res.* 36 (2016) 2881–2887.
- [6] A.N. Hughes, M.E.R. O'Brien, W.J. Petty, et al., Overcoming CYP1A1/1A2 mediated induction of metabolism by escalating erlotinib dose in current smokers, *J. Clin. Oncol.* 27 (2009) 1220–1226.
- [7] J. Ling, S. Fettner, B.L. Lum, et al., Effect of food on the pharmacokinetics of erlotinib, an orally active epidermal growth factor receptor tyrosine-kinase inhibitor, in healthy individuals, *Anticancer Drugs* 19 (2008) 209–216.
- [8] J.F. Lu, S.M. Eppler, J. Wolf, et al., Clinical pharmacokinetics of erlotinib in patients with solid tumors and exposure-safety relationship in patients with non-small cell lung cancer, *Clin. Pharmacol. Ther.* 80 (2006) 136–145.
- [9] J. Ling, K.A. Johnson, Z. Miao, et al., Metabolism and excretion of erlotinib, a small molecule inhibitor of epidermal growth factor receptor tyrosine kinase, in healthy male volunteers, *Drug Metab. Dispos.* 34 (2006) 420–426.
- [10] Y. Togashi, K. Masago, M. Fukudo, et al., Pharmacokinetics of erlotinib and its active metabolite OSI-420 in patients with non-small cell lung cancer and chronic renal failure who are undergoing hemodialysis, *J. Thorac. Oncol.* 5 (2010) 601–605.
- [11] L. Faivre, C. Gomo, O. Mir, et al., A simple HPLC-UV method for the simultaneous quantification of gefitinib and erlotinib in human plasma, *J. Chromatogr. B Anal. Technol. Biomed. Life Sci.* 879 (2011) 2345–2350.
- [12] T. Ishida, T. Naito, J. Kawakami, Simultaneous determination of erlotinib and its isomeric major metabolites in human plasma using isocratic liquid chromatography-tandem mass spectrometry and its clinical application, *Biomed. Chromatogr.* 29 (2015) 643–646.
- [13] H. Hayashi, Y. Kita, H. Iihara, et al., Simultaneous and rapid determination of gefitinib, erlotinib and afatinib plasma levels using liquid chromatography/tandem mass spectrometry in patients with non-small-cell lung cancer, *Biomed. Chromatogr.* 30 (2016) 1150–1154.
- [14] H.M. Maher, N.Z. Alzoman, S.M. Shehata, Simultaneous determination of erlotinib and tamoxifen in rat plasma using UPLC-MS/MS: application to pharmacokinetic interaction studies, *J. Chromatogr. B Anal. Technol. Biomed. Life Sci.* 1028 (2016) 100–110.
- [15] R.W. Sparidans, H. Rosing, J.J.M. Rood, et al., Liquid chromatography-tandem mass spectrometric assay for therapeutic drug monitoring of the B-Raf inhibitor encorafenib, the EGFR inhibitors afatinib, erlotinib and gefitinib and the O-desmethyl metabolites of erlotinib and gefitinib in human plasma, *J. Chromatogr. B Anal. Technol. Biomed. Life Sci.* 1033–1034 (2016) 390–398.
- [16] H.M. Maher, N.Z. Alzoman, S.M. Shehata, et al., UPLC-ESI-MS/MS study of the effect of green tea extract on the oral bioavailability of erlotinib and lapatinib in rats: potential risk of pharmacokinetic interaction, *J. Chromatogr. B Anal. Technol. Biomed. Life Sci.* 1049–1050 (2017) 30–40.
- [17] M.W. Ni, J. Zhou, H. Li, et al., Simultaneous determination of six tyrosine kinase inhibitors in human plasma using HPLC-Q-Orbitrap mass spectrometry, *Bioanalysis* 9 (2017) 925–935.
- [18] T. Saita, M. Shin, H. Fujito, Development of a specific and sensitive enzyme-linked immunosorbent assay for the quantification of imatinib, *Biol. Pharm. Bull.* 36 (2013) 1964–1968.
- [19] T. Saita, Y. Yamamoto, S. Noda, et al., Quantification of sorafenib in human serum by competitive enzyme-linked immunosorbent assay, *Biol. Pharm. Bull.* 38 (2015) 1788–1793.
- [20] T. Saita, Y. Yamamoto, K. Hosoya, et al., An ultra-specific and sensitive sandwich ELISA for imatinib using two anti-imatinib antibodies, *Anal. Chim. Acta* 969 (2017) 72–78.
- [21] A.F. Habeeb, Determination of free amino groups in proteins by trinitrobenzenesulfonic acid, *Anal. Biochem.* 14 (1966) 328–336.
- [22] B.K. van Weeman, A.H. Schuur, The influence of heterologous combinations of antiserum and enzyme-labeled estrogen on the characteristics of estrogen enzyme-immunoassays, *Immunochemistry* 12 (1975) 667–670.
- [23] K. Fujiwara, H. Saikusa, M. Yasuno, et al., Enzyme immunoassay for the quantification of mitomycin C using β -galactosidase as a label, *Cancer Res.* 42 (1982) 1487–1491.
- [24] H. Hosoda, Y. Sakai, T. Nambara, A direct enzyme immunoassay of 6 beta-hydroxycortisol in human urine, *Chem. Pharm. Bull.* 29 (1981) 170–175.
- [25] N.A. Lankheet, E.E. Schaake, S.A. Burgers, et al., Concentrations of erlotinib in tumor tissue and plasma in non-small-cell lung cancer patients after neoadjuvant therapy, *Clin. Lung Cancer* 16 (2015) 320–324.
- [26] N.F. Smith, S.D. Baker, F.J. Gonzalez, et al., Modulation of erlotinib pharmacokinetics in mice by a novel cytochrome P450 3A4 inhibitor, BAS 100, *Br. J. Cancer* 98 (2008) 1630–1632.



Contents lists available at ScienceDirect

Journal of Pharmaceutical Analysis

journal homepage: www.elsevier.com/locate/jpa
www.sciencedirect.com

Original Research Article

Ultrasensitive electrochemical determination of metronidazole based on polydopamine/carboxylic multi-walled carbon nanotubes nanocomposites modified GCE

Satar Tursynbolat¹, Yrysgul Bakytkarim¹, Jianzhi Huang¹, Lishi Wang*

School of Chemistry and Chemical Engineering, South China University of Technology, Guangzhou 510641, China

ARTICLE INFO

Article history:

Received 26 May 2017

Received in revised form

5 November 2017

Accepted 16 November 2017

Available online 21 November 2017

Keywords:

Metronidazole

Polydopamine

Carboxylic multi-walled carbon nanotubes

Nanocomposites

Electrochemical determination

Electrochemical sensor

ABSTRACT

An ultrasensitive electrochemical sensor based on polydopamine/carboxylic multi-walled carbon nanotubes (MWCNTs–COOH) nanocomposites modified glassy carbon electrode (GCE) was presented in this work, which has been developed for highly selective and highly sensitive determination of an antimicrobial drug, metronidazole. The preparation of polydopamine/MWCNTs–COOH nanocomposites/GCE sensor is simple and possesses high reproducibility, where polydopamine can be coated on the surface of MWCNTs–COOH via a simple electropolymerization process. Under optimized conditions, the proposed sensor showed ultrasensitive determination for metronidazole with a wide linear detection range from 5 to 5000 $\mu\text{mol}/\text{dm}^3$ and a low detection limit of 0.25 $\mu\text{mol}/\text{dm}^3$ ($S/N = 3$). Moreover, the proposed sensor has been successfully applied for the quantitative determination of metronidazole in real drug samples. This work may provide a novel and effective analytical platform for determination of metronidazole in application of real pharmaceutical and biological samples analysis.

© 2017 Xi'an Jiaotong University. Production and hosting by Elsevier B.V. This is an open access article under the CC BY-NC-ND license (<http://creativecommons.org/licenses/by-nc-nd/4.0/>).

1. Introduction

Metronidazole, one of nitroimidazole derivative drugs (Fig. 1) well-known for its antimicrobial properties, is effective against trichomonas [1–3], Vincent's organisms [4] and anaerobic bacteria [5–7]. However, overuse and long-term use of metronidazole will cause toxicity [8], peripheral neuropathies [9] and optic neuropathy [10,11]. Therefore, it is necessary to monitor metronidazole concentration in patients under antibiotic therapy. Several analytical methods have been reported for the determination of metronidazole, including spectrophotometry [12,13] and chromatography [14–17]. However, these methods could not realize high selectivity of metronidazole determination, and such determination processes were costly and time consuming. Hence, it is important to develop an alternative method for metronidazole determination with high sensitivity and selectivity.

Nowadays, electrochemical methods have been widely used in environmental analysis and biological samples analysis [18–22]. Particularly, electrochemical sensors and biosensors have been developed for pharmaceutical, food, agricultural and

environmental analyses due to the advantages of fast response and good sensitivity [23–26].

Electrochemical determination based on electrochemical sensor possesses the advantages of high sensitivity low cost and easy operation, which was widely used in analytical chemistry, and separation step is usually used to increase the selectivity prior to the determination [27–29]. Electrochemical sensors fabricated by different modified electrode materials have been developed for electrochemical determination [27,29]. Polydopamine is a conductive and biocompatible polymer, which has versatile applications due to its many attractive properties [30–33]. Polydopamine can be coated on different materials and can be a good support for loading metal nanoparticle to form nanocomposites [34,35], which finally was applied in various electrochemical biosensors [36–39]. Moreover, the polymerization method of dopamine was facile, and its surface morphology and layer thickness can be better controlled [40–42]. Furthermore, polydopamine can be easily coated on the materials surface through a very strong chemical bond [43,44]. Carboxylic multi-walled carbon nanotubes (MWCNTs–COOH) have been widely applied for the development of chemical sensors due to their excellent electrical conductivity, high surface area, remarkable mechanical strength and good chemical stability [45,46].

In this work, we developed a novel electrochemical sensor based on polydopamine/MWCNTs–COOH nanocomposites, where polydopamine can be easily electropolymerized to the surface of

Peer review under responsibility of Xi'an Jiaotong University.

* Corresponding author.

E-mail address: wanglsh@scut.edu.cn (L. Wang).¹ These authors contributed equally to this work.

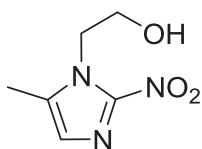


Fig. 1. Chemical structure of metronidazole.

MWCNTs–COOH to form nanocomposites, and finally successfully realized the ultrasensitive determination for metronidazole with a wide linear detection range from 5 to 5000 $\mu\text{mol}/\text{dm}^3$ and a low detection limit of 0.25 $\mu\text{mol}/\text{dm}^3$ ($S/N = 3$). Most importantly, the proposed sensor has been successfully applied for the quantitative determination of metronidazole in real drug samples. This work would provide an effective analytical strategy for metronidazole determination in application of real pharmaceutical and biological samples analysis.

2. Experimental

2.1. Reagents

Metronidazole (99%, analytical grade) was purchased from Macklin Biochemical Co., Ltd. (Shanghai, China). Carboxylic multi-walled carbon nanotubes were purchased from Aladdin Industrial Company (Shanghai, China). Dopamine hydrochloride (98%, analytical grade) was purchased from J&K Chemical (Beijing, China). Drug samples were obtained from Huayueyang Biotechnology Co., Ltd. (Beijing, China). All other reagents were of analytical grade and used without further purification. 0.1 M phosphate buffer solution (PBS) was prepared by mixing NaH_2PO_4 and Na_2HPO_4 , and then adjusted to the required pH values with H_3PO_4 or NaOH solution. All aqueous solutions were prepared with doubly distilled water.

2.2. Fabrication of polydopamine/MWCNTs–COOH nanocomposites/GCE sensor

First, the bare GCE was polished with 0.3 and 0.05 μm of alumina powders, then rinsed ultrasonically with absolute alcohol and distilled water, and finally dried in the nitrogen stream. 5 μL of 0.5 mg/mL MWCNTs–COOH homogeneous suspension was dropped onto the electrode surface and then was dried under the infrared lamp, thus obtaining MWCNTs–COOH/GCE. Finally the polydopamine was electropolymerized onto the surface of MWCNTs–COOH by cyclic voltammetry in 5 mmol/ dm^3 dopamine in 0.1 M PBS (pH = 5) between -0.4 V and $+0.7$ V at a scan rate of

50 mV/s for 10 cycles, thus obtained polydopamine/MWCNTs–COOH nanocomposites/GCE sensor.

2.3. Apparatus and method

Cyclic voltammetry (CV), electrochemical impedance spectroscopy (EIS) and differential pulse voltammetry (DPV) experiments were performed on a CHI 660B electrochemical workstation, purchased from Chenhua Co, Ltd. (Shanghai, China). A conventional three-electrode system was used with a glassy carbon electrode (3 mm diameter) as the working electrode, a saturated calomel reference electrode (SCE) and a Pt wire as the counter electrode. The differential pulse voltammetry scans ranged from -0.4 V to -1.0 V with amplitude of 0.05 V, pulse width of 0.05 s, pulse period of 0.5 s, sampling width of 0.0167, and increment of 0.004 V. For CV, scan rate was 50 mV/s, sample interval was 0.001 V. Electrochemical impedance spectroscopy was obtained in 5 mmol/ dm^3 $\text{K}_3[\text{Fe}(\text{CN})_6]/\text{K}_4[\text{Fe}(\text{CN})_6]$ solution containing 0.1 M KCl under open circuit potential with frequency range from 0.1 Hz to 100 kHz and 5 mV amplitude. The surface morphology was characterized using a field emission scanning electron microscope (FE-SEM; Zeiss Ultra55, Germany).

For the determination of metronidazole, the detection limit (C_m) was obtained using the following equation:

$$C_m = 3S_b/m$$

Where m is the slope of the calibration plot in the linear range, and S_b is the standard deviation of the blank response which was obtained from 20 replicate measurements of the blank PBS buffer solution.

3. Results and discussion

3.1. Characterization of polydopamine/MWCNTs–COOH nanocomposites modified GCE

The SEM images of MWCNTs–COOH/GCE and polydopamine/MWCNTs–COOH nanocomposites/GCE are shown in Fig. 2. The MWCNTs–COOH can be obviously observed in Fig. 2A, when the polydopamine was electropolymerized onto the electrode surface, a rough polymer film could be obviously observed on the surface of MWCNTs–COOH, indicating the successful preparation of polydopamine/MWCNTs–COOH nanocomposites/GCE sensor (Fig. 2B).

Fig. 3A shows cyclic voltammograms of bare GCE, MWCNTs–COOH/GCE and polydopamine/MWCNTs–COOH nanocomposites/GCE in the presence of 5 mmol/ dm^3 $\text{K}_3\text{Fe}(\text{CN})_6/\text{K}_4[\text{Fe}(\text{CN})_6]$ solution containing 0.1 M KCl. A pair of reversible oxidation and reduction peaks were observed at 0.26 and 0.17 V, respectively, for the bare GCE (curve a). After being modified with the MWCNTs–COOH (curve b), it showed obvious increased redox peak currents because MWCNTs–COOH can dramatically increase the electrode

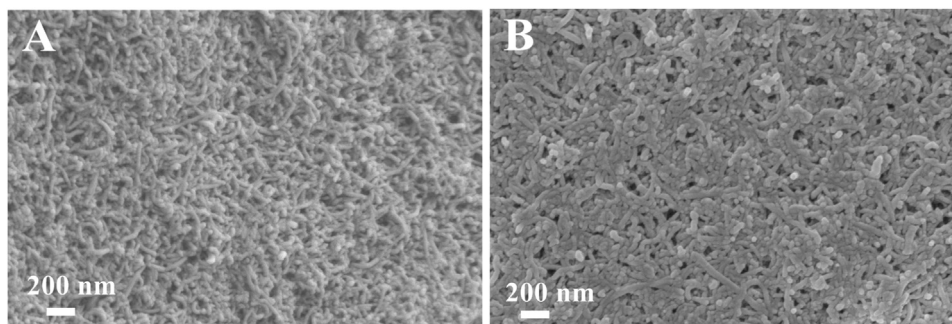


Fig. 2. SEM images of (A) MWCNTs–COOH/GCE and (B) polydopamine/MWCNTs–COOH nanocomposites/GCE.

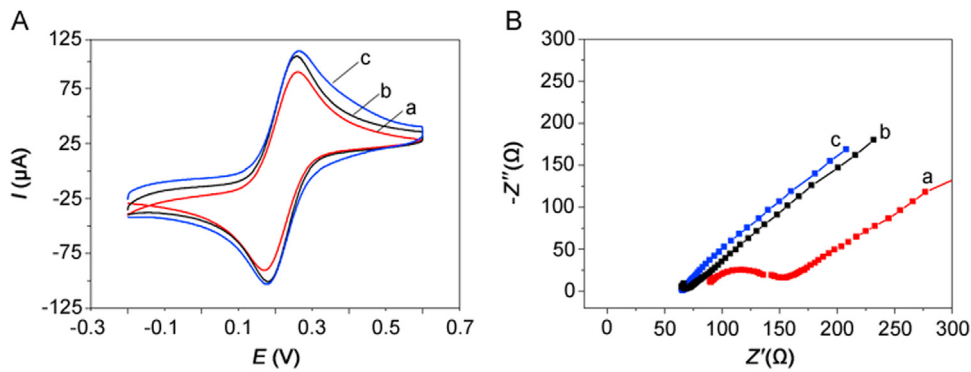


Fig. 3. (A) Cyclic voltammograms and (B) Electrochemical impedance spectroscopy obtained at (a) bare GCE, (b) MWCNTs–COOH/GCE and (c) polydopamine/MWCNTs–COOH nanocomposites/GCE in 5 mmol/dm^3 $\text{K}_3[\text{Fe}(\text{CN})_6]/\text{K}_4[\text{Fe}(\text{CN})_6]$ solution containing 0.1 M KCl.

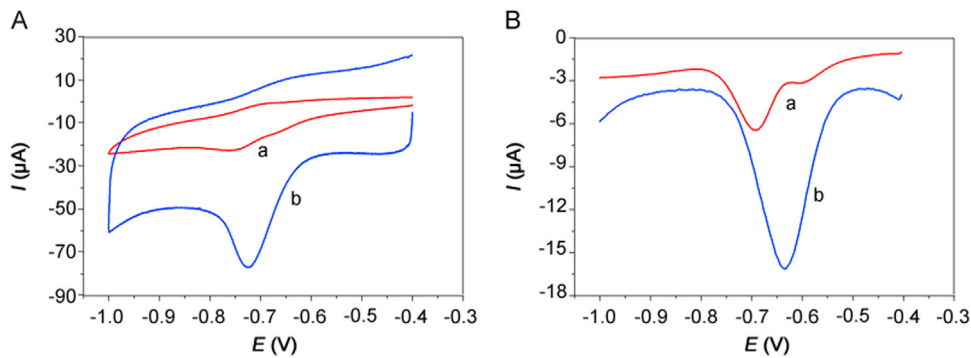


Fig. 4. (A) CVs and (B) DPVs of 500 µmol/dm^3 metronidazole in 0.1 M PBS ($\text{pH} = 10$) buffer solution at (a) bare GCE and (b) polydopamine/MWCNTs–COOH nanocomposites/GCE.

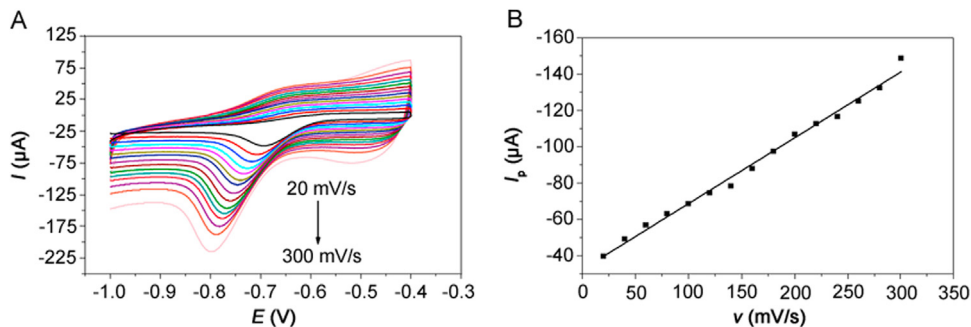


Fig. 5. (A) CVs of 500 µmol/dm^3 metronidazole at the polydopamine/MWCNTs–COOH nanocomposites/GCE in 0.1 M PBS ($\text{pH} = 10$) buffer solution at different scan rates. (B) The relationship between the reduction peak currents and scan rates.

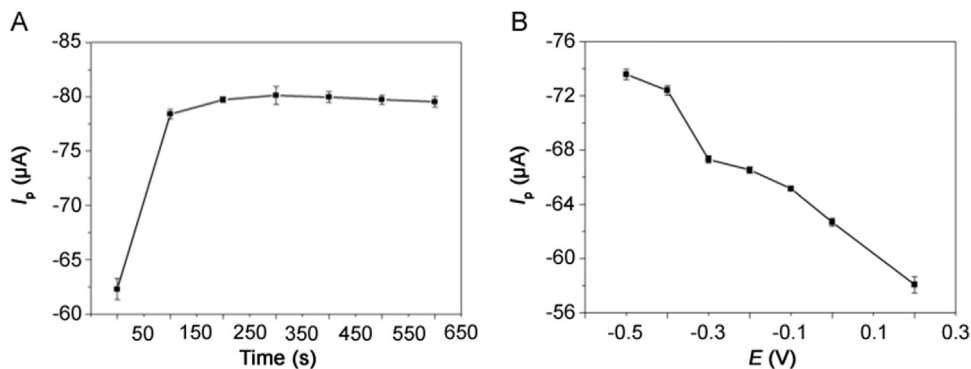


Fig. 6. The effect of (A) accumulation time and (B) accumulation potential on the reduction peak current of 500 µmol/dm^3 metronidazole in 0.1 M PBS ($\text{pH} = 10$) buffer solution at the polydopamine/MWCNTs–COOH nanocomposites/GCE.

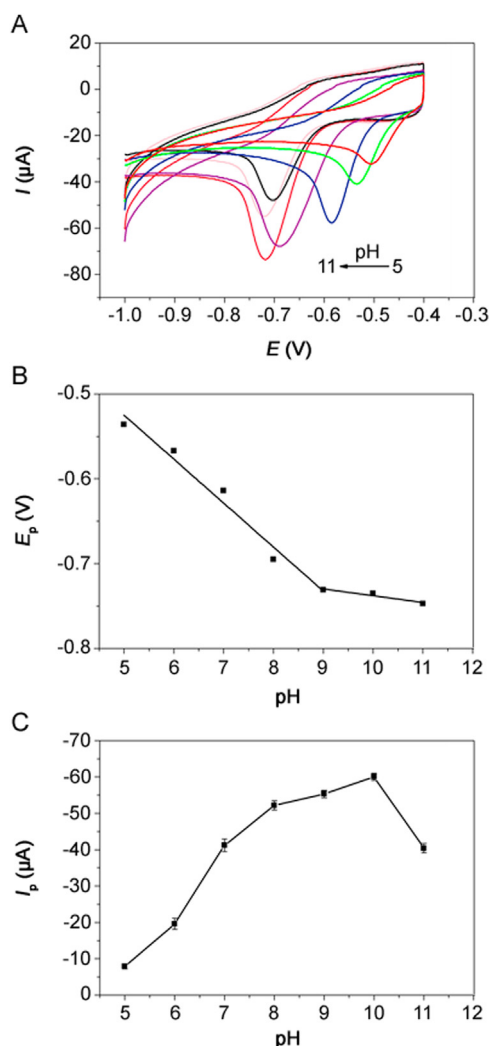


Fig. 7. (A) CVs of 500 $\mu\text{mol}/\text{dm}^3$ metronidazole in 0.1 M PBS (pH = 10) buffer solution at different pH values at the polydopamine/MWCNTs–COOH nanocomposites/GCE. The relationship of (B) reduction peak potentials vs. pH values and (C) reduction peak currents vs. pH values.

surface area and possesses good electrical conductivity [47]. Moreover, the polydopamine/MWCNTs–COOH nanocomposites/GCE (curve c) showed further enhanced redox peak currents compared with MWCNTs–COOH/GCE because polydopamine can accelerate the electron transfer efficiency between the electrode surface and solution.

Electrochemical impedance spectroscopy (EIS) is a powerful tool for studying the surface-modified electrode. Fig. 3B shows the EIS plots of bare GCE, MWCNTs–COOH/GCE, polydopamine/MWCNTs–COOH nanocomposites/GCE at 5 mmol/dm³ K₃[Fe(CN)₆]/K₄[Fe(CN)₆] in 0.1 M KCl. The bare GCE (curve a) possesses a small resistance. When MWCNTs–COOH was modified onto the bare GCE surface (curve b), it displayed a straight line in the Nyquist plot because the resistance was significantly decreased. Moreover, the polydopamine/MWCNTs–COOH nanocomposites/GCE (curve c) also displayed a straight line in the Nyquist plot, which almost showed the resistance same as MWCNTs–COOH/GCE, because polydopamine/MWCNTs–COOH nanocomposites also possess excellent electron transfer efficiency. Therefore, both the CV and EIS plots proved the successful preparation of polydopamine/MWCNTs–COOH nanocomposites/GCE sensor.

3.2. Electrochemical behavior of metronidazole at the polydopamine/MWCNTs–COOH nanocomposites/GCE sensor

The electrochemical behavior of bare GCE and polydopamine/MWCNTs–COOH nanocomposites/GCE for determination of 500 $\mu\text{mol}/\text{dm}^3$ metronidazole in 0.1 M PBS (pH 10.0) buffer solution is shown in Fig. 4A. The reduction peak current and peak potential of metronidazole at the bare GCE (curve a) were $I_p = -8.44 \mu\text{A}$ and $E_p = -0.749 \text{ V}$. However, compared to the bare GCE, the polydopamine/MWCNTs–COOH nanocomposites/GCE (curve b) exhibited significantly increased reduction peak current ($I_p = -41.12 \mu\text{A}$) and significantly increased reduction peak potential ($E_p = -0.721 \text{ V}$) of metronidazole. The significantly increased reduction peak potential and significantly increased reduction peak current both confirmed the polydopamine/MWCNTs–COOH nanocomposites possess strong catalytic activity towards the reduction of metronidazole. Moreover, the DPVs results in Fig. 4B correspond with the CVs in Fig. 4A. Therefore, the polydopamine/MWCNTs–COOH nanocomposites/GCE sensor can be successfully utilized for the determination of metronidazole.

3.3. The effect of scan rate

The CVs of polydopamine/MWCNTs–COOH nanocomposites/GCE in 500 $\mu\text{mol}/\text{dm}^3$ metronidazole at different scan rates are shown in Fig. 5A, where the reduction peak currents showed linearity with the scan rates. And the linear regression equation can be expressed as $I_p(\mu\text{A}) = -0.363v(\text{mV}/\text{s}) - 32.399$ ($R = -0.9914$) in Fig. 5B, indicating that the reduction of the metronidazole is a typical adsorption controlled process. Therefore, it is necessary to study the effect of accumulation time and accumulation potential in order to obtain more sensitive determination for metronidazole.

3.4. The effect of accumulation time and accumulation potential

The effect of accumulation time and accumulation potential for the determination of metronidazole was studied by DPVs in Fig. 6. As shown in Fig. 6A, at the accumulation potential of -0.5 V , the reduction peak current increased gradually with the accumulation time and reached the maximum value when the accumulation time was 200 s. However, the reduction peak current almost remained the same after 200 s due to the saturation of surface active catalytic sites of polydopamine/MWCNTs–COOH nanocomposites/GCE. Thus, the optimal accumulation time of 200 s was employed in our experiments. With the optimal accumulation time determined above, we further studied the effect of accumulation potential on reduction peak current of metronidazole. As shown in Fig. 6B, the reduction peak current decreased gradually with the increase of accumulation potential; therefore, the accumulation potential was chosen at -0.5 V for determination of metronidazole in our later experiments.

3.5. The pH effect

The effect of pH value on the electrochemical response of 500 $\mu\text{mol}/\text{dm}^3$ metronidazole in 0.1 M PBS with pH value ranging from 5.0 to 11.0 at the polydopamine/MWCNTs–COOH nanocomposites/GCE was investigated by CV (Fig. 7A). The reduction peak potentials showed linearity with pH values ranging from 5.0–9.0 and 9.0–11.0, with the linear regression equations of $E_p = -0.0518\text{pH} - 0.266$ ($R = -0.9687$) and $E_p = -0.008\text{pH} - 0.658$ ($R = -0.9462$), respectively (Fig. 7B), indicating two different reaction mechanisms of metronidazole. According to previous reports [39,48], the reaction mechanisms of metronidazole are listed below:

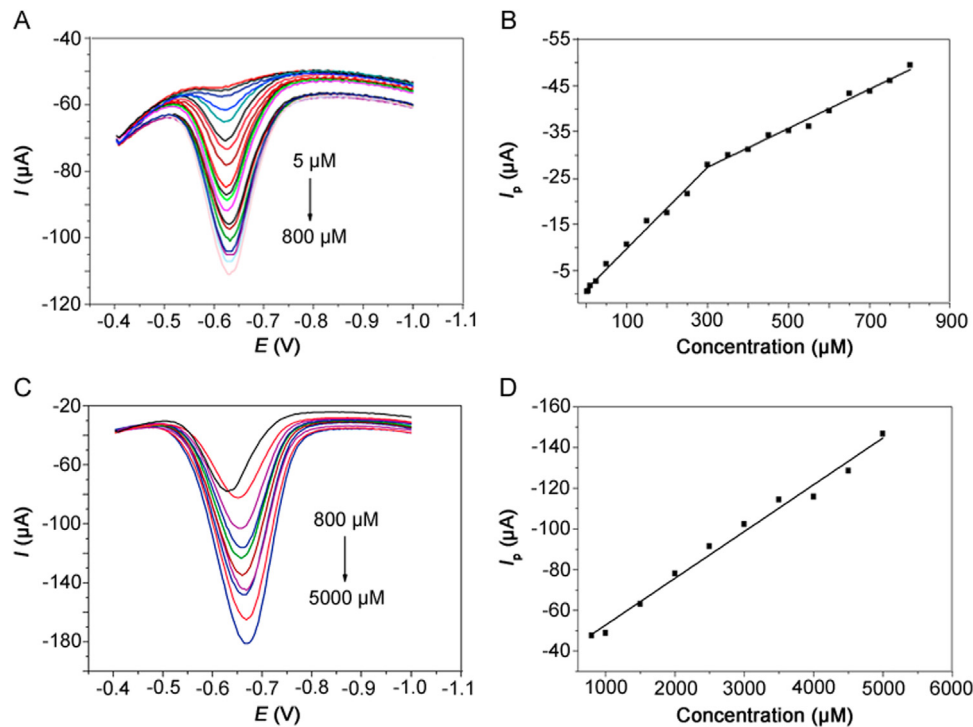
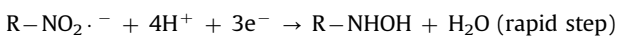
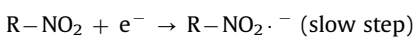


Fig. 8. DPVs of metronidazole at (A) 5–800 $\mu\text{mol}/\text{dm}^3$ and (C) 800–5000 $\mu\text{mol}/\text{dm}^3$ in 0.1 M PBS (pH = 10) buffer solution at the polydopamine/MWCNTs–COOH nanocomposites/GCE. Linear relationships between reduction peak currents and concentrations at (B) 5–800 $\mu\text{mol}/\text{dm}^3$ and (D) 800–5000 $\mu\text{mol}/\text{dm}^3$.

Table 1
Linear regression equations of metronidazole under different concentration ranges.

Equation	Concentration range (μM)	Linear regression equation	R
1	5–300	$I_p(\mu\text{A}) = -0.08837c (\mu\text{M}) - 0.91$	$R = -0.9881$
2	300–800	$I_p(\mu\text{A}) = -0.0423c (\mu\text{M}) - 14.71$	$R = -0.9842$
3	800–5000	$I_p(\mu\text{A}) = -0.02298c (\mu\text{M}) - 29.78$	$R = -0.9813$

In pH values of 5.0–9.0:



In pH values of 9.0–11.0:

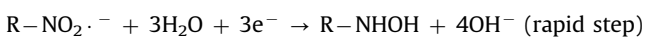


Table 2
Comparison of performances of the polydopamine/MWCNTs–COOH nanocomposites/GCE with other modified electrodes.

Electrode	Detection limit/ $(\mu\text{mol}/\text{dm}^3)$	Linear range/ $(\mu\text{mol}/\text{dm}^3)$	Ref.
P-AgSA-CE	0.6	2–100	[49]
Carbon fiber microdisk electrode	0.5	1–22	[50]
Carbon nanotubes/GCE	0.063	0.1–200	[51]
DNA/GCE	1	1.0–54.3	[52]
Activated GCE	1.1	2–600	[53]
Graphene-ionic liquid/GCE	0.047	0.1–25	[54]
Cu-poly(Cys)/GCE	0.37	0.5–400	[55]
Polydopamine/MWCNTs–COOH nanocomposites/GCE	0.25	5–5000	This work

Moreover, as shown in Fig. 7C, because the reduction peak current achieved the maximum value in pH = 10.0, the pH value of 10.0 was chosen as the best pH value for the determination of metronidazole.

3.6. The quantitative determination of metronidazole

The quantitative determination of metronidazole at the polydopamine/MWCNTs–COOH nanocomposites/GCE was achieved by DPV under optimal conditions addressed above. As shown in Fig. 8, the reduction peak currents of metronidazole at the polydopamine/MWCNTs–COOH nanocomposites/GCE increased linearly with concentration ranges of 5–300 $\mu\text{mol}/\text{dm}^3$, 300–800 $\mu\text{mol}/\text{dm}^3$ and 800–5000 $\mu\text{mol}/\text{dm}^3$, and their corresponding linear regression equations are listed in Table 1.

The detection limit of metronidazole was determined to be 0.25 $\mu\text{mol}/\text{dm}^3$ (S/N = 3). Moreover, compared with recently most reported electrochemical sensors [49–55] for determination of metronidazole, our proposed nanocomposites sensor could finish the ultrasensitive determination of metronidazole with a much wider linear ranges and a much lower detection limits (Table 2).

Table 3

Practical determination of metronidazole in real drug samples ($n = 3$). (Sample responses are expressed as a confidence interval of 95% probability).

Sample	Added ($\mu\text{mol}/\text{dm}^3$)	Founded ($\mu\text{mol}/\text{dm}^3$)	Recovery (%)	RSD (%)
1	20	23.66 \pm 1.86	118.3	3.2
2	50	55.70 \pm 3.97	110.1	2.9
3	200	206.64 \pm 3.21	103.3	0.6
4	300	291.39 \pm 3.84	93.4	0.6
5	500	506.70 \pm 2.35	104.9	0.2

3.7. Selectivity, stability and reproducibility of the polydopamine/MWCNTs–COOH nanocomposites/GCE sensor

Selectivity, stability and reproducibility of the proposed sensors are key factors for their practical application. The proposed sensor was not affected by additions of 100-fold concentrations of various inorganic ions (K^+ , Mg^{2+} , Zn^{2+} , Na^+ , Ca^{2+} , PO_4^{3-} , SO_4^{2-} , F^- , CO_3^{2-} , NO_3^- and Cl^- , signal change below 3%) and 10-fold concentrations of some organic compounds (oxalic acid, ascorbic acid, glucose, citric acid, cystine, alanine and tartaric acid, signal change below 6%). This results suggested that the proposed sensor possesses excellent selectivity for the determination of metronidazole. After the prepared electrode was stored at 4 °C in a refrigerator for 1 month, the reduction peak current of metronidazole remained 95.2% of its initial value, indicating that the proposed sensor possesses good stability. Moreover, four modified electrodes were fabricated to estimate the sensor's reproducibility, and the relative standard deviation (RSD) of detection measurements was calculated to be 2.5% for metronidazole, suggesting that the proposed sensor possesses high reproducibility. Therefore, the polydopamine/MWCNTs–COOH nanocomposites/GCE sensor is promising for determination of metronidazole with excellent selectivity, stability and reproducibility.

3.8. Real samples determination

The practical analytical application of the polydopamine/MWCNTs–COOH nanocomposites/GCE sensor was evaluated by determination of metronidazole in real drug samples by standard-addition technique. Three parallel experiments were performed on all measurements. As shown in Table 3, the recovery of the real samples ranged between 93.4% and 118.3%, and the RSD values were less than 4%, indicating that the our proposed sensor can be successfully applied for the practical determination of metronidazole in real samples.

4. Conclusions

In summary, we successfully develop an ultrasensitive electrochemical sensor for metronidazole determination, which was based on polydopamine/MWCNTs–COOH nanocomposites. Moreover, the fabrication of polydopamine/MWCNTs–COOH nanocomposites/GCE sensor was simple, where polydopamine can coat on the surface of MWCNTs–COOH via a simple electropolymerization process. Under optimized conditions, the proposed sensor showed wider linear detection range from 5 to 5000 $\mu\text{mol}/\text{dm}^3$ and a low detection limit of 0.25 $\mu\text{mol}/\text{dm}^3$ ($S/N = 3$) for metronidazole, and was successfully applied for the practical determination of metronidazole in real drug samples. The proposed sensor shows broad potential in application of real pharmaceutical and biological samples analysis.

Conflicts of interest

The authors declare that there are no conflicts of interest.

Acknowledgments

This work was financially supported by the National Natural Science Foundation of China (Grant Nos. 21475046, 21427809).

References

- [1] N.C. Desai, A.S. Maheta, K.M. Rajpara, et al., Green synthesis of novel quinolone based imidazole derivatives and evaluation of their antimicrobial activity, *J. Saudi Chem. Soc.* 18 (2014) 963–971.
- [2] A.M. Jarrad, T. Karoli, A. Debnath, et al., Metronidazole–triazole conjugates: activity against *Clostridium difficile* and parasites, *Eur. J. Med. Chem.* 101 (2015) 96–102.
- [3] L.A. Dunn, K.T. Andrews, J.S. McCarthy, et al., The activity of protease inhibitors against *Giardia duodenalis* and metronidazole-resistant *Trichomonas vaginalis*, *Int. J. Antimicrob. Agents* 29 (2007) 98–102.
- [4] A.H. Davies, J.A. Mafadzean, S. Squires, Treatment of Vincent's stomatitis with metronidazole, *Br. Med. J.* 5391 (1964) 1149–1150.
- [5] N. Dione, S. Khelafifa, J.C. Lagier, et al., The aerobic activity of metronidazole against anaerobic bacteria, *Int. J. Antimicrob. Agents* 45 (2015) 537–540.
- [6] A. Katsandri, A. Avlami, A. Pantazatou, et al., In vitro activities of Tigecycline against recently isolated Gram-negative anaerobic bacteria in Greece, including metronidazole-resistant strains, *Diagn. Microbiol. Infect. Dis.* 55 (2006) 231–236.
- [7] A.V. Scorza, M.R. Lappin, Metronidazole for the treatment of feline giardiasis, *J. Feline Med. Surg.* 6 (2004) 157–160.
- [8] M.W. Carroll, D. Jeon, J.M. Mountz, et al., Efficacy and safety of metronidazole for pulmonary multidrug-resistant tuberculosis, *J. Antimicrob. Agents Chemother.* 57 (2013) 3903–3909.
- [9] A. Etxeberria, S. Lonneville, M.P. Rutgers, et al., Metronidazole-cerebellopathy associated with peripheral neuropathy, downbeat nystagmus and bilateral ocular abduction deficit, *Rev. Neurol.* 168 (2012) 193–195.
- [10] N.M. McGrath, B. Kent-Smith, D.M. Sharp, Reversible optic neuropathy due to metronidazole, *Clin. Exp. Ophthalmol.* 35 (2007) 585–586.
- [11] M.P. Prabhakaran, M. Zamani, B. Felice, et al., Electrospaying technique for the fabrication of metronidazole contained PLGA particles and their release profile, *Mater. Sci. Eng. C* 56 (2015) 66–73.
- [12] A.K. Mishra, A. Kumar, A. Mishra, et al., Development of ultraviolet spectroscopic method for the estimation of metronidazole benzoate from pharmaceutical formulation, *J. Nat. Sci. Biol. Med.* 5 (2014) 261–264.
- [13] G.O. El-Sayed, Polarographic determination of metronidazole in pharmaceutical formulations and urine, *Microchem. J.* 55 (1997) 110–114.
- [14] W. Tian, L. Gao, Y. Zhao, et al., Simultaneous determination of metronidazole, chloramphenicol and 10 sulfonamide residues in honey by LC–MS/MS, *Anal. Methods* 5 (2013) 1283–1288.
- [15] C. Ho, D.W.M. Sin, K.M. Wong, et al., Determination of dimetridazole and metronidazole in poultry and porcine tissues by gas chromatography–electron capture negative ionization mass spectrometry, *Anal. Chim. Acta* 530 (2005) 23–31.
- [16] H.M. Maher, R.M. Youssef, R.H. Khalil, et al., Simultaneous multi residue determination of metronidazole and spiramycin in fish muscle using high performance liquid chromatography with UV detection, *J. Chromatogr. B* 876 (2008) 175–181.
- [17] J. Li, Y.B. Wang, L. Wu, et al., Fabrication of multi-walled carbon nanotubes/oxide reinforced hollow fibers by sol–gel technique for rapid determination of metronidazole in milk, *Anal. Methods* 6 (2014) 1401–1411.
- [18] M.M. Ardakani, H. Beitollahi, Z. Taleat, et al., Selective voltammetric determination of D-penicillamine in the presence of tryptophan at a modified carbon paste electrode incorporating TiO_2 nanoparticles and quinizarine, *J. Electroanal. Chem.* 644 (2010) 1–6.
- [19] M.M. Ardakani, Z. Taleat, H. Beitollahi, et al., Electrocatalytic oxidation and nanomolar determination of guanine at the surface of a molybdenum (VI) complex- TiO_2 nanoparticle modified carbon paste electrode, *J. Electroanal. Chem.* 624 (2008) 73–78.
- [20] S. Tajika, M.A. Taher, H. Beitollahi, Simultaneous determination of dioxidopa and carbidopa using a carbon nanotubes paste electrode, *Sens. Actuators B Chem.* 188 (2013) 923–930.
- [21] V. Vyskocil, J. Barek, Polarographic and voltammetric study of genotoxic 2,7-dinitrofluoren-9-one and its determination using mercury electrodes, *Collect. Czech Chem. C* 74 (2009) 1675–1696.
- [22] O. Yosypchuk, J. Barek, V. Vyskocil, Voltammetric determination of carcinogenic derivatives of pyrene using a boron-doped diamond film electrode, *Anal. Lett.* 45 (2012) 449–459.
- [23] H. Beitollahi, H.K. Maleh, H. Khabazzadeh, Nanomolar and selective determination of epinephrine in the presence of norepinephrine using carbon paste electrode modified with carbon nanotubes and novel 2-(4-Oxo-3-phenyl-3,4-dihydro-quinazolinyl)-N-phenyl-hydrazinecarbothioamide, *Anal. Chem.* 80 (2008) 9848–9851.
- [24] H. Beitollahi, M.M. Ardakani, H. Naemi, et al., Electrochemical characterization of 2', 2'-[1,2-ethanediyldis (nitriolethylidene)]-bis-hydroquinone-carbon nanotube paste electrode and its application to simultaneous voltammetric

- determination of ascorbic acid and uric acid, *J. Solid State Electrochem.* 13 (2009) 353–363.
- [25] M.M. Ardakani, H. Beitollahi, M.K. Amini, et al., Simultaneous determination of epinephrine and uric acid at a gold electrode modified by a 2-(2,3-dihydroxy phenyl)-1,3-dithiane self-assembled monolayer, *J. Electroanal. Chem.* 651 (2011) 243–249.
- [26] M. Baghayeri, M. Namadchian, H.K. Maleh, et al., Determination of nifedipine using nanostructured electrochemical sensor based on simple synthesis of Ag nanoparticles at the surface of glassy carbon electrode: application to the analysis of some real samples, *J. Electroanal. Chem.* 697 (2013) 53–59.
- [27] V. Vyskocil, J. Barek, Mercury electrodes-possibilities and limitations in environmental electroanalysis, *Crit. Rev. Anal. Chem.* 39 (2009) 173–188.
- [28] V. Vyskocil, J. Barek, Electroanalysis of nitro and amino derivatives of polycyclic aromatic hydrocarbons, *Curr. Org. Chem.* 15 (2011) 3059–3076.
- [29] J. Gajdar, E. Horakova, J. Barek, et al., Recent applications of mercury electrodes for monitoring of pesticides: a critical review, *Electroanalysis* 28 (2016) 2659–2671.
- [30] M.L. Lyng, R. van der Westen, A. Posta, et al., Polydopamine a nature-inspired polymer coating for bilchemical science, *Nanoscale* 3 (2011) 4916–4928.
- [31] Y. Li, Y. Su, X. Zhao, et al., Antifouling, high-flux nanofiltration membranes enabled by dual functional polydopamine, *ACS Appl. Mater. Interfaces* 6 (2014) 5548–5557.
- [32] C. Wang, J. Zhou, P. Wang, et al., Robust nanoparticle-DNA conjugates based on mussel-inspired polydopamine coating for cell imaging and tailored self-assembly, *Bioconjug. Chem.* 27 (2016) 815–823.
- [33] Q. Liu, N. Wang, J. Caro, et al., Bio-inspired polydopamine: a versatile and powerful platform for covalent synthesis of molecular sieve membranes, *J. Am. Chem. Soc.* 135 (2013) 17679–17682.
- [34] J. Ryu, S.H. Ku, H. Lee, et al., Mussel-inspired polydopamine coating as a universal route to hydroxyapatite crystallization, *Adv. Funct. Mater.* 20 (2010) 2132–2139.
- [35] W. Zhang, Y. Tang, J. Liu, et al., An electrochemical sensor for detecting triglyceride based on biomimetic polydopamine and gold nanocomposite, *J. Mater. Chem. B* 2 (2014) 8490–8495.
- [36] M. Amiri, E. Amali, A. Nematollahzadeh, et al., Poly-dopamine films: voltammetric sensor for pH monitoring, *Sens. Actuators B-Chem.* 228 (2016) 53–58.
- [37] M. Amiri, E. Amali, A. Nematollahzadeh, Poly-dopamine thin film for voltammetric sensing of atenolol, *Sens. Actuators B-Chem.* 216 (2015) 551–557.
- [38] L. Zheng, L. Xiong, Y. Li, et al., Facile preparation of polydopamine-reduced graphene oxide nanocomposite and its electrochemical application in simultaneous determination of hydroquinone and catechol, *Sens. Actuators B-Chem.* 177 (2013) 344–349.
- [39] H.B. Ammar, M.B. Brahim, R. Abdelhedi, et al., Boron doped diamond sensor for sensitive determination of metronidazole: mechanistic and analytical study by cyclic voltammetry and square wave voltammetry, *Mater. Sci. Eng. C* 59 (2016) 604–610.
- [40] J.Z. Huang, X.L. Shen, R.L. Wang, et al., A highly sensitive metronidazole sensor based on a Pt nanospheres/polyfurfural film modified electrode, *RSC Adv.* 7 (2017) 535–542.
- [41] E.L. Ciolkowski, B.R. Cooper, J.A. Jankowski, et al., Direct observation of epinephrine and norepinephrine cosecretion from individual adrenal medullary chromaffin cells, *J. Am. Chem. Soc.* 114 (1992) 2815–2821.
- [42] E.L. Ciolkowski, K.M. Maness, P.S. Cahill, et al., Disproportionation during electrooxidation of catecholamines at carbon-fiber microelectrodes, *Anal. Chem.* 66 (1994) 3611–3617.
- [43] Y.S. Choi, H. Kang, D.G. Kim, et al., Mussel-inspired dopamine- and plant-based cardanol-containing polymer coatings for multifunctional filtration membranes, *ACS Appl. Mater. Interfaces* 6 (2014) 21297–21307.
- [44] H. Lee, S.M. Dellatore, W.M. Miller, et al., Mussel-inspired surface chemistry for multifunctional coatings, *Science* 318 (2007) 426–430.
- [45] D. Eder, Carbon nanotube-inorganic hybrids, *Chem. Rev.* 110 (2010) 1348–1385.
- [46] H. Beitollahi, S. Mohammadi, Selective voltammetric determination of norepinephrine in the presence of acetaminophen and tryptophan on the surface of a modified carbon nanotube paste electrode, *Mater. Sci. Eng. C* 33 (2013) 3214–3219.
- [47] J.Z. Huang, S.L. Bai, G.Q. Yue, et al., Coordination matrix/signal amplifier strategy for simultaneous electrochemical determination of cadmium (II), lead (II), copper (II), and mercury (II) ions based on polyfurfural film/multi-walled carbon nanotube modified electrode, *RSC Adv.* 7 (2017) 28556–28563.
- [48] A. Hajkova, J. Hranicek, J. Barek, et al., Voltammetric determination of trace amounts of 2-aminofluoren-9-one at a mercury meniscus modified silver solid amalgam electrode, *Electroanalysis* 25 (2013) 295–302.
- [49] V. Vyskocil, T. Navratil, A. Danhel, et al., Voltammetric determination of selected nitro compounds at a polished silver solid amalgam composite electrode, *Electroanalysis* 23 (2011) 129–139.
- [50] P. Bartlett, E. Ghoneim, G. El-Hefnawy, et al., Voltammetry and determination of metronidazole at a carbon fiber microdisk electrode, *Talanta* 66 (2005) 869–874.
- [51] A. Salimi, M. Izadi, R. Hallaj, et al., Simultaneous determination of ranitidine and metronidazole at glassy carbon electrode modified with single wall carbon nanotubes, *Electroanalysis* 19 (2007) 1668–1676.
- [52] A.M. Brett, S.H. Serrano, I.G. Gutz, et al., Comparison of the voltammetric behavior of metronidazole at a DNA-modified glassy carbon electrode, a mercury thin film electrode and a glassy carbon electrode, *Electroanalysis* 9 (1997) 110–114.
- [53] S.A. Özkan, Y. Özkan, Z. Şentürk, Electrochemical reduction of metronidazole at activated glassy carbon electrode and its determination in pharmaceutical dosage forms, *J. Pharm. Biomed. Anal.* 17 (1998) 299–305.
- [54] J. Peng, C. Hou, X. Hu, Determination of metronidazole in pharmaceutical dosage forms based on reduction at graphene and ionic liquid composite film modified electrode, *Sens. Actuators B-Chem.* 169 (2012) 81–87.
- [55] Y. Gu, X.Y. Yan, W.L. Liu, et al., Biomimetic sensor based on copper-poly(cysteine) film for the determination of metronidazole, *Electrochim. Acta* 152 (2015) 108–116.



Original Research Article

Eco-friendly reduced graphene oxide for the determination of mycophenolate mofetil in pharmaceutical formulations

Prashanth S. Narayan^a, Nagappa L. Teradal^a, Seetharamappa Jaldappagari^{a,*}, Ashis K. Satpati^b^a Department of Chemistry, Karnatak University, Dharwad 580003, India^b Analytical Chemistry Division, Bhabha Atomic Research Centre, Trombay, Mumbai 400085, India

ARTICLE INFO

Article history:

Received 21 April 2017

Received in revised form

21 November 2017

Accepted 4 December 2017

Available online 8 December 2017

Keywords:

Mycophenolate mofetil

Electroreduced graphene oxide

Electrochemical sensor

Analytical application

ABSTRACT

Graphene oxide (GO) was synthesized and characterized by scanning electron microscopy (SEM), energy dispersive X-ray spectroscopy (EDX), atomic force microscopy (AFM), X-ray diffraction (XRD), Fourier transform-infrared spectroscopy (FT-IR) and thermogravimetric analysis (TGA). GO was then electrochemically reduced and used for electrochemical study of mycophenolate mofetil (MMF). The electrochemically reduced graphene oxide (ERGO) film on glassy carbon electrode (GCE) showed enhanced peak current for electrooxidation of MMF. MMF exhibited two irreversible oxidation peaks at 0.84 V (peak a₁) and 1.1 V (peak a₂). Effects of accumulation time, pH and scan rate were studied and various electrochemical parameters were calculated. A differential pulse voltammetric method was developed for the determination of MMF in bulk samples and pharmaceutical formulations. Linear relationship was observed between the peak current and concentration of MMF in the range of 40 nM–15 μM with a limit of detection of 11.3 nM. The proposed method is simple, sensitive and inexpensive and, hence, could be readily adopted in clinical and quality control laboratories.

© 2018 Xi'an Jiaotong University. Production and hosting by Elsevier B.V. This is an open access article under the CC BY-NC-ND license (<http://creativecommons.org/licenses/by-nc-nd/4.0/>).

1. Introduction

Graphene, a one-atom-thick sp²-bonded carbon sheet, has attracted the attention of scientific and technological researchers since its discovery in 2004 because of its unique properties such as high surface area, excellent electrical conductivity and high mechanical strength [1]. Compared to carbon nanotubes, graphene has the advantages of high conductivity, ease of production and function, good biocompatibility and abundance of inexpensive source material [2]. It possesses high potentials for fabricating transparent electrodes, electrochemical sensors, field effect transistors, nanocomposites, and microelectrical devices [3–6]. These properties make it a good candidate for the fabrication of inexpensive electrochemical sensors and biosensors [2,7–9].

Graphene oxide (GO) is an insulator with a large band gap and band structure that depends on stoichiometry [10,11]. It is reported that GO could be reduced by chemical reduction using reducing agents viz., hydrazine, hydroquinone, and sodium borohydride. Electrochemical methods are effective in modifying electronic states by adjusting the external power source to alter

the Fermi energy level of electrode materials. In view of this, we have adopted a green method for the reduction of graphene oxide and developed an electrochemical sensor for an immunosuppressant, mycophenolate mofetil (MMF).

MMF, chemically known as 2-morpholin-4-ylethyl (E)-6-(4-hydroxy-6-methoxy-7-methyl-3-oxo-1H-2-benzofuran-5-yl)-4-methylhex-4-enoate, is a morpholinoethyl derivative of mycophenolic acid (MPA). MPA, a fermentation product of several *Penicillium* species, is a potent, noncompetitive, and reversible inhibitor of eukaryotic inosine monophosphate (IMP) dehydrogenase. MPA thus inhibits the synthesis of guanosine monophosphate. This enzyme (IMP dehydrogenase) plays an important role in the purine metabolism of lymphocytes [12,13]. It is used in the prophylaxis of graft rejection in kidney [14], heart [15], and liver transplantation [16]. It is also used following lung [17], pancreas [18] or intestine transplantation [19]. Due to its clinical advantages, several formulations of MMF are available in the market.

Recently, we have reported the electrochemical oxidation and determination of MMF in bulk sample and formulations at bare glassy carbon electrode (GCE) [20]. In order to improve the detection limits of the electrochemical method for the assay of MMF at nano molar level, we have fabricated an electrochemical sensor based on electroreduced graphene oxide (ERGO) film on GCE.

Peer review under responsibility of Xi'an Jiaotong University.

* Corresponding author.

E-mail address: jseetharam97@gmail.com (S. Jaldappagari).

2. Experimental

2.1. Apparatus

Electrochemical investigations were carried out on a CHI-1110a Electrochemical Analyzer (CH Instruments Ltd. Co., USA, version 12.23). GCE (3 mm diameter)/ERGO-GCE and saturated calomel electrode (SCE) were used as working and reference electrodes, respectively. For reproducible results, improved detection limits and good resolution of voltammetric peaks, the working electrode was polished with 1.0, 0.3 and 0.05 μm alumina powder on a polishing cloth. Then, it was thoroughly rinsed with ultrapure water from millipore system. All the reported potentials were against SCE. Thermogram was recorded on a SDT Q 600 TG analyzer and FT-IR spectra were recorded on a Nicolet-5700 FT-IR spectrometer (Waltham, MA, USA).

A Shimadzu Maxima-7000 X-ray diffractometer with $\text{Cu K}\alpha$ radiation ($\lambda = 1.5406 \text{ \AA}$) was used for recording powder X-ray diffraction (XRD). Scanning electron micrographs (SEM) were recorded on a Hitachi S-3400 (Japan) scanning electron microscope with an accelerating voltage of 15 kV. Composition analyses of samples were carried out on a Hitachi S-3400 SEM (Japan) coupled with a Thermo Scientific energy dispersive spectroscopic (EDS) detector at an accelerating voltage of 15 kV and a magnification of $\times 2 \text{ K}$. Atomic force micrographs (AFM) were taken on a Multi-Mode Nanosurf easy scan atomic force microscope (Nanosurf, Switzerland). Commercially available AFM cantilever tips (Tap190Al-G) with a force constant of 48 N/m and resonance vibration frequency of $\sim 160 \text{ kHz}$ were used.

2.2. Reagents

Graphite powder was obtained from Sigma-Aldrich ($< 20 \mu\text{m}$). Pure MMF was a gratis sample from Dr. Reddy's Laboratories at Hyderabad, India. Tablets of MMF were obtained from commercial sources. A stock solution of MMF (0.5 mM) was prepared in a mixture of water and methanol (1:1, v/v) and stored in a refrigerator at 4 °C. In the present study, phosphate buffer solutions of pH 3.0–10.6 were used. All aqueous solutions were prepared in ultrapure water from Millipore water system (Purelab Classic Corp., USA) and the chemicals used were of analytical reagent grade. Tablet containing 500 mg of MMF (Panacea Biotec Ltd., India) was purchased commercially from the local market.

2.3. SEM/EDX

Films for SEM and EDX analysis were prepared by placing the sample suspension on a carbon film coated on a sample holder and then drying at room temperature.

2.4. Preparation of GO

GO was prepared from graphite powder (Sigma-Aldrich) by Hummers method and then dried in the oven at 120 °C [21]. The GO suspension was prepared by dispersing 10 mg of GO in 10 mL ultrapure water using ultrasonic agitation for 1 h. The yellowish brown suspension obtained was centrifuged to remove the unexfoliated GO [22]. It also resulted in the exfoliation of graphite oxide to graphene oxide. This GO suspension was used to modify the GCE.

2.5. Electrode preparation, modification and electroreduction of GO-GCE

Before modification, the GCE was carefully abraded with 1.0, 0.3 and 0.05 μm α -alumina on a smooth polishing cloth to obtain a

fresh surface. It was rinsed with ultrapure water. 5 μL GO suspension was coated on GCE and then dried under an infrared lamp to obtain the GO modified electrode, denoted as GO-GCE. After modification, the electrode was rinsed with ultrapure water to remove any loosely adsorbed GO. The GO-GCE was then electroreduced in phosphate buffer of pH 6.0 by applying 25 cyclic potential sweeps between 0.6 and -1.6 V [23–25]. The modified electrode was then put in 10 mL phosphate buffer (pH 7.0) containing MMF for 120 s. After this, voltammogram (either cyclic voltammogram or differential pulse voltammogram) was recorded.

Working solutions were prepared by diluting the stock solution with 0.2 M phosphate buffer of the desired pH. All electrochemical experiments were carried out at $25 \pm 1 \text{ }^\circ\text{C}$. After each measurement, a new ERGO-GCE was prepared.

2.6. Analysis of tablets

Ten tablets containing MMF were ground to fine powder in a mortar. 0.2167 g of MMF was dissolved in 100 mL of water and methanol mixture (1:1, v/v) so as to obtain 0.5 mM MMF solution. Contents of the flask (0.5 mM MMF solution) were sonicated for 10 min to effect complete dissolution and for homogenization. Suitable aliquots (containing 0.05–15.0 μM MMF) of the clear liquid were diluted with the supporting electrolyte.

3. Results and discussion

3.1. Characterization

The surface morphologies of graphene derivatives such as GO and ERGO films were characterized and the corresponding SEM images are shown in Figs. 1A and B. EDX spectra of GO and ERGO are shown in Figs. 1C and D, respectively and chemical compositions of GO and ERGO are recorded in Table 1. Decreased amount of oxygen in ERGO (by about 10%) compared to that in GO indicated the reduction of oxygenated functional moieties. Further, trace amount of potassium in ERGO was observed as electrochemical reduction was carried out in phosphate buffer prepared from potassium salts. Upon electrochemical reduction of GO, the ERGO film showed a larger wrinkled and a rougher surface (Figs. 1A and B). Such rougher surface enhanced the incursion and diffusion of electrolyte ions. The electrochemical reduction of GO exposed more electrochemically active sites.

Exfoliated GO dispersion (in water) was deposited on a freshly cleaved mica sheet, dried and its surface morphology was analyzed by AFM (Fig. 2A). Height profile of the GO film is shown in Fig. 2B. The average film thickness was noticed to be approximately 7.2 nm, indicating that the film was composed of overlaying a few layers of GO sheets. Therefore, the GO film consisted of approximately 6 layers of individual GO sheets. It is also evident from 3D AFM images (Fig. 2C) that the surface morphology of GO film consisted of grooves and pores resulting in an increased microscopic area of the electrode, thereby facilitating the interlayer diffusion of analyte species.

XRD patterns of graphite and graphite oxide are illustrated in Fig. 3. A peak at $\sim 26.48^\circ$ was observed with pristine graphite. Disappearance of this peak and appearance of a new peak at 10.3° revealed that the graphite was successfully oxidized. Further, inter-graphene layers can be intercalated by various molecular species or ions, during which the interlayer spacing along the c-axis has changed from 3.36 to 8.55 \AA . During the oxidation of graphite to graphite oxide, hydroxyl, carbonyl, epoxy and peroxy groups could be formed on the edges of basal planes of the graphite network [26]. Further, carbon hydrolyzation could occur and

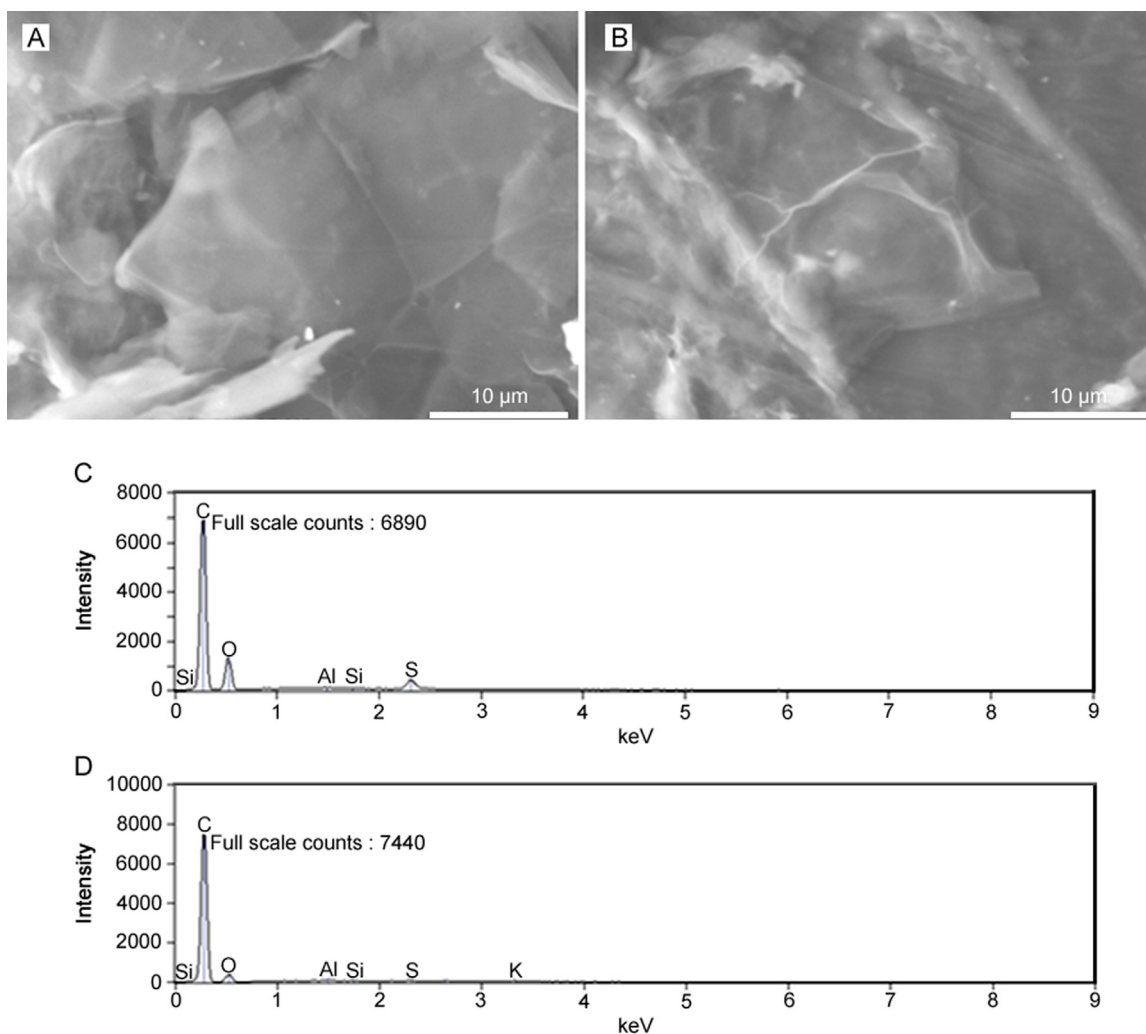


Fig. 1. Scanning electron micrographic images of (A) GO and (B) ERGO, and EDX spectra of (C) GO and (D) ERGO.

Table 1

Chemical composition (%) of GO and ERGO obtained from energy dispersive X-ray spectroscopic (EDX) analysis.

Element	Carbon	Oxygen	Aluminium	Silicon	Sulphur	Potassium	Total
GO	77.69	17.10	0.39	0.30	4.52	–	100
ERGO	91.51	5.90	0.26	0.15	0.78	1.40	100

the sp^2 bonds could be changed to sp^3 bonds. At the same time, H_2O , NO_3^- or SO_4^{2-} ions could insert themselves into the graphene layers and increase the interlayer spacing [26–28].

To determine the degree of oxidation and to determine the percentage of oxygen containing groups in graphite oxide, the synthesized graphite oxide was characterized by FT-IR spectroscopy and thermogravimetric analysis (Figs. S1 and S2). Thermogram was recorded at a heating rate of $10\text{ }^\circ\text{C}/\text{min}$ under nitrogen atmosphere from ambient temperature to $1000\text{ }^\circ\text{C}$. The weight loss at initial stages of heating corresponded to the liberation of small amounts of water. Significant amount of weight loss (around 20%) accompanied by a DTA peak was noticed at $\sim 200\text{ }^\circ\text{C}$, indicating the decomposition of oxygen containing groups in GO. Another weight loss noticed at $\sim 700\text{ }^\circ\text{C}$ was assigned to the burning of carbon backbone [29,30]. The relative amount of functional groups was found to be 32%.

FT-IR spectrum of GO exhibited bands at 1713 and 1100 cm^{-1} due to the presence of a large number of carboxyl and epoxide groups, respectively [30].

3.2. Electrochemical reduction of GO-GCE

The electrochemical reduction of GO-GCE was carried out in 0.2 M phosphate buffer of pH 7.0 by cycling the potential between 0.6 and -1.6 V for 25 cycles. The first cycle showed a broad reduction peak at a potential of -1.4 V due to the reduction of oxygen containing surface groups [25,31]. With successive cycles, the reduction peak diminished considerably and vanished after a few cycles. This showed that the electrochemical reduction of oxygen containing groups in graphene oxide was complete. Effective electrode area of the modified electrode was determined using $1\text{ mM K}_3[\text{Fe}(\text{CN})_6]$ as a redox probe and found to be 6 times more than that of bare GCE.

3.3. Electrochemical oxidation of MMF at ERGO-GCE

Cyclic voltammograms of $5\text{ }\mu\text{M}$ MMF in phosphate buffer of pH 7.0 at bare GCE and ERGO-GCE with a scan rate of 100 mV/s were recorded. It was observed that MMF exhibited two irreversible

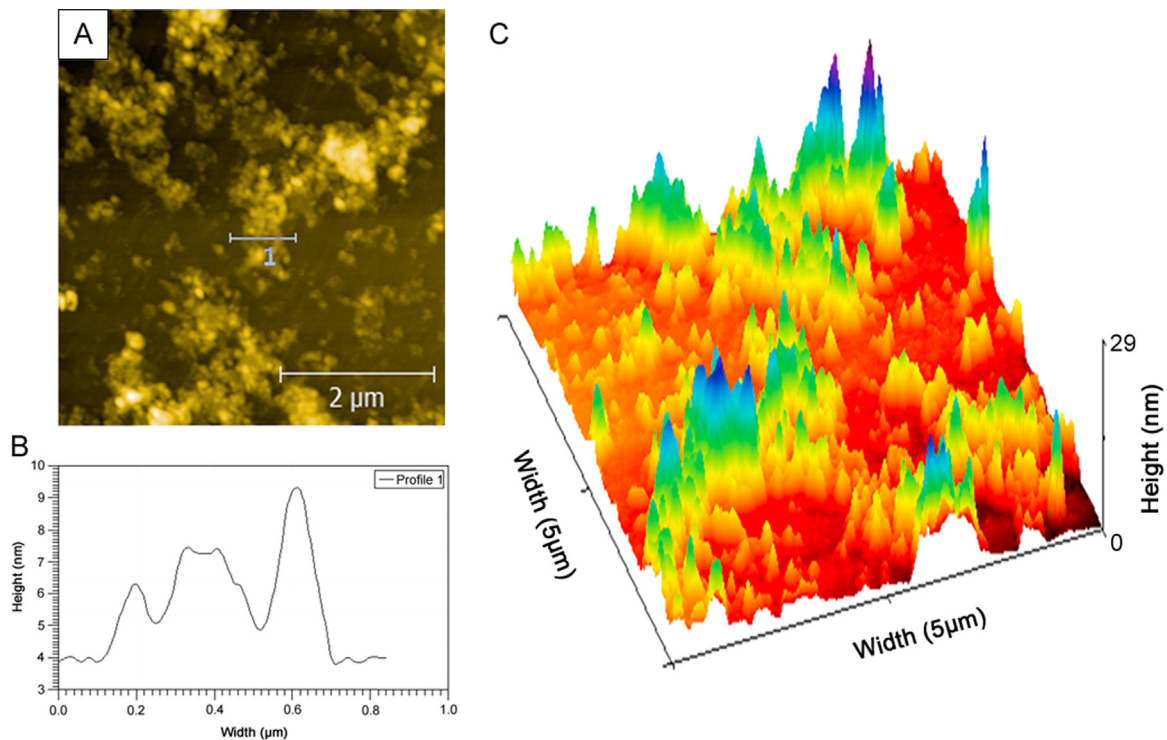


Fig. 2. (A) AFM images of GO, (B) Height profile of GO and (C) 3D AFM image of GO film coated on a freshly cleaved mica sheet.

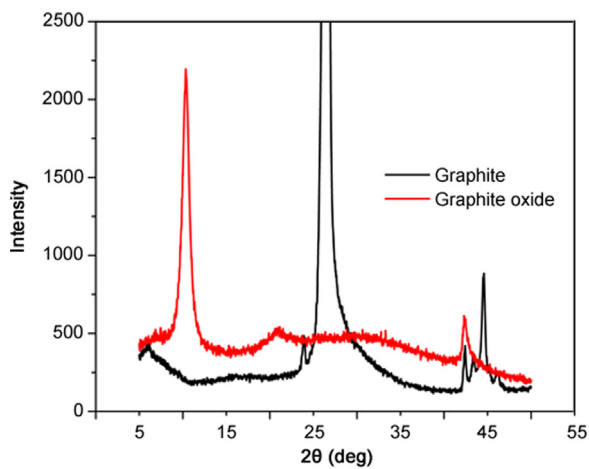


Fig. 3. X-ray diffraction patterns of graphite oxide (red) and pristine graphite (black).

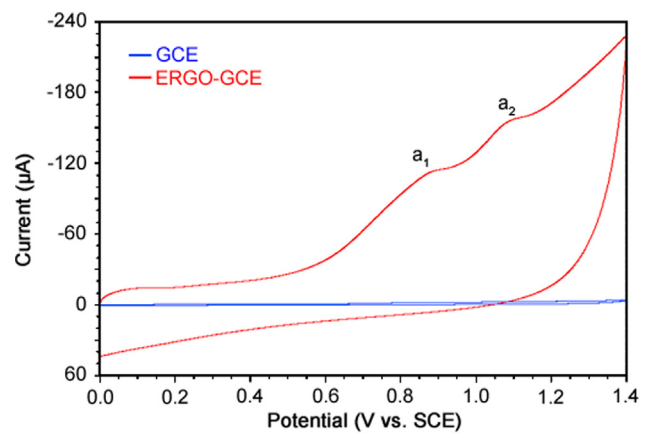


Fig. 4. Cyclic voltammograms of 5 μM MMF in phosphate buffer of pH 7.0 at a scan rate of 100 mV/s at bare and ERGO-GCE.

oxidation peaks designated as peak a_1 and a_2 respectively (Fig. 4). A large background current was observed at ERGO-GCE compared to that at bare GCE due to larger surface area of ERGO film on GCE [32]. The oxidation signal of MMF was enhanced to a greater extent at ERGO-GCE in comparison with that at bare GCE, signifying that the ERGO enhanced the electro-oxidation of MMF. It might be related to exceptional properties of graphene such as high electrical conductivity and specific surface area, and good adsorption characteristics.

To study the adsorption characteristics of MMF or its oxidation products, multi-sweep cyclic voltammograms of 5 μM MMF were recorded in phosphate buffer of pH 7.0 at a sweep rate of 100 mV/s. Peak currents were found to decrease with consecutive voltammetric sweeps, signifying that the oxidation products of MMF were adsorbed on ERGO-GCE surface and caused fouling of the electrode. This could be attributed to poor solubility of the

oxidized product of MMF that was accumulated on the electrode surface during the electrode process. This reduced the effective reaction sites on the modified electrode surface [33].

3.4. Effect of accumulation time

Accumulation time plays an important role in electrochemical oxidation of molecules. So, the effect of accumulation time on electrochemical oxidation of MMF was investigated by cyclic voltammetry. For this, cyclic voltammograms of MMF were recorded in phosphate buffer of pH 7.0 by varying accumulation time from 0 to 240 s. As the accumulation time increased from 0 to 120 s, peak currents increased gradually owing to the increased surface area of MMF on ERGO. After 120 s, the peak currents did not show any substantial change, indicating the surface saturation by the analyte. Therefore, 120 s was chosen as optimum accumulation time for further studies.

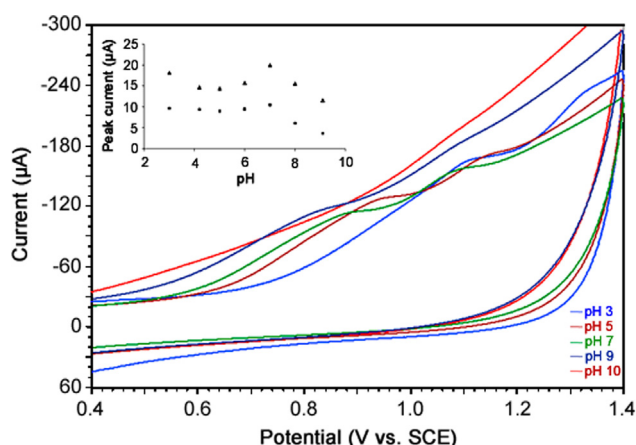


Fig. 5. Cyclic voltammograms of 5 μM MMF in phosphate buffer of different pH at a scan rate of 100 mV/s. Inset: Plots of peak currents versus pH for oxidation peaks a_1 (\blacktriangle) and a_2 (\blacksquare).

3.5. Effect of pH on the electrochemical oxidation of MMF

The effect of electrolyte pH on electrochemical oxidation of MMF was investigated by cyclic voltammetry in phosphate buffer of pH 3.0–10.0 (Fig. 5). The peak currents of both oxidation peaks, a_1 and a_2 , showed variation and maximum peak current was noticed at pH 7.0 (inset of Fig. 5). Hence, phosphate buffer of pH 7.0 was selected as supporting electrolyte for further investigations.

Peak potentials of peak a_1 and a_2 exhibited negative shift with increase in pH of the solution (3.0–9.0), indicating the involvement of protons in the electrochemical oxidation of MMF. Further, the plots of E_p versus pH revealed the linear relationship in the pH range of 3.0–8.0 with slope values of 64 mV/pH and 55 mV/pH for oxidation peaks, a_1 and a_2 , respectively, indicating that an equal number of electrons and protons were involved in the electrode process. The corresponding regression equations are shown below:

$$E_{pa}(\text{V}) = -0.064 \text{ pH} + 1.3 \quad (\text{for peak } a_1)$$

$$E_{pa}(\text{V}) = -0.055 \text{ pH} + 1.5 \quad (\text{for peak } a_2)$$

3.6. Effect of scan rate

Considerable information regarding the type of electrode process can be obtained from the study of effect of scan rate on electrochemical oxidation. So, the effect of scan rate on peak currents and peak potentials of both oxidation peaks a_1 and a_2 of MMF (5 μM) was studied in phosphate buffer of pH 7.0 and the results are shown in Fig. 6. The peak currents (I_p) increased linearly with scan rate (ν) (inset of Fig. 6) in the range of 10–300 mV/s, indicating the adsorption controlled electrode process for both peaks a_1 and a_2 [34], and the corresponding regression equations are indicated below:

$$I_p(\text{A}) = 1.20 \times 10^{-4} \nu + 2.81 \times 10^{-6} \quad (r = 0.992) \quad (\text{for peak } a_1)$$

$$I_p(\text{A}) = 7.61 \times 10^{-5} \nu + 2.09 \times 10^{-7} \quad (r = 0.991) \quad (\text{for peak } a_2)$$

Further, to confirm the electrode process, we plotted the values of $\log I_p$ versus $\log \nu$. The slope value of 0.75 for peak a_1 indicated the contribution from diffusion to the electrode process. Hence, it was proposed that the electrode reaction for peak a_1 of MMF at ERGO-GCE was a “mixed” diffusion–adsorption controlled process [35]. However, the slope value of 1.01 for peak a_2 confirmed the adsorption controlled electrode process [36].

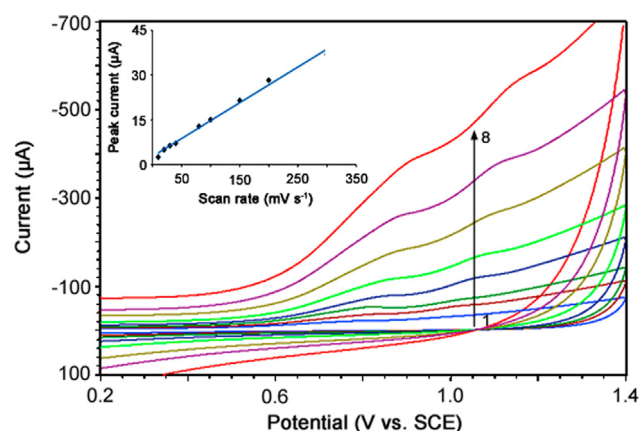


Fig. 6. Effect of scan rate on cyclic voltammograms of 5 μM MMF at 10 (1), 30 (2), 40 (3), 80 (4), 100 (5), 150 (6), 200 (7) and 300 mV/s (8). Inset: Plot of peak current versus scan rate for electrooxidation of 5 μM MMF in phosphate buffer of pH 7.0.

The corresponding regression equations are given below:

$$\log I_{pa} = 0.75 \log \nu - 4.06 \quad (r = 0.995) \quad (\text{for peak } a_1)$$

$$\log I_{pa} = 1.01 \log \nu - 4.11 \quad (r = 0.978) \quad (\text{for peak } a_2)$$

3.7. Analytical features

3.7.1. Construction of calibration plot

We have developed a differential pulse voltammetric (DPV) method for the determination of MMF in bulk sample because the peaks were sharper and better defined at lower concentrations of MMF with a lower background current, resulting in better resolution between the peaks compared to those obtained by CV. The following parameters were maintained for the determination of MMF by DPV: sweep rate, 20 mV/s; pulse amplitude, 50 mV; pulse width, 30 ms; and pulse period, 500 ms. The differential pulse voltammograms of increased concentrations of bulk MMF samples were recorded in phosphate buffer of pH 7.0 (Fig. 7). Under optimized conditions, the peak current was found to vary linearly with increasing concentrations of MMF in the range of 40 nM–15 μM (Inset of Fig. 7). Deviation from linearity was observed at higher concentrations of MMF owing to the adsorption of oxidation products of MMF on the electrode surface.

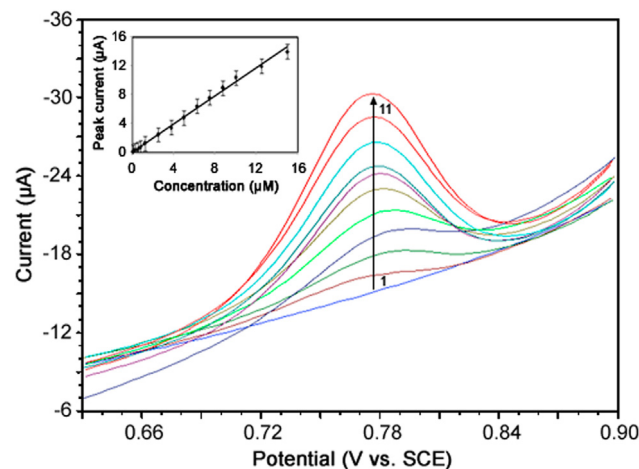


Fig. 7. Differential pulse voltammograms of MMF in phosphate buffer of pH 7.0 for (1) 0.04, (2) 1.25, (3) 2.5, (4) 3.75, (5) 5.00, (6) 6.25, (7) 7.50, (8) 8.75, (9) 10.00, (10) 12.50 and (11) 15.00 μM MMF. Inset: Plot of peak current versus concentration of MMF in phosphate buffer of pH 7.0.

Table 2
Results of analysis of MMF in tablets.

Tablet	Labeled claim (mg)	Amount found (mg)	Recovery ^b (%)	t-value ^a	F-value ^a
Mycept ^a	500.0	496.7	99.34	0.14	4.39
Mycept [#]	500.0	490.0	98.00	–	–

^a @ 95% confidence level.

^a Mycept contains 500 mg MMF and it is marketed by Panacea Biotech.

^b Average of 5 determinations.

[#] Reported voltammetric method using GCE [20].

Validation of the proposed DPV method for quantification of MMF was examined by calculating the values of limit of detection (LOD) and limit of quantification (LOQ) using the following equations [37]:

$$\text{LOD} = 3 s/m; \text{LOQ} = 10 s/m$$

where s is the standard deviation of the lowest concentration value within the linear range and m is the slope of the calibration plot. Low values of LOD (11.3 nM) and LOQ (37.5 nM) highlighted the sensitivity of the proposed method. Characteristics of the calibration plot are shown in Table S1. The values of RSD for intra-day and inter-day assay were found to be 2.46% and 2.13%, respectively, indicating good reproducibility of results.

Recently, multiwalled carbon nanotube (MWCNT) modified GCE was applied for the determination of MMF and mycophenolic acid [38]. The proposed/developed DPV method has lower value of LOD (11.3 nM) compared to that of the reported (900 nM) electrochemical method [38]. The major advantage of graphene modified electrode is the incorporation of thin layer diffusion channel in addition to the semi-infinite planar diffusion. This additional channel of mass transport has enhanced the amount of mass transfer, which eventually improved the LOD of the method by many folds. The other important advantage of graphene is the ease of renewability compared to MWCNTs due to its thinner layer (helpful in bringing back the analyte after oxidation). As a result, the LOD of the proposed method was achieved at a nano molar level.

3.7.2. Stability and reproducibility of ERGO-GCE

The ERGO film sensor was used for solitary measurement and the reproducibility of the proposed sensor (ERGO-GCE) was examined by parallel determinations of 5 μM MMF by DPV. The value of RSD was found to be 3.2% for 5 GO film sensors, thereby revealing good reproducibility. The ERGO-GCE exhibited 95% of its original current response when stored in a refrigerator (at 4 $^{\circ}\text{C}$) for 3 weeks, indicating that the electrode had long-term stability.

3.7.3. Interference studies

In order to demonstrate practical application of the proposed method, the effect of some common excipients generally present in pharmaceutical formulations was examined in the determination of MMF. The results showed that a 75-fold excess of glucose, lactose, sucrose, talc, gum acacia, cellulose and starch had a negligible influence on oxidation signals of MMF with peak current deviations below 5.0%. These results clearly supported the reasonable selectivity of the proposed method.

3.7.4. Analysis of pharmaceutical formulations and comparison with the reported method

In order to examine applicability of the proposed method, the sensor was used to determine MMF in commercially available tablets under optimized conditions. The results of assay of tablets containing MMF are summarized in Table 2. Accuracy of the proposed method was evaluated by performing recovery test after spiking known amounts of the samples. Higher recovery (more

than 99.5%) and low bias values (0.5%) confirmed the accuracy of the proposed method.

The results were compared statistically by Student t -test and by the variance ratio F -test with those obtained by the reported method [20]. The calculated Student t -value at 95% confidence level did not exceed the tabulated value, thereby revealing that there was no significant difference in accuracy between the proposed and reported methods. Further, it was also observed that the variance ratio F -value calculated for $p = 0.05$ did not exceed the tabulated value, indicating that there was no significant difference in precision of the proposed and reported methods.

4. Conclusions

In the present work, we have used an eco-friendly electrochemical method for the reduction of GO to ERGO. AFM, SEM, EDX, XRD, FT-IR and TGA techniques were employed to characterize the synthesized GO. The fabricated electrode showed good sensing performance for MMF. Wide linearity, lower LOD value and excellent reproducibility highlighted ERGO-GCE as a promising sensor for MMF.

Conflicts of interest

The authors declare that there are no conflicts of interest.

Acknowledgments

We are grateful to the Board of Research in Nuclear Sciences, Mumbai, for financial assistance (No.2012/37C/8/BRNS/637 dated 28-05-2012). Thanks also go to the authorities of the Karnatak University, Dharwad, for providing the necessary facilities.

Appendix A. Supplementary material

Supplementary data associated with this article can be found in the online version at doi:10.1016/j.jpha.2017.12.001.

References

- [1] K.S. Novoselov, A.K. Geim, S.V. Morozov, et al., Electric field effect in atomically thin carbon films, *Science* 306 (2004) 666–669.
- [2] M. Pumera, A. Ambrosi, A. Bonanni, et al., Graphene for electrochemical sensing and biosensing, *Trends Anal. Chem.* 29 (2010) 954–965.
- [3] P. Blake, P.D. Brimicombe, R.R. Nair, et al., Graphene-based liquid crystal device, *Nano Lett.* 8 (2008) 1704–1708.
- [4] H.A. Becerril, J. Mao, Z. Liu, et al., Evaluation of solution-processed reduced graphene oxide films as transparent conductors, *ACS Nano* 2 (2008) 463–470.
- [5] D. Li, M.B. Muller, S. Gilje, et al., Processable aqueous dispersions of graphene nanosheets, *Nat. Nanotechnol.* 3 (2008) 101–105.
- [6] I. Meric, M.Y. Han, A.F. Young, et al., Current saturation in zero-bandgap, top-gated graphene field-effect transistors, *Nat. Nanotechnol.* 3 (2008) 654–659.
- [7] Y. Shao, J. Wang, H. Wu, et al., Graphene based electrochemical sensors and biosensors: a review, *Electroanalysis* 22 (2010) 1027–1036.
- [8] B.J. Sanghavi, W. Varhue, J.L. Chávez, et al., Electrokinetic preconcentration and detection of neuropeptides at patterned graphene-modified electrodes in a nanochannel, *Anal. Chem.* 86 (2014) 4120–4125.
- [9] B.J. Sanghavi, S. Sitaula, M.H. Griep, et al., Real-time electrochemical monitoring of adenosine triphosphate in the picomolar to micromolar range using graphene-modified electrodes, *Anal. Chem.* 85 (2013) 8158–8165.
- [10] J. Yan, L. Xian, M.Y. Chou, Structural and electronic properties of oxidized graphene, *Phys. Rev. Lett.* 103 (2009) 086802.
- [11] D.W. Boukhvalov, M.I. Katsnelson, Modeling of graphite oxide, *J. Am. Chem. Soc.* 130 (2008) 10697–10701.
- [12] P. Leyssen, N. Charlier, J. Paeshuyse, et al., Prospects for antiviral therapy, *Adv. Virus Res.* 61 (2003) 511–553.
- [13] B. Tönshoff, A. Melk, Book Chapter 59, Immunosuppression in pediatric kidney transplantation, *Comprehensive Pediatric Nephrology*, Springer, Heidelberg, 2008: 905–929.

- [14] D.C. Brennan, M.J. Koch, Pierratos A: daily nocturnal hemodialysis - a paradigm shift worthy of disrupting current dialysis practice, *Nat. Clin. Pract. Nephrol.* 3 (2007) 602–603.
- [15] P. Mathieu, M. Carrier, M. White, et al., Effect of mycophenolate mofetil in heart transplantation, *Can. J. Surg.* 43 (2000) 202–206.
- [16] T.M. Manzia, N.D.L. Carino, G. Orlando, et al., Use of mycophenolate mofetil in liver transplantation: a literature review, *Transplant. Proc.* 37 (2005) 2616–2617.
- [17] A. Zuckermann, T. Birsan, S. Thaghavi, et al., Mycophenolate mofetil in lung transplantation, *Transplant. Proc.* 30 (1998) 1514–1516.
- [18] R.W. Gruessner, D.E. Sutherland, M.B. Drangstveit, et al., Mycophenolate mofetil in pancreas transplantation, *Transplantation* 66 (1998) 318–323.
- [19] M. Cantarovich, N.W. Brown, M.H.H. Ensom, et al., Mycophenolate monitoring in liver, thoracic, pancreas, and small bowel transplantation: a consensus report, *Transplant. Rev.* 25 (2011) 65–77.
- [20] S.N. Prashanth, K.C. Ramesh, J. Seetharamappa, Electrochemical oxidation of an immunosuppressant, mycophenolate mofetil, and its assay in pharmaceutical formulations, *Int. J. Electrochem.* 2011 (2011) 1–7.
- [21] H. Yu, B. Zhang, C. Bulin, et al., High-efficient Synthesis of graphene oxide based on improved Hummers method, *Sci. Rep.* 6 (2016) 36143.
- [22] S. Park, R.S. Ruoff, Chemical methods for the production of graphenes, *Nat. Nanotechnol.* 4 (2009) 217–224.
- [23] J. Wang, S. Yang, D. Guo, et al., Comparative studies on electrochemical activity of graphene nanosheets and carbon nanotubes, *Electrochem. Commun.* 11 (2009) 1892–1895.
- [24] N.L. Teradal, P.S. Narayan, A.K. Satpati, et al., Fabrication of electrochemical sensor based on green reduction of graphene oxide for an antimigraine drug, rizatriptan benzoate, *Sens. Actuators B* 196 (2014) 596–603.
- [25] T. Chen, Z. Sheng, K. Wang, et al., Determination of explosives using electrochemically reduced graphene, *Chem. Asian J.* 6 (2011) 1210–1216.
- [26] C. Hontoria-Lucas, A.J. López-Peinado, J. de D. López-González, et al., Study of oxygen-containing groups in a series of graphite oxides: physical and chemical characterization, *Carbon* 33 (1995) 1585–1592.
- [27] H.Y. He, T. Riedl, A. Lerf, et al., Solid-state NMR studies of the structure of graphite oxide, *J. Phys. Chem.* 100 (1996) 19954–19958.
- [28] H.Y. He, J. Klinowski, M. Forster, et al., A new structural model for graphite oxide, *Chem. Phys. Lett.* 287 (1998) 53–56.
- [29] G. Wang, J. Yang, J. Park, et al., Facile synthesis and characterization of graphene nanosheets, *J. Phys. Chem. C* 112 (2008) 8192–8195.
- [30] M. Jin, H. Jeong, T. Kim, et al., Synthesis and systematic characterization of functionalized graphene sheets generated by thermal exfoliation at low temperature, *J. Phys. D: Appl. Phys.* 43 (2010) 275402.
- [31] H.L. Guo, X.F. Wang, Q.Y. Qian, et al., A green approach to the synthesis of graphene nanosheets, *ACS Nano* 3 (2009) 2653–2659.
- [32] S.F. Wang, F.R. Xie, F. Hu, Carbon-coated nickel magnetic nanoparticles modified electrodes as a sensor for determination of acetaminophen, *Sens. Actuators B* 123 (2007) 495–500.
- [33] A. Veiga, A. Dordio, A.J.P. Carvalho, et al., Ultra-sensitive voltammetric sensor for trace analysis of carbamazepine, *Anal. Chim. Acta* 674 (2010) 182–189.
- [34] Y. Guo, S. Guo, J. Li, et al., Cyclodextrin-graphene hybrid nanosheets as enhanced sensing platform for ultrasensitive determination of carbendazim, *Talanta* 84 (2011) 60–64.
- [35] S.N. Prashanth, N.L. Teradal, J. Seetharamappa, et al., Fabrication of electro-reduced graphene oxide-bentonite sodium composite modified electrode and its sensing application for linezolid, *Electrochim. Acta* 133 (2014) 49–56.
- [36] P.S. Narayan, N.L. Teradal, S.S. Kalanur, et al., Fabrication of an electrochemical sensor based on multiwalled carbon nanotubes for almotriptan, *Electroanalysis* 25 (2013) 2684–2690.
- [37] S. Skrzypek, W. Ciesielski, A. Sokolowski, et al., Square wave adsorptive stripping voltammetric determination of famotidine in urine, *Talanta* 66 (2005) 1146–1151.
- [38] T. Madrakian, M. Soleimani, A. Afkhami, Simultaneous determination of mycophenolate mofetil and its active metabolite, mycophenolic acid, by differential pulse voltammetry using multi-walled carbon nanotubes modified glassy carbon electrode, *Mater. Sci. Eng. C* 42 (2014) 38–45.



Contents lists available at ScienceDirect

Journal of Pharmaceutical Analysis

journal homepage: www.elsevier.com/locate/jpa
www.sciencedirect.com



Original Research Article

Surrogate potency assays: Comparison of binding profiles complements dose response curves for unambiguous assessment of relative potencies

Robert Karlsson, Veronica Fridh, Åsa Frostell*

Purification and Analysis, GE Healthcare Life Sciences, Uppsala, Sweden

ARTICLE INFO

Article history:

Received 8 August 2017

Received in revised form

28 November 2017

Accepted 21 December 2017

Available online 21 December 2017

Keywords:

Surface plasmon resonance

EC50

Sensorgram comparison

Calibration free concentration analysis

Surrogate potency assay

TNF- α

ABSTRACT

Surface plasmon resonance (SPR) systems are widely used for detailed characterization of antibody activities including antigen and Fc-receptor binding. During the later stages of development, where the focus is to ensure that established critical quality attributes (CQAs) are maintained during cell culture, purification and formulation processes, analysis is simplified, and relative potencies are often determined. Here, simulation of binding data revealed that relative potency values, determined via parallel line analysis (PLA) and half maximal effective concentration (EC50) analysis accurately reflect changes in active concentration only if binding kinetics remain unchanged. Changes in the association rate constant shifted dose response curves, and therefore relative potencies, in the same way as changes in analyte concentration do. However, for interactions characterized by stable binding, changes in the dissociation rate constant did not result in any shift, suggesting that this type of change may go unnoticed in the dose response curve. Thus, EC50 and PLA analyses of dose response curves obtained with an anti-TNF- α antibody were complemented with the Biacore functionality for sensorgram comparison analysis, whereby changes in antigen and Fc-receptor binding profiles could be detected. Next, analysis of temperature stressed TNF- α antibody revealed that calibration free concentration analysis (CFCA) data correlated perfectly with relative potency values. Together, these results demonstrate that combinations of SPR based dose response curves, sensorgram comparison and CFCA can be used to strengthen the confidence in relative potency assessments, and suggest that SPR can potentially be used as a surrogate potency assay in the quality control of biotherapeutic medicines.

© 2018 Xi'an Jiaotong University. Production and hosting by Elsevier B.V. This is an open access article under the CC BY-NC-ND license (<http://creativecommons.org/licenses/by-nc-nd/4.0/>).

1. Introduction

During early antibody development, surface plasmon resonance (SPR) is widely used for epitope binning and for kinetic characterization of candidates [1,2]. Selected candidates may further be characterized with respect to Fc γ -receptor [3–5] and FcRn binding [6,7]. An array of SPR binding data (antigen, Fc-receptors and C1q) related to the molecular mechanisms of action [8–10] may therefore be available for a candidate that enters clinical studies. This is in line with FDA guidelines on biosimilars [11], which state that functional assays should reflect mechanisms of

action as far as possible and that multiple functional assays can be performed as part of the analytical similarity assessment. The same reasoning can be applied to any biotherapeutic medicine and is not only valid for biosimilars. When the manufacturing process is developed, and later during production, the analytical focus may shift from detailed characterization to assays that aim to ensure the maintenance of binding properties of the drug substance and drug product. By comparison to a reference preparation of the drug, it should also be possible to determine drug potency to ensure correct dosage. For this purpose, SPR assays based on dose response curves related to Fc-receptor [12], antigen [13] or hemagglutinin content in the influenza vaccine [14] have been described; the Fc-receptor assay involved the capture of histidine tagged receptor; the antigen assay was based on the covalent binding of antigen to the sensor surface; and the hemagglutinin assay employed the capture of biotinylated synthetic glycans to neutravidin surfaces.

The purpose of this study is to illustrate new possibilities with SPR assays for binding activity measurements. We describe the use of reversible biotin capture to establish dose response curves for

Peer review under responsibility of Xi'an Jiaotong University.

Abbreviations: SPR, Surface Plasmon Resonance; EC50, the concentration that corresponds to a response that is 50% of the maximum response; IC50, the concentration of inhibitor that reduce the response to 50% of the maximum response; CFCA, Calibration Free Concentration Analysis; CQA, Critical Quality Attribute; PLA, Parallel Line Analysis

* Corresponding author.

E-mail address: asa.frostell@ge.com (Å. Frostell).

<https://doi.org/10.1016/j.jpha.2017.12.008>

2095-1779/© 2018 Xi'an Jiaotong University. Production and hosting by Elsevier B.V. This is an open access article under the CC BY-NC-ND license (<http://creativecommons.org/licenses/by-nc-nd/4.0/>).

the measurement of relative potency via PLA and EC50 analysis and illustrate this using anti-TNF- α antibodies. This assay is extended to demonstrate how SPR can be used to monitor both antigen and receptor binding in a single assay setup. By combining analysis of dose response curves with sensorgram comparison, introduced [15] for single analyte comparisons and here extended to multiple injections, we demonstrate that the shortcomings of PLA or EC50 analysis, which may not always be able to detect changes in critical quality attributes, can be remedied. Finally, we describe the use of calibration free concentration analysis (CFCA) [16,17] as an alternative to EC50 analysis for the analysis of stressed anti-TNF- α antibody samples.

2. Materials and methods

2.1. Equipment and software

Biacore™ T200 system (GE Healthcare, Uppsala, Sweden) with Control software version 2.0.2 and Evaluation software version 3.1 was used for interaction analysis.

2.2. Sensor chips, reagents and buffers

The Biotin CAPture Kit, including Sensor Chip CAP, Biotin CAPture reagent and regeneration solutions, Sensor Chip PEG, Recombinant MabSelect™ SuRe™ ligand, anti-TNF- α antibody, amine coupling kit and PBS-P+ Buffer 10 \times (0.2 M phosphate buffer with 27 mM KCl, 1.37 M NaCl and 0.5% Surfactant P20 (Tween 20)) were from GE Healthcare. Recombinant biotinylated human TNF- α (Val 77 - Leu 233) was from ACRO Biosystems (Beijing, China), recombinant human TNF receptor I protein was from Abcam (Cambridge, United Kingdom), recombinant human Fc γ R1IIa Val 158 and Fc γ RI expressed in CHO cells were kind gifts from Boehringer-Ingelheim, and bovine serum albumin (BSA) was from Sigma-Aldrich (Stockholm, Sweden).

2.3. Biotin capture assay procedures

The sample compartment of the Biacore T200 system was set to 20 °C, the analysis temperature to 25 °C, and the data collection rate to 1 Hz. PBS-P+ was used as the running buffer. In each cycle, biotin capture reagent was injected for 300 s at a flow rate of 2 μ L/min, followed by a 30–60 s capture of biotinylated TNF- α at 1–2 μ g/mL in PBS-P+ with 0.5% BSA, to reach minimum capture levels of around 40 RU. Anti-TNF- α antibody, 0.02–360 μ g/mL in PBS-P+, was injected for 120 s and the surface was regenerated at the oligonucleotide level per kit instructions. To study antibody binding to both the captured antigen and a receptor in the same assay, an additional sample injection of receptor was included. Receptors, Fc γ R1IIa Val 158, Fc γ RI and TNF- α receptor, were injected for 60 s at concentrations of 5 μ g/mL, 5.4 μ g/mL and 10 μ g/mL, respectively.

Heat stressed antibody samples were analyzed after exposing the antibody at 1 mg/mL to 60 °C for 1, 2 or 3 h prior to analysis.

Data analysis was performed using Microsoft Excel as described in section 2.4 and with the sensorgram comparison functionality in Biacore T200 evaluation software version 3.1.

2.4. PLA and EC50/IC50 analysis

For PLA and EC50 analysis, response and concentration data from the Biacore assay were pasted into Microsoft Excel.

For determination of EC50 and IC50 values, the equation

$$R_{hi} - (R_{hi} - R_{lo}) / \left(1 + \left(\frac{Conc}{A1} \right)^{A2} \right)$$

was used to calculate response curves. R_{hi} (response high) and R_{lo} (response low) are response values at the upper and lower asymptotes, and $A1$ corresponds to EC50/IC50 and $A2$ to the Hill slope. A response curve was first calculated using default values for each parameter. The solver (Data/Solver in Microsoft Excel) functionality using the evolutionary solving method was then used to find parameter values that minimized the squared difference between the observed Biacore data and data calculated from the four-parameter equation. The parameter values at this minimum constitute the result.

For PLA the slope and intercepts of the parallel line were calculated using data regression (Data/Data analysis/Regression in Microsoft Excel) with input of response values (y), log (conc) ($x1$) and a curve differentiating parameter, ($x2$). $X2$ was set to 1 for the reference sample and to 0 for the new sample. The concentration values in PLA typically ranged from 0.5 to 1.5 times of the EC50. Relative potency values were calculated based on EC50 ratios and in PLA on the difference in intersect with the log(conc) axis.

2.5. Simulation of dose response curves

Response data for a 1:1 interaction model were calculated from the equation

$$R(t) = Ra \times e^{-k_d \times t_d}$$

with

$$Ra = Ra(t_a) = Req - Req \times e^{-(k_a \times C + k_d) \times t_a}$$

and

$$Req = \frac{C \times R_{max}}{C + \frac{k_d}{k_a}}$$

where t_a is the interaction time, t_d is the dissociation time, R_{max} is the maximum binding capacity, C is the concentration, k_a is the association rate constant, and k_d the dissociation rate constant. The equations were used to calculate dose response curves in Microsoft Excel. Input parameters in the simulations were k_a , k_d , R_{max} , t_a and t_d . From these inputs, dose response curves with 18 data points covering the concentration range from k_d/k_a :32 to k_d/k_a :4096 (two-fold concentration change between points) were calculated. By designing for the separate input, of k_a and k_d values to one reference curve and three sample curves, four dose response curves were directly displayed in the same graph. By varying the injection time, t_a , the impact of interaction time on the position of the dose response curve could be studied, and by varying the dissociation time, the effect of dissociation could be observed.

The 1:1 binding model used in simulations assumes that analyte A in solution binds to an immobilized/captured binding partner B to form an AB complex. The same model can be used in cases where the immobilized ligand has several identical binding sites, e.g. antigen binding to immobilized antibody. Only the R_{max} value must be adjusted to reflect this situation. However, if the analyte has multiple binding sites for the immobilized ligand, binding becomes more complex and involves several rate constants. The most striking effect is that the observed dissociation rate becomes slower as the analyte remains bound even when one binding site is released. This is typically the case for a bivalent antibody binding to an immobilized antigen.

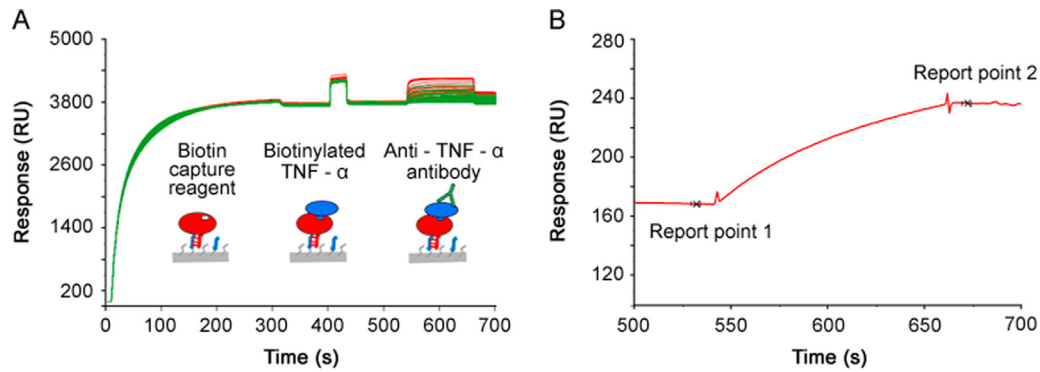


Fig. 1. Biotin capture assay set-up. (A) In the biotin capture assay, the biotin capture reagent (streptavidin modified with an oligonucleotide) is first injected and hybridizes to the Sensor Chip CAP containing a complementary oligonucleotide. Biotinylated TNF- α is then injected (here 1 $\mu\text{g}/\text{mL}$) to reach a defined RU level (in this example around 40 RU) followed by the injection of an anti-TNF- α antibody at varying concentrations (range 0.02–360 $\mu\text{g}/\text{mL}$). The figure is an overlay plot of 128 analytical cycles and shows binding events in the active flow cell. The color coding refers to two users. (B) Samples are injected over both active and reference spots. Biotinylated TNF- α is not present on the reference spot. Reference subtraction removes the buffer effects seen as an offset during antibody injection in Fig. 1A. In Fig. 1B, the antibody binding part of one representative reference subtracted sensorgram is shown. The antibody response is calculated from the difference in binding levels: Report point 2 minus Report point 1.

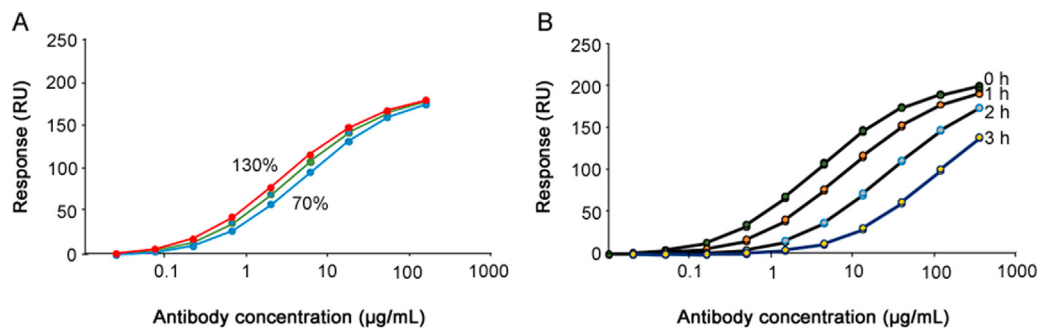


Fig. 2. Dose response curves for PLA and EC50 analysis. (A) Antibody response levels, obtained with concentrations corresponding to 130%, 100% and 70% of the nominal concentrations, plotted versus nominal (100%) concentration values. (B) Antibody response levels obtained with unstressed (0 h stress) and stressed samples (1, 2 and 3 h) plotted versus the antibody concentration. For PLA and EC50 PLA analysis, see Table 3.

2.6. CFCA assay procedures

The sample compartment temperature of the Biacore T200 system and the analysis temperature were set to 25 °C and the data collection rate to 10 Hz. PBS-P+ was used as running buffer.

CFCA was performed on stressed and non-stressed antibody samples using two different ligands: TNF- α and MabSelect SuRe. With this, it was possible to compare the effects of heat stress paratope and on the Fc-domain.

TNF- α and MabSelect SuRe ligand were immobilized on the Sensor Chip PEG using amine coupling. Immobilizations were performed at 25 °C per kit instructions except for the following: for immobilization of TNF- α , the surface was activated by EDC/NHS for 15 s only. TNF- α at 10 $\mu\text{g}/\text{mL}$ in 10 mM acetate buffer (pH 5.0) was injected for 7 min and the remaining NHS-esters were blocked by injecting the ethanolamine solution for 7 min. For immobilization of SuRe ligand, the surface was activated by EDC/NHS for 10 s, SuRe ligand at 1 mg/mL in acetate buffer (pH 5.0) was injected for 7 min and the surface was blocked with ethanolamine for 7 min. These procedures resulted in immobilization levels of 1,550 and 730 RU for TNF- α and SuRe ligand, respectively.

Antibodies were diluted to a nominal concentration of 10 nM and further diluted 2, 4 and 8 times in running buffer. Each antibody concentration was injected for 36 s using flow rates of 5 and 100 $\mu\text{L}/\text{min}$.

Surfaces immobilized with the SuRe ligand were regenerated with a 30 s injection of 10 mM glycine (pH 1.5), and surfaces with immobilized TNF- α were regenerated with a 30 s injection of 3 M magnesium chloride.

The TNF- α surface required 5–10 start-up cycles with antibody injections prior to sample injections. The dilution series were

globally fitted using the CFCA functionality in Biacore T200 evaluation software v 3.1. For the analysis, a diffusion coefficient of $4.0 \times 10^{-11} \text{ m}^2/\text{s}$ and an antibody molecular weight of 144,000 Da were used. The concentration of non-stressed samples was set to 100% and relative concentration values were calculated for stressed samples.

3. Results and discussion

3.1. Repeatability of biotin capture procedure

The set-up of the biotin capture assay and an overlay plot comprising 128 full analytical cycles of the interaction between TNF- α and anti-TNF- α antibody is shown in Fig. 1A. The color coding represents data obtained by two users and was introduced to detect user-dependent differences. User 1 and user 2 injected broad and partly overlapping antibody concentration series and used three and four replicates of the antibody injections, respectively.

At the baseline level, the buffer flowed over the Sensor Chip CAP, a sensor chip with pre-immobilized oligonucleotide. Upon injection of the biotin capture reagent, streptavidin modified with the complementary oligonucleotide, hybridization occurred on the surface resulting in the capture of approximately 3,700 RU. Antigen was then captured (between 35 and 40 RU) following a short injection of biotinylated TNF- α at 1–2 $\mu\text{g}/\text{mL}$. Anti-TNF- α antibody at varying concentrations were then injected, resulting in concentration-dependent response levels. Fig. 1B demonstrates how report points before and after the antibody injection were

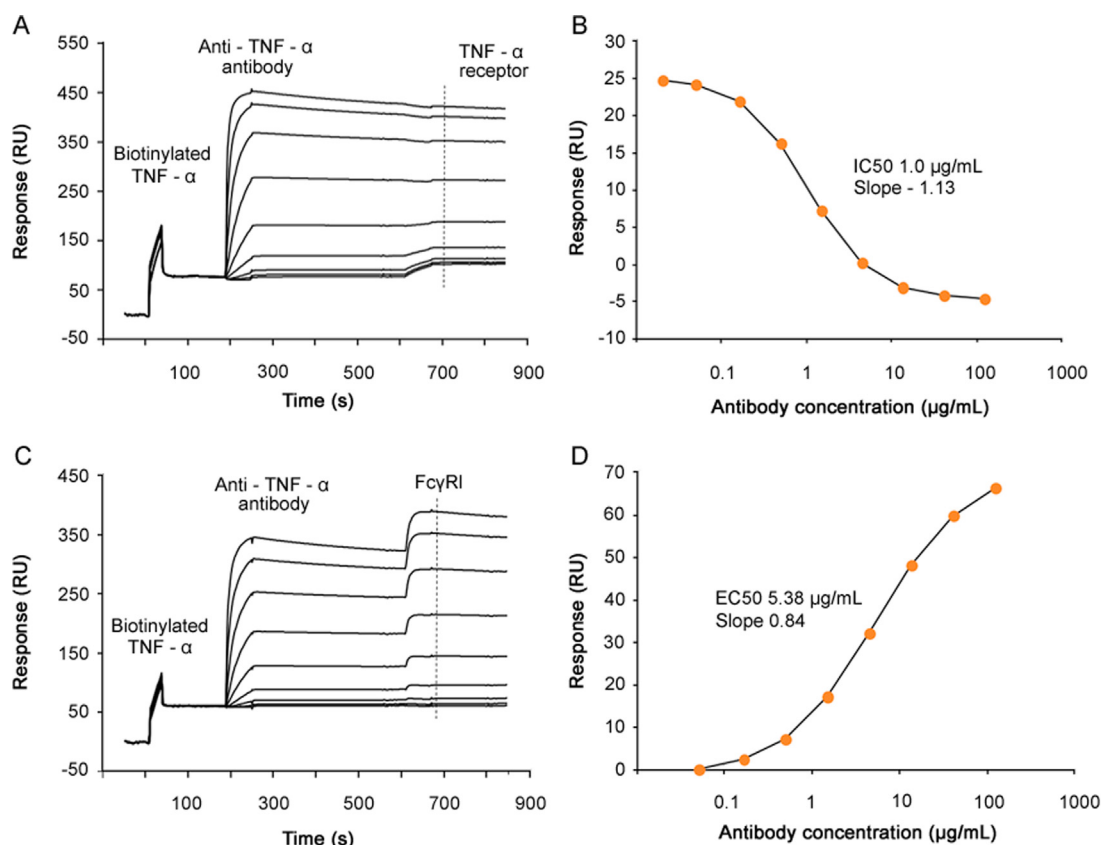


Fig. 3. Dual potency assays. (A) Dual potency assay with anti-TNF- α antibody, injected at varying concentrations (0.02–120 $\mu\text{g/mL}$), binding to biotinylated TNF- α captured on the sensor surface, followed by injection of TNF- α -receptor (10 $\mu\text{g/mL}$) binding to free TNF- α . The dashed line shows the position from where the receptor response is obtained. (B) Reference subtracted TNF- α -receptor response plotted versus antibody concentration. The IC₅₀ value was 1.0 $\mu\text{g/mL}$ and the Hill slope -1.13 . (C) Dual potency assay with anti-TNF- α antibody, injected at varying concentrations (0.05–120 $\mu\text{g/mL}$), binding to biotinylated TNF- α captured on the sensor chip, followed by injection of Fc γ RI (5.4 $\mu\text{g/mL}$). The dashed line shows the position from where the receptor response is obtained. (D) Reference subtracted Fc γ RI response plotted versus antibody concentration. The EC₅₀ value was 5.38 $\mu\text{g/mL}$ and the Hill slope 0.84.

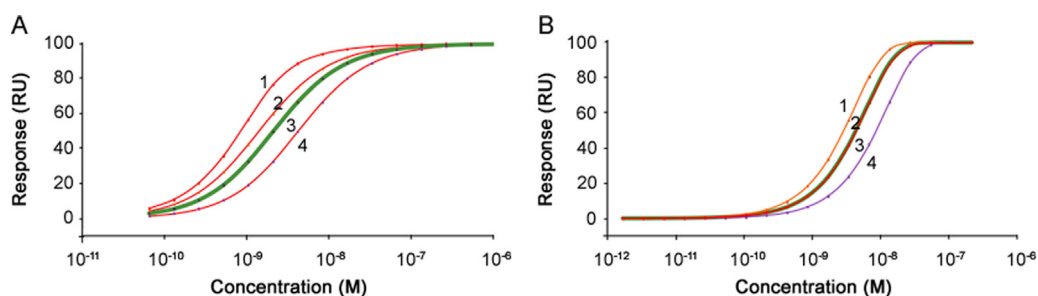


Fig. 4. Simulated dose response curves. Simulated dose response curves demonstrate how changes in concentration and kinetic rate constants shift the dose response curve. Response levels were obtained after 100 s interactions on surfaces with a maximum binding capacity of 100 RU. In Fig. A, the interaction is characterized by rapid dissociation and in Fig. B, the dissociation is much slower. (A) Curve 3 marked with a thick green line is the reference. This dose response curve was obtained with k_a $1.2 \times 10^7 \text{ M}^{-1} \text{ s}^{-1}$ and k_d $2.5 \times 10^{-2} \text{ s}^{-1}$. In curve 1, the dissociation rate constant was four times lower than that of the reference. In curve 2, the concentrations were doubled but still plotted versus the nominal concentration of the reference. In curve 4, the association rate constant was changed to half the value of that of the reference. (B) Curve 3 marked with a thick line is the reference. This dose response curve was obtained with k_a $1.6 \times 10^9 \text{ M}^{-1} \text{ s}^{-1}$ and k_d $8.5 \times 10^{-5} \text{ s}^{-1}$. In curve 1, the concentrations were doubled but still plotted versus the nominal concentration of the reference. In curve 2, that overlaps almost completely with the reference curve, the dissociation rate constant was changed to $3.4 \times 10^{-4} \text{ s}^{-1}$ (four times faster than that of the reference). In curve 4, the association rate constant was two times lower than that of the reference, i.e. $8.0 \times 10^5 \text{ M}^{-1} \text{ s}^{-1}$. In both A and B changes in concentration and association rate constant shifted the dose response curves and hence the EC₅₀ values. The impact of changes in the dissociation rate constant varied, and was significant for high dissociation rate constants but negligible for low dissociation rate constants.

used to define antibody responses that were used to create dose response curves.

Response levels for biotin capture reagent and biotinylated TNF- α injections were repeatable with coefficient of variations (CV) of less than 1.2% Table 1. Very repeatable antigen capture levels are important for assay performance and were obtained here by the addition of 0.5% BSA to the TNF- α solution.

Similarly, Table 2 shows that CV values are below 1% for antibody injections except at the lowest concentrations, where response levels were very low. CVs for these concentrations were less than 15%.

These results demonstrate that antibody concentrations up to 360 $\mu\text{g/mL}$ can be used for dose response curves and that three replicates are sufficient, as the assay performance was not

Table 1

Reproducibility of capture steps. Data were collected on two Biacore T200 systems and on two different Sensor Chip CAP. Hybridization of the biotin capture reagent shows reproducibility over Biacore systems and sensor chips. The small variation between users in capture of biotinylated TNF- α may be due to individual reagent preparations being used.

User	Biotin capture reagent		Biotinylated TNF- α	
	Average (RU)	CV (%)	Average (RU)	CV (%)
User 1 (63 repeats)	3768	0.23	39.4	0.77
User 2 (65 repeats)	3745	0.51	36.4	1.12

Table 2

Response values from concentration series. Data from two overlapping concentration series generated by users 1 and 2. Note that user 1 and user 2 set up the assay using slightly different concentration series and a different number of replicates for each antibody concentration. Average values for series one (0.02–360 $\mu\text{g/mL}$) were based on three replicates and for series 2 (0.02–160 $\mu\text{g/mL}$) on four replicates. Except for very low response values, CVs were less than 1%.

Concentration ($\mu\text{g/mL}$)	Average response (RU)	SD (RU)	CV (%)
0.02	-0.9	0.12	13.3
0.05	2.4	0.00	0.0
0.16	11.1	0.15	1.4
0.49	31.3	0.26	0.8
1.48	65.2	0.35	0.5
4.44	105.7	0.56	0.5
13.33	144.9	0.86	0.6
40.0	174.0	1.22	0.7
120.0	190.0	0.1	0.1
360.0	199.4	1.14	0.6
0.02	-1.0	0.15	14.6
0.07	2.4	0.13	5.5
0.22	11.7	0.08	0.7
0.66	32.9	0.13	0.4
1.98	66.4	0.25	0.4
5.93	104.8	0.46	0.4
17.78	139.7	0.34	0.2
53.33	164.4	0.54	0.3
160.0	179.2	0.54	0.3

markedly improved by using four replicates, although CVs were slightly lower with four replicates.

The use of biotin capture can clearly provide reproducible data. A distinct advantage with this approach is that the need for assay development is minimized because biotin capture is reversible. This is important from a perspective of cost. For assays based on covalent immobilization [13], immobilization and regeneration conditions have to be developed. Similarly, for capture of biotinylated molecules to streptavidin or neutravidin [14] regeneration conditions must be found. However, these steps are not necessary with the current approach as they are part of the kit design. In theory, histidine capture as described by Harrison et al. [12] can also reduce assay development efforts but in contrast to biotin capture, molecules captured through a histidine tag may dissociate more rapidly from the sensor surface [18]; therefore, a histidine capture approach sometimes has to be abandoned.

3.2. PLA and EC50 analysis of dose response curves

The effect on the position of the dose response curve after deliberate changes in antibody concentrations was investigated Fig. 2A. As expected, higher concentrations shifted the dose response curves to the left, and lower concentrations shifted the dose response curve to the right. The assay was further able to detect stress-induced changes in the antibody as shown in Fig. 2B.

The relative potency dropped with increasing stress, and was about 40% of the untreated reference already after 1 h of stress.

Table 3

EC50 and PLA values. PLA and EC50 analysis are in good agreement using a broad range of concentrations. In the PLA analysis, the ratio between the standard errors of slopes and intercepts with respective parameter values were calculated. The relative standard error in common slopes was less than 1% and the largest relative standard error in any intercept was 9% (range 1.2%–9.0%). In the stress test, the relative standard error in common slopes was close to or less than 1% and the largest standard error in any intercept was 7.2% (range 0.85%–7.2%). All regression coefficients were larger than 0.99.

Tests	EC50 ($\mu\text{g/mL}$)	Relative potency EC50 ratio (%)	PLA concentration range ($\mu\text{g/mL}$)	Relative potency PLA (%)
Linearity test				
70%	5.42	70.6	0.66 to 17.78	72.0
100%	3.83	100.0	0.66 to 17.78	100.0
130%	2.95	129.8	0.66 to 5.93	129.2
Stress test				
0 h stress	3.50	100.0	1.48 to 13.33	100.0
1 h stress	8.11	43.1	4.44 to 40.0	41.8
2 h stress	28.4	12.3	13.33 to 120.0	12.0
3 h stress	75.0	4.6	40.0 to 360.0	3.1

Relative EC50 and relative potency values from PLA (Table 3) concurred and indicated that the shift in relative potency was linear and that PLA could be performed over a range of antibody concentrations surrounding the EC50 value for each sample.

In conclusion, the assay based on the capture of biotinylated TNF- α was repeatable and the relative potency values could be calculated from PLA and EC50 analysis. Furthermore, EC50 values proved linear with respect to changes in concentration, and relevant data were obtained with stressed samples. At this stage we considered the assay as “fit for purpose” but not validated per ICH guidelines [19] since this would require further investigations on dependence of different lots of materials and a stricter SOP for the assay with defined acceptance criteria for different assay steps.

3.3. Analysis of several critical quality attributes in a single assay

Therapeutic anti-TNF- α antibodies function by blocking sites on TNF- α to prevent the binding of TNF- α to its receptors [20]. Additionally, binding of anti-TNF- α antibodies, such as infliximab, to Fc γ RIIIa has been implicated in Crohns disease [21] whereas enhanced levels of Fc γ RI may reduce the efficacy of infliximab in inflammatory bowel diseases [22]. The mechanisms of action for anti-TNF- α biotherapeutics and the links to molecular properties may not be fully understood [23], but may potentially be linked to epitope specificity or Fc-functionalities.

By including a second injection of receptor after the antibody injection in the biotin capture assay described above, we performed proof-of-principle studies to determine potency values related to several antibody functions in a single sensorgram.

A fixed concentration of TNF- α receptor I was injected after each antibody concentration Fig. 3A. No binding of TNF- α receptor to captured TNF- α was seen after high antibody concentrations, whereas receptor binding was clearly visible at low antibody concentrations, verifying that the antibody could block receptor binding to TNF- α . By plotting the receptor response versus antibody concentration (Fig. 3B) an IC50 of 1.0 $\mu\text{g/mL}$ was determined. Similarly, binding of Fc γ RI increased with increasing antibody concentrations (Fig. 3C) and from a plot of receptor response versus antibody concentration an EC50 value of 5.38 $\mu\text{g/mL}$ was determined for Fc γ RI-binding (Fig. 3D). These results indicate that SPR can be used to quickly define an array of potency data in order to provide a comprehensive potency profile of the antibody. As long as the antibody does not dissociate from the antigen surface, this type of assay may be extended to include additional binding events. In such a scenario, receptors that dissociate rapidly, such as

FcγRII, can be injected first, followed by injections of higher affinity receptors.

Sequential binding of a bispecific antibody to immobilized antigen 1 followed by antigen 2 binding has been reported previously [13]. In that paper, data were combined to derive a single potency value for antibody-antigen binding. Here we extend the analysis beyond antigen binding and demonstrate sequential binding in competitive (TNF-α receptor) and secondary (FcγRI) modes. Thus, from a single assay, potency values for both antibody binding to antigen and receptor binding to antibody (Fig. 3) can be derived.

3.4. Simulation of dose response curves

With potency and relative potency values determined from dose response curves, it is essential that the underlying data accurately reflect a concentration but not changes in binding properties. This is because changes in binding properties may not be compensated for by adjusting the dose.

The impacts of changes in either concentration or in binding kinetics on the shape and position of dose response curves were investigated by simulating interaction data (see Section 2.5 for equations). Two cases presented in Fig. 4 were considered. In both simulations, the binding capacity was set to 100 RU, the injection time to 100 s, and the dissociation time to 0 s. These response levels and injection times reflect a practical experimental design.

In Fig. 4A, response values for the reference sample were calculated based on inputs of kinetic data resembling the binding of Interferon-α 2a to its receptor [15] with k_a $1.2 \times 10^7 \text{ M}^{-1} \text{ s}^{-1}$ and k_d $2.5 \times 10^{-2} \text{ s}^{-1}$. This represents a fairly unstable interaction with a half time of the complex of less than 30 s. Furthermore, with an injection time of 100 s, binding levels are close to steady state. In Fig. 4A, curve 3 marked with a thick line corresponds to the reference. In curve 1, the dissociation rate constant was changed to $6.25 \times 10^{-3} \text{ s}^{-1}$, i.e. the binding was four times more stable than the reference. The shift of curve 1 to the left and the altered slope reflect the higher affinity obtained with this condition. For curve 2, the concentrations were doubled but still plotted versus the nominal concentration of the reference. Again, the curve was shifted to the left as higher response values were obtained in the simulation. In curve 4, the association rate constant was $6.0 \times 10^6 \text{ M}^{-1} \text{ s}^{-1}$, i.e. half the value of the reference. In this case the curve was shifted to the right reflecting a lower affinity.

In the second simulation, an interaction characterized by significantly higher binding stability (slower dissociation rate, Fig. 4B) was studied. Input values for the reference sample resembled TNF-α binding to anti-TNF-α antibody with rate constants k_a $1.6 \times 10^6 \text{ M}^{-1} \text{ s}^{-1}$ and k_d $8.5 \times 10^{-5} \text{ s}^{-1}$. For this case the half time of the complex is 136 min, but with an injection time of 100 s, response levels are far from steady state. In Fig. 4B curve 3 marked with a thick line corresponds to the reference sample. First, for curve 1, the concentration was doubled but still plotted versus the nominal concentration of the reference. As shown in Fig. 4A, the use of a higher concentration resulted in higher response values and thus shifted the dose response curve to the left. Next, changes in the dissociation rate were simulated. For curve 2, the dissociation rate constant was increased to $3.4 \times 10^{-4} \text{ s}^{-1}$ (four times faster than the reference). For this input, the dose response curve still almost overlapped with the reference despite a fourfold lower affinity. Notably when the dissociation rate constants were instead decreased, making the interaction more stable, this change did not shift the dose response curve at all, even for a twenty-fold decrease. Finally, for curve 4, the association rate constant was two times lower than the reference, i.e. $8.0 \times 10^5 \text{ M}^{-1} \text{ s}^{-1}$. Here the dose response curve was shifted to the right as response levels were lower for each concentration.

Clearly the position of the dose response curve and hence EC50 values depend not only on changes in concentration but also on changes in kinetic properties.

Changes in concentration and association rate constants always shifted the dose response curves, but a change in dissociation rate constant gave variable results. In the second example, that is likely to be representative of many therapeutic antibodies, changes in dissociation properties can go unnoticed when only dose response curves are considered.

Simulations based on the 1:1 interaction model can be considered as an ideal case. With antigen captured or immobilized to the sensor surface, the 1:1 binding model is strictly not valid as avidity effects may impact binding kinetics. The interaction becomes more complex, but binding levels will still be determined by the kinetic properties of the interaction. Since avidity typically leads to slower dissociation, changes in dissociation rate constants may therefore be even more difficult to detect.

Therefore, these simulations demonstrate that relative potency data based on PLA or EC50 analysis will accurately reflect changes in concentration only if kinetic properties are unchanged and that common slope and asymptotes of dose response curves cannot be interpreted as unchanged binding properties.

3.5. Sensorgram comparison and dose response curves

Because the dose and kinetics of binding contribute to the safety and efficacy of the drug, it will be important to use an assay that is capable not only of EC50 analysis but also of kinetic analysis. In contrast to ELISA, which only provides a response that can lead to an affinity value, SPR assays inherently provide both a response and a sensorgram that can reflect not only the affinity, but more importantly, the kinetics of binding.

The sensorgram comparison tool in the Biacore software was now used to define a comparison window (Fig. 5A) that reflects the binding properties of the reference anti-TNF-α antibody. The reference window was determined with replicates by using sensorgrams obtained with 4.4 μg/mL of antibody and by using the min/max algorithm to create the comparison window. With this algorithm, the upper and lower limit sensorgrams correspond to sensorgrams that give the highest and lowest response values at any given time. Distances from the median sensorgram are used for calculations of similarity scores. A sample curve that falls between the upper and lower limit sensorgrams will receive a similarity score of 100%. Samples with data outside the comparison window will receive a lower similarity score [15].

We have previously demonstrated that the analysis would be focused on curve shapes by normalizing response levels to the highest response in each sensorgram [15]. The comparison window reflects an expected result, and a sample that falls inside the comparison window meets the kinetic criteria of the assay. A second preparation of reference sample running at the same concentration was within the comparison window, indicating unchanged kinetic properties (Fig. 5B).

The comparison window defined in Fig. 5B was very narrow. By incorporating potential errors into the analyte concentration, a wider and perhaps more realistic comparison window can readily be defined. Assuming a 10% error in analyte concentration, this would correspond to running the 4.4 μg/mL sample deliberately diluted to 4.0 and 4.8 μg/mL.

In Figs. 5C and D, binding of heat stressed anti-TNF-α antibodies to TNF-α followed by binding of FcγRIIIa Val 158 is presented. Antigen binding of stressed antibodies was reduced (Fig. 5C), and it was difficult to interpret if antibody dissociation and FcγRIIIa binding were impacted by stress. Binding curves obtained with the non-stressed antibody at concentrations of 1.5 and 4.4 μg/mL were used to define a broad comparison

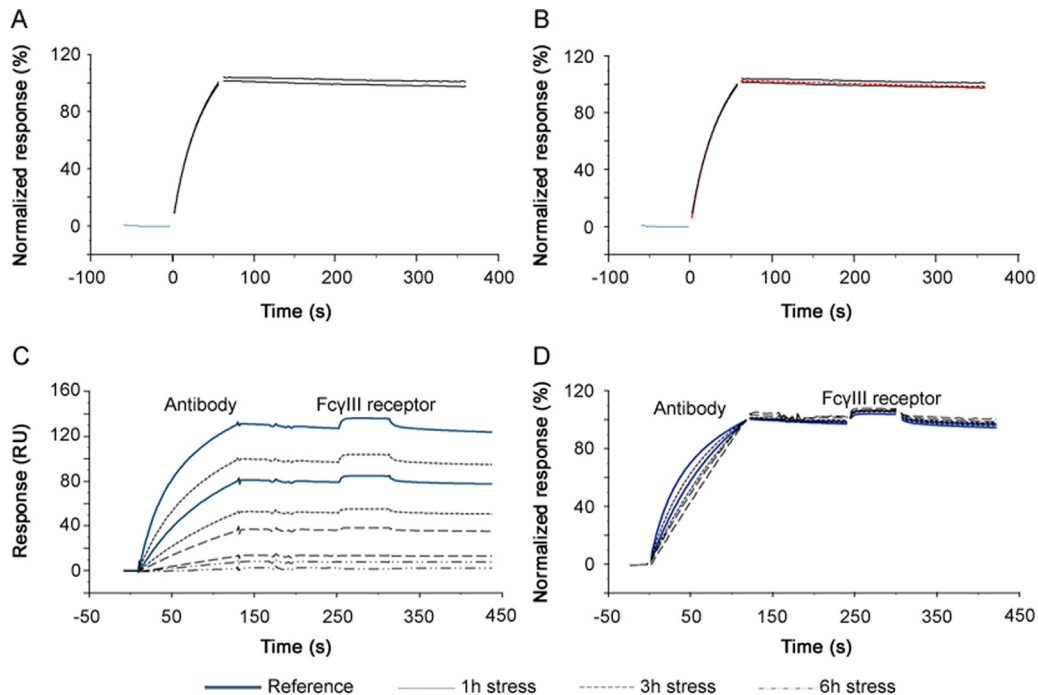


Fig. 5. Sensorgram comparison. (A) Maximum and minimum sensorgrams obtained with a reference antibody using repeat injections of a constant (4.44 $\mu\text{g/mL}$) antibody concentration. (B) A new sample was within the comparison window defined by the sensorgrams in Fig. 5A, demonstrating the new sample shares the kinetic profile of the reference. (C) Dual potency assay with antibody, injected at varying concentrations, binding to antigen followed by injection of Fc γ RIIIa Val158 at a constant concentration. The thick blue lines correspond to the reference antibody injections at 1.5 and 4.4 $\mu\text{g/mL}$. The dashed lines represent the same antibody concentrations injected after 1, 3 and 6 h of stress. Stressed antibodies produced lower responses. (D) By normalizing each sensorgram from Fig. 6C, all sensorgrams are displayed in the same relative scale. The reference antibody curves (thick blue lines) defined a comparison window for both antibody and receptor binding. Stressed antibodies share dissociation and Fc γ RIIIa binding profiles, but kinetic profiles differ during antibody binding. This can be due to changes in either antibody concentration or in the antibody association rate constant.

window using the min/max algorithm. In Fig. 5D, normalized binding curves are shown. The solid blue lines represent the non-stressed sample and define the comparison window. Data from stressed samples obtained at the same two concentrations as the reference are shown as dashed lines. After 1 h of stress, antibodies started to fall outside the antibody association phase of the comparison window, but antibody dissociation and Fc γ RIIIa binding fell almost completely inside the comparison window. After 3 h of stress, both antibody samples were clearly outside the association phase comparison window. Since binding levels were much lower for these samples, the noise was more apparent and antibody dissociation and Fc γ RIIIa binding curves were shifted slightly upwards; however, the antibody dissociation and Fc γ RIIIa curves still resembled reference curves. Samples stressed for 6 h were characterized by low response levels and became too noisy to analyze when normalized to 100%. These curves are therefore not shown in Fig. 5D.

The comparison window, defined in the sensorgram comparison tool, should reflect an expected outcome. With a very narrow comparison window, as in the first example (Figs. 5A and B), new samples that only differ marginally from the reference, may fall outside the comparison window, and small differences may be overinterpreted. In the second example (Figs. 5C and D) the comparison window was wider, and two concentrations flanking the EC50 value were used to define the comparison window. Stressed antibody samples still fell outside the antigen binding phase, indicating large effects of heat stress on antigen binding. However, antibody dissociation and Fc γ RIIIa binding were similar for stressed samples and the reference.

3.6. CFCA for determination of relative antibody concentration

CFCA is an independent measurement of active concentration, where results are obtained under at least partial mass transport

limited conditions. Binding responses and therefore concentration values are largely independent of the kinetics of binding [24]. CFCA of stressed antibodies allowed active concentration data, with respect to both TNF- α (Fig. 6A) and SuRe ligand binding (Fig. 6B), to be determined. The data shown in Fig. 6 are for the 2 h stressed samples. In each figure, six sensorgrams are shown with two curves each for dilution factors 2, 4 and 8. For each dilution the top curve was recorded at a flow rate of 100 $\mu\text{L/min}$ and the lower curve at a flow rate of 5 $\mu\text{L/min}$. Data from the first 25 s of the injections were fitted and resulted in calculated concentrations of 5.8 (TNF- α surface) and 5.5 nM (SuRe ligand surface) for the undiluted sample. CFCA results can be affected by uncertainties in the diffusion coefficient and molecular weight of the sample (two parameters needed for CFCA) and by the conversion of the SPR signal to a mass value as discussed previously [17]. However, these uncertainties cancel out when the ratio between a sample antibody and a reference antibody is used. Relative CFCA values were therefore calculated by setting the non-stressed antibody concentration to 100%. Interestingly, relative CFCA data for the paratope and Fc-domain were very close, indicating identical changes in active concentrations of both parts of the antibody. Furthermore, relative concentrations correlated perfectly with relative potency values determined with PLA (Fig. 6C). The data strongly support the interpretation that the change in EC50 was due to changes in the active concentration and not changes in the association rate constant. Additionally, the data suggest that CFCA can be used as an alternative to dose response curves for the determination of relative potencies. This merits further investigations, as data were obtained only for the anti-TNF- α antibody, and other antigens and antibodies were not tested.

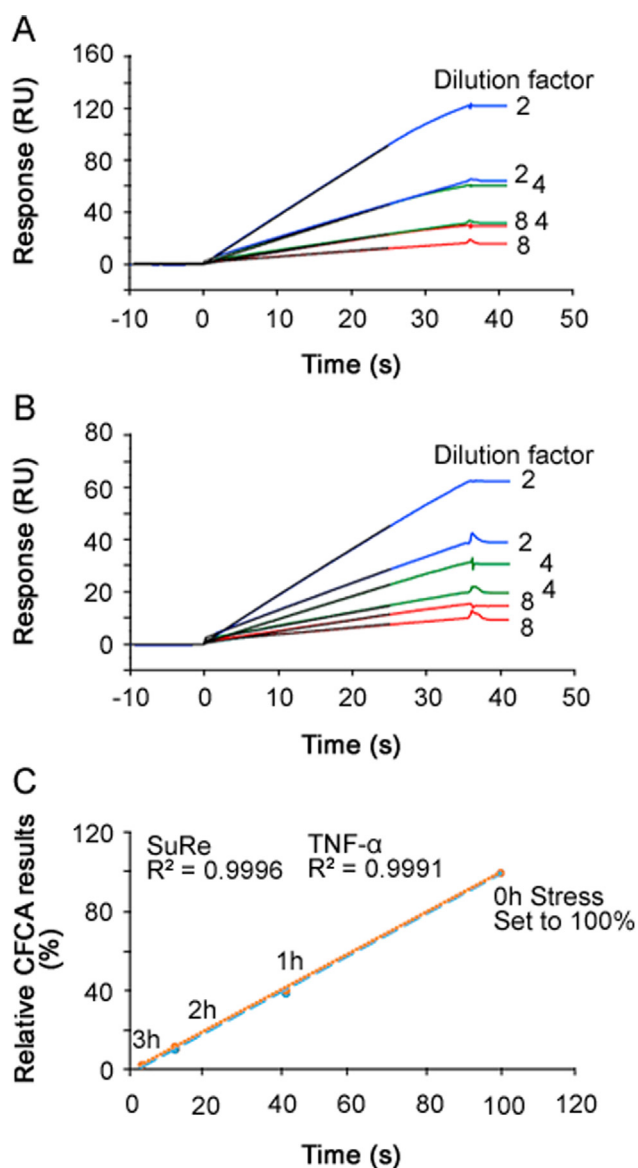


Fig. 6. Calibration Free Concentration Analysis (CFCA). (A) Three dilutions of anti-body, stressed for 2 h, were injected using flow rates of 5 and 100 $\mu\text{L}/\text{min}$ for binding to immobilized TNF- α . The black lines, present up to 25 s into the injection, represent CFCA fitted curves. The concentration of the undiluted sample was calculated to be 5.8 nM. (B) Three dilutions of antibody, stressed for 2 h, were injected using flow rates of 5 and 100 $\mu\text{L}/\text{min}$ for binding to immobilized MabSelect SuRe ligand (a protein A variant). The black lines, present up to 25 s into the injection, represent CFCA fitted curves. The concentration of the undiluted sample was calculated to be 5.5 nM. (C) Relative CFCA data plotted versus relative potency values determined via PLA (Table 3). Data for TNF- α and SuRe ligand binding are very close and CFCA data correlated perfectly with relative potency values. In this way, for any change in active concentration related to two different functional domains, the paratope and the Fc region of the antibody could be investigated.

4. Summary and conclusions

Potency determinations are required for the release of every lot of a therapeutic antibody [25]. While the release assay is typically a bioassay, alternatives such as ELISA as a surrogate potency assay have been in use for almost four decades [26]. While initially used to correlate a binding level to lethal doses of antivenoms, the use of ligand binding assays is now much greater [27], as mechanisms of actions are better understood. The potency assay format is not only used as a release assay, but can be used throughout the development process in comparability studies and formulation studies to ensure consistency between drug substance and drug product.

Compared to the panel of bioassays [23] described for anti-TNF- α biotherapeutics, ligand binding assays as described in this paper appear far easier to set up and maintain. PLA and EC50 analysis on SPR platforms have traditionally been focused on comparison of dose response curves [12–14]. Here, we have demonstrated that the position of dose response curves and therefore relative potency determinations are not only sensitive to changes in active concentration but also to changes in binding properties. Such changes may not always be compensated for by adjustment of the dose. For instance, large differences between the reference and sample in dissociation properties, which may go undetected in dose response curve analysis, can impact drug residence time and therefore potentially affect the drug efficacy [28]. By complementing dose response curves with sensorgram comparisons, such deviations, can be detected as sensorgram comparison checks for compliance with kinetic properties. The analysis compares reference and sample curves directly, and can be applied to both simple and complex binding data and can be used even with slow off-rates [29]. Furthermore, several injections can be compared in the software such that several critical quality attributes can be compared in a single assay.

For the current assay set-up, we used reversible biotin capture to avoid common bottle necks associated with SPR assay development such as optimization of immobilization and regeneration conditions. By using this setup, it was possible (1) to set up surrogate potency assays with the capture of biotinylated target molecules in a straightforward fashion without the need of optimizing regeneration conditions, (2) to estimate the potency related to several CQAs (antigen and receptor binding) in a single sensorgram, and (3) to combine dose response curves with sensorgram comparison to ensure consistent interaction kinetics for correct interpretation of EC50 values as a dose.

To resolve remaining uncertainties in the interpretation of dose response curves obtained with stressed anti-TNF- α antibodies, CFCA was used in an attempt to differentiate between changes due to changes either in active concentration or in association rate constants. CFCA data linked to the paratope and to the Fc-domain were close and indicated that the differences were related to changes in the active concentration. The correlation established between the relative CFCA and relative potency values further indicated that CFCA and sensorgram comparison can be used directly to determine the relative potency without the need to establish full dose response curves. Ideally, CFCA determines concentrations directly with no impact of kinetics on the concentration data. It is typically used in the concentration range from 1 to 100 nM; it is rapid, and the linearity of the assay is demonstrated by fitting an entire dilution series to obtain a single concentration value. While CFCA data related to antigen and Fc functionalities were shown, the use of CFCA as a general potency tool still needs to be demonstrated with direct measurements of CFCA on a range of relevant antigens and Fc-receptors. If this can be demonstrated, the use of relative CFCA data and the sensorgram comparison functionality can potentially replace the use of the full dose response curves and PLA that are typically used for determination of relative potencies based on ligand binding assays. CFCA can be used to calculate relative potencies directly from the ratio between sample and reference concentrations, whereas sensorgram comparison can be used to detect unwanted changes in binding properties/kinetics.

Finally, as the links between molecular properties and clinical effects become more established, ligand binding assays may be more frequently used not only for comparability and biosimilarity studies, but also for batch release.

Conflicts of interest

All authors were employed by GE Healthcare during the preparation of this article. GE Healthcare is the provider of Biacore systems, sensor chips and reagents.

References

- [1] M. Schröml, M. Biehl, Kinetic screening in the antibody development process, *Antib. Methods Protoc.* 901 (2012) 171–181.
- [2] Y.N. Abdiche, R. Harriman, X. Deng, et al., Assessing kinetic and epitopic diversity across orthogonal monoclonal antibody generation platforms, *MAbs* 8 (2016) 264–277.
- [3] P. Bruhns, B. Iannascoli, P. England, et al., Specificity and affinity of human Fcγ receptors and their polymorphic variants for human IgG subclasses, *Blood* 113 (2009) 3716–3725.
- [4] K.H. Heider, K. Kiefer, T. Zenz, et al., A novel Fc-engineered monoclonal antibody to CD37 with enhanced ADCC and high proapoptotic activity for treatment of B-cell malignancies, *Blood* 118 (2011) 4159–4168.
- [5] J.M. Hayes, A. Frostell, E.F. Cosgrave, et al., Fc gamma receptor glycosylation modulates the binding of IgG glycoforms: a requirement for stable antibody interactions, *J. Proteome Res.* 13 (2014) 5471–5485.
- [6] W.F. Dall'Acqua, P.A. Kiener, H. Wu, Properties of human IgG1s engineered for enhanced binding to the neonatal Fc receptor (FcRn), *J. Biol. Chem.* 281 (2006) 23514–23524.
- [7] T. Suzuki, A. Ishii-Watabe, M. Tada, et al., Importance of neonatal FcRn in regulating the serum half-life of therapeutic proteins containing the Fc domain of human IgG1: a comparative study of the affinity of monoclonal antibodies and Fc-fusion proteins to human neonatal FcRn, *J. Immunol.* 184 (2010) 1968–1976.
- [8] D.C. Swinney, J. Anthony, How were new medicines discovered? *Nat. Rev. Drug Discov.* 10 (2011) 507–519.
- [9] B.C. Barnhart, M. Quigley, Role of Fc–FcγR interactions in the antitumor activity of therapeutic antibodies, *Immunol. Cell Biol.* 95 (2016) 340–346.
- [10] E.S. Ward, S.C. Devanaboyina, R.J. Ober, Targeting FcRn for the modulation of antibody dynamics, *Mol. Immunol.* 67 (2015) 131–141.
- [11] **Quality Considerations in Demonstrating Biosimilarity of a Therapeutic Protein Product to a Reference Product**, FDA Guidance to Industry, April, 2015.
- [12] A. Harrison, Z. Liu, S. Makweche, et al., Methods to measure the binding of therapeutic monoclonal antibodies to the human Fc receptor FcγRIII (CD16) using real time kinetic analysis and flow cytometry, *J. Pharm. Biomed. Anal.* 63 (2012) 23–28.
- [13] C. Gassner, F. Lipsmeier, P. Metzger, et al., Development and validation of a novel SPR-based assay principle for bispecific molecules, *J. Pharm. Biomed. Anal.* 102 (2015) 144–149.
- [14] S. Khurana, L.R. King, J. Manischewitz, et al., Novel antibody-independent receptor-binding SPR-based assay for rapid measurement of influenza vaccine potency, *Vaccine* 32 (2014) 2188–2197.
- [15] R. Karlsson, E. Pol, A. Frostell, Comparison of surface plasmon resonance binding curves for characterization of protein interactions and analysis of screening data, *Anal. Biochem.* 502 (2016) 53–63.
- [16] E. Pol, H. Roos, F. Markey, et al., Evaluation of calibration-free concentration analysis provided by Biacore™ systems, *Anal. Biochem.* 510 (2016) 88–97.
- [17] R. Karlsson, Biosensor binding data and its applicability to the determination of active concentration, *Biophys. Rev.* 8 (2016) 347–358.
- [18] L. Nieba, S.E. Nieba-Axmann, A. Persson, et al., BIACORE analysis of histidine-tagged proteins using a chelating NTA sensor chip, *Anal. Biochem.* 252 (1997) 217–228.
- [19] **ICH Quality Guidelines. Validation of Analytical Procedures Q2 (R1)**, November 1996.
- [20] K. Lis, O. Kuzawińska, E. Bałkowiec-Iskra, Tumor necrosis factor inhibitors—state of knowledge, *Arch. Med. Sci.* 10 (2014) 1175–1185.
- [21] E. Louis, Z. El Ghouli, S. Vermeire, et al., Association between polymorphism in IgG Fc receptor IIIa coding gene and biological response to infliximab in Crohn's disease, *Aliment. Pharmacol. Ther.* 19 (2004) 511–519.
- [22] K.A. Wojtal, G. Rogler, M. Scharl, et al., Fc gamma receptor CD64 modulates the inhibitory activity of infliximab, *PLoS One* 7 (2012) e43361.
- [23] A. Nesbitt, G. Fossati, M. Bergin, et al., Mechanism of action of certolizumab pegol (CDP870): In vitro comparison with other anti-tumor necrosis factor alpha agents, *Inflamm. Bowel. Dis.* 13 (2007) 1323–1332.
- [24] L.H. Christensen, Theoretical analysis of protein concentration determination using biosensor technology under conditions of partial mass transport limitation, *Anal. Biochem.* 249 (1997) 153–164.
- [25] **FDA Code of Federal Regulation Title 21/FDA Code of Federal Regulation Title 21**, < https://www.ecfr.gov/cgi-bin/text-idx?SID=49548554bcf36480326bd48e48599365&mc=true&tpl=/ecfrbrowse/Title21/21cfrv7_02.tpl#0 > .
- [26] R.D. Theakston, H.A. Reid, Enzyme-linked immunosorbent assay (ELISA) in assessing antivenom potency, *Toxicol.* 17 (1979) 511–515.
- [27] N. Rieder, H. Gazzano-Santoro, M. Schenerman, et al., The roles of bioactivity assays in lot release and stability testing, *BioProcess Int.* 8 (2010) 33–42.
- [28] R.A. Copeland, The drug–target residence time model: a 10-year retrospective, *Nat. Rev. Drug Discov.* 15 (2016) 87–95.
- [29] N. Papadopoulos, J. Martin, Q. Ruan, et al., Binding and neutralization of vascular endothelial growth factor (VEGF) and related ligands by VEGF Trap, ranibizumab and bevacizumab, *Angiogenesis* 15 (2012) 171–185.